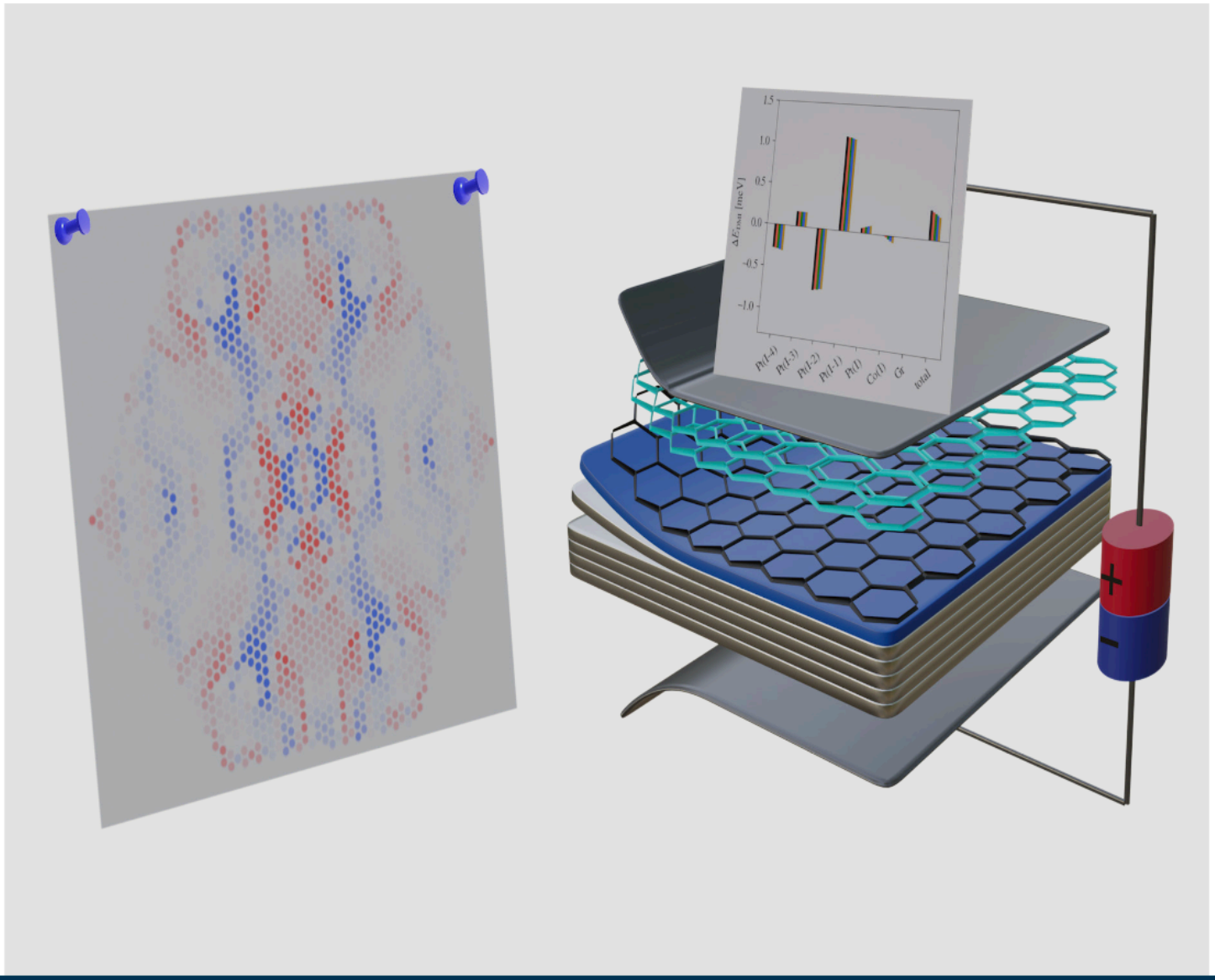



# Ab initio investigations of spin-orbit functionalized graphene

Donya Mazhjoo

Schlüsseltechnologien / Key Technologies
Band / Volume 299
ISBN 978-3-95806-847-6

Mitglied der Helmholtz-Gemeinschaft

JÜLICH
Forschungszentrum

# Ab initio investigations of spin-orbit functionalized graphene

Von der Fakultät für Mathematik, Informatik und Naturwissenschaften der RWTH Aachen University zur Erlangung des akademischen Grades einer Doktorin der Naturwissenschaften genehmigte Dissertation

vorgelegt von

**Donya Mazhjoo, M.Sc.**
aus
Teheran, Iran

Berichter: Univ.-Prof. Dr. rer. nat. Stefan Blügel

Univ.-Prof. Dr. rer. nat. Carsten Honerkamp

Tag der mündlichen Prüfung: 16. Juni 2025

Diese Dissertation ist auf den Internetseiten der Universitätsbibliothek verfügbar.

Forschungszentrum Jülich GmbH
Peter Grünberg Institut (PGI)
Quanten-Theorie der Materialien (PGI-1)

# Ab initio investigations of spin-orbit functionalized graphene

Donya Mazhjoo

Schriften des Forschungszentrums Jülich
Reihe Schlüsseltechnologien / Key Technologies Band / Volume 299

ISSN 1866-1807 ISBN 978-3-95806-847-6

Bibliografische Information der Deutschen Nationalbibliothek.
Die Deutsche Nationalbibliothek verzeichnet diese Publikation in der
Deutschen Nationalbibliografie; detaillierte Bibliografische Daten
sind im Internet über http://dnb.d-nb.de abrufbar.

| | |
|---|---|
| Herausgeber und Vertrieb: | Forschungszentrum Jülich GmbH<br>Zentralbibliothek, Verlag<br>52425 Jülich<br>Tel.: +49 2461 61-5368<br>Fax: +49 2461 61-6103<br>zb-publikation@fz-juelich.de<br>www.fz-juelich.de/zb |
| Umschlaggestaltung: | Grafische Medien, Forschungszentrum Jülich GmbH |
| Druck: | Grafische Medien, Forschungszentrum Jülich GmbH |
| Copyright: | Forschungszentrum Jülich 2025 |

Schriften des Forschungszentrums Jülich
Reihe Schlüsseltechnologien / Key Technologies, Band / Volume 299

D 82 (Diss. RWTH Aachen University, 2025)

ISSN 1866-1807
ISBN 978-3-95806-847-6

Vollständig frei verfügbar über das Publikationsportal des Forschungszentrums Jülich (JuSER)
unter www.fz-juelich.de/zb/openaccess.

This is an Open Access publication distributed under the terms of the Creative Commons Attribution License 4.0,
which permits unrestricted use, distribution, and reproduction in any medium, provided the original work is properly cited.

**Eidesstattliche Erklärung**

*Donya Mazhjoo*

erklärt hiermit, dass diese Dissertation und die darin dargelegten Inhalte die eigenen sind und selbstständig, als Ergebnis der eigenen originären Forschung, generiert wurden.

Hiermit erkläre ich an Eides statt

1. Diese Arbeit wurde vollständig oder größtenteils in der Phase als Doktorand dieser Fakultät und Universität angefertigt;

2. Sofern irgendein Bestandteil dieser Dissertation zuvor für einen akademischen Abschluss oder eine andere Qualifikation an dieser oder einer anderen Institution verwendet wurde, wurde dies klar angezeigt;

3. Wenn immer andere eigene- oder Veröffentlichungen Dritter herangezogen wurden, wurden diese klar benannt;

4. Wenn aus anderen eigenen- oder Veröffentlichungen Dritter zitiert wurde, wurde stets die Quelle hierfür angegeben. Diese Dissertation ist vollständig meine eigene Arbeit, mit der Ausnahme solcher Zitate;

5. Alle wesentlichen Quellen von Unterstützung wurden benannt;

6. Wenn immer ein Teil dieser Dissertation auf der Zusammenarbeit mit anderen basiert, wurde von mir klar gekennzeichnet, was von anderen und was von mir selbst erarbeitet wurde;

7. Kein Teil dieser Arbeit wurde vor deren Einreichung veröffentlicht.

*12.09.2024*

*The secrets of eternity, neither you know nor I.*
*The riddle of this tale, neither you read nor I.*
*Behind the veil a dialogue goes on, between you and me;*
*And when the veil is lifted, neither you remain, nor I.*

*— Omar Khayyam*

*For my family*

# Abstract

Graphene (Gr) has obtained significant attention in the realm of advanced information technologies due to its remarkable electronic properties, such as high carrier mobility, an unusual quantum Hall effect, and long spin lifetimes at room temperature. These attributes make Gr a promising candidate for various applications, particularly in spintronics. There, research on Co/Pt(111) ultra-thin films, widely utilized in perpendicular magnetic recording, focuses on enhancing material properties by adding buffer layers and alloying with other elements.
This thesis explores the electronic and magnetic properties of Gr when deposited on Co/heavy metal (HM) substrates, particularly focusing on Pt and Ir as HMs. Our investigation aims to elucidate the impact of Gr on Co/HM on magnetic exchange interactions, with a particular focus on understanding the spin-orbit coupling (SOC) effects like magnetocrystalline anisotropy (MCA) and the interfacial Dzyaloshinskii-Moriya interaction (DMI) at both Gr/Co and Co/HM interfaces. These interactions are pivotal in influencing various magnetic dynamics, including ferromagnetic resonance, spin waves, and the behavior of chiral domain walls and skyrmions.
Modern electronic systems aspire to achieve high-speed operation and low energy consumption, driving the development of electric-field-controlled spintronic devices. The experimental reports reveal evidence of interfacial DMI at the Gr/Co interface, contrasting with the SOC-induced DMI observed at the Co/HM interface. Additionally, we find that depositing Gr leads to a reduction in DMI, potentially enhancing the susceptibility of these structures to electric fields.
Efforts to manipulate DMI and MCA involve the application of electric fields and the introduction of various capping layers, including oxide capping layers and an HM overlayer, to engineer electronic and magnetic properties. Our exploration also extends to Gr-covered Co/Pt multilayers, known for their perpendicular magnetic anisotropy, contributing further to our understanding of the intricate interplay between material compositions and magnetic properties. These insights hold potential implications for engineering DMI and MCA in future spintronic devices.
Theoretical advancements, particularly in density functional theory (DFT), play a crucial role in unraveling material properties. The Full-potential Linearized Augmented Planewave (FLAPW) method is renowned for its versatility and accuracy, making it a widely accepted computational approach in materials science. Utilizing the FLAPW method enables us to handle complex systems, encompassing those with heavy atoms and pronounced SOC effects. In this thesis, we utilize the FLEUR code, which employs the film FLAPW method to compute the DMI in the electric field, an essential parameter in spintronics research. Our calculations consider SOC effects both in a first-order perturbation theory for the DMI and self-consistently for the MCA, aiming to stimulate SOC-induced effects and deepen our understanding of these phenomena.

# Kurzfassung

Graphen (Gr) hat aufgrund seiner bemerkenswerten elektronischen Eigenschaften wie der hohen Ladungsträgerbeweglichkeit, dem ungewöhnlichen Quanten-Hall-Effekt und der langen Spin-Lebensdauer bei Raumtemperatur große Aufmerksamkeit im Bereich der fortgeschrittenen Informationstechnologien erhalten. Diese Eigenschaften machen Gr zu einem vielversprechenden Kandidaten für verschiedene Anwendungen, insbesondere in der Spintronik. Dort konzentriert sich die Forschung auf ultradünnen Co/Pt(111)-Filmen, die in der magnetischen Senkrechtaufzeichnung weit verbreitet sind, auf die Verbesserung der Materialeigenschaften durch das Hinzufügen von Pufferschichten und die Legierung mit anderen Elementen.
In dieser Arbeit werden die elektronischen und magnetischen Eigenschaften von Gr untersucht, wenn es auf Co/Schwermetall (HM)-Substraten deponiert wird, wobei der Schwerpunkt auf Pt und Ir als HMs liegt. Unsere Untersuchung zielt darauf ab, die Auswirkungen von Gr auf Co/HM auf magnetische Austauschwechselwirkungen zu klären, mit einem besonderen Fokus auf das Verständnis der Spin-Bahn-Kopplungseffekte (SOC) wie magnetokristalline Anisotropie (MCA) und die Grenz-flächen-Dzyaloshinskii-Moriya-Wechselwirkung (DMI) sowohl an Gr/Co- als auch an Co/HM-Grenzflächen. Diese Wechselwirkungen spielen eine zentrale Rolle bei der Beeinflussung verschiedener magnetischer Dynamiken, einschließlich ferromagnetischer Resonanz, Spinwellen und dem Verhalten chiraler Domänenwände und Skyrmionen.
Moderne elektronische Systeme streben einen hohe Geschwindigkeiten und einen niedrigen Energieverbrauch an, was die Entwicklung von durch elektrische Felder gesteuerten spintronischen Bauelementen vorantreibt. Die experimentellen Arbeiten zeigen Hinweise auf Grenzflächen-DMI an der Gr/Co-Grenzfläche, die im Gegensatz zu der SOC-induzierten DMI an der Co/HM-Grenzfläche stehen. Darüber hinaus stellen wir fest, dass die Deposition von Gr zu einer Verringerung der DMI führt, was möglicherweise die Empfindlichkeit dieser Strukturen gegenüber elektrischen Feldern erhöht. Unsere Bemühungen zur Beeinflussung von DMI und MCA umfassen die Anwendung elektrischer Felder und die Einführung verschiedener Deckschichten, einschließlich Oxid-Deckschichten und einer HM-Überschicht, um die elektronischen und magnetischen Eigenschaften zu verbessern. Unsere Untersuchungen erstrecken sich auch auf Gr-bedeckte Co/Pt-Multischichten, die für ihre senkrechte magnetische Aniso-tropie bekannt sind, und tragen weiter zu unserem Verständnis des komplizierten Zusammenspiels zwischen Materialzusammensetzung und magnetischen Eigenschaften bei. Diese Erkenntnisse haben potenzielle Auswirkungen auf den Einsatz von DMI und MCA in zukünftigen spintronischen Bauelementen.
Theoretische Fortschritte, insbesondere in der Dichtefunktionaltheorie (DFT), spielen eine entscheidende Rolle bei der Entschlüsselung von Materialeigenschaften. Die FLAPW-Methode (Full-potential Linearized Augmented Planewave) ist bekannt

für ihre Vielseitigkeit und Genauigkeit, was sie zu einem weithin akzeptierten Berechnungsansatz in der Materialwissenschaft macht. Die Verwendung der FLAPW-Methode ermöglicht es uns, komplexe Systeme mit schweren Atomen und ausgeprägten SOC-Effekten zu behandeln. In dieser Arbeit verwenden wir den FLEUR-Code, der die Film-FLAPW-Methode zur Berechnung des DMI im elektrischen Feld einsetzt, einem wesentlichen Parameter in der Spintronikforschung. Unsere Berechnungen berücksichtigen SOC-Effekte sowohl in einer Störungstheorie erster Ordnung für die DMI als auch selbstkonsistent für die MCA, mit dem Ziel, SOC-induzierte Effekte zu stimulieren und unser Verständnis dieser Phänomene zu vertiefen.

# Contents


**1. Introduction** **5**

**2. Density Functional Theory** **11**
2.1. Hamiltonian in many-body systems . . . . . 11
2.2. The Thomas-Fermi model . . . . . 12
2.3. Hohenberg-Kohn theorem . . . . . 13
2.4. Kohn-Sham equation . . . . . 14
2.5. Exchange-correlation energy approximations . . . . . 15
2.6. Vector-spin DFT . . . . . 15
2.7. Relativistic effects . . . . . 16

**3. Augmented planewave methods** **19**
3.1. Basis set for density functional theory . . . . . 20
3.1.1. Augmented planewaves . . . . . 20
3.1.2. Linearized augmented planewaves . . . . . 21
3.1.3. Full-potential linearized augmented planewave method . . . 22
3.1.4. Extending the basis set with local orbitals . . . . . 23
3.2. Brillouin zone . . . . . 23
3.3. The FLAPW method for the film geometry . . . . . 24
3.3.1. Treatment of External Electric Fields . . . . . 26
3.4. Magnetic calculations . . . . . 27
3.4.1. Collinear magnetism . . . . . 27
3.4.2. Non-collinear magnetism . . . . . 28
3.4.3. The implementation of non-collinear magnetism in the FLAPW method . . . . . 30
3.5. Spin-spirals . . . . . 30
3.5.1. Generalized Bloch theorem . . . . . 31
3.6. Spin-orbit coupling and spin-spirals . . . . . 32

**4. Spin models** **35**
4.1. Heisenberg-type exchange interaction . . . 36
4.2. Dyzaloshinskii-Moriya interaction . . . 37
4.3. Magnetic anisotropy . . . 38
4.3.1. Magnetic shape anisotropy . . . 39
4.3.2. Magnetocrystalline anisotropy . . . 40

**5. Exploring graphene coverage on Co/HM(111) substrates** **41**
5.1. Investigating the electronic structure . . . 42
5.2. Exchange interaction in Gr on Co/Pt(111) . . . 46
5.3. Tailoring interlayer distances of Gr and Co . . . 49
5.4. DMI in Gr/Co/HM(111) . . . 51
5.4.1. DMI across various stackings of Gr on Co/Pt(111) . . . 56
5.5. MCA in Gr/Co/HM . . . 60

**6. The role of Co thickness in DMI enhancement** **67**
6.1. Enhancing structural optimization . . . 68
6.2. Evolution of spin texture of Gr adjacent to 3ML Co/5ML Pt(Ir) . . . 69
6.3. DMI variations across different Co thicknesses . . . 71
6.3.1. Enhancing the thickness in HM layers . . . 76

**7. DMI manipulation through electric field and oxide capping** **81**
7.1. Applying an external electric field . . . 82
7.1.1. Structural optimization . . . 82
7.1.2. DMI . . . 86
7.1.3. MCA . . . 91
7.2. Implementing an oxide capping layer . . . 93
7.2.1. Structural optimization . . . 93
7.2.2. DMI . . . 96
7.3. Electrical control of BeO/GrCoPt(111) . . . 101
7.3.1. Structural optimization . . . 101
7.3.2. DMI . . . 102

**8. Evolution of material composition** **107**
8.1. Heavy metal capping layer . . . 108
8.1.1. Structural optimization . . . 108
8.1.2. DMI . . . 111
8.1.3. MCA . . . 115
8.2. Co/Pt multilayered films . . . 118
8.2.1. Structural optimization . . . 118
8.2.2. DMI . . . 121
8.2.3. MCA . . . 123

**9. Summary and Conclusions** **127**

**List of Figures** **131**

**List of Tables** **137**

**List of Abbreviations** **141**

**Appendix A. Computational details** **144**

**Bibliography** **147**

**Publication** **161**

**Acknowledgement** **163**

# 1 Introduction

As traditional silicon-based technologies encounter limitations, various alternative approaches like nanoelectronics, molecular electronics, and spintronics have gained interest [1, 2]. Spintronics, in particular, revolutionizes information processing by encoding data in the direction of spin, transporting it along designated paths, and reading it at the final destination. Ensuring the spin orientation of conduction electrons is sustained along the transport path for several nanoseconds is crucial for their viability in electrical circuits and chips. A common method to achieve this is by passing current through a ferromagnetic (FM) material and transmitting the spin-polarized electrons to a receiver. Successful implementation of spintronic devices and circuits depends on various functionalities, including spin detection, spin transport, spin manipulation, spin-optical interaction, and single spin devices [3].
Moreover, perpendicular magnetic anisotropy (PMA) assumes a pivotal role in spin-orbitronic devices, particularly in downsizing data storage spintronic devices like spin transfer torque magnetic random access memories (STT-MRAM) [4, 5]. Maximizing PMA is essential for modern spintronic devices, including STT MRAM and spin-orbit torque (SOT) MRAM [6, 7].
In the pursuit of advanced information technologies, high-speed operation, and low-energy consumption [8] are prioritized. Non-collinear magnetic structures, such as skyrmions, have received significant interest due to their unique properties and potential applications in information technology [9]. Similarly, localized non-collinear magnetic textures like domain walls (DWs) have emerged as promising candidates for innovative advancements, especially in the realm of information storage [10].
Materials with suitable spin transport channels, offering long spin lifetimes, extended spin propagation distances, and topologically stable spin textures have attracted attention for their potential to realize high-density, low-power, and fast-spin devices [9]. The emergence of two-dimensional (2D) materials offers new opportunities, which possess numerous attractive characteristics. Among the proposed materials, carbon nanotubes stand out as a prominent example of nontraditional materials whose properties can be modulated by an electric field [11]. Carbon nan-

otubes and graphene (Gr) are notable examples of such materials, with Gr exhibiting long spin lifetimes and propagation lengths at room temperature [12].
The technique of micromechanical cleavage enables the deposition of a single Gr sheet onto an insulating substrate, facilitating electron transport experiments on this 2D system [13]. Furthermore, the observation of the electric field effect in a naturally occurring two-dimensional material referred to as few-layer Gr on top of an oxidized Si wafer [14], highlights the substantial influence of Gr's surroundings, particularly its substrate, on its electronic characteristics [15]. To develop Gr-based spintronics devices, it's essential to integrate additional active properties into Gr. Recent breakthroughs have demonstrated the generation of long-range magnetic order and spin filtering in Gr through molecular functionalization [16]. Additionally, significant progress has been made in introducing "giant" spin-orbit coupling (SOC) into Gr's electronic bands via intercalation techniques [17, 18]. It has been demonstrated that the characteristic electronic structure of Gr experiences significant alteration that can be reduced by intercalation upon chemisorption on Co, Ni, and Pd [19]. Inducing significant SOC in Gr without compromising its inherent Dirac cone structure is crucial for practical applications utilizing spin-orbit effects.
Moreover, the discovery of a potent Dzyaloshinskii-Moriya interaction (DMI) at the interface of Gr and FM materials [20] is a pivotal development in advancing SO technology, as it facilitates the electrical modulation of transport and manipulation of magnetically (topologically) protected structures. The successful integration of Gr as an efficient spin transport medium into technologies reliant on chiral spin textures hinges on our ability to fabricate Gr-based PMA systems with finely tuned interfacial SOC. The realization of Gr-mediated antiferromagnetic coupling between ferromagnets [21] and the groundwork laid for engineering ferroelectricity for various ferroelectric memory applications demonstrate significant advancements. These achievements highlight the adept manipulation of SOC through metal intercalation [22] and the precise modulation of critical magnetic interactions, including perpendicular anisotropy and interfacial DMI, via layer engineering. Besides, significant progress has been made in studying the electric field-induced changes in magnetization in thin films and advancing the development of 2D magnetic tunnel junctions (2D-MTJ) [23, 24]. Extensive research has been conducted on the source of PMA at both the HM/FM and FM/oxide interfaces [25, 26, 27, 28, 29, 30]. Utilizing both the top and bottom interfaces of the FM layer is a common strategy to enhance the overall PMA of the system [31]. For instance, multilayers consisting of repeated FM/HM bilayers, like Co/Pt multilayers, serve as the reference layer for STT-MRAM [32].
Comprehending magnetic interactions is fundamentally significant in condensed matter physics and the development of spintronic devices. The stabilization of non-collinear magnetic states relies on the interplay of various competing interactions [33]. Owing to the inversion asymmetric structure, an anisotropic exchange coupling known as the (interfacial) DMI arises at the interface between the heavy metal (HM), such as Pt, and an FM layer, such as Co. This interfacial DMI plays a

crucial role in stabilizing non-trivial topological magnetic solitons, such as magnetic skyrmions [33, 34] and chiral DWs [35, 36]. The DMI is prominent in systems characterized by large SOC and broken inversion symmetry, such as at the interfaces of Co and Ir or Pt [37]. Utilizing both the top and bottom interfaces of the FM layer can enhance the overall PMA of the system [31]. Cobalt-based multilayer systems have become a focal point of research, spurred by the exciting revelation of magnetic skyrmions existing at room temperature [38, 39, 40]. Furthermore, the interfacial DMI influences various types of magnetic dynamics, including ferromagnetic resonance, spin waves, and the motion of chiral DWs and skyrmions [41].
In thin films, Néel-type DWs and bulks, Bloch-type DWs are usually two common magnetic DW structures. The magnitude of the SOC influences the DMI vector, as well as the effective magnetic anisotropy constant, which in turn determines the profile of various magnetization textures such as DWs. Also, the sign of the DMI vector, $D$, determines the chirality of the DW [42].
In addition to facilitating the formation of chiral DWs, the interfacial DMI also promotes the creation of skyrmions [43, 44]. The radius of a skyrmion is determined by numerically solving the equation that describes its profile. In the limit of small skyrmions, an analytical expression for the skyrmion radius, $R_{\mathrm{Sk}}$, in the absence of an external magnetic field, the DMI forms the foundation of chiral magnetism [45], a contemporary and vibrant study area in modern magnetism. This interaction, along with the MA, is responsible for a range of novel static and dynamic magnetic properties such as skyrmions in 2D structures and Hopfions in 3D structures. Hence, enhancing the DMI and MA offers the potential to control magnetic properties externally without altering temperature.
This thesis focuses on investigating the electronic as well as magnetic properties of Gr deposited on Co/HM structures, choosing Pt and Ir(111) films as HMs. The role of nonmagnetic elements in modifying magnetic exchange interactions is explored, with a particular focus on the MA and the DMI at the Co/Pt interface. The Z element not only determines the interlayer distances between 4$d$-Pt and 4$d$-Co but also slightly alters the Co/Pt interlayer distance and can modify the sign and magnitude of the DMI [46]. To engineer the electronic and magnetic properties, a range of techniques are employed. These include utilizing electric fields, applying oxide capping layers, and sandwiching the FM layer between two non-magnetic (NM) layers.
Modern electronics rely on the ability to control the electronic properties of materials through externally applied voltage [14]. The realization of electric-field modulation in magnetic semiconductors and metals has initiated the development of electric-field-controlled spintronics devices. The first observation of a direct electric-field effect on magnetism in metal was reported for thin layers of FePt and FePd, where utilizing an electric double layer enabled large electric fields to induce surface charges [47]. Previously, it was widely believed that observing significant electric-field effects in metals would be challenging due to their short screening length [48]. However, subsequent theoretical investigations revealed that electric-field effects on surface magnetization and magnetocrystalline anisotropy (MCA) can

be substantial even in metal FMs like Fe, Ni, and Co, owing to the spin-dependent screening of the electric field [49]. These findings prompted extensive research into electric-field effects in various materials, including the Co(Fe)/MgO system, leading to the observation of room-temperature electric-field-induced changes in MA, attributed to modulation of interface MA [50, 51]. The intrinsic electric dipole at the FM/oxide interface drives the increase (decrease) of PMA under an electric field, associated with a decrease (increase) of the interfacial electric dipole field, which spontaneously exists even without the application of any electrical field. This effect has been observed and quantified at the Fe/MgO interface [52].
In these developments, theoretical advancements have played a crucial role e.g. by unraveling the properties of new materials. State-of-the-art ab initio methods, particularly density functional theory (DFT), have emerged as powerful tools for both interpreting experimental findings and exploring novel materials, allowing predictions of their properties before experimental validation. The calculations presented in this thesis represent the cutting edge of research, delving into the intricate interplay of structural and magnetic complexities.
Electronic structure calculations for solids pose significant challenges due to the complex interactions between nuclei and electrons within a many-body system. The Born-Oppenheimer approximation enables a focus solely on electron dynamics, considering their interaction with frozen, positively charged atomic nuclei. However, the complexity of electron-electron interactions, mediated by Coulomb forces, necessitates approximations, even for a moderate number of particles. DFT, pioneered by Hohenberg and Kohn [53] and further developed by Kohn and Sham [54], has revolutionized our possibilities to predict electronic properties of complex structures. This parameter-free approach facilitates the calculation of total energy using the electron density as a fundamental variable, eliminating the need for many-body wavefunctions. Ab initio methods, prominently DFT, have become essential in materials science, aiding in the interpretation of experimental data and the prediction of material properties prior to experimental validation. This method facilitates the development of ideal materials tailored for specific purposes without the need for extensive experimental iterations.
In this thesis, the calculations employ the FLEUR code [55, 56], based on the full-potential linearized augmented plane-wave (FLAPW) method rooted in DFT principles. Notably, the FLEUR code uniquely facilitates the calculation of relativistic, magnetic interactions e.g. the DMI, a key parameter in spintronics research. However, calculating the DMI presents challenges, requiring non-collinear calculations and the presence of SOC. Consequently, it is necessary to employ either large supercells with commensurate magnetic moments or more sophisticated perturbative approaches.
The thesis follows the structure outlined below:
Chapter 2 provides a comprehensive overview of the fundamental principles of DFT and the Kohn-Sham framework. This chapter extends these foundational concepts to include spin systems and non-collinear magnetic structures, laying the groundwork for the following discussions.

Following this, Chapter 3 delves into the FLAPW method, which forms the basis of all calculations conducted in this study. These computations utilize the FLEUR code, an advanced FLAPW code capable of dealing with non-collinear magnetic structures.
To determine the magnetic ground state of the system, our methodology involves employing an atomistic spin model, explained in detail in Chapter 4. We consider three pivotal energy contributions. Firstly, the Heisenberg exchange interaction characterizes the exchange coupling between spins on different atoms. Secondly, the DMI emerges from SOC in systems lacking inversion symmetry, giving rise to complex magnetic structures such as spin spirals. Lastly, the MCA is introduced, accounting for the energy dependence on the magnetization direction relative to the crystal lattice.
Focusing on Heisenberg exchange, MCA, and the DMI, Chapter 5 investigates the essential magnetic interactions in Gr/Co/HM (111) heterostructures, taking Pt and Ir as HM. This investigation sheds light on the interfacial DMI at both interfaces of Gr/Co and Co/HM. Continuing in Chapter 6, we explore the impact of Co thickness on both MCA and DMI. In Chapter 7, we investigate the modulation of DMI and MCA through the application of an electric field and utilization of an oxide capping layer. In Chapter 8, we introduce an HM capping layer, employing again Pt or Ir to modulate DMI and MCA effectively. We also delve into the investigation of Co/Pt compositions' effects on MCA and DMI, offering insights into the intricate interplay between material compositions and magnetic properties. The thesis is concluded in Chapter 9, summarizing the main findings and conclusions reached throughout the study.

# 2 Density Functional Theory

**Contents**


2.1. Hamiltonian in many-body systems . . . . . 11
2.2. The Thomas-Fermi model . . . . . 12
2.3. Hohenberg-Kohn theorem . . . . . 13
2.4. Kohn-Sham equation . . . . . 14
2.5. Exchange-correlation energy approximations . . . . . 15
2.6. Vector-spin DFT . . . . . 15
2.7. Relativistic effects . . . . . 16


In order to study the structural or electronic properties of condensed matter such as conductivity, or interaction between local spins, that leads to magnetic textures, one must understand the electronic properties of such materials. Density functional theory (DFT) has gained popularity in the last few decades for investigating electronic properties of condensed matter [57]. Moreover, the significance of DFT calculations in the field of magnetism is widely accepted. The DFT formalism indicates that the ground state and additional properties of an electron system can be determined solely from the electron density distribution. Therefore, only a few input parameters have to be known to calculate the ground state properties such as magnetic order, magnetic moments as well as magnetic interactions.

## 2.1 Hamiltonian in many-body systems

In the majority of solid state physics problems, the solution of the time-independent Schrödinger Equation is greatly simplified by employing the Born-Oppenheimer approximation [58]. This approximation allows for the many-body wavefunction to be approximated as a product of wavefunctions for the nuclear and electronic coordinates. Consequently, the purely electronic eigenvalue problem can be addressed independently of the nuclei.

The initial step in computing the electronic structure involves considering the electronic Hamiltonian,

$$\hat{\mathcal{H}} = \hat{T} + \hat{V}_{\text{ext}} + \hat{V}_{\text{ee}}, \tag{2.1}$$

where $\hat{T}$ represents the kinetic energy of the system, $\hat{V}$ the interaction of electrons with an external potential (including the atomic nuclei potential), and $\hat{V}_{ee}$ the electron-electron interaction. One can extend the Hamiltonian to a wave equation:

$$\begin{aligned}\hat{\mathcal{H}}\psi(\boldsymbol{r}_1, ..., \boldsymbol{r}_N) &= \left\{ -\frac{\hbar^2}{2m} \sum_{i=1}^{N} \nabla_{\boldsymbol{r}_i}^2 + \frac{1}{2} \sum_{i \neq j}^{N} \frac{e^2}{|\boldsymbol{r}_i - \boldsymbol{r}_j|} - \sum_{\mu=1}^{M} \sum_{i=1}^{N} \frac{e^2 Z_i}{|\boldsymbol{R}_\mu - \boldsymbol{r}_i|} \right\} \psi(\boldsymbol{r}_1, ..., \boldsymbol{r}_N) \\ &= \epsilon\psi(\boldsymbol{r}_1, ..., \boldsymbol{r}_N).\end{aligned} \tag{2.2}$$

Here $Z_i$ is the nuclear number, $\boldsymbol{R}_i$ and $\boldsymbol{r}_i$ are the nuclear and electronic coordinates, respectively. The behavior of electrons in the ground state can be described by a many-body system wave function, $\psi$, which is a complex quantity in $3N$-dimensional space, where $N$ represents the number of electrons, and $M$ denotes the number of nuclei. If spin and time dependency are contemplated, the problem becomes even more complex.

## 2.2 The Thomas-Fermi model

Thomas and Fermi [59, 60, 61] pioneered an initial density-based approach to electronic structure, deriving explicit expressions for the kinetic energy, electron-electron interaction, and nuclear potential in Equation (2.2) in terms of the electronic many-body density, $n(\boldsymbol{r})$. In this model, electrons are treated as independent particles with a purely electrostatic mutual interaction, known as the Hartree term, given by

$$V_{\text{H}}[n(\boldsymbol{r})] = \frac{1}{2} \int \int \frac{n(\boldsymbol{r}) n(\boldsymbol{r}')}{|\boldsymbol{r} - \boldsymbol{r}'|} d^3r d^3r' \tag{2.3}$$

The external potential formed by the nuclei can be expressed as a functional of the density:

$$V_{\text{ext}}[n(\boldsymbol{r})] = -\int \sum_{\mu} \frac{Z_i}{|\boldsymbol{R}_\mu - \boldsymbol{r}|} n(\boldsymbol{r}) d^3r \tag{2.4}$$

Thomas and Fermi addressed the challenge of representing the kinetic energy by considering a locally uniform electron gas of independent non-interacting particles. Within this local density approximation, which will be discussed in Section (2.5), the kinetic energy functional is given by

$$T[n(\boldsymbol{r})] = \int t[n] n(\boldsymbol{r}) d^3r = C_k \int n^{5/3}(\boldsymbol{r}) d^3r, \tag{2.5}$$

with $C_k = 3\hbar(3\pi^2)^{2/3}/10m$. This fulfills the total energy functional,

$$E[n(\boldsymbol{r})] = T[n(\boldsymbol{r})] + V_{\text{ext}}[n(\boldsymbol{r})] + V_{\text{H}}[n(\boldsymbol{r})], \tag{2.6}$$

in the Thomas-Fermi model. By minimizing the total energy functional under the condition that the overall number of electrons $N = \int n(\boldsymbol{r})d^3\boldsymbol{r}$ remains constant and using the Lagrange multiplier $\lambda$, the Thomas-Fermi equation is obtained:

$$\frac{1}{2}(3\pi^2)^{2/3}n^{2/3}(\boldsymbol{r}) + \int \frac{n(\boldsymbol{r}')}{|\boldsymbol{r}-\boldsymbol{r}'|}d^3r' - \sum_{\mu}\frac{Z_\mu}{|\boldsymbol{R}_\mu - \boldsymbol{r}|} + \lambda = 0 \tag{2.7}$$

The Thomas-Fermi approximation, despite its historical significance and frequent use in the past, has notable limitations. While it can provide a reasonable approximation of the charge density, it fails in several critical aspects. For instance, the Thomas-Fermi charge density diverges at the nuclei and decays as $r^{-6}$ away from them, rather than exhibiting exponential decay. Additionally, this approximation cannot account for the binding of molecules or solids, nor does it capture the periodicity of properties in solids relative to the nuclear number. Furthermore, the Thomas-Fermi approach does not lead to ferromagnetism [62]. Despite these limitations, the Thomas-Fermi approximation represents an exact solution in the limit of infinite nuclear charge.

## 2.3 Hohenberg-Kohn theorem

DFT made it possible to calculate the energy of a solid, using only the electron density, $n(\boldsymbol{r})$. Initially, we will consider a non-magnetic material with spin degeneracy, and later we will extend our discussion to spin-polarized systems. Let's take the many-body Hamiltonian in Equation (2.1), which comprises the kinetic energy $T$, the external potential $V$ due to the nuclei, and the electron-electron interaction $V_{ee}$. According to the first theorem by Hohenberg and Kohn, there exists a unique functional relationship between the total energy and the electronic density of the many-body system. It is based on two theorems and established by Hohenberg and Kohn [53] and Kohn and Sham [54].
Theorem 1: For a given external potential $v$, the total energy of a system is a unique functional of the ground state electron density

$$E\left[n\left(\boldsymbol{r}\right)\right] = T\left[n\left(\boldsymbol{r}\right)\right] + V_{\text{ext}}\left[n\left(\boldsymbol{r}\right)\right] + V_{\text{ee}}\left[n\left(\boldsymbol{r}\right)\right]. \tag{2.8}$$

Theorem 2: The exact ground state density, $n_0$, minimizes the energy functional

$$E[n_0(\boldsymbol{r})] \leq E[n(\boldsymbol{r})]. \tag{2.9}$$

Having an explicit expression for $E[n(\boldsymbol{r})]$ would enable the minimization of this functional concerning the electron density. This approach allows for the calculation of the ground state energy [63]. Given the complex nature of electron-electron interactions, certain approximations are still necessary to derive an explicit expression for $E[n(\boldsymbol{r})]$. These approximations will be outlined in the subsequent discussion.

## 2.4 Kohn-Sham equation

As it has been discussed, DFT is based on the Hohenberg-Kohn theorem, supplying the basis for the substitution of the many-body wavefunction with an electronic density in the description of a quantum-mechanical system. The success of DFT lies in the fact that the minimal energy of a certain system is directly provided by the ground state density. The electron density can be obtained by integration over all but one spatial variable,

$$n(\boldsymbol{r}) = N \int d\boldsymbol{r}_2 ... \int d\boldsymbol{r}_N \psi^\star(\boldsymbol{r}, \boldsymbol{r}_2, ..., \boldsymbol{r}_N)\psi(\boldsymbol{r}, \boldsymbol{r}_2, ..., \boldsymbol{r}_N). \tag{2.10}$$

Note that we use atomic units where the charge of an electron is unity. In this case, the energy functional expressing the total energy is stationary for small variations of the electron density around the ground state density [64]. One can write the energy functional as

$$E[n(\boldsymbol{r})] = \int V_{\text{ext}}(\boldsymbol{r})n(\boldsymbol{r})d\boldsymbol{r} + F[n(\boldsymbol{r})], \tag{2.11}$$

where the first term represents the Coulomb interaction of density with the external potential, and the functional $F$ captures the kinetic energy of the electrons and their mutual Coulomb repulsion. All terms in equation (2.11) that can be supplied for a known $n(\boldsymbol{r})$, the kinetic energy for a non-interacting electron system with density $n(\boldsymbol{r})$, $T_0[n(\boldsymbol{r})]$, and the Coulomb interaction of electrons may be taken out separately

$$F[n(\boldsymbol{r})] = T_0[n(\boldsymbol{r})] + \frac{1}{2}\int\int \frac{n(\boldsymbol{r})n(\boldsymbol{r}')}{|\boldsymbol{r} - \boldsymbol{r}'|}d\boldsymbol{r}d\boldsymbol{r}' + E_{\text{xc}}[n(\boldsymbol{r})]. \tag{2.12}$$

The term $E_{\text{xc}}[n(\boldsymbol{r})]$ is then just a small correction which is called the exchange-correlation functional. According to the Kohn-Sham theory, the ground state density of a many-body system can be obtained from an effective single-particle Schrödinger equation, the Kohn-Sham equation:

$$\left[-\frac{\hbar^2}{2m}\nabla^2 + \int \frac{n(\boldsymbol{r}\prime)}{|\boldsymbol{r} - \boldsymbol{r}\prime|}d\boldsymbol{r}' + V_{\text{ext}}(\boldsymbol{r}) + V_{\text{xc}}(\boldsymbol{r})\right]\phi_i(\boldsymbol{r}) = \epsilon_i\phi_i(\boldsymbol{r}). \tag{2.13}$$

Where $n(\boldsymbol{r} = \sum_i \omega_i|\phi|^2)$ and the exchange-correlation potential,$V_{\text{xc}}$, the functional derivation of the exchange-correlation energy contains all the many-body effects, and the second term represents the Hartree potential. The Kohn-Sham equations take the form of one-particle Schrödinger Equations for $N_e$ non-interacting electrons within an effective potential,

$$V_{\text{eff}}(\boldsymbol{r}) = V_{\text{ext}}(\boldsymbol{r}) + V_{\text{H}}(\boldsymbol{r}) + V_{\text{xc}}(\boldsymbol{r}). \tag{2.14}$$

The $\epsilon_i$ are so-called Lagrange parameters, due to the normalization condition. However, they resemble eigen-energies of a Schrödinger equation. The $\phi_i$ are wave-functions of auxiliary particles, not quasi-particles. As equation (2.13) includes the density both implicitly and explicitly via the Hartree and the exchange-correlation potential, it has to be solved self-consistently. In DFT, this process is accomplished by iteratively solving the Kohn-Sham equation, gradually converging towards the ground state density starting from an initial guess.

## 2.5 Exchange-correlation energy approximations

Considering that the effective potential relies on the density, and conversely, the density is constructed from the solutions of Equation (2.13), the Kohn-Sham equations constitute a self-consistent problem. Two different approximations, the local density approximation (LDA) as well as the generalized gradient approximation (GGA), are usually used in order to parameterize the exchange-correlation energy. These approaches are based on quantum Monte-Carlo simulations for intermediate values of the electron gas [65].
The LDA, originally proposed by Kohn and Sham in 1965, assumes that the electronic density varies slowly [66]. It is exact for a constant electron density, such as in a homogeneous electron gas. The LDA exchange-correlation energy density can be decomposed into exchange and correlation parts. The exchange part can be obtained, for instance, from Hartree-Fock calculations for a homogeneous electron gas [67], while the correlation part can be calculated using the quantum Monte-Carlo method [68]. LDA approximation is derived from the limit of a uniform electron gas, even for the cases in which the density varies in space.

$$E_{\mathrm{xc}}^{\mathrm{LDA}}[n(\boldsymbol{r})] = \int \epsilon_{\mathrm{xc}}[n(\boldsymbol{r})]n(\boldsymbol{r})d\boldsymbol{r}, \tag{2.15}$$

here $\epsilon_{\mathrm{xc}}[n(\boldsymbol{r})]$ is the so-called the exchange-correlation energy density. If the density is spin-polarized, i.e., $n = n^{\uparrow} + n^{\downarrow}$ and $n^{\uparrow} \neq n^{\downarrow}$, through the LDA, the exchange-correlation energy density can be written as $\epsilon_{\mathrm{xc}}(n^{\uparrow}, n^{\downarrow})$. This approximation is sufficient when the spin density changes slowly in space.
However, GGA is a more suitable approximation to describe real atoms, molecules, and solids as it explicitly takes into account the variation of the density, incorporating both the density $n(\boldsymbol{r})$ itself and its gradient:

$$E_{\mathrm{xc}}^{\mathrm{GGA}}\left[n^{\uparrow}, n^{\downarrow}\right] = \int f\left(n^{\uparrow}, n^{\downarrow}, \nabla n^{\uparrow}, \nabla n^{\downarrow}\right) d\boldsymbol{r}. \tag{2.16}$$

In fact, different GGAs are available for exchange-correlation functionals. Many studies have been performed to determine the most compatible expression for $f$ with experiments on various materials. One of the most successful ones is the PBE functional conducted by Perdew, Burke, and Erzernhof [69].
Apart from LDA and GGA, another notable class of approximations worth mentioning is the use of hybrid functionals to approximate the exchange-correlation potential. This technique combines elements of the Hartree-Fock formalism with a standard DFT contribution, such as LDA or GGA [70].

## 2.6 Vector-spin DFT

The magnetic ground state features are completely described by the many-body wavefunctions which are substituted by the density. Since no functional is known to obtain the magnetization from density, only the spin density gives a clear picture

of magnetization. A spin-polarized scheme for the Kohn-Sham equation can be derived for magnetic systems. The spin-dependent version of DFT is defined by spinor wavefunctions. The spin density, $\boldsymbol{s}(\boldsymbol{r})$, can be expressed as [64]:

$$\boldsymbol{s}(\boldsymbol{r}) = \langle \phi(\boldsymbol{r}) | \underline{\boldsymbol{\sigma}} | \phi(\boldsymbol{r}) \rangle, \quad \phi(\boldsymbol{r}) = \begin{pmatrix} \phi_i^{\uparrow}(\boldsymbol{r}) \\ \phi_i^{\downarrow}(\boldsymbol{r}) \end{pmatrix}. \tag{2.17}$$

Here, $\underline{\sigma}$ is referring to $2 \times 2$ Pauli matrices. The corresponding density matrix can be written in the form of

$$\underline{n}(\boldsymbol{r}) = \frac{1}{2}(n(\boldsymbol{r})\underline{I} + \underline{\boldsymbol{\sigma}} \cdot \boldsymbol{s}(\boldsymbol{r})), \tag{2.18}$$

where $\underline{I}$ is $2 \times 2$ unit matrix. The spin-polarized version of DFT, derived by von Barth and Hedin [71], extends the Kohn-Sham equation (2.13) in the form of

$$\left[ \left( -\frac{\hbar^2}{2m}\nabla^2 + \int \frac{n(\boldsymbol{r}\prime)}{|\boldsymbol{r} - \boldsymbol{r}\prime|} d\boldsymbol{r}' \right) \underline{I} + \underline{v}(\boldsymbol{r}) + \underline{V}_{\mathrm{xc}}(\boldsymbol{r}) \right] \begin{pmatrix} \phi_i^{\uparrow}(\boldsymbol{r}) \\ \phi_i^{\downarrow}(\boldsymbol{r}) \end{pmatrix} = \epsilon_i \begin{pmatrix} \phi_i^{\uparrow}(\boldsymbol{r}) \\ \phi_i^{\downarrow}(\boldsymbol{r}) \end{pmatrix}, \tag{2.19}$$

where $\underline{v}(\boldsymbol{r}) = V_{\mathrm{ext}}(\boldsymbol{r})\underline{I} + \mu_{\mathrm{B}}\underline{\boldsymbol{\sigma}} \cdot \boldsymbol{B}(\boldsymbol{r})$ is a $2 \times 2$ potential matrix. Besides, $\underline{V}_{\mathrm{xc}}$ is determined as the functional derivative of the exchange-correlation energy with respect to the density matrix. If both potentials are diagonal matrices, the equation (2.19) would split into two equations for spin-up and spin-down in spin space. In this case, the local spin density approximation (LSDA) is taken into account for calculating the exchange-correlation energy, which can be cast in the form of

$$E_{\mathrm{xc}}^{\mathrm{LSDA}} = \int n(\boldsymbol{r}) \epsilon_{\mathrm{xc}} \left[ n^{\uparrow}(\boldsymbol{r}), n^{\downarrow}(\boldsymbol{r}) \right] d\boldsymbol{r}, \tag{2.20}$$

which follows the equation (2.15), and that means the exchange-correlation energy couples $n^{\uparrow}$ and $n^{\downarrow}$. Spin-polarized DFT allows us to determine different magnetic configurations, as well as to calculate the magnetic interactions between atoms. Different strategies are provided to find ground-states and the global energy minimum, which are based on atomistic models. The simplest one is the classical Heisenberg model. This model will be discussed in Chapter 4.

## 2.7 Relativistic effects

When describing systems with heavy atoms, relativistic effects become significant due to the high kinetic energy of electrons near the nucleus [63]. The relativistic theory for an electron with charge $-e$ and mass $m$ in the presence of an external scalar potential $V$ and vector potential $\boldsymbol{A}$ can be described through the Dirac equation, which is expressed as:

$$\mathcal{H}\Psi = +i\hbar\frac{\partial}{\partial t}\Psi = E'\Psi; \quad \mathcal{H} = -eV(\boldsymbol{r}) + \underline{\beta}mc^2 + \underline{\boldsymbol{\alpha}} \cdot (c\boldsymbol{p} + e\boldsymbol{A}(\boldsymbol{r})). \tag{2.21}$$

Here, $c$ is the speed of light. Besides, $\underline{\boldsymbol{\alpha}}$ is a vector composed of $4 \times 4$ matrices, expressed in terms of the Pauli spin matrices, whereas $\beta$, a matrix of the same dimension, is represented using the $2 \times 2$ identity matrix:

$$\underline{\boldsymbol{\alpha}} = \begin{pmatrix} 0 & \underline{\boldsymbol{\sigma}} \\ \underline{\boldsymbol{\sigma}} & 0 \end{pmatrix}, \quad \beta = \begin{pmatrix} \underline{I} & 0 \\ 0 & -\underline{I} \end{pmatrix}$$

$\Psi$ is a spinor wavefunction with four components, which can be split into two parts, so-called large and small components, $\boldsymbol{\psi}$ and $\boldsymbol{\chi}$, each with two spin components,

$$\boldsymbol{\psi} = \begin{pmatrix} \psi^{\uparrow} \\ \psi^{\downarrow} \end{pmatrix}, \quad \boldsymbol{\chi} = \begin{pmatrix} \chi^{\uparrow} \\ \chi^{\downarrow} \end{pmatrix}$$

With these four components, the Dirac equation reads now

$$\left(E' - mc^2 + eV(\boldsymbol{r})\right) \begin{pmatrix} \psi^{\uparrow} \\ \psi^{\downarrow} \end{pmatrix} = (\underline{\boldsymbol{\sigma}} \cdot (c\boldsymbol{p} + e\boldsymbol{A}(\boldsymbol{r}))) \begin{pmatrix} \chi^{\uparrow} \\ \chi^{\downarrow} \end{pmatrix}, \tag{2.22}$$

$$\left(E' + mc^2 + eV(\boldsymbol{r})\right) \begin{pmatrix} \chi^{\uparrow} \\ \chi^{\downarrow} \end{pmatrix} = (\underline{\boldsymbol{\sigma}} \cdot (c\boldsymbol{p} + e\boldsymbol{A}(\boldsymbol{r}))) \begin{pmatrix} \psi^{\uparrow} \\ \psi^{\downarrow} \end{pmatrix}. \tag{2.23}$$

Assuming that the total energy is close to the rest mass energy in the non-relativistic limit and neglecting $eV(\boldsymbol{r}) \ll E' + mc^2 \approx 2mc^2$, $\chi$ can be eliminated. Moreover, considering $E = E' - mc^2$, these equations simplify to a single equation for the large component:

$$\left[E + eV(\boldsymbol{r}) - \frac{1}{2m}\left(\boldsymbol{p}(\boldsymbol{r}) + \frac{e}{c}\boldsymbol{A}(\boldsymbol{r})\right)^2\right] \begin{pmatrix} \psi^{\uparrow} \\ \psi^{\downarrow} \end{pmatrix} = 0. \tag{2.24}$$

This represents a minimal extension of the Schrödinger equation for a particle in a vector potential [72].
To derive terms that explicitly include spin matrices, we need to refine our approximation of the Dirac equation. This involves approximating $\chi$ based on the previous equations, substituting this approximation into Equation (2.22), and keeping terms up to order $(v/c)^2$. By accomplishing this, we can again derive an equation for just the large component:

$$\begin{aligned} &\left[E + eV(\boldsymbol{r}) - \frac{1}{2m}\left(\boldsymbol{p}(\boldsymbol{r}) + \frac{e}{c}\boldsymbol{A}(\boldsymbol{r})\right)^2 + \frac{1}{2mc^2}(E + eV(\boldsymbol{r}))^2 + \right. \\ &\left. i\frac{e\hbar}{(2mc)^2}\boldsymbol{E}(\boldsymbol{r}) \cdot \boldsymbol{p} - \frac{e\hbar}{(2mc)^2}\underline{\boldsymbol{\sigma}} \cdot (\boldsymbol{E}(\boldsymbol{r}) \times \boldsymbol{p}) - \frac{e\hbar}{2mc}\underline{\boldsymbol{\sigma}} \cdot \boldsymbol{B}(\boldsymbol{r})\right] \begin{pmatrix} \psi^{\uparrow} \\ \psi^{\downarrow} \end{pmatrix} = 0. \end{aligned} \tag{2.25}$$

In our DFT calculations, we neglect the vector potential, $\boldsymbol{A}$, but retain the coupling to the magnetic (exchange) field in the last term. In the so-called scalar-relativistic approximation, the third and fourth terms are included as they do not explicitly couple to the spin. The fifth term describes the spin-orbit coupling that plays an important role in the following.

# 3 Augmented planewave methods

**Contents**


3.1. Basis set for density functional theory . . . . . 20
3.1.1. Augmented planewaves . . . . . 20
3.1.2. Linearized augmented planewaves . . . . . 21
3.1.3. Full-potential linearized augmented planewave method . . . 22
3.1.4. Extending the basis set with local orbitals . . . . . 23
3.2. Brillouin zone . . . . . 23
3.3. The FLAPW method for the film geometry . . . . . 24
3.3.1. Treatment of External Electric Fields . . . . . 26
3.4. Magnetic calculations . . . . . 27
3.4.1. Collinear magnetism . . . . . 27
3.4.2. Non-collinear magnetism . . . . . 28
3.4.3. The implementation of non-collinear magnetism in the FLAPW method . . . . . 30
3.5. Spin-spirals . . . . . 30
3.5.1. Generalized Bloch theorem . . . . . 31
3.6. Spin-orbit coupling and spin-spirals . . . . . 32


In Chapter 2, the density functional theory (DFT) was presented as a reliable and well-established method for analyzing the electronic structure of condensed matter systems. However, the solution of the Kohn-Sham Equation (2.13) necessitates a precise ab-initio technique to simulate the electronic properties of structures accurately. The Full-potential Linearized Augmented Planewave (FLAPW) method [73], stands out as a widely accepted approach due to its precision and applicability to all atoms across the periodic table [74].
Originating from the framework of augmented planewave (APW) methods, this chapter delves into the intricate details of the full crystal potential. It outlines the

formulation of the generalized Kohn-Sham eigenvalue problem, achieved by constructing the Hamiltonian matrix within the non-orthogonal LAPW basis. Finally, we explain the implementation of non-collinear magnetism, offering a comprehensive understanding of electronic structure calculations of complex magnetic systems.

## 3.1 Basis set for density functional theory

According to Bloch's theorem, one can use the periodicity of the crystal lattice to define the crystal momentum $\boldsymbol{k}$ as a good quantum number to label the crystal's wavefunction, $\phi_{\boldsymbol{k}}$. The Bloch functions can be written as a phase factor times a lattice periodic function

$$\psi_{\boldsymbol{k}}(\boldsymbol{r}) = e^{i\boldsymbol{k}\cdot\boldsymbol{r}} u(\boldsymbol{k},\boldsymbol{r}) = e^{i\boldsymbol{k}\cdot\boldsymbol{r}} \sum_{\boldsymbol{G}} c_{\boldsymbol{k}}^{\boldsymbol{G}}(\boldsymbol{k}) e^{\boldsymbol{G}.\boldsymbol{r}}, \tag{3.1}$$

where $\boldsymbol{G}$ and $c_{\boldsymbol{k}}^{\boldsymbol{G}}$ are reciprocal lattice vectors and variational coefficients used in the expansion of the lattice periodic part, respectively [75].
The wavefunction of Bloch vector $\boldsymbol{k}$ and band index $\nu$, $\psi_{\boldsymbol{k},\nu}$, can be written as a linear combination of basis functions $\phi_{\boldsymbol{k}}(\boldsymbol{r})$. One can expand the wavefunction into planewaves

$$\psi(\boldsymbol{k},\nu) = \sum_{|\boldsymbol{k}+\boldsymbol{G}|\leq \boldsymbol{K}_{max}} c_{\boldsymbol{k},\boldsymbol{G}}^{\nu} \phi_{\boldsymbol{k}}^{\boldsymbol{G}}(\boldsymbol{r}), \tag{3.2}$$

where $\boldsymbol{K}_{max}$ indicates a cutoff parameter that limits the number of planewaves in the expansion of the wavefunctions. A planewave basis would simplify the calculation since planewaves are diagonal in momentum space, but it fails to describe the states near the nucleus.

### 3.1.1 Augmented planewaves

In the APW method, at the center of each atom site, one sphere is assumed which is the so-called muffin-tin (MT), and the remaining region is called the interstitial region. Inside the MT spheres, the potential is supposed to be spherically symmetric. Besides, the MT spheres do not overlap, which should be considered if structural relaxation is allowed. Therefore, they nearly fill the maximum possible space. The schematic illustration of MT spheres and interstitial region is shown in Figure (3.1). Thus, the single wavefunctions are represented in terms of the APW basis functions:

$$\phi_{\boldsymbol{G}}(\boldsymbol{k},\boldsymbol{r}) = \begin{cases} \frac{1}{\sqrt{V}} e^{i(\boldsymbol{k}+\boldsymbol{G})\boldsymbol{r}} & \text{interstitial region} \\ \sum_{lm} a_{l,m}^{\boldsymbol{G},i}(\boldsymbol{k})\, u_l^i(r) Y_m^l(\widehat{\boldsymbol{r}-\boldsymbol{R}_i}) & \text{MT sphere } i \end{cases}. \tag{3.3}$$

Here, $\boldsymbol{R}_i$ is the position of the MT sphere and $u_l$ is the regular solution of the radial Schrödinger equation that can be written

$$\left\{-\frac{\hbar^2}{2m}\frac{\partial^2}{\partial r^2}+\frac{\hbar^2}{2m}\frac{l(l+1)}{r^2}+V(r)-E\right\}ru_l(r)=0, \tag{3.4}$$

where $E$ and $V(r)$ are the energy and spherical component of the potential $V(r)$. The wavefunction coefficients are also assumed to be continuous at the boundary of MT spheres to achieve a well-defined kinetic energy.
Unfortunately, it turns out that through the APW method, at the fixed energy, it is not easy to solve the Kohn-Sham equations numerically in an efficient way, as in MTs, the basisfunction depends on energy. Also, it can happen that the radial functions, $u_l$, vanish at the MT radius. If the planewaves and the radial functions become decoupled, then boundary conditions on the spheres cannot be satisfied [76].

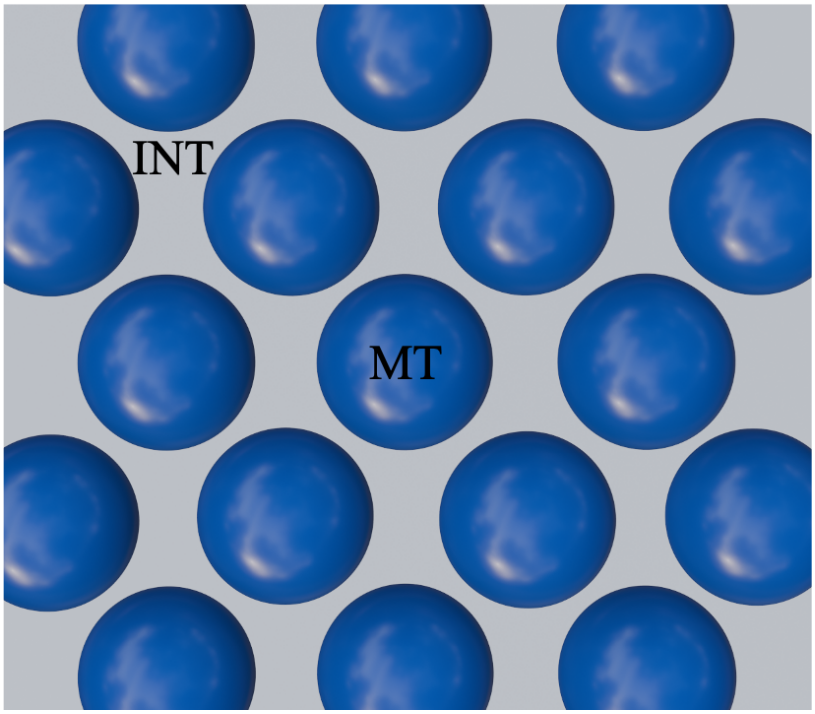



Figure 3.1.: unit cell partitioned into muffin-tin (MT) spheres of one type of atom and the interstitial (INT) region.

### 3.1.2 Linearized augmented planewaves

To address the issues associated with the energy dependence of the Hamiltonian in the APW method, an alternative approach known as the linearized augmented planewave method (LAPW) was introduced [77, 78]. LAPW is a modified APW

basis set, wherein $E_l$ is introduced as an energy parameter to replace the $E$ to be determined for each Bloch vector and thus extend the freedom of variation. For this purpose, the basis functions within the MTs were extended by including their energy derivatives [79]. However, both the original basis function $u_l$ and its derivative $\dot{u}_l = \partial u_l / \partial E$ are now evaluated at a fixed energy $E_l$. Consequently, the initial energy dependence of the radial basis function is substituted by a Taylor series expansion:

$$u_l(E) = u_l(E_l) + (E - E_l)\dot{u}_l(E_l) + \mathcal{O}\left((E - E_l)^2\right) \tag{3.5}$$

Summarizing, the basic idea of the LAPW is to evaluate Equation (3.4) at a fixed energy $E_l$ and add variational freedom to the basis inside the MTs. In this case, the basis functions are of the form

$$\phi_{\boldsymbol{G}}(\boldsymbol{k}, \boldsymbol{r}) = \begin{cases} \frac{1}{\sqrt{V}} e^{i(\boldsymbol{k}+\boldsymbol{G})\boldsymbol{r}} & \text{interstitial} \\ \sum_{lm} \left[ a_{l,m}^{\boldsymbol{G},i}(\boldsymbol{k})\, u_l^i(r) + b_{l,m}^{\boldsymbol{G},i}(\boldsymbol{k})\, \dot{u}_l^i(r) \right] Y_m^l\left(\widehat{\boldsymbol{r} - \boldsymbol{R}_i}\right) & \text{MT sphere } i \end{cases}. \tag{3.6}$$

Here, compared to APW, there is an additional term, $b_{l,m}^{\boldsymbol{G}}(\boldsymbol{k})\, \dot{u}_l(r) Y_m^l(\hat{\boldsymbol{r}})$, where $\dot{u}$ is an energy derivation of $u$. The additional coefficients require the basis functions to be continuous at the sphere boundaries [75]. Differentiating Equation (3.4) results in

$$\left\{ -\frac{\hbar^2}{2m}\frac{\partial^2}{\partial r^2} + \frac{\hbar^2}{2m}\frac{l(l+1)}{r^2} + V(r) - E_l \right\} r\dot{u}_l(r) = r u_l(r), \tag{3.7}$$

and the solution of this equation gives $\dot{u}_l$. The radial functions $u_l$ are normalized over the MT radius; it follows from the energy derivative of the normalization that the functions $u_l$ and their energy derivative $\dot{u}_l$ are orthogonal. However, the entire LAPW basis set is not. This lack of orthogonality needs to be considered when setting up and diagonalizing the Hamiltonian matrix. Despite this, LAPW basis functions are advantageous as they provide a suitable basis for describing the Hamiltonian with a relatively small number of functions [80].

### 3.1.3 Full-potential linearized augmented planewave method

As the basis presents enough variational freedom, the LAPW method can be extended to non-spherical MT potentials with little difficulty. This gives rise to the FLAPW method. Although the LAPW method yields accurate results for closed-packed metals, it becomes difficult to study crystals with open structures, such as surfaces. In the FLAPW method, any shape approximations in the interstitial region and within the MTs are dropped [81, 73]. While in LAPW, the potential in the unit cell $V(r)$ is approximated by $V_0(r)$, using a constant potential in the interstitial region and a spherically symmetric potential inside each sphere, in the FLAPW method, $V(r)$ remains general. By relaxing the constant interstitial potential, $V_0^I$, and spherical MT approximation, $V_0^{MT}$, the potential can be written as

$$V(\boldsymbol{r}) = \begin{cases} \sum_{\boldsymbol{G}} V_{\boldsymbol{G}}^I e^{i\boldsymbol{G}\cdot\boldsymbol{r}} & \text{interstitial} \\ \sum_{l,m} V_{l,m}^{MT}(r) Y_m^l(\hat{\boldsymbol{r}}) & \text{MT} \end{cases}. \tag{3.8}$$

This method emerged as a technique capable of deriving the Coulomb potential for a general periodic charge density, without shape approximations. Notably, it considers the Hamiltonian matrix elements arising from the warped interstitial and non-spherical terms of the potential.

### 3.1.4 Extending the basis set with local orbitals

The LAPW basis is adapted and used to represent only the valence electrons. The separation from the core electrons is possible because one can show that the LAPW basis is orthogonal to core electron states as long as these states are completely confined in MT spheres [82]. This condition can only be approximately fulfilled. Energetically high-lying core electron states can be too far extended beyond the MT sphere boundary, such that the approximate orthogonality cannot be assumed anymore. These so-called semicore states thus have to be described as valence electrons. However, the energetically linearized LAPW basis description around the chosen energy parameters is not adapted to represent them. For a high-quality representation of these states, one, therefore, adds local orbitals (LOs) [83] to the LAPW basis.
These additional basis functions are explicitly designed to overcome the limitations of the linearization in the LAPW method. It is possible to construct them to represent semicore states [83], unoccupied states [84, 85], or to generally eliminate the linearization error for the valence states [86]. They are linear combinations of the already specified radial functions $u_l$ and $\dot{u}_l$ along with an additional radial function $u_l^{\mathrm{lo}}$, each multiplied by spherical harmonics. For the representation of semicore states or unoccupied states, the additional radial function typically is a conventional $u_l$, evaluated at an energy parameter near the respective state. For the general elimination of the linearization error, one chooses for the third radial function a second energy derivative $\ddot{u}_l$, evaluated at the conventional energy parameter. Overall, a local orbital basis function is given by

$$\phi^{lo}_{\boldsymbol{G}_{\mathrm{lo}}}(\boldsymbol{k},\boldsymbol{r}) = \sum_m \left( a_{\mathrm{lo}}^{m,\boldsymbol{G}_{\mathrm{lo}}}(\boldsymbol{k}) u_l(r) + b_{\mathrm{lo}}^{m,\boldsymbol{G}_{\mathrm{lo}}}(\boldsymbol{k}) \dot{u}_l(r) + c_{\mathrm{lo}}^{m,\boldsymbol{G}_{\mathrm{lo}}}(\boldsymbol{k}) u_l^{\mathrm{lo}}(r) \right) Y_m^l(\hat{\boldsymbol{r}}), \tag{3.9}$$

where the coefficients $a_{\mathrm{lo}}^{m,\boldsymbol{G}_{\mathrm{lo}}}$, $b_{\mathrm{lo}}^{m,\boldsymbol{G}_{\mathrm{lo}}}$, and $c_{\mathrm{lo}}^{m,\boldsymbol{G}_{\mathrm{lo}}}$ are constructed by enforcing a normalization condition and vanishing value and slope of the LOs at the MT boundary. For each $m$, these coefficients are then scaled according to the related $m$-channel of a Rayleigh expansion of a plane wave with wave vector $\boldsymbol{k} + \boldsymbol{G}_{\mathrm{lo}}$ at the MT boundary. With differing, LO-dependent $\boldsymbol{G}_{\mathrm{lo}}$, a set of $2l+1$ linearly independent LOs can be defined that each has the symmetry properties of the related plane waves, e.g., they are real-valued for inversion-symmetric setups.

## 3.2 Brillouin zone

Following Bloch's theorem, for the calculation of electron density and energy of an infinite periodic solid, quantities require the summation over all electrons require

the integration over all $k$-points in the Brillouin zone (BZ) and all occupied states or in other words, over the bands with energy $\epsilon_\nu$ located below the Fermi level. Consequently, the integral is in the form of

$$\frac{1}{V_{BZ}} \int_{BZ} \sum_{\nu, \epsilon_\nu(\boldsymbol{k}) < E_F} f_\nu(\boldsymbol{k}) d^3k, \tag{3.10}$$

where $f$ is the function to be integrated. Numerically, integration is replaced by a summation over a discrete mesh in the BZ. Due to symmetry, the Equation (3.10) may reduce to a summation over the irreducible wedge of the BZ (IBZ). One can write it in the form of

$$\frac{1}{V_{BZ}} \sum_{\boldsymbol{k} \in IBZ} \sum_{\nu, \epsilon_\nu(\boldsymbol{k}) < E_F} f_\nu(\boldsymbol{k}) w(\boldsymbol{k}), \tag{3.11}$$

where $w(\boldsymbol{k})$ gives the weight of the $k$-points. A sufficient number of $k$-points need to be taken in order to obtain an accurate result. According to the Equation (3.2) if the function $f_\nu(\boldsymbol{k})$ is given by $|\psi(\boldsymbol{k}, \nu)|^2$, the summation yields the electron density.

## 3.3 The FLAPW method for the film geometry

The study of surfaces and thin films is a highly active field of research, driven by the intriguing properties that emerge partially from their reduced dimensionality. The physics of surfaces and thin films is difficult to treat since they break the translation symmetry. Consequently, there is only a 2D symmetry parallel to the surface in such problems. Also, perpendicular to the surface, a semi-infinite problem has to be considered. In the case of film calculations, space is divided into three distinct regions, the MTs, the interstitial, and the vacuum region [87]. The interstitial region is extended from $-D/2$ to $D/2$ in the $z$ direction, perpendicular to the film. The wavefunction representation inside the MT spheres remains exactly the same as in the bulk case. However, the periodicity along the $z$-direction does not exist anymore. Therefore, the unit cell expands additionally from $D/2$ to $\infty$ in $z$-direction, where the wavefunctions can be developed in terms of 2D planewaves and $z$-dependent functions. In Figure (3.2), the film geometry is shown. Note that the 3D planewaves fill a region from $-\tilde{D}/2$ to $\tilde{D}/2$ in order to avoid nodal planes at the boundary between interstitial and vacuum. As a consequence, the form for the planewaves is assumed to be

$$\phi_{\boldsymbol{G}_\parallel, G_\perp}(\boldsymbol{k}_\parallel, \boldsymbol{r}) = e^{i(\boldsymbol{G}_\parallel + \boldsymbol{k}_\parallel) \cdot \boldsymbol{r}_\parallel} e^{iG_\perp z}, \tag{3.12}$$

where the wave vector $G_\perp$ is defined as an integer multiple of $2\pi/\tilde{D}$, perpendicular to the film. $\boldsymbol{G}_\parallel$ and $\boldsymbol{k}_\parallel$ are the 2D reciprocal lattice and Bloch vectors, and $\boldsymbol{r}_\parallel$ is the parallel component of $\boldsymbol{r}$. In the vacuum region, the basis functions are constructed akin to those in the MTs. They comprise plane waves aligned parallel to the film, accompanied by a $z$-dependent function of $u_{\boldsymbol{G}_\parallel}(\boldsymbol{k}_\parallel, z)$ and its energy derivative

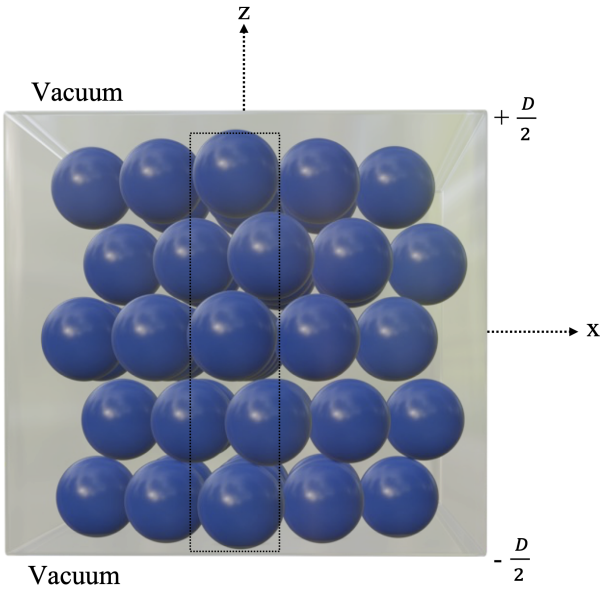



Figure 3.2.: Side view of a slab model used in film calculations, showing a finite-thickness slab (center) separated by two vacuum regions. The blue spheres represent atoms in the slab, and the dashed box indicates the unit cell.

$\dot{u}_{G_\parallel}(k_\parallel, z)$, which solves the corresponding one-dimensional Schrödinger equation:

$$\left\{-\frac{\hbar^2}{2m}\frac{\partial^2}{\partial z^2} + V_0(z) - E_{vac} + \frac{\hbar^2}{2m}(G_\parallel + k_\parallel)^2\right\} u_{G_\parallel}(k_\parallel, z) = 0, \tag{3.13}$$

$$\left\{-\frac{\hbar^2}{2m}\frac{\partial^2}{\partial z^2} + V_0(z) - E_{vac} + \frac{\hbar^2}{2m}(G_\parallel + k_\parallel)^2\right\} \dot{u}_{G_\parallel}(k_\parallel, z) = u_{G_\parallel}(k_\parallel, z). \tag{3.14}$$

Here, $E_{vac}$ and $V_0(z)$ are the vacuum energy parameters and the planar averaged part of the vacuum potential. To enhance the variational freedom in vacuum treatment, the energy parameter can be substituted with $E_{vac} - \frac{1}{2}G_\perp^2$, which results in the $G_\perp$ dependent basis functions. Accordingly, the wavefunction in two-dimensional geometries is expanded using a basis that takes the following form:

$$\phi_{G_\parallel G_\perp}(k_\parallel, r) = \begin{cases} \frac{1}{\sqrt{V}} e^{i(k_\parallel + G_\parallel)\cdot r_\parallel} e^{iG_\perp z} & \text{interstitial} \\ \sum_{lm}\left[a^G_{l,m}(k)u_l(r) + b^G_{l,m}(k)\dot{u}_l(r)\right] Y^l_m(\hat{r}) & \text{MT} \\ \left[a_{G_\parallel G_\perp}(k_\parallel)u_{G_\parallel}(k_\parallel, z) \right. & \\ \left. + b_{G_\parallel G_\perp}(k_\parallel, z)\dot{u}_{G_\parallel}(k_\parallel, z)\right] e^{i(G_\parallel + k_\parallel)\cdot r_\parallel} & \text{vacuum} \end{cases} . \tag{3.15}$$

### 3.3.1 Treatment of External Electric Fields

The application of an external electric field to a thin film induces a distinct potential gradient across the slab, reflecting the redistribution of electronic charge in response to the field. This gradient vanishes in the absence of the field, as illustrated schematically in Figure (3.3).
The influence of the electric field can be incorporated within the framework of classical electrostatics, leading to an additional term in the total energy functional:

$$\int d\boldsymbol{r}\, V_{\text{ext}}(\boldsymbol{r}) n(\boldsymbol{r}), \tag{3.16}$$

where $V_{\text{ext}}(\boldsymbol{r})$ denotes the Coulomb potential due to the external field, and $n(\boldsymbol{r})$ is the electron density [88].
To impose a uniform external field in DFT calculations, a sheet of charge is introduced at a distance from the film, placed far enough to avoid overlap with the electronic density [89, 90, 91, 92]. This setup generates a homogeneous electric field, $\boldsymbol{E} = 4\pi\sigma\hat{\boldsymbol{n}}$. The resulting potential variation across the slab depends on the dipole moment formed between the applied field and the induced charge redistribution. Consequently, the field's effects within both the interstitial region and the muffin-tin spheres are captured by adapting the boundary conditions at the vacuum–interstitial interface.
Defining electric fields in terms of external surface charges results in a shift of the

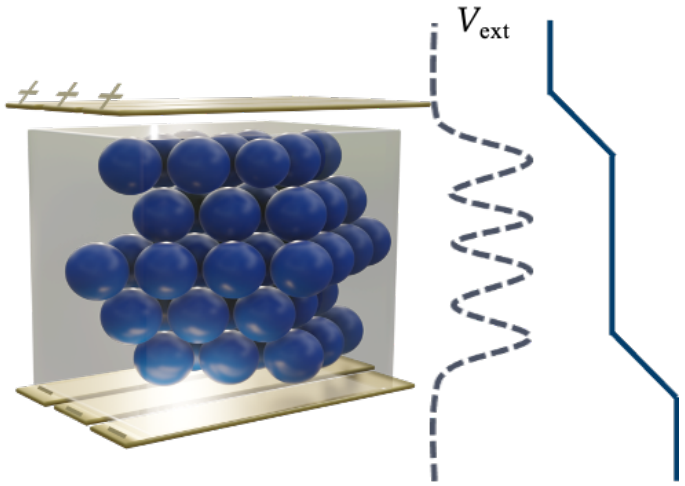



Figure 3.3.: The diagram on the left illustrates the slab geometry, with the electric field oriented normal (perpendicular) to the slab surface. On the right, the external potential $V_{\text{ext}}(z)$ is plotted as a function of the out-of-plane coordinate $z$. The slope $dV_{\text{ext}}/dz$ corresponds to the local electric field strength. Note the distinctly different potential behavior in the vacuum regions compared to the slab interior.

electrostatic potential and, consequently, in the work function. This shift affects the total energy of the system.

## 3.4 Magnetic calculations

Through the magnetism, the symmetry of the ground state density between spin up and spin down is broken. This is a consequence of $\mu_B \underline{\sigma} \cdot B_{xc}(\boldsymbol{r})$ appearing as an additional term in the Kohn-Sham Equation (2.13). Here, $\mu_B$ and $\underline{\sigma}$ are Bohr magneton and Pauli matrices, while $\mathbf{B}_{xc}$ is the magnetic exchange field. The energy functional of the ground state depends only implicitly on magnetization density $\boldsymbol{m}(\boldsymbol{r})$ that gives rise to $\mathbf{B}_{xc}$. In general, the magnetic moment in a MT sphere $i$ can be written as

$$\boldsymbol{M}_i = \int_{MT_i} d\boldsymbol{r}\, \boldsymbol{m}(\boldsymbol{r}). \tag{3.17}$$

The set of magnetic moments of all atoms, $\{\boldsymbol{M}_i\}$, describes the magnetic structure. Therefore, the Kohn-Sham equation for the magnetic case can be modified as follows:

$$\begin{pmatrix} \mathcal{H}_0 + B_{xc}\frac{m_z}{|\boldsymbol{m}|} & B_{xc}\frac{m_x - i m_y}{|\boldsymbol{m}|} \\ B_{xc}\frac{m_x + i m_y}{|\boldsymbol{m}|} & \mathcal{H}_0 - B_{xc}\frac{m_z}{|\boldsymbol{m}|} \end{pmatrix} \begin{pmatrix} \psi_\nu^\uparrow \\ \psi_\nu^\downarrow \end{pmatrix} = \epsilon_\nu \begin{pmatrix} \psi_\nu^\uparrow \\ \psi_\nu^\downarrow \end{pmatrix}, \tag{3.18}$$

where $\mathcal{H}_0 = \boldsymbol{p}^2 + V_{\text{eff}}$ has been employed, and the influence of an external magnetic field has been disregarded. In the FLAPW method, distinguishing between collinear and non-collinear configurations is beneficial.

### 3.4.1 Collinear magnetism

In the case of collinear magnetism, containing ferro-, ferri-, and antiferromagnetic structures, by neglecting SOC, one can choose $\boldsymbol{m} \| \boldsymbol{z}$. Therefore, the Hamiltonian in Equation (3.18) becomes diagonal in spin space. In this case, the magnetization density $m_z$ can be restricted only to spin-up and down densities. One can define the magnetization density as

$$m_z = -\mu_B \sum_i \omega_i |\langle \boldsymbol{\psi}_i | \underline{\sigma}_z | \boldsymbol{\psi}_i \rangle|^2 \Rightarrow m_z(\boldsymbol{r}) = -\mu_B \left( n^\uparrow(\boldsymbol{r}) - n^\downarrow(\boldsymbol{r}) \right), \tag{3.19}$$

where $n^\uparrow = \sum_\nu \omega_\nu^\uparrow |\psi_\nu^\uparrow(\boldsymbol{r})|^2$ and $n^\downarrow = \sum_\nu \omega_\nu^\downarrow |\psi_\nu^\downarrow(\boldsymbol{r})|^2$ are the electron densities of spin up and down, respectively. $\psi^\uparrow$ and $\psi^\downarrow$ are the solutions of Kohn-Sham equation with respect to $V^\uparrow = \frac{1}{2}(V_0 - \mu_B B_z)$ for spin up and $V^\downarrow = \frac{1}{2}(V_0 + \mu_B B_z)$ for spin down.
However, for a complex magnetic structure, spin up and down are no longer decoupled, one has lower symmetry, and one has to calculate more states or over a much larger fraction of the BZ, as will be argued in the following.

### 3.4.2 Non-collinear magnetism

The energy functional of a general magnetic structure can be described either by the charge density $n$ and the spin density vector field $\boldsymbol{m}$ or by a density matrix $\boldsymbol{\rho}$, which is a $2 \times 2$ hermitian matrix. That can be written as

$$\boldsymbol{\rho} = \frac{1}{2}(n\underline{I}_2 + \underline{\boldsymbol{\sigma}} \cdot \boldsymbol{s}) = \frac{1}{2}\begin{pmatrix} n + s_z & s_x - is_y \\ s_x + is_y & n - s_z \end{pmatrix}. \tag{3.20}$$

$\underline{I}_2$ is the unitary matrix in spin space and $\sigma$ is the vector of the Pauli matrices [93]. Also, the potential matrix can be defined in the same way:

$$\underline{V} = V\underline{I}_2 + \mu_B \underline{\boldsymbol{\sigma}} \cdot \mathbf{B}, \tag{3.21}$$

where $V$ involves the external, Hartree, and the exchange-correlation potential, averaged over two spin directions, in the local frame. In this frame, the local $z$-axis is parallel to the spin-quantization axis. Also, $\mathbf{B}$ consists of the external field as well as the exchange field, which is diagonal in the local frame. The exchange field is declared as the difference of exchange correlation potential for spin up and spin down, in the local frame. The particle density, $n(\boldsymbol{r})$, and spin density, $\boldsymbol{s}(\boldsymbol{r})$, can be written as

$$n(\boldsymbol{r}) = \sum_{i=1}^{N} \boldsymbol{\psi}_i^\star(\boldsymbol{r})\underline{I}_2\boldsymbol{\psi}_i(\boldsymbol{r}), \tag{3.22}$$

$$\boldsymbol{s}(\boldsymbol{r}) = \sum_{i=1}^{N} \boldsymbol{\psi}_i^\star(\boldsymbol{r})\underline{\boldsymbol{\sigma}}\boldsymbol{\psi}_i(\boldsymbol{r}). \tag{3.23}$$

The $i$ is a composite index for the $\boldsymbol{k}$ and state, $i = (\boldsymbol{k}, \nu)$ and $N$ is the number of occupied states. The density matrix, $\rho_{\alpha\beta}$, can be expressed in terms of the solutions of Kohn-Sham equations:

$$\rho_{\alpha\beta} = \sum_{i=1}^{N} \psi_{i,\alpha}^\star \psi_{i,\beta} \quad \text{with} \quad \alpha, \beta \in 1, 2. \tag{3.24}$$

Kohn-Sham equation for a given $\boldsymbol{k}$-point is conveyed in the form

$$\left\{ -\frac{\hbar^2}{2m}\nabla^2 I_2 + \underline{V} \right\} \psi_\nu = \epsilon_\nu \psi_\nu. \tag{3.25}$$

The off-diagonal part of the $2 \times 2$ potential matrix is the only part of this hermitian matrix coupling the two components of Pauli spinor $\phi_i$.
As mentioned in chapter 2, the exchange-correlation energy can be calculated in different parametrizations such as the local spin-density approximation (LSDA) and the generalized gradient approximation (GGA). These approximations have been developed mostly for collinear calculations. In LSDA, the $\epsilon_{xc}$ depends only

on the magnitude of magnetization $m(\boldsymbol{r})$, due to its local feature. Hence, this approximation can be equally applied to noncollinear systems. However, in the GGA, through the gradients of the densities, the environment of a point in space has to be considered in order to state the exchange-correlation energy.
Non-collinear magnetism has been developed within the FLAPW method. The variant of the FLAPW method for noncollinear magnetism was developed by Nordström and co-workers [94], [95]. Moreover, a hybrid method was introduced, assuming a collinear **B** field in the vicinity of atomic nuclei, i.e. the MT spheres, and the continuous **B** field in the interatomic region and in the vacuum [93]. Thus, inside the non-overlapping spheres, the off-diagonal elements of the potential matrix are assumed to be zero in the local frame. In this frame, the magnetic moment of atom $\alpha$ points to the local $z$ direction, which can be specified as $\hat{e}^i_M$ direction in the global coordinate frame.
Since in the FLAPW method MT spheres are used, the hybrid method, in which the full magnetization density is collinear in the MT spheres and a continuous vector field in the interstitial region and the vacuum is applied, can be implemented [96]. The result, which is shown in Figure (3.4), can easily be formulated in

$$\boldsymbol{m}(\boldsymbol{r}) = \begin{cases} \boldsymbol{m}(\boldsymbol{r}) & \text{interstitial and vacuum} \\ m_i(\boldsymbol{r})\hat{e}^i_M & \text{MT sphere } i \end{cases} . \tag{3.26}$$

This variant is used in the FLEUR code applied here.

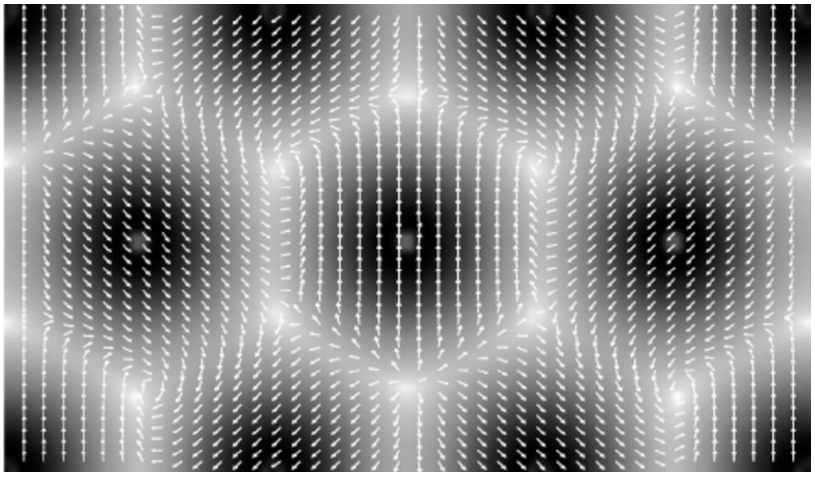


Figure 3.4.: Illustration of the representation of non-collinear magnetization density. In the interstitial region, the magnetization is a continuous vector field. However, within each MT sphere, the magnetization has a fixed direction and can only vary in magnitude [97].

### 3.4.3 The implementation of non-collinear magnetism in the FLAPW method

In the collinear calculation, two sets of radial basis functions inside the MTs for the two different spin directions are used. These are constructed from the $u_l(\boldsymbol{r})$ as shown in Equation (3.4). Therefore, for each spin direction the spherical part of the corresponding potential is specified as $V_\uparrow(\boldsymbol{r})$ or $V_\downarrow(\boldsymbol{r})$ and the same for the corresponding energy parameter $\epsilon_{l\uparrow}$ or $\epsilon_{l\downarrow}$. These are used to determine the $u_l^\uparrow(\boldsymbol{r})$ and $u_l^\downarrow(\boldsymbol{r})$as shown in Equation (3.4).
According to Equation (3.26) in the non-collinear case, the magnetization in the MT spheres can be restricted to the local quantization axis. $\tilde{V}$ determines the quantities in the local ($l$) coordinate frame. Consequently, $\tilde{V}_\uparrow(\boldsymbol{r})$ or $\tilde{V}_\downarrow(\boldsymbol{r})$ can still be used with respect to the local axis. A spin rotation matrix $\underline{U}_{\mathrm{MT}\,i}$ connects the local and global coordinate frames. The potential can then be expressed as:

$$\tilde{V} = \underline{U}^\dagger_{\mathrm{MT}\,i} V \underline{U}_{\mathrm{MT}\,i} = (V_\mathrm{H} + V_\mathrm{ext})\underline{I}_2 + \begin{pmatrix} \tilde{V}_\mathrm{xc}^{\uparrow\uparrow} & \tilde{V}_\mathrm{xc}^{\uparrow\downarrow} \\ \tilde{V}_\mathrm{xc}^{\downarrow\uparrow} & \tilde{V}_\mathrm{xc}^{\downarrow\downarrow} \end{pmatrix}. \tag{3.27}$$

The augmented plane waves are constructed by adding a two-component spinor, $\phi_\sigma^g$, and the functions are represented in the global ($g$) spin frame. In this local frame, the $\phi_\sigma^l$ in the MTs has two-component spinors $\phi_\uparrow$ and $\phi_\downarrow$, the same as a global spin frame in the collinear calculations. However, overall, the potential matrix $V$ is not diagonal in the two-dimensional spin space. The basis sets should change just inside MT spheres, as a local spin coordinate frame is used, which is rotated with respect to the global frame. The alignment of both local spin components of the basis functions within the MT with the interstitial wavefunction at the MT/interstitial boundary is essential.

## 3.5 Spin-spirals

The term spin-spiral is specifically given to a magnetic structure with the rotation of the local moments $\boldsymbol{M}$ by a constant angle from atom to atom along a certain direction of the crystal. This is defined by the propagation vector of the spin-spiral is called $\boldsymbol{q}$. Under the translation by a lattice vector $\boldsymbol{R}$, the magnetic moment of an atom rotates by an angle

$$\varphi = \boldsymbol{q} \cdot \boldsymbol{R} \tag{3.28}$$

and the magnetic moment at an atomic position $R_i$ is given by

$$\boldsymbol{M}_i = M \begin{cases} \cos(\boldsymbol{q} \cdot \boldsymbol{R}_i) \sin\theta, \\ \sin(\boldsymbol{q} \cdot \boldsymbol{R}_i) \sin\theta, \\ \cos\theta, \end{cases} \tag{3.29}$$

where the $\theta$ is the relative angle between the magnetic moment and rotation axis (cone angle) [93]. In this case, the rotation axis is assumed to be in the $z$ direction. To define a spin-spiral uniquely, three parameters are needed: the rotation axis (direction matters, only if SOC is included), the relative angle $\theta$ between the magnetic moment and the rotation axis, and the spin-spiral vector $\boldsymbol{q}$. Figure (3.5) shows four examples of spin-spirals with spin rotation axes perpendicular and parallel to the spin-spiral vector.
The spin-spiral vector $\boldsymbol{q}$ is a vector in real space, while the spin rotation axis is a vector in the spin coordinate frame. In the absence of SOC, these two coordinate frames are totally independent from each other. As a result, the angle between the spin-spiral vector $\boldsymbol{q}$ and the spin rotation axis becomes meaningless. In this case, the system is rotationally invariant in spin space, meaning its energy remains unchanged under a uniform rotation of all spin directions when SOC is absent. However, the spin spirals with different cone angles $\theta$ are not equivalent. If there is only a single magnetization in the unit cell, the magnitude of the magnetic moment of each atom is the same, and all see the same local environment. Only the angle between the local moment and the lattice changes from site to site. Nevertheless, it is only significant in the presence of SOC. Without the SOC, this leads to the possibility of calculating spin-spirals of arbitrary $\boldsymbol{q}$ in the chemical unit cell by using a generalization of the Bloch theorem [98].

### 3.5.1 Generalized Bloch theorem

According to the Bloch theorem, one can write the wavefunction of a system with a periodic potential in the form Equation (3.1)

$$\psi_{\boldsymbol{k}}(\boldsymbol{r}) = e^{i\boldsymbol{k}\cdot\boldsymbol{r}} u_{\boldsymbol{k}}(\boldsymbol{r}), \tag{3.30}$$

where the $\boldsymbol{k}$ is the Bloch vector and $u_k(\boldsymbol{r})$ has the periodicity of the potential. The generalized Bloch Theorem is applied to the systems in which the spin-spiral has broken the chemical translation symmetry. When spin-space and crystal lattice are decoupled, a generalized Bloch theorem becomes applicable. This theorem enables the description of any homogeneous spiral spin-density waves (SSDW) using the chemical unit cell instead of the magnetic one [99]. When examining a spin-spiral configuration within a crystal devoid of an external magnetic field, and incorporating the rotational axis $\varphi = \boldsymbol{q} \cdot \boldsymbol{R}$, the resulting potential matrix is expressed as:

$$\underline{V} = V\underline{I}_2 + \mu_{\mathrm{B}}\underline{\boldsymbol{\sigma}} \cdot \mathbf{B}_{\mathrm{xc}} \tag{3.31}$$

Introducing the $\boldsymbol{m}$ and $\mathbf{B}_{\mathrm{xc}}$ in the spherical coordinates as

$$\boldsymbol{m} = m\left(\sin\theta\cos\varphi\,\hat{\boldsymbol{e}}_x + \sin\theta\sin\varphi\,\hat{\boldsymbol{e}}_y + \cos\theta\,\hat{\boldsymbol{e}}_z\right), \tag{3.32}$$

$$\mathbf{B}_{\mathrm{xc}} = \mathrm{B}_{\mathrm{xc}}\left(\sin\theta\cos\varphi\,\hat{\boldsymbol{e}}_x + \sin\theta\sin\varphi\,\hat{\boldsymbol{e}}_y + \cos\theta\,\hat{\boldsymbol{e}}_z\right), \tag{3.33}$$

leads to the characterization of homogeneous SSDWs by

$$\begin{aligned} m(\boldsymbol{r}+\boldsymbol{R}) &= m(\boldsymbol{r}), \quad & \mathrm{B}_{\mathrm{xc}}(\boldsymbol{r}+\boldsymbol{R}) &= \mathrm{B}_{\mathrm{xc}}(\boldsymbol{r}), \\ \theta(\boldsymbol{r}+\boldsymbol{R}) &= \theta(\boldsymbol{r}), \quad & \varphi(\boldsymbol{r}+\boldsymbol{R}) &= \varphi(\boldsymbol{r}) + \boldsymbol{q}\cdot\boldsymbol{R}, \end{aligned} \tag{3.34}$$

where $\boldsymbol{R}$ and $\boldsymbol{q}$ determine the chemical lattice vector and direction of spatial propagation of the SSDW. The sign of $\boldsymbol{q}$ specifies the spiral's rotational direction. Then, the generalized Bloch theorem can be written in [100, 101]

$$\psi_{k,\nu}(\boldsymbol{r}|\boldsymbol{q}) = \begin{pmatrix} \psi^{\uparrow}_{k,\nu} \\ \psi^{\downarrow}_{k,\nu} \end{pmatrix} = \begin{pmatrix} e^{i(k-q/2)\cdot r} u^{\uparrow}_{k,\nu}(\boldsymbol{r}) \\ e^{i(k+q/2)\cdot r} u^{\downarrow}_{k,\nu}(\boldsymbol{r}) \end{pmatrix}, \tag{3.35}$$

with lattice periodic functions $u^{(\sigma)}_{k,\nu}(\boldsymbol{r}) = u^{(\sigma)}_{k,\nu}(\boldsymbol{r}+\boldsymbol{R})$. The $q$-dependent phase factor signifies a spin rotation around the $z$-axis.
It is very efficient to implement the spin-spiral into the FLAPW method since this method relies on planewave expansions and Fourier transforms. Therefore, it is necessary to formulate the theory in terms of periodic functions. In such circumstances, the eigenstate of the Hamiltonian can be written in the form [93]

$$\psi_k(\boldsymbol{r}) = e^{ik\cdot r} \begin{pmatrix} e^{-iq\cdot r/2} a_k(\boldsymbol{r}) \\ e^{+iq\cdot r/2} b_k(\boldsymbol{r}) \end{pmatrix}. \tag{3.36}$$

Here, $a_k(\boldsymbol{r})$ and $b_k(\boldsymbol{r})$ are functions with translational periodicity.

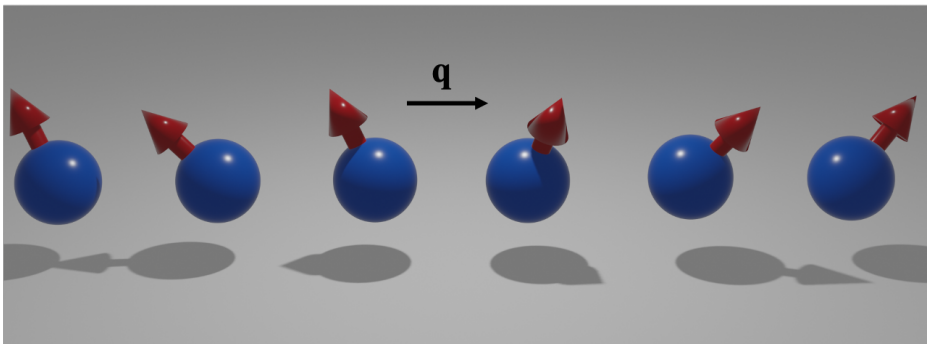



Figure 3.5.: An example of spin-spiral with spin rotation axis perpendicular to the spin-spiral vector $\boldsymbol{q}$.

## 3.6 Spin-orbit coupling and spin-spirals

The SOC , as discussed in section(2.7), is approximated [102, 103] by

$$\mathcal{H}_{\mathrm{SO}} = \sum_n \xi_n(r_n)\underline{\boldsymbol{\sigma}}\cdot\hat{\boldsymbol{L}}_n, \tag{3.37}$$

where $\boldsymbol{L}$ is the orbital momentum operator and $\xi_i(R_i)$ explains the SOC strength as a function of the distance $r_n$ from the $n$th nucleus. Implemented within the FLAPW method [104], SOC is exclusively accounted for within the MTs, while being disregarded in the interstitial and vacuum regions. Therefore, the SOC operator in each MT can be written as

$$\mathcal{H}_{\mathrm{SO}} = \xi(r) \begin{pmatrix} +\hat{L}_z & \hat{L}_- \\ \hat{L}_+ & -\hat{L}_z \end{pmatrix}, \tag{3.38}$$

with $\hat{L}_\pm = \hat{L}_x \pm i\hat{L}_y$. If the $z$-axis doesn't align with the spin-quantization axis, a rotation matrix $\underline{U}$ becomes necessary to align the global spin coordinate frame with respect to the lattice. Achieving this involves rotating the SOC operator,

$$\underline{U}^\dagger \mathcal{H}_{\mathrm{SO}} \underline{U} = \xi(r) \underline{U}^\dagger (\underline{\boldsymbol{\sigma}} \cdot \hat{\boldsymbol{L}}) \underline{U} = \xi(r) \begin{pmatrix} \hat{L}^{\uparrow\uparrow} & \hat{L}^{\uparrow\downarrow} \\ \hat{L}^{\downarrow\uparrow} & \hat{L}^{\downarrow\downarrow} \end{pmatrix}. \tag{3.39}$$

The manner in which this adjustment integrates into the scalar-relativistic Hamiltonian varies according to the specific system under investigation (such as spin-spiral systems) and the particular parameter of interest (like Dzyaloshinskii-Moriya interaction (DMI) or magnetocrystalline anisotropy (MCA)).
Since SOC distinguishes between different magnetization directions with respect to the lattice in the chemical unit cells, using the generalized Bloch theorem is no longer possible. As SOC is typically a weak effect compared to the rest of the Hamiltonian, one approach could be to include it perturbatively. Hence, first, we neglect SOC and calculate the spin-spirals within one chemical unit cell and periodic boundary conditions, and then the action of the spin-orbit operator on these solutions will be considered in the next step [99]. Thus, it can be determined by

$$\langle \psi_{0,\nu} | \hat{\mathcal{H}}_{\mathrm{SO}} | \psi_{0,\nu} \rangle = \begin{pmatrix} \langle \psi^\uparrow_{0,\nu} | & \langle \psi^\downarrow_{0,\nu} | \end{pmatrix} \begin{pmatrix} \mathcal{H}^{\uparrow,\uparrow}_{\mathrm{SO}} & \mathcal{H}^{\uparrow,\downarrow}_{\mathrm{SO}} \\ \mathcal{H}^{\downarrow,\uparrow}_{\mathrm{SO}} & \mathcal{H}^{\downarrow,\downarrow}_{\mathrm{SO}} \end{pmatrix} \begin{pmatrix} |\psi^\uparrow_{0,\nu}\rangle \\ |\psi^\downarrow_{0,\nu}\rangle \end{pmatrix}, \tag{3.40}$$

where $\psi_{0,\nu}$ are the unperturbed states. In first-order perturbation theory, the correction to the band energies remains uniform across all atoms. Each of the four components, $\mathcal{H}^{\sigma\sigma'}_{\mathrm{SO}}$ of the spin-orbit operator exhibits lattice periodicity. When acting on a Bloch function, it yields the same Bloch factor while introducing another periodic Bloch function, denoted as $\tilde{u}(\boldsymbol{r})$. This can be expressed as:

$$\mathcal{H}^{\sigma\sigma'}_{\mathrm{SO}} e^{i(\boldsymbol{k}\mp\boldsymbol{q}/2)\cdot\boldsymbol{r}} u^{\sigma'}_\nu(\boldsymbol{r}) = e^{i(\boldsymbol{k}\mp\boldsymbol{q}/2)\cdot\boldsymbol{r}} \tilde{u}^{\sigma'}_\nu(\boldsymbol{r}). \tag{3.41}$$

# 4 Spin models

**Contents**


4.1. Heisenberg-type exchange interaction . . . . . 36
4.2. Dyzaloshinskii-Moriya interaction . . . . . 37
4.3. Magnetic anisotropy . . . . . 38
4.3.1. Magnetic shape anisotropy . . . . . 39
4.3.2. Magnetocrystalline anisotropy . . . . . 40


The properties of magnetic materials are often described using model Hamiltonians, assuming that each atom exhibits a magnetization. In the case of strong local magnetic moment formation, i.e., when $|M_\nu|$ does not depend significantly on $\hat{e}_\nu$, the cooperation of local spins on a global length scale at finite temperature can be calculated. The magnetic ground state or the response to an excitation can thus be determined. Consequently, the spin structures depend on slight modifications of the exchange interactions.
The physical origin of these interactions lies in the Coulomb interaction of electrons whose wavefunctions overlap with electron wavefunctions from the neighboring atoms. Continuing this simple picture, the magnetic moment of an atom is then generated by localized electrons. A general bilinear interaction between two spins can be expressed as

$$\mathcal{H} = \sum_{ij} \boldsymbol{M}_i^\top \underline{V}_{ij} \boldsymbol{M}_j, \tag{4.1}$$

where $\underline{V}_{ij}$ is a real $3 \times 3$ matrix given by:

$$\underline{V}_{ij} = \begin{pmatrix} V_{ij}^{11} & V_{ij}^{12} & V_{ij}^{13} \\ V_{ij}^{21} & V_{ij}^{22} & V_{ij}^{23} \\ V_{ij}^{31} & V_{ij}^{32} & V_{ij}^{33} \end{pmatrix}. \tag{4.2}$$

Breaking down the interaction matrix, it can be decomposed into three components: an isotropic part, $J_{ij}$, a symmetric traceless part, $\underline{V}_{ij}^{+}$, and an antisymmetric part, $\underline{V}_{ij}^{-}$. These components can be defined as

$$J_{ij} = \frac{\mathrm{Tr}(\underline{V}_{ij})}{3}, \tag{4.3}$$

$$\underline{V}_{ij}^{+} = \frac{(\underline{V}_{ij} + \underline{V}_{ij}^{\top})}{2} - J_{ij}, \tag{4.4}$$

$$\underline{V}_{ij}^{-} = \frac{(\underline{V}_{ij} - \underline{V}_{ij}^{\top})}{2}. \tag{4.5}$$

Employing these expressions, the Equation (4.1) can be rewritten as:

$$\mathcal{H} = \sum_{ij} \left( J_{ij} \boldsymbol{M}_i \cdot \boldsymbol{M}_j + \boldsymbol{M}_i^{\top} \underline{V}_{ij}^{+} \boldsymbol{M}_j + \boldsymbol{M}_i^{\top} \underline{V}_{ij}^{-} \boldsymbol{M}_j \right). \tag{4.6}$$

The first component corresponds to the Heisenberg model, while the third component is referred to as the Dzyaloshinskii-Moriya interaction (DMI). The second part of the interaction, the symmetric traceless matrix, is commonly known as the anisotropic exchange [105]. This component arises from relativistic two-particle effects, contributing minimally to the overall energy. Alternatively, the magnetocrystalline anisotropy energy (MCA) can be considered within the on-site term of $\underline{V}_{ij}^{+} = \underline{V}_{ii}^{+}$.
In conclusion, the magnetism of complex spin systems can be described within the framework of a classical spin Hamiltonian, which can be written in the form of

$$\mathcal{H} = -\sum_{ij} J_{ij} \left( \boldsymbol{M}_i \cdot \boldsymbol{M}_j \right) + \sum_{ij} \boldsymbol{D}_{ij} \cdot \left( \boldsymbol{M}_i \times \boldsymbol{M}_j \right) + \sum_{i} K_i M_i^2 \cos^2 \xi_i, \tag{4.7}$$

where $J_{ij}$ represents the exchange interactions between spins, $\boldsymbol{D}_{ij}$ represents DMI, and $K_i$, due to the spin-orbit coupling (SOC), represents the anisotropy constant with $\xi_i$ being the angle between the magnetization $\boldsymbol{M}_i$ and the easy axis. In the following, each term will be discussed separately.

## 4.1 Heisenberg-type exchange interaction

In the Heisenberg model [106], one can refer to the classical version by substituting the Pauli matrices with classical vectors $\boldsymbol{M} = \left(M_x, M_y, M_z\right)$, in which the $i, j$ are considered different lattice sites.

$$\mathcal{H} = -\sum_{ij} J_{ij} \left( \boldsymbol{M}_i \cdot \boldsymbol{M}_j \right) \tag{4.8}$$

The exchange interaction is isotropic and characterized by the pair-wise interaction constants $J_{ij}$. According to Equation (4.8), in localized model spin structures, a

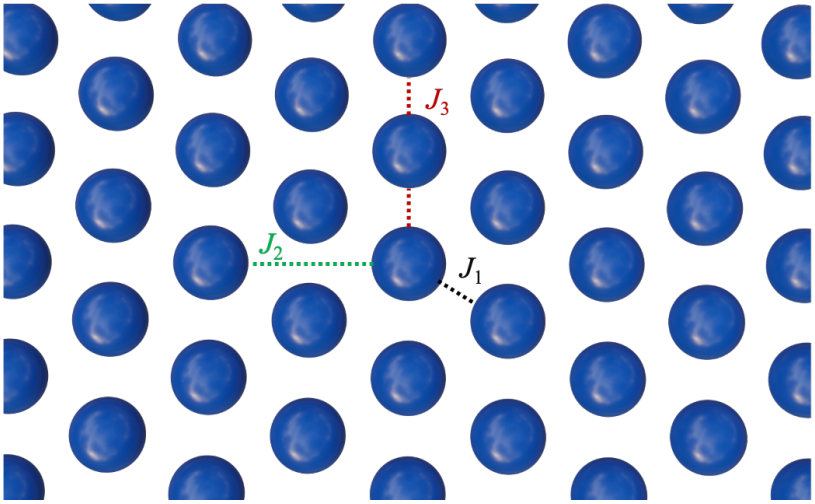



Figure 4.1.: $J_1$ is counted as the first-neighbour exchange parameter and $J_2$ and $J_3$ are the second- and third-exchange terms.

positive $J_{ij}$ favors ferromagnetic interactions, while a negative $J_{ij}$ favors antiferromagnetic ones. The exchange interactions up to third neighbors on a square lattice are shown in Figure (4.1). The general solution of Equation (4.8) is the spin-spiral discussed in Section (3.5).
Also, higher-order corrections such as a four-spin interaction or a bi-quadratic interaction can be derived from a Hubbard model expansion [107, 108, 109]:

$$\mathcal{H}_{\text{biquad.}} = B_{ij}(\boldsymbol{M}_i \cdot \boldsymbol{M}_j)^2, \tag{4.9}$$

$$\mathcal{H}_{4\text{–spin}} = K_{ijkl}\left[(\boldsymbol{M}_i \cdot \boldsymbol{M}_j)(\boldsymbol{M}_k \cdot \boldsymbol{M}_l) + (\boldsymbol{M}_j \cdot \boldsymbol{M}_k)(\boldsymbol{M}_l \cdot \boldsymbol{M}_i) - (\boldsymbol{M}_i \cdot \boldsymbol{M}_k)(\boldsymbol{M}_j \cdot \boldsymbol{M}_l)\right]. \tag{4.10}$$

Whereas bi-quadratic interaction describes a higher-order two-spin interaction, while the four-spin exchange term expresses interactions among spins at four distinct lattice sites.

## 4.2 Dyzaloshinskii-Moriya interaction

Dyzaloshinskii-Moriya interaction (DMI) (antisymmetric exchange interaction) was derived based on symmetry by Dyzaloshinskii [110, 111] and has the form:

$$\mathcal{H}_{\text{DMI}} = \sum_{ij} \boldsymbol{D}_{ij} \cdot \left(\boldsymbol{M}_i \times \boldsymbol{M}_j\right). \tag{4.11}$$

Here, $\boldsymbol{D}_{ij}$ is called the Dzyaloshinskii-vector, which depends on the symmetry of the structure as well as the real space direction given by two sites $i$ and $j$. Both the sign and value of $\boldsymbol{D}_{ij}$ can influence the stability of collinear uniaxial ferromagnetic or antiferromagnetic structures. Hence, one can describe the collinear system with

a directional $\boldsymbol{c} = \boldsymbol{S}_i \times \boldsymbol{S}_{i+1}$. The DMI is usually much smaller than the exchange interaction. However, it plays a major role in weak ferromagnetism and naturally prefers non-collinear magnetic systems. Both SOC and an inversion-asymmetric environment are crucial for the existence of the DMI. The chemical structure can be carefully designed to meet both critical requirements for a strong DMI.
In the case of two spins, the energy solely depends on the angle between these spins. In Figure (4.2), the relation between the spins and $D$-vector is pictured. First-principles calculations of DMI can be conducted using methods that involve

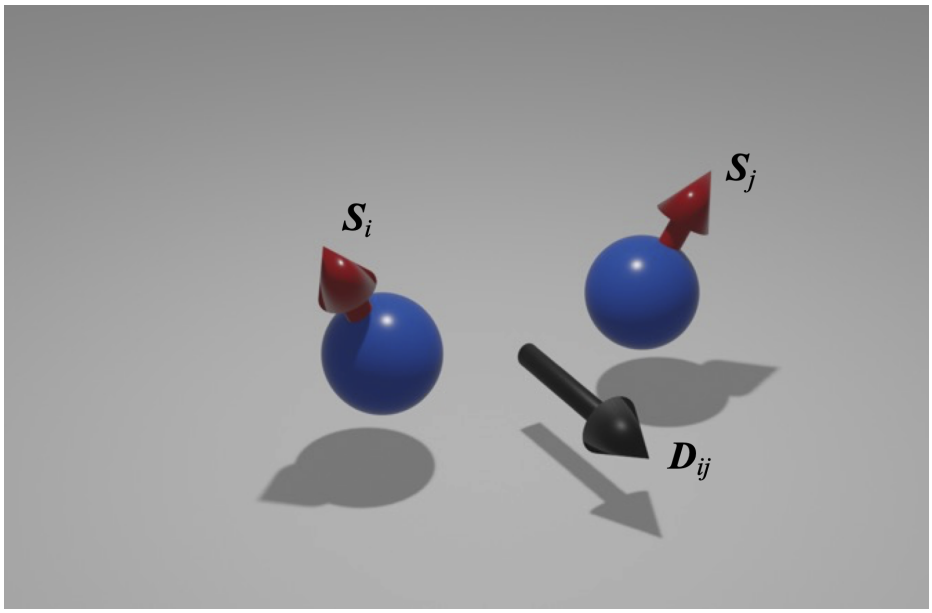



Figure 4.2.: Dzyalonshinskii-Moriya interaction (DMI) is an asymmetric interaction that is observed in thin films with strong spin-orbit coupling (SOC) and symmetry breaking.

mapping either the total energies or the energy derivatives. In total-energy mapping methods, the $\boldsymbol{D}_{ij}$ coefficients can be obtained from non-collinear DFT calculations, such as those involving spin spirals. Subsequently, the energy change can be analytically computed using perturbation theory [112].
DMI favors twisted spin configurations, resulting in the creation of various chiral topological magnetic structures, such as skyrmions, and significantly influences spin dynamics [113, 114].

## 4.3 Magnetic anisotropy

The third contribution in Equation (4.7) is caused by spin-orbit coupling, which connects the spin-degree of freedom to the motion of the electron. Besides, it depends basically on the symmetry of the lattice, and the crystal field determines the orbital moment of the atom. Therefore, it is assumed to be a one-site interaction.

In uniaxial systems, it can be expanded in the form of

$$\mathcal{H} = \sum_i K_i M_i^2 \cos^2 \xi_i, \tag{4.12}$$

where $\xi$ is the angle between the spin and the unique axis. $K_i$ is a parameter depending on the material. On the atomic scale, the magnetic moments at the lattice site tend to align along a specific direction known as the easy axis. Deviating from this preferred direction and aligning in a different direction leads to an energy cost. The direction perpendicular to the easy axis, so-called the hard axis, represents the orientation with the highest energy for magnetization. The strength of this directional preference can be quantified by the magnetic anisotropy energy (MAE), which is the energy difference between the magnetic moments aligned along the hard and easy axes. Two main contributions to MAE will be discussed. The first is magnetic shape anisotropy (MSA) energy, which arises from the macroscopic shape of the structure and can be described using classical physics. The second contribution is magnetocrystalline anisotropy (MCA), which results from the anisotropic arrangement of atoms within the crystal lattice and is dependent on the presence of SOC.

### 4.3.1 Magnetic shape anisotropy

The magnetic field generated by a dipole moment $\boldsymbol{M}_i$ located at position $\boldsymbol{R}_i$ is described by

$$\mathbf{B}_i(\boldsymbol{r}) = -\frac{\mu_\mathrm{B}}{2r_i^5}\left[r_i^2 \boldsymbol{M}_i - 3(\boldsymbol{r}_i \cdot \boldsymbol{M}_i)\boldsymbol{r}_i\right], \tag{4.13}$$

where $\mu_\mathrm{B}$ and $\boldsymbol{r}_i$ are the Bohr magneton and $\boldsymbol{r}_i = \boldsymbol{r} - \boldsymbol{R}_i$, respectively. When a second dipole moment $\boldsymbol{M}_j$ is positioned at $\boldsymbol{r}_j$, it interacts with the magnetic field $\mathbf{B}_i(\boldsymbol{r})$, leading to the dipole-dipole interaction energy given by:

$$E_{\mathrm{dipole-dipole}} = -\frac{\mu_\mathrm{B}}{2r_{ij}^5}\left[r_{ij}^2(\boldsymbol{M}_i \cdot \boldsymbol{M}_j) - 3(\boldsymbol{r}_{ij} \cdot \boldsymbol{M}_i)(\boldsymbol{r}_{ij} \cdot \boldsymbol{M}_j)\right]. \tag{4.14}$$

If both dipole moments $\boldsymbol{M}_i$ and $\boldsymbol{M}_j$ are aligned in the same direction, as is known as a ferromagnet, the dipole-dipole interaction energy simplifies to

$$E_{\mathrm{dipole-dipole}} = -\frac{\mu_\mathrm{B}}{r_{ij}^3} M_i M_j \left[1 - 3\cos^2\theta\right], \tag{4.15}$$

where $\theta$ represents the angle between $\boldsymbol{M}_i$ and $\boldsymbol{r}_{ij}$. In thin films, the MSA is always confined to the plane of the sample, causing the magnetization to align within this plane due to the shape effects naturally. In this thesis, as we are primarily interested in the SOC-induced effects, the dipole-dipole interaction is neglected in comparison to the corresponding MCA value.

### 4.3.2 Magnetocrystalline anisotropy

MCA is influenced by the orientation of spins within the crystal lattice, influencing the total energy of the structure only when SOC is considered.
The anisotropy can be calculated from DFT including SOC by comparing the total energy for different angles, $\xi$. The spin-orbit coupling term is introduced in Equation (3.37) with the spin-orbit coupling constant $\xi$. In a crystal, the primary contribution to the spin-orbit interaction comes from the region near the nucleus, where $\xi$ is larger for heavier atoms. The MCA arises from the anisotropy in the spin-orbit interaction, specifically the energy difference between Hamiltonians that include the SOC term with the magnetization oriented in different directions. In practice, this involves first solving the Schrödinger equation, then incorporating the SOC term into the Hamiltonian and adjusting the spin-quantization axis using a spin-rotation matrix $\underline{U}$:

$$\begin{aligned}\langle \underline{U}\boldsymbol{\psi}_0|\hat{\mathcal{H}}_0 + \hat{\mathcal{H}}_{\mathrm{SO}}|\underline{U}\boldsymbol{\psi}_0\rangle &= \langle \boldsymbol{\psi}_0|\hat{\mathcal{H}}_0|\boldsymbol{\psi}_0\rangle + \langle \underline{U}\boldsymbol{\psi}_0|\hat{\mathcal{H}}_{\mathrm{SO}}|\underline{U}\boldsymbol{\psi}_0\rangle \\ &= \epsilon_0 + \xi \begin{pmatrix} \psi_0^{\uparrow} \\ \psi_0^{\downarrow} \end{pmatrix}^{\dagger} \underline{U}^{\dagger} \begin{pmatrix} L_z & L_x - iL_y \\ L_x + iL_y & -L_z \end{pmatrix} \underline{U} \begin{pmatrix} \psi_0^{\uparrow} \\ \psi_0^{\downarrow} \end{pmatrix}\end{aligned} \tag{4.16}$$

If the orbital moment is small, the last term only provides a minor correction to the energy, $\epsilon_0$, obtained from the Schrödinger equation, causing the magnetization direction of the solution to align with the spin-quantization axis described by $U$. Similar to the Heisenberg Hamiltonian used to describe exchange interactions in a crystal, SOC is represented as $\sum_i \xi_i \mathbf{L}_i \cdot \mathbf{S}_i$, where $i$ denotes a specific atomic site. Additionally, there can be a term that couples the spin at site $i$ to the orbital motion at site $j$, expressed as $\sum_{i,j} C_{ij} \mathbf{L}_j \cdot \mathbf{S}_i$. This spin-other-orbit interaction, analogous to the dipole-dipole interaction, is derived from the Breit equation. Although it was included in ab initio calculations using the Hartree approximation, it was found to be much weaker than the spin-same-orbit interaction [27].
It is evident that both strong SOC and a sizable orbital moment are necessary for a significant contribution to MAE. Ab initio calculations are essential for determining the relative significance of various contributions to MA. Most calculations focus on SOC, using an effective one-particle, Schrödinger-like approach, and the classical dipole-dipole energy, within a DFT framework.

# 5

# Exploring graphene coverage on Co/HM(111) substrates

**Contents**


5.1. Investigating the electronic structure . . . . . 42
5.2. Exchange interaction in Gr on Co/Pt(111) . . . . . 46
5.3. Tailoring interlayer distances of Gr and Co . . . . . 49
5.4. DMI in Gr/Co/HM(111) . . . . . 51
5.4.1. DMI across various stackings of Gr on Co/Pt(111) . . . . . 56
5.5. MCA in Gr/Co/HM . . . . . 60


Graphene (Gr), a single atomic layer of graphite, is a suitable candidate to develop spin transport channels with long spin lifetimes as well as propagation lengths at room temperature. However, the development of Gr-spintronic devices demands the generation of long-range magnetic order and spin filtering in Gr. Due to the exceedingly low intrinsic spin-orbit coupling (SOC) in Gr, which is calculated to be less than a few tens of $\mu eV$ [115], the practical observation of such effects is unviable. Considerable efforts have been made to identify a practical approach for enhancing and customizing the strength of SOC from an external perspective. These have been accomplished by intercalation of heavy metal (HM) atoms in order to propose a giant SOC in the electronic bands of Gr [116, 18].
Comparing Co/Pt(111) with Gr/Co/Pt(111) suggests that engineering an epitaxial structure with a Co layer sandwiched between Gr and an epitaxial Pt(111) buffer grown on MgO(111) reveals substantial evidence of Dzyaloshinskii-Moriya interaction (DMI) at the Gr/Co interface. This DMI opposes the SOC-induced DMI at the Co/Pt interface. Also, it stabilized a left-handed Néel-type spin-spiral or domain walls (DWs) [12]. Moreover, the research exploring the structural and magnetic characteristics of Gr intercalated with Co on an Ir(111) substrate discovered that Co naturally arranges into monolayer islands, aligning structurally with the Ir(111)

surface, then is covered by a Gr overlayer. Nevertheless, the robust interaction between Gr and Co results in a significant lattice mismatch when deposited on the Ir(111) substrate [22].
These magnetic configurations are achieved within noncentrosymmetric multilayer assemblies exhibiting Perpendicular Magnetic Anisotropy (PMA). Maximizing the PMA is crucial for reducing the size of data storage spintronic devices, such as Spin Transfer Torque Magnetic Random Access Memories (STT-MRAM) [4]. They are further influenced by the antisymmetric exchange interaction (DMI), which promotes a chiral alignment of spins within the DWs [35]. This DMI also stabilizes magnetic skyrmions, which are nanometer-sized, topologically protected magnetic structures. They have been observed in the presence of strong magnetic fields and at low temperatures [34, 113], and more recently, they have been detected at room temperature even under minimal or no magnetic fields [117, 118].
In this chapter, we embark on an investigation of Gr/1ML Co/5ML HM using DFT calculations, conducting separate analyses for both Pt and Ir as HMs.

## 5.1 Investigating the electronic structure

The electronic properties of Gr depend critically on its environment, and in particular, on its substrate [15]. Hence, we investigated Gr on both Co/Pt(111) and Co/Ir(111) substrates. This further allowed us to explore the interaction between Gr and Co in different HM substrate environments. The slab under study comprises Gr, a single Co, and five Pt(Ir) layers. It was proposed that the ground state of the Co monolayer on Pt is oriented along the fcc(111) direction [119]. Therefore, we examined Gr on top of Co/Pt(Ir) on the fcc(111) plane, considering the lattice constant of Pt(Ir). Taking into account the difference in lattice constants between Gr at 2.46 Å and Co/Pt(Ir) at 2.76 (2.73) Å, it's possible to have three distinct configurations of Gr through the formation of moiré patterns. Consequently, within a moiré lattice, top-fcc, top-hcp, and hollow stacking of Gr on Co/Pt(Ir) are within the bounds of possibility, as depicted in Figure (5.1). The top site refers to the first C atom positioned directly above a Co atom. The fcc, as well as hcp, corresponds to the second C occupying a fcc or hcp site in the Co/Pt(111) structure. The hollow site, in this notation, represents one C in the fcc and the other one in the hcp site.
An investigation demonstrates that the bonding of Gr on Ir(111) is primarily of van der Waals (vdW) type, with a chemical modulation [120]. Also, the moiré pattern arises due to the lattice mismatch between the Gr and the Ir(111) surface [121]. When Co is deposited onto a Gr/Ir(111) sample leads to the emergence of intercalation regions characterized by moiré patterns, particularly when deposition occurs at or slightly above room temperature [22]. Experimental observations suggest that the formation of intercalated islands is driven by the migration of Co atoms from the edges of the Gr patches [122].
To thoroughly explore the electronic and magnetic structures of Gr/Co/HM films, we conducted individual optimizations for three specific configurations of Gr on one ML of Co supported by a 5 ML substrate of either Pt or Ir. These configura-

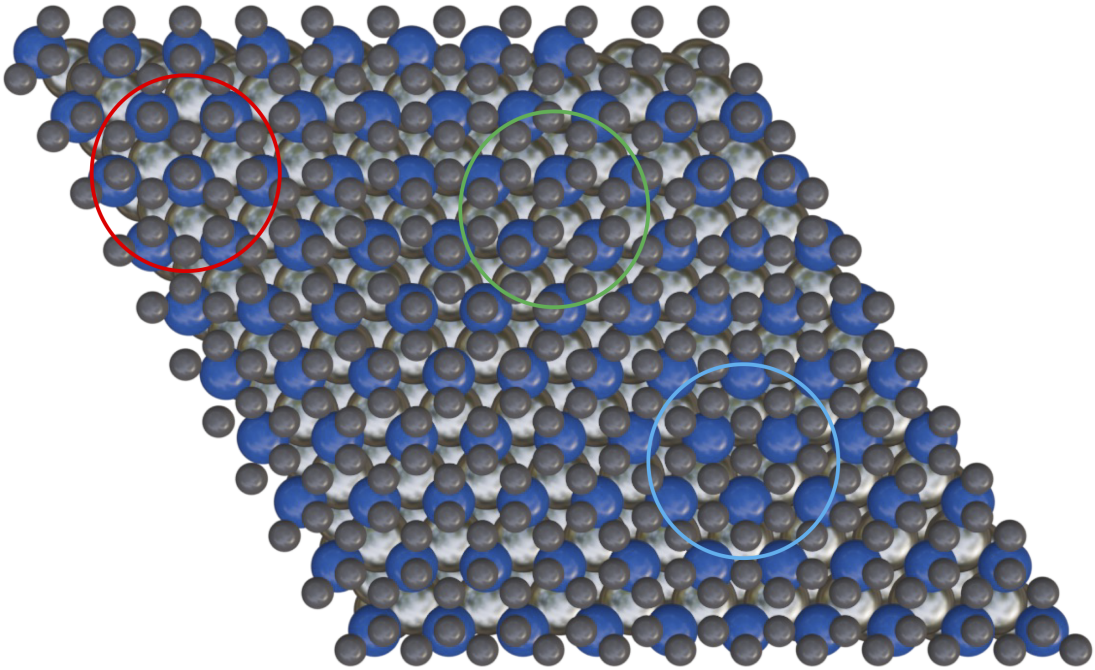


Figure 5.1.: Within the formation of moiré configurations, three distinct arrangements of Gr(10 × 10) on Co/Pt(111)(9 × 9) can be observed: top-hcp (green), top-fcc (red), and hollow (blue) sites.

tions are depicted in Figure (5.1). Our study focused on the distinct arrangements of Gr on Co/HM without employing the supercell approach. This decision was made to manage computational time effectively, ensuring that our calculations provide a comprehensive understanding of how the interface interactions influence the overall electronic and magnetic properties of the heterostructure. This optimization included stacking in the top-fcc and top-hcp, as well as a hollow on the Co/HM(111) configuration. The structural relaxations were performed using the FLEUR-code [55, 56] employing the FLAPW method. To treat combined systems of Gr, 3*d*-, and 5*d*-transition metals, DFT with GGA was employed. Since Gr on Co is chemisorbed, no vdW corrections were necessary. We utilized a cutoff parameter of $K_{\max} = 4.0\, a_B^{-1}$ for the basis functions, in conjunction with 21 $k$-points encompassing the p3m1 symmetry class of primitive hexagonal (2D) BZ. In this context, $a_B$ denotes the Bohr radius. The structural relaxation iterations were conducted until the forces reached magnitudes below 0.05 eV/Å, in order to identify the interfacial geometries that exhibit the highest stability. As shown in Table (5.1),

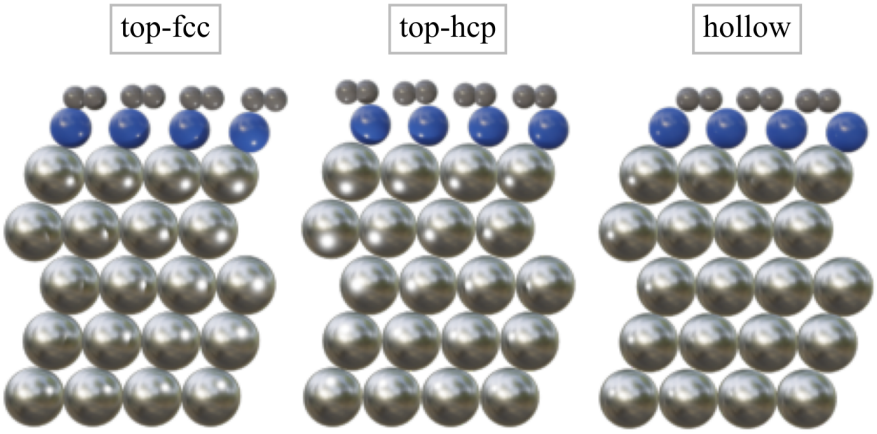



Figure 5.2.: A lateral depiction showcases three potential stacking configurations of Gr atop Co/Pt(111). Gr on Co/Ir(111) is essentially identical to the Gr on Co/Pt(111) where Pt is substituted with adjacent metal, Ir.

our calculations suggest that the ground state of Gr on both Co/Pt(111) as well as Co/Ir(111) is obtained with the top-fcc stacking. Furthermore, it is worth noting that both energetically favored top-fcc and top-hcp configurations are rather similar. Although Gr appears chemisorbed (the C/Co distance is less than 2 Å), almost no buckling in Gr is observed. In the Co/Pt(111) configuration, for the fcc stacking position, the interlayer distances $d_{\mathrm{Co/Pt(I)}}$ and $d_{\mathrm{Pt(I)/Pt(I-1)}}$ are reported as 2.02 Åand 3.37 Å, respectively [119]. It's clear that the presence of the Gr overlayer reduces the distance between Co/Pt(I) layers. Moreover, the interlayer distances between Ir layers, particularly near the bottom of the slab, approach the ideal bulk value of 2.23 Å. Ultrathin films are well described by a general classical extended Heisenberg

| HM | Pt | | | Ir | | |
|---|---|---|---|---|---|---|
| $a$ | 2.76 | | | 2.73 | | |
| Gr/Co stacking | top-fcc | top-hcp | hollow | top-fcc | top-hcp | hollow |
| $d_{\mathrm{C(I-1)/C(I)}}$ | 0.02 | 0.02 | 0.0 | 0.02 | 0.02 | 0.0 |
| $d_{\mathrm{C(I)/Co}}$ | 1.95 | 1.98 | 1.97 | 1.96 | 2.00 | 1.95 |
| $d_{\mathrm{Co/HM(I)}}$ | 2.04 | 2.04 | 2.04 | 2.04 | 2.05 | 2.06 |
| $d_{\mathrm{HM(I)/HM(I-1)}}$ | 2.37 | 2.36 | 2.37 | 2.27 | 2.27 | 2.26 |
| $d_{\mathrm{HM(I-1)/HM(I-2)}}$ | 2.33 | 2.33 | 2.33 | 2.26 | 2.25 | 2.26 |
| $d_{\mathrm{HM(I-2)/HM(I-3)}}$ | 2.32 | 2.32 | 2.32 | 2.24 | 2.23 | 2.24 |
| $d_{\mathrm{HM(I-3)/HM(I-4)}}$ | 2.35 | 2.34 | 2.34 | 2.20 | 2.20 | 2.20 |
| Total energy | 0.0 | 0.07 | 0.71 | 0.0 | 0.10 | 0.69 |

Table 5.1.: $a$ and $d$ indicate in-plane lattice parameters and interlayer distances for different stacking positions of Gr on Co/Pt(111), respectively. Distances are given in Å and total energies in eV relative to the top-fcc stacking of Gr on Co/Pt(111). HM(I) denotes the interface Pt(Ir).

Hamiltonian. The extended Heisenberg Hamiltonian assigns magnetic moments to individual atomic sites. Considering Heisenberg exchange interaction ($J_{ij}$), DMI, and magnetic anisotropy (MA) parameters enables a precise characterization of the energy landscape in 2D itinerant magnets.

## 5.2 Exchange interaction in Gr on Co/Pt(111)

In order to determine exchange interactions, we investigated the total energy of the spin-spiral using the generalized Bloch theorem. This approach is applicable in cases where the spin space and crystal lattice are not coupled, enabling us to describe any homogeneous spiral spin-density wave (SSDW) using the chemical unit cell. The generalized Bloch theorem [123, 101] postulates that the eigenstates of a Schrödinger-type Hamiltonian

$$\mathcal{H}_0 = \frac{1}{2m_e}\boldsymbol{p}^2 + V(\boldsymbol{r}) + \underline{\boldsymbol{\sigma}} \cdot \boldsymbol{B}(\boldsymbol{r}) \tag{5.1}$$

with a lattice periodic scalar potential, $V$, and an exchange-correlation **B**-field can be written in

$$\psi_{\boldsymbol{k},\nu}(\boldsymbol{r}|\boldsymbol{q}) = \begin{pmatrix} \psi^{\uparrow}_{\boldsymbol{k},\nu} \\ \psi^{\downarrow}_{\boldsymbol{k},\nu} \end{pmatrix} = \begin{pmatrix} e^{i(\boldsymbol{k}-\boldsymbol{q}/2)\cdot\boldsymbol{r}} u^{\uparrow}_{\boldsymbol{k},\nu}(\boldsymbol{r}) \\ e^{i(\boldsymbol{k}+\boldsymbol{q}/2)\cdot\boldsymbol{r}} u^{\downarrow}_{\boldsymbol{k},\nu}(\boldsymbol{r}) \end{pmatrix}, \tag{5.2}$$

with lattice periodic functions

$$u^{\sigma}_{\boldsymbol{k},\nu}(\boldsymbol{r}) = u^{\sigma}_{\boldsymbol{k},\nu}(\boldsymbol{r}+\boldsymbol{R}), \tag{5.3}$$

with $\boldsymbol{k}$, $\nu$, and $\sigma$ representing crystal momentum, band index, and spin index, respectively. The $\boldsymbol{q}$-dependent phase factor represents a spin rotation around the $z$-axis. This theorem allows us to deduce the complete solution of the Kohn-Sham Schrödinger equation by confining the computation to the chemical unit cell and the first Brillouin zone.
We iteratively solve the unperturbed Kohn-Sham equation until self-consistency is achieved:

$$\mathcal{H}_0\psi_{0,\nu} = \epsilon_{0,\nu}\psi_{0,\nu}. \tag{5.4}$$

Subsequently, these energies are mapped to the extended Heisenberg model to extract $J_{ij}$ parameters. Since we neglect the SOC, the orientation of magnetic moments with respect to the crystal lattice becomes irrelevant, allowing us to compute the electronic structure of a homogeneous spin spiral using the generalized Bloch theorem. Thanks to the generalized Bloch theorem, even long-wavelength spin spirals with small values for $|\boldsymbol{q}|$, where the spin-spiral period length is given by $\lambda = 2\pi/|\boldsymbol{q}|$, can be efficiently treated within the chemical unit cell, eliminating the need for large supercells. This theorem is thoroughly discussed in Section (3.5.1).
Enhancing the proficiency of studying magnetism on a periodic lattice involves

expressing quantities in terms of their Fourier components. Thus, the spins are represented at lattice sites by discrete Fourier components:

$$\boldsymbol{S}_{\boldsymbol{q}} = \frac{1}{N}\sum_{n}^{N} S_n e^{-i\boldsymbol{q}\cdot\boldsymbol{R}_n}. \tag{5.5}$$

Here, the summation is over the reciprocal lattice vector $\boldsymbol{q}$ and the real-space coordinate of lattice site $n$ is denoted as $\boldsymbol{R}_n$, with the total number of lattice sites in the crystal being denoted as $N$. By replacing the localized spins $\boldsymbol{S}_n$ with their Fourier components in the Heisenberg Hamiltonian, we obtain:

$$\mathcal{H} = -N\sum_{\boldsymbol{q}} J(\boldsymbol{q})\boldsymbol{S}_{\boldsymbol{q}}\cdot\boldsymbol{S}_{-\boldsymbol{q}}. \tag{5.6}$$

It is essential to ensure that the squared length of all spins, $\boldsymbol{S}_n^2 = S^2$, remains conserved on all sites. This condition is, for example, met by adopting a spin configuration described by:

$$\boldsymbol{S}_n = S\Big(\hat{\boldsymbol{e}}_x\cos(\boldsymbol{q}\cdot\boldsymbol{R}_n) + \hat{\boldsymbol{e}}_y\sin(\boldsymbol{q}\cdot\boldsymbol{R}_n)\Big). \tag{5.7}$$

This equation characterizes an SSDW in the $xy$-plane. The spin configuration of conical spin-spiral, which precesses on a cone with an opening angle $\theta$ around $\hat{e}_z$, can be expressed as:

$$\boldsymbol{S}_n = S\Big(\hat{\boldsymbol{e}}_x\cos(\boldsymbol{q}\cdot\boldsymbol{R}_n)\sin\theta + \hat{\boldsymbol{e}}_y\sin(\boldsymbol{q}\cdot\boldsymbol{R}_n)\sin\theta + \hat{\boldsymbol{e}}_z\cos\theta\Big), \tag{5.8}$$

Such SSDWs represent general solutions of the classical Heisenberg model for a periodic lattice. From Equation (5.6), it can be deduced that the lowest total energy corresponds to the propagation vector $\boldsymbol{Q}$, where $\pm\boldsymbol{Q}$ are the values of $\boldsymbol{q}$ that maximize the function $J(\boldsymbol{q})$. This implies that $\boldsymbol{Q}$ tends to favor high-symmetry points within the BZ and subsequently high-symmetry lines. For example, if $\boldsymbol{Q} = 0$ maximizes $J(\boldsymbol{q})$, the solutions correspond to the ferromagnetic state. To describe the spin structure, we represent $\boldsymbol{S}_{\boldsymbol{Q}}$ in terms of real ($\boldsymbol{R}_{\boldsymbol{Q}}$) and imaginary ($\boldsymbol{I}_{\boldsymbol{Q}}$) parts:

$$\boldsymbol{S}_{\boldsymbol{Q}} = \boldsymbol{R}_{\boldsymbol{Q}} + i\boldsymbol{I}_{\boldsymbol{Q}}. \tag{5.9}$$

Substituting Equation (5.9) into Equation (5.5) for $+\boldsymbol{Q}$ and $-\boldsymbol{Q}$ yields the spin configuration at lattice sites:

$$\boldsymbol{S}_n = 2\Big(\boldsymbol{R}_{\boldsymbol{Q}}\cos(\boldsymbol{Q}\cdot\boldsymbol{R}_n) - \boldsymbol{I}_{\boldsymbol{Q}}\sin(\boldsymbol{Q}\cdot\boldsymbol{R}_n)\Big). \tag{5.10}$$

As we are not considering spin-orbit terms in the Hamiltonian, we can assume that the plane spanned by the two vectors $\boldsymbol{R}_{\boldsymbol{Q}}$ and $\boldsymbol{I}_{\boldsymbol{Q}}$ lies in the $xy$-plane. Consequently, the spin of the helix rotates around the $z$-axis within the $xy$-plane as one moves along the lattice plane in the direction of $\boldsymbol{Q}$. In the following, we will identify potential candidates for the ground state to determine the BZ of a two-dimensional hexagonal lattice and minimize the Heisenberg Hamiltonian.

Self-consistent calculations without SOC are performed for flat spirals and arbitrary spin-spiral vector q. In pursuit of a precise characterization of surfaces and interfaces, we have employed GGA. The total energy of spin-spiral states was converged in non-relativistic approximation using a $45 \times 45\,k$-point mesh. The size of the basis set was determined by $K_{\max} = 4.3\,a_B^{-1}$. The calculated total energies as a function of q, along with those fitted within the Heisenberg model, along the high symmetry line, are illustrated in Figure (5.3). In order to discuss the energy of magnetic states on the

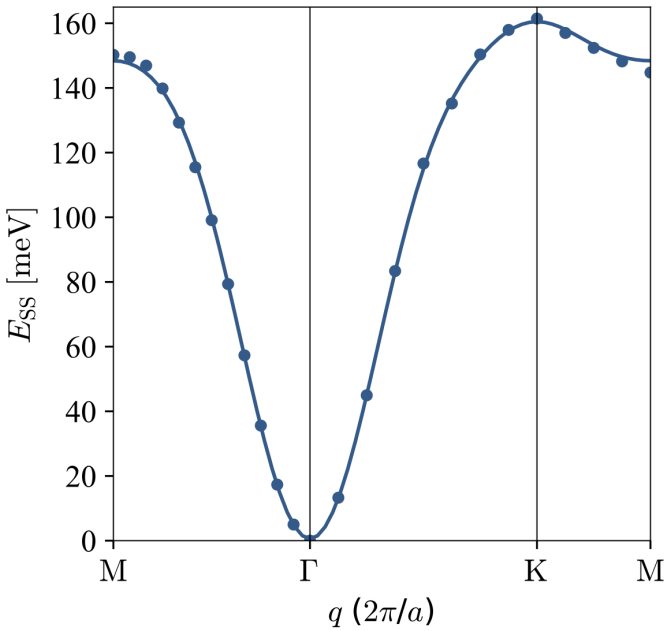



Figure 5.3.: The self-consistently calculated total energies as a function of the spin-spiral $q$-vectors along the high symmetry path are depicted by blue dots. Subsequently, these energies are mapped within the framework of the Heisenberg model to extract the exchange interactions, $(J(\boldsymbol{q}))$.

2D hexagonal lattice within the Heisenberg model up to the third nearest neighbor interaction. We include the exchange constants $J_1$, $J_2$, and $J_3$. In a hexagonal lattice one can parameterize the $q$-vectors on the line $\overline{\Gamma K}$ by $\boldsymbol{q} = (q_x, 0)$. The energy on the $q$-vectors of this line can be calculated and written as

$$\begin{aligned} E_{\overline{\Gamma K}}(\vec{q}) = -S^2\Big\{ & J_1[2\cos(aq_x) + 4\cos(\frac{1}{2}aq_x)] \\ & + J_2[4\cos(\frac{3}{2}aq_x) + 2] \\ & + J_3[2\cos(2aq_x) + 4\cos(aq_x)]\Big\}. \end{aligned} \tag{5.11}$$

However, the $q$-vectors on the line $\overline{\Gamma M}$ are parameterized by $\boldsymbol{q} = (0, q_y)$. In this case, the energy dependent on $q$-vectors is formulated as

$$\begin{aligned} E_{\overline{\Gamma M}}(\vec{q}) = -S^2\Big\{ & J_1[2 + 4\cos(\frac{\sqrt{3}}{2}aq_y)] \\ & + J_2[4\cos(\frac{\sqrt{3}}{2}aq_y) + 2\cos(\sqrt{3}aq_y)] \\ & + J_3[2 + 4\cos(\sqrt{3}aq_y)]\Big\}. \end{aligned} \tag{5.12}$$

The exchange interaction between nearest neighbors is summarized in Table (5.2), and we have also conducted a comparative analysis with the findings from Co/Pt(111) [119]. Comparing the Heisenberg parameters, it's notable that $J_1$ decreases by nearly half

| ML | $S^2J_1$ | $S^2J_2$ | $S^2J_3$ |
|---|---|---|---|
| Co/Pt(111)[119] | 27.8 | 2.5 | −0.20 |
| Gr(top-fcc)/Co/Pt(111) | 15.61 | 2.54 | 1.65 |

Table 5.2.: It indicates that the $J_{ij}$ coefficients are derived by fitting the energy dispersion of spin-spirals, expressed in meV. Here, we regard the top-fcc stacking of Gr on Co/Pt as the energetically most stable configuration.

as a result of Gr doping. In contrast, $J_3$ shows an increase, while $J_2$ remains relatively unchanged. This observation, particularly the changes in $J_{ij}$, reflects distinct modifications in the electronic structure, which in turn influence the hybridization of Co and Pt following Gr doping. To delve into this observation further, we're analyzing the bandstructure of Gr subsequent to doping on Co/Pt(111).

## 5.3 Tailoring interlayer distances of Gr and Co

Based upon various experiments, consistent with prior theoretical predictions, Gr displays semi-metallic behavior attributed to Dirac cones at the K points in the BZ [124, 125]. These Dirac points result in a zero bandgap and a vanishing DOS at the Fermi energy [13]. Moreover, it is revealed that depositing a single Gr sheet on a series of metal substrates causes the Fermi level to move away from the conical points in Gr, due to doping with either electrons or holes. According to the DFT findings, metals can be categorized into two groups. Gr exhibits chemisorption on Co, Ni, and Pd(111). Conversely, its adsorption on Al, Cu, Ag, Au, and Pt(111) results in physisorption, i.e., a weaker bonding [19]. In experiments involving Gr adsorbed on Pt(111) and Ni(111)/Au, it is observed that hybridization locally opens mini-gaps [126]. In Figure (5.4), the orbital weight of Gr along the bandstucture is depicted. The optimized distance of Gr and Co is 1.95 Å, as shown in Table (5.1). When Gr chemisorbs on Co, the unique electronic structure of Gr is perturbed,

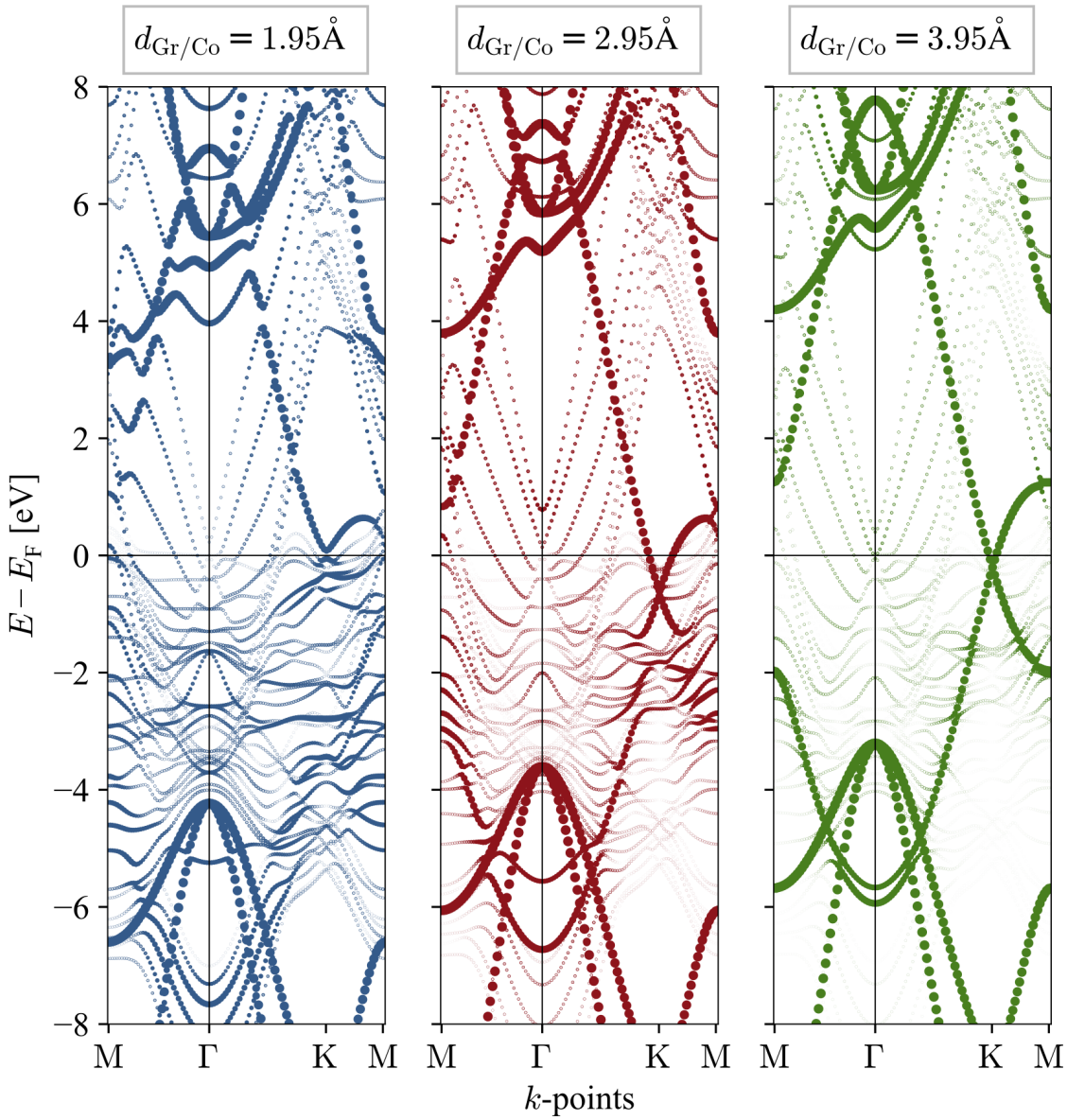



Figure 5.4.: The figure illustrates the orbital weight of Gr in the bandstructure of Gr/Co/Pt(111). Here, $d_{\mathrm{Gr-Co}}$ denotes the interlayer distance of Gr on Co. Only the top-fcc stacking of Gr on Co is considered in all three cases. By decreasing $d_{\mathrm{Gr/Co}}$, we show the effect of the chemisorption of Gr on Co. As Gr is positioned further away, the bonding weakens. The Dirac point aligns with the crossing of the $p_z$ bands of Gr at K.

resulting in the splitting of the Dirac cone and the acquisition of a mixed Gr-metal character. The lower part hybridizes with the Co bands, represented in blue dots. It is evident that the conical point at K has been disrupted. However, shifting Gr by 1 Å indicates a restoration of the Dirac cone and a downward shift at K point, resulting in *n*-type doping as Co donates electrons to Gr, illustrated by the red dots. This aligns with the chemisorption bonding between Gr and the substrate metal [19]. At a 3.95 Å distance, the valence and conduction bands of Gr come close to the Fermi level, a characteristic feature of Gr, shown as green dots. The hybridization of Gr with Co, which results in the opening of a gap at the K point, can significantly impact the electronic structure of Co/Pt(111). This, in turn, affects the strength of the RKKY interactions.

## 5.4 DMI in Gr/Co/HM(111)

To achieve a comprehensive understanding and determine the Dzyaloshinskii-Moriya interaction (DMI) parameters, we focus on all three configurations to investigate the influence of graphene (Gr) on the electronic and magnetic properties of Co/HM(111).
Similar to the exchange interaction, we employ the generalized Bloch theorem to explore the total energy of spin-spiral states using the FLEUR code [56, 55]. Self-consistent calculations, initially disregarding SOC, are conducted for arbitrary spin-spiral wave vectors, ($\boldsymbol{q}$). The generalized Bloch theorem cannot be directly applied in this context due to the presence of spin-orbit interaction. Consequently, we employ a perturbative approach to address the magnetic structure.
Incorporating SOC within the framework of the generalized Bloch theorem would significantly escalate computational costs, as it couples the wavefunctions at different $k$-points. Furthermore, in practice, SOC often exhibits a relatively weak influence and can be efficiently handled using perturbation theory. Initially, we disregard SOC and compute homogeneous SSDWs within a single chemical unit cell while employing generalized periodic boundary conditions. In a subsequent step, we take SOC into account. After obtaining the self-consistent solution of the Kohn-Sham Schrödinger equation with the spiral boundary conditions as shown in Equation (5.4), we introduce the SOC operator into the framework,

$$\hat{\mathcal{H}}_{\mathrm{soc}} = \sum_{\mu} \xi^{(\mu)}(r^{(\mu)}) \underline{\boldsymbol{\sigma}} \cdot \boldsymbol{L}(\mu). \tag{5.13}$$

In this context, $\boldsymbol{L}(\mu)$ represents the orbital momentum operator concerning the position of the $\mu$-the nucleus, while $\xi^{(\mu)}(r^{(\mu)})$ characterizes the strength of the SOC as a function of the distance $r^{(\mu)}$ from the $\mu$-th nucleus [127, 128].
Subsequently, we incorporate the impact of SOC as a first-order perturbative term as follows:

$$\left\langle \boldsymbol{\psi}_{\boldsymbol{k}',\nu'} | \hat{\mathcal{H}}_{\mathrm{soc}} | \boldsymbol{\psi}_{\boldsymbol{k},\nu} \right\rangle = \sum_{\sigma'\sigma} \left\langle \psi^{\sigma'}_{\boldsymbol{k}',\nu'} | \hat{\mathcal{H}}^{\sigma\sigma'}_{\mathrm{soc}} | \psi^{\sigma}_{\boldsymbol{k},\nu} \right\rangle, \tag{5.14}$$

$|\psi_{k,\nu}\rangle$ is an eigenstate to the unperturbed problem. The perturbative scheme is carried out with 2025 $k$-points across the 2D BZ, setting $K_{\max} = 4.3\, a_{\mathrm{B}}^{-1}$. As the Gr lattice aligns with the Pt(Ir)(111) lattice, the K and M symmetry points within the BZ of Pt(Ir) coincide. Accounting for ferromagnetic configurations, one can express Equation (5.14) as the Hamiltonian matrix, which illustrates the SOC as a first-order perturbation theory:

$$\begin{aligned} &\langle \psi^{\uparrow}_{\boldsymbol{k}',\nu'} | \mathcal{H}^{\uparrow\uparrow}_{\mathrm{soc}} | \psi^{\uparrow}_{\boldsymbol{k},\nu} \rangle \\ &\langle \psi^{\uparrow}_{\boldsymbol{k}',\nu'} | \mathcal{H}^{\uparrow\downarrow}_{\mathrm{soc}} | \psi^{\downarrow}_{\boldsymbol{k},\nu} \rangle \\ &\langle \psi^{\downarrow}_{\boldsymbol{k}',\nu'} | \mathcal{H}^{\downarrow\uparrow}_{\mathrm{soc}} | \psi^{\uparrow}_{\boldsymbol{k},\nu} \rangle \\ &\langle \psi^{\downarrow}_{\boldsymbol{k}',\nu'} | \mathcal{H}^{\downarrow\downarrow}_{\mathrm{soc}} | \psi^{\downarrow}_{\boldsymbol{k},\nu} \rangle \end{aligned} \tag{5.15}$$

These expectation values vanish for the collinear states. However, it is a solid approximation for the antisymmetric exchange interaction in noncollinear configurations. Presuming that the magnetization is constrained to the $xz$-plane, the only remaining component of $\mathcal{H}_{\mathrm{soc}}$, according to the Equation (5.13), would be $\langle \boldsymbol{\psi} | \xi \underline{\sigma}_y l_y | \boldsymbol{\psi} \rangle$ [99]. This method offers flexibility by enabling access to both regimes of slowly and rapidly rotating non-collinear magnetic structures in a more realistic manner through self-consistent calculations.
Our initial objective is to analyze the impact of Gr covering on Co/Pt(111). In particular, the strength of DMI can be finely adjusted by employing two active interfaces [129]. Using the generalized Bloch theorem, the behavior of the DMI near the Γ-point is in Figure (5.5). The integration of Gr on Co/Pt(111), as an epitaxial asymmetric, leads to chiral Néel-type domain walls stabilized by DMI at Gr/Co and Co/Pt. However, the chirality relies on the stacking of Gr on Co/Pt. It is evident from Figure (5.5) that the top-fcc and hollow stacking configurations exhibit left-handed Néel-type domain walls ($D < 0$), while the top-hcp configuration results in right-handed Néel-type domain walls ($D > 0$). Indeed, the observation reveals that the contribution of Co in the top-fcc stacking is almost negligible. Additionally, Pt(I) exhibits the same chirality as the total DMI. Across these three stackings, minor variations in magnitude are noticeable within the bottom layers of the Pt layer.

Embracing SOC through perturbation theory can be analogously related to the atomistic $\boldsymbol{D}_{ij}$ parameters. In the discrete atomistic limit, the formulation of the DMI is articulated as [110, 111]

$$E_{\mathrm{DMI}} = \sum_{i,j} \boldsymbol{D}_{ij} \cdot \left( \boldsymbol{S}_i \times \boldsymbol{S}_j \right). \tag{5.16}$$

By employing the spin configuration as defined in Equation (5.8), and considering a flat spin-spiral ($\theta = \pi/2$) where both $\boldsymbol{S}_i$ and $\boldsymbol{S}_j$ exclusively rotate within the $xz$-plane, achieving a linear chain of DMI along $\boldsymbol{q}$ can be accomplished by

$$E_{\mathrm{DMI}}(\boldsymbol{q}) = S^2 D_y \sin(\phi_{ij}), \tag{5.17}$$

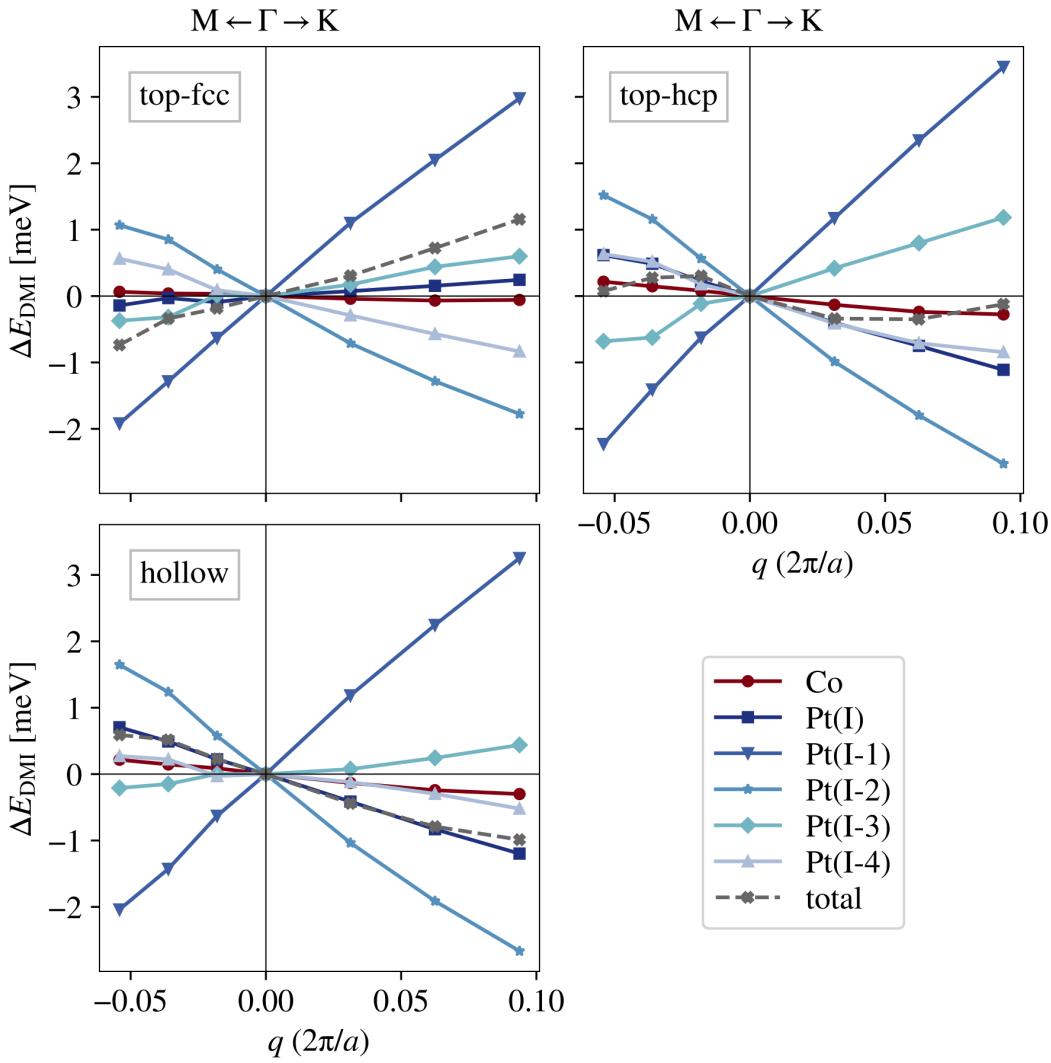



Figure 5.5.: The impact of Gr coverage on the DMI of various configurations in Co/Pt(111) is illustrated. When we observe the dashed lines depicting the total DMI, a noticeable distinction arises: the top-fcc stacking of Gr demonstrates a different chirality in contrast to the other stacking configurations.

with $\phi_{ij} = \boldsymbol{q} \cdot (\boldsymbol{R}_j - \boldsymbol{R}_i)$, as the corresponding angle between spins. To account for all six nearest neighbors in a hexagonal lattice, which is illustrated in the diagram shown in Figure (5.6), Equation (5.17) can be modified as

$$\begin{aligned} E_{\mathrm{DMI}} &= 2S^2 D_y \sin(\phi_{ij}) + 2S^2 D_y \sin(2\phi_{ij}) \\ &= 2D_y S^2 \sin(\phi_{ij})(1 + 2\cos(\phi_{ij})). \end{aligned} \tag{5.18}$$

The $D_y$ values obtained from the fit are interpreted as effective, since additional contributions beyond those accounted for in Equation (5.18) can also produce linear terms in $q$ for $E^y_{\mathrm{DMI}}$. These include, for example, interplanar nearest-neighbor bonds [130], as well as second-nearest and more distant neighbors. For a flat spin-

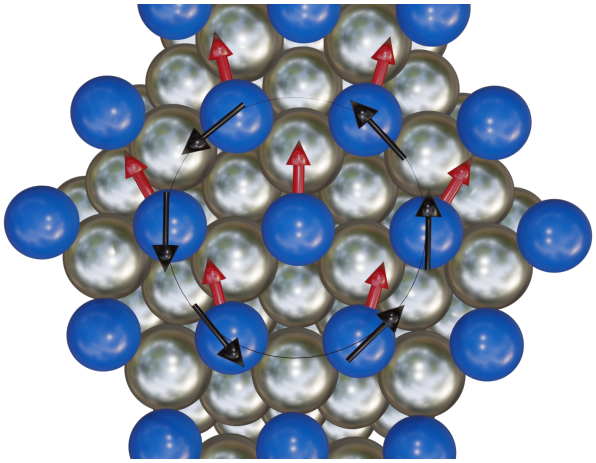


Figure 5.6.: The diagram illustrates the short-range DMI vectors between the first in-plane Co–Co nearest neighbors. Red arrows indicate the magnetization directions, while black arrows represent the corresponding $D$ vectors.

spiral configuration, where $\boldsymbol{q} = \frac{2\pi}{a}(\frac{1}{N}, \frac{1}{N}, 0)$, we can write $\phi_{ij} = \frac{2\pi}{N}$ [131]. Observing the linear of DMI around the Γ-point in Figure (5.12), led us to calculate the $D_y$ up to $\boldsymbol{q} = \frac{2\pi}{a}(\frac{1}{64}, \frac{1}{64}, 0)$, where the first calculated point along the ΓK direction is located. Analysis of the effective $\boldsymbol{D}$ calculation reveals that doping Gr leads to a reduction in DMI magnitude. Specifically, it impacts the chirality in both the top-hcp and hollow configurations.
We replicated the procedure by substituting Pt(111) with Ir(111). The reduction in DMI magnitude across all Gr configurations, along with the alteration in chirality for the top-hcp and hollow configurations, is also observed in the Gr/Co/Ir(111) system. However, it's noteworthy that the magnitude of DMI in the Gr(top-fcc)/Co/Ir configuration is less than half compared to that of Gr(top-fcc)/Co/Pt.
To examine the influence of different layers on DMI, we computed the layer-resolved DMI for $\boldsymbol{q} = \frac{2\pi}{a}(\frac{1}{64}, \frac{1}{64}, 0)$. We extensively examined each of the three configurations of Gr on Co/Pt(Ir)(111). The results are depicted in Figure (5.7). Examining the distinct atomic contributions, it becomes apparent that the sense of the rotation follows

| ML | $D_y$ |
|---|---|
| Co/Pt(111)[119] | 0.89 |
| Gr(top-fcc)/Co/Pt(111) | 0.15 |
| Gr(top-hcp)/Co/Pt(111) | −0.17 |
| Gr(hollow)/Co/Pt(111) | −0.22 |
| Gr(top-fcc)/Co/Ir(111) | 0.06 |
| Gr(top-hcp)/Co/Ir(111) | −0.27 |
| Gr(hollow)/Co/Ir(111) | −0.15 |

Table 5.3.: The effective component of $\boldsymbol{D}$ is determined within a range extending up to $\boldsymbol{q} = \frac{2\pi}{a}(\frac{1}{64}, \frac{1}{64}, 0)$ of the BZ edge $\overline{\Gamma K}$, calculated in meV$\mu_B^{-2}$. Given that the magnetic moment of Co is denoted as $m_{Co} = 1.84\,\mu_B$.

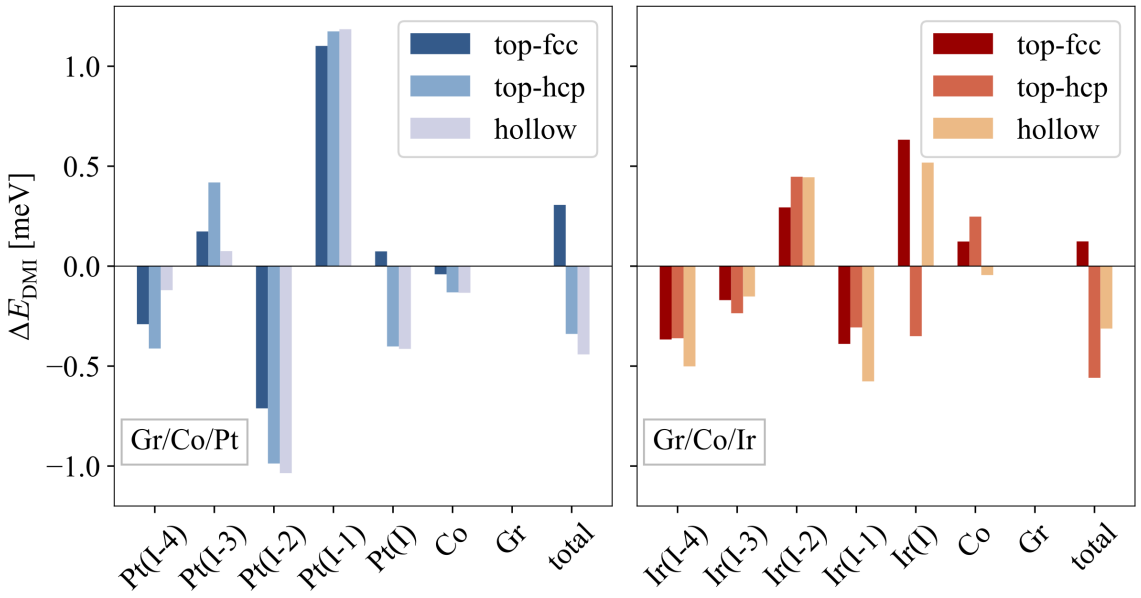



Figure 5.7.: Layer-resolved DMI is illustrated. The rotation sense follows Pt(I) contributions. In the case of Ir, Co plays a decisive role in top-fcc stacking, whereas other contributions of Ir influence strongly both top-hcp and hollow stackings.

the contribution of the Pt(I). A substantial contribution from Pt(I-1) effectively compensates for Pt(I-2), mirroring a similar pattern between Pt(I-3) and Pt(I-4). Notably, the influence of Co in the DMI is notably smaller compared to that of the Pt(I) and is nearly negligible in the case of the top-fcc configuration. For Gr/Co/Ir(111), Co exerts a significant influence on the top-fcc stacking configuration, while other contributions of Ir notably impact both the top-hcp and hollow stacking arrangements. In a manner consistent with the experimental findings, our results indicate that Gr exerts a modest yet noteworthy influence on the DMI. However, this influence can primarily derive from the interface Pt contribution, which contrasts with previous findings regarding the Rashba nature of the DMI at the Gr and Co interface [12].

### 5.4.1 DMI across various stackings of Gr on Co/Pt(111)

The observed different senses of rotation in the various stacking arrangements sparked our curiosity to delve deeper into the study of DMI. Continuing our investigation, we examine the DMI at a representative $q = (\frac{2\pi}{a})(\frac{1}{64}, \frac{1}{64}, 0)$ along $\overline{\Gamma\mathrm{K}}$ direction. To achieve a detailed analysis of DMI quantities with respect to $\boldsymbol{k}$, we employ the expression:

$$\Delta E_{\boldsymbol{k}}^{\mathrm{DMI}} = \sum_{\nu}^{E_{\mathrm{F}}} \left( \epsilon_{\boldsymbol{k},\nu}^{\mathrm{soc}} - \epsilon_{\boldsymbol{k},\nu}^{0} \right) = \sum_{\nu}^{E_{\mathrm{F}}} \epsilon_{\boldsymbol{k},\boldsymbol{\nu}}^{\mathrm{DMI}}. \tag{5.19}$$

In Figure (5.8), the bandstructure of top-fcc, top-hcp, as well as hollow configurations are presented, with each colored point indicating the change of band energy attributed to the SOC. Based on the schematics, the sign contrast between top-fcc and top-hcp or hollow configurations emerges near the M-point, close to the $E_{\mathrm{F}}$. This can be observed in the interface contribution of Pt, emphasizing its pivotal role in driving DMI in Gr/Co/Pt(111), as depicted in Figure (5.9). Overall, extracting the differences among various stackings of Gr on Co/Pt is challenging due to the presence of all bands. It's worth noting that the contributions, while significant, exhibit a compensatory effect due to opposing influences below the Fermi level.
To analyze the spectral behavior of the DMI chirality, we plot the corresponding energies integrated over $k$ as a function of the number of electrons ($n_e$) for each $\boldsymbol{q}$. This method is analogous to calculating magnetocrystalline anisotropy (MCA) using the force theorem approach [132, 131, 133],

$$\Delta E_{\boldsymbol{k}}^{\mathrm{DMI}}(n_e; \boldsymbol{q}) = \sum_{k,\nu} \epsilon_{k,\nu}^{\mathrm{DMI}}(\boldsymbol{q}) f\left( \epsilon_{k,\nu}^{\mathrm{DMI}}(\boldsymbol{q}) - \epsilon_{\mathrm{F}}(n_e; \boldsymbol{q}) \right). \tag{5.20}$$

The functions $f$ represent the Fermi–Dirac distribution functions, which depend on the magnetization axes through the Fermi energy. In our analysis, the finite electronic temperature denoted by $k_{\mathrm{B}}T$ plays a crucial role as a smearing parameter. To maintain precision, we adopt a value of 0.001 for this parameter. The corresponding results are illustrated in Figure (5.10). When examining different arrangements of Gr on Co/Pt(111) near the Fermi energy, particularly around 0.2 eV below the

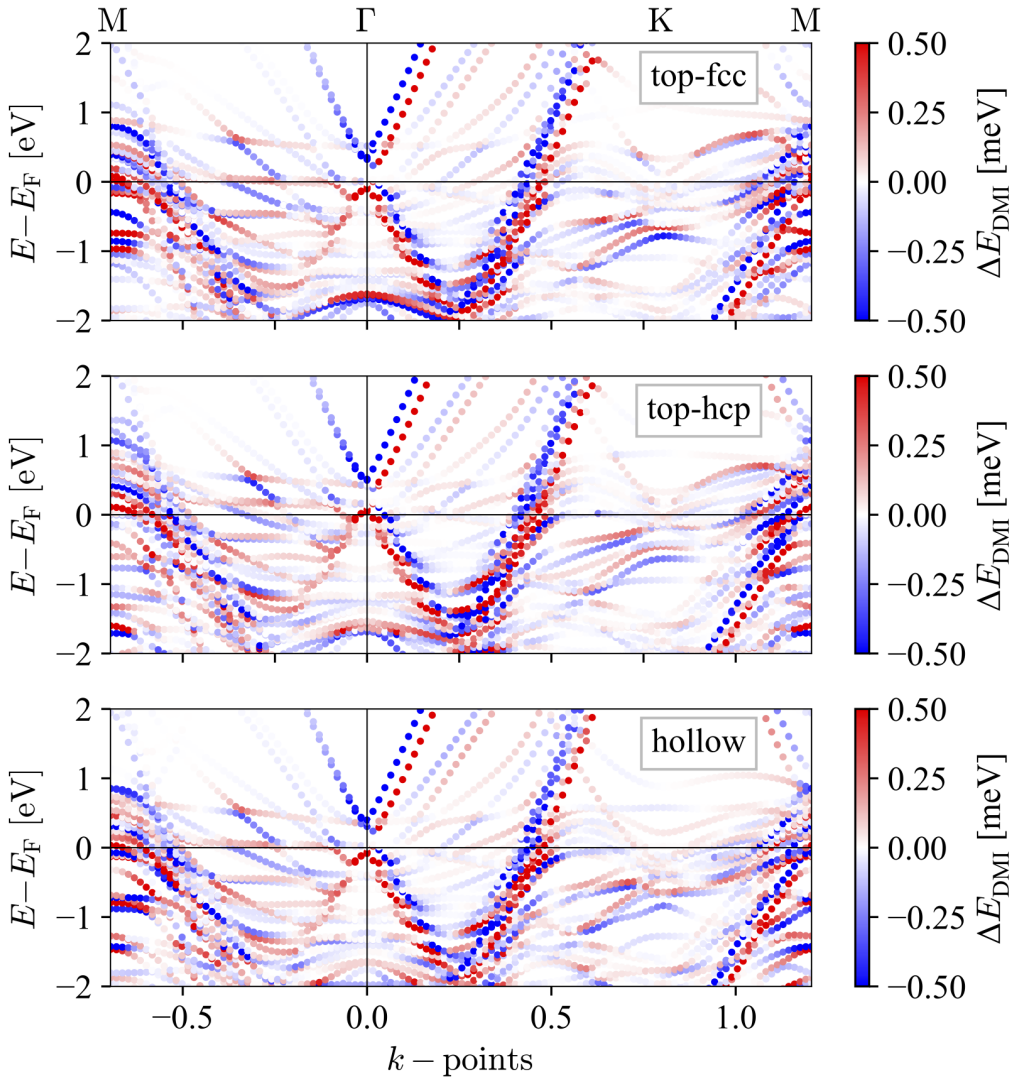



Figure 5.8.: The bandstructure is displayed for top-fcc, top-hcp, and hollow configurations, with colors corresponding to the DMI values. The color of the points represents their direction, while the size of the points corresponds to DMI magnitudes.

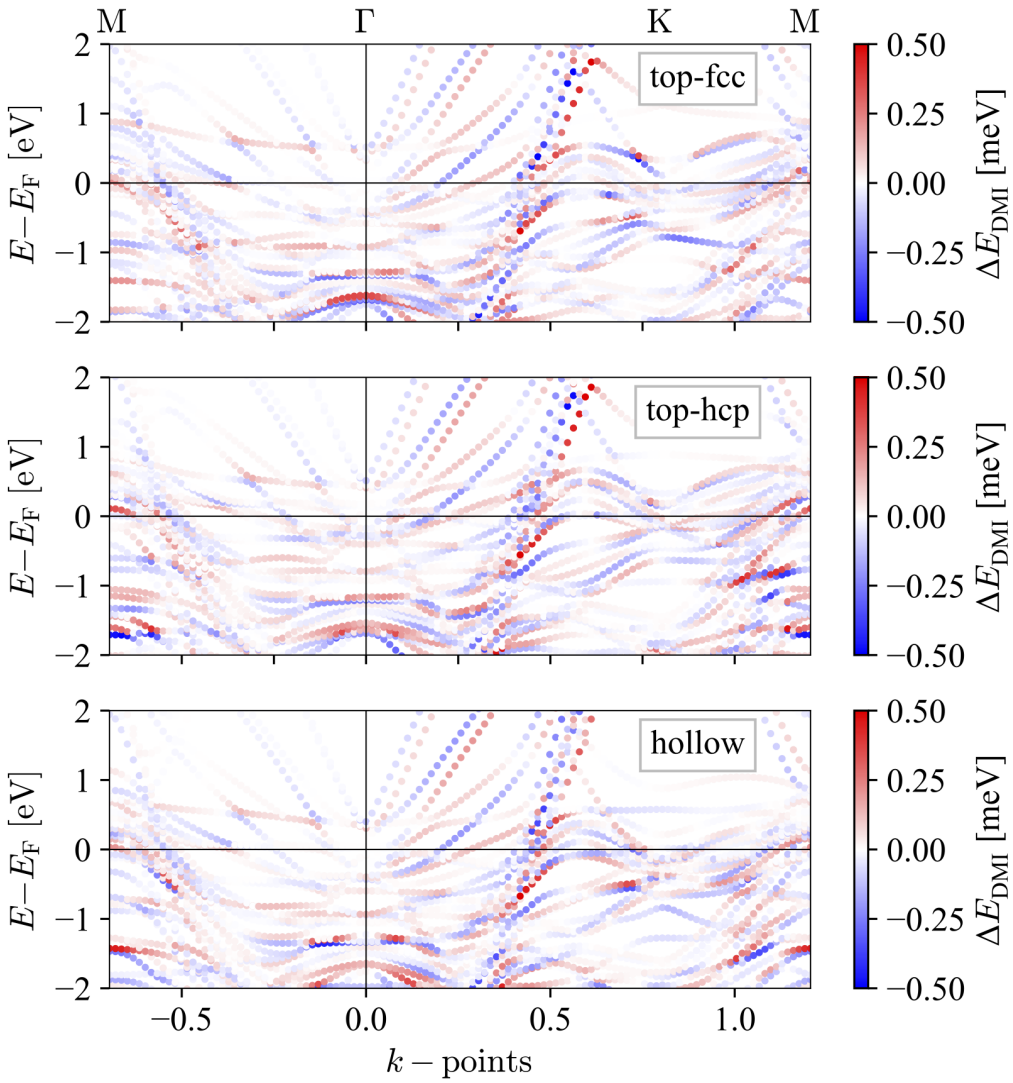



Figure 5.9.: The bandstructure plots illustrate top-fcc, top-hcp, and hollow configurations, showcasing Pt(I) contributions to DMI values. Point colors indicate direction, while sizes denote DMI magnitudes.

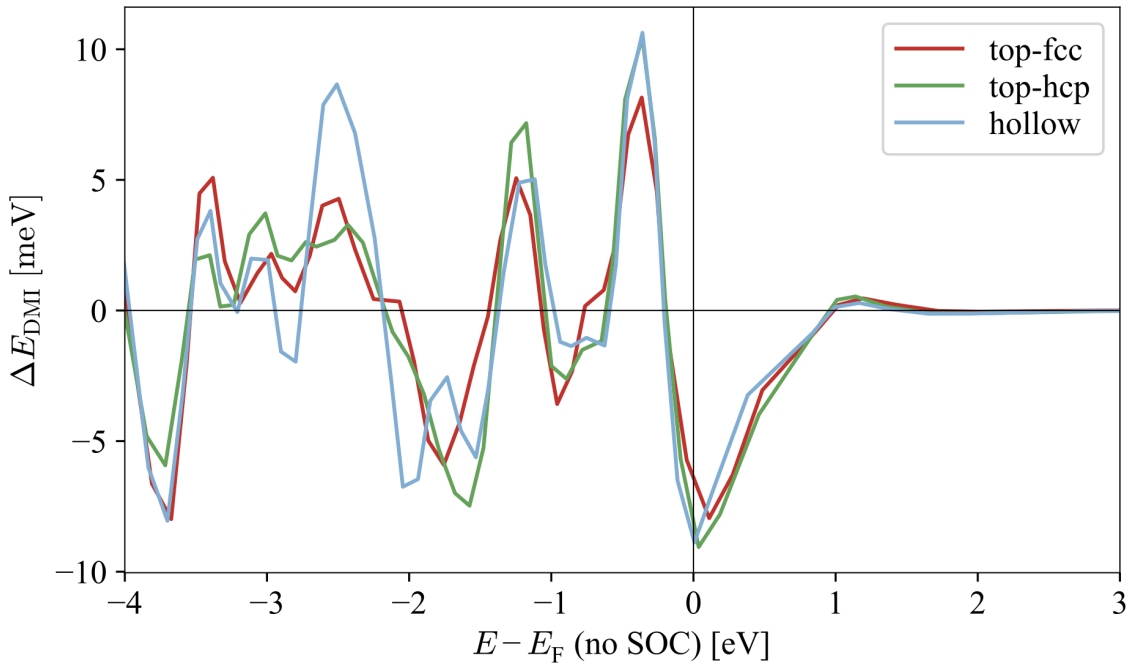



Figure 5.10.: The DMI values are plotted as a function of energy, relative to the Fermi levels of each slab calculated without SOC, for the representative point $q = (\frac{2\pi}{a})(\frac{1}{64}, \frac{1}{64}, 0)$ along $\overline{\Gamma\mathrm{K}}$.

Fermi level, it becomes evident that all configurations contribute equally to the Dzyaloshinskii-Moriya Interaction (DMI). However, subtle distinctions in the values of DMI emerge near the Fermi level. This is also reflected in the bandstructure plot. For a thorough analysis of the atomic contributions in the DMI, we generate a plot by integrating the corresponding energies over $k$-space within the BZ for various Gr stacking arrangements. Utilizing Equation (5.19), we turn to a $\boldsymbol{k}$-resolved analysis of DMI quantities in the entire BZ. This finding is presented in Figure (5.11). Examining the DMI contributions within BZ, the primary disparity lies in the vicinity of the $\Gamma$ point. In this region, the contributions of Pt(I) (right panel) emerge as notably significant.
To study the effect of Gr coverage on Co/Pt(111), it is valuable to analyze the variations in DMI. Therefore, we performed DMI calculations for the three aforementioned structures depicted in Figure (5.4). Considering top-fcc stacking, Gr was initially located at the optimized distance (1.95 Å) and subsequently shifted to achieve an interlayer distance of 2.95 Å as well as 3.95 Å. As previously mentioned, the DMI at the Gr/Co interface points opposite the SOC-induced DMI at the Gr/Pt interface. However, increasing the interlayer distance between Gr and Co leads to a reduced DMI contribution from the Gr/Co interface. As a result, the overall DMI of the Gr/Co/Pt system closely resembles that of the Co/Pt system. Besides, an opposite behavior is observed in the Co contribution. Shifting Gr causes the rotation direction of the DMI vector for Co to reverse, and its magnitude increases. Therefore, the majority of the DMI originates from Co and Pt(I), while the contribution from Pt(I-1) diminishes.

## 5.5 MCA in Gr/Co/HM

Depositing ultrathin layers of magnetic materials, such as Co or Fe, and HMs like Pt or Ir, a SOC can be induced at the interfaces through a proximity effect [134]. Experimental results confirmed the presence of a well-defined PMA in $Gr/Co_n/HM$ heterostructures, identified at 300 K below a critical Co thickness ($n_C \approx 20$ for Pt and $n_C \approx 10$ for Ir) [135]. The magnetic anisotropy of metallic multilayers, owing to their 2D nature and the monatomic thickness of the ferromagnetic Co layer, is primarily determined by the interface anisotropy [46].
To accurately determine the MCA values, we incorporate SOC terms fully self-consistently, employing 2025 $k$-points across the 2D BZ with $K_{max}$ value of $4.0\, a_B^{-1}$.
When considering spins aligned along both in-plane ($E_{tot}^{\parallel}$) and out-of-plane ($E_{tot}^{\perp}$) axes, MCA can be expressed as:

$$\Delta E_{MCA} = E_{tot}^{\parallel} - E_{tot}^{\perp}. \tag{5.21}$$

$E_{tot}$ represents the total energies, including fully self-consistently computed SOC. Focusing on Gr in the top-fcc configuration on Co/HM(111), with regard to both Ir and Pt, we present MCA in the Table (5.4). Another study employing DFT confirmed a similar MAE of approximately 2.4 meV for the $Gr(1\times1)/Co_1/Pt_5$ system,

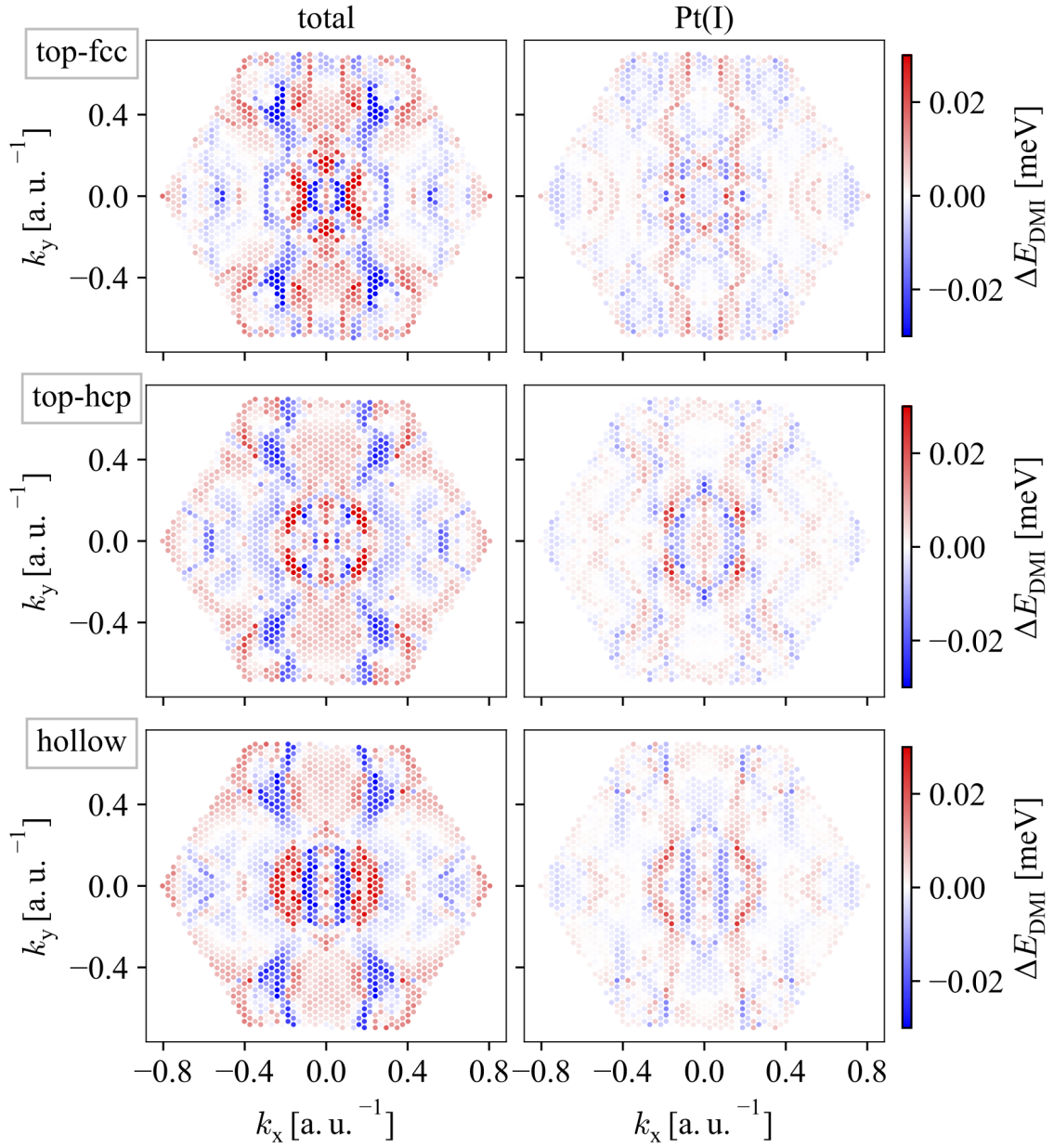



Figure 5.11.: The DMI, computed across the entire BZ, is illustrated, including the total DMI contributions, particularly from the interface Pt.

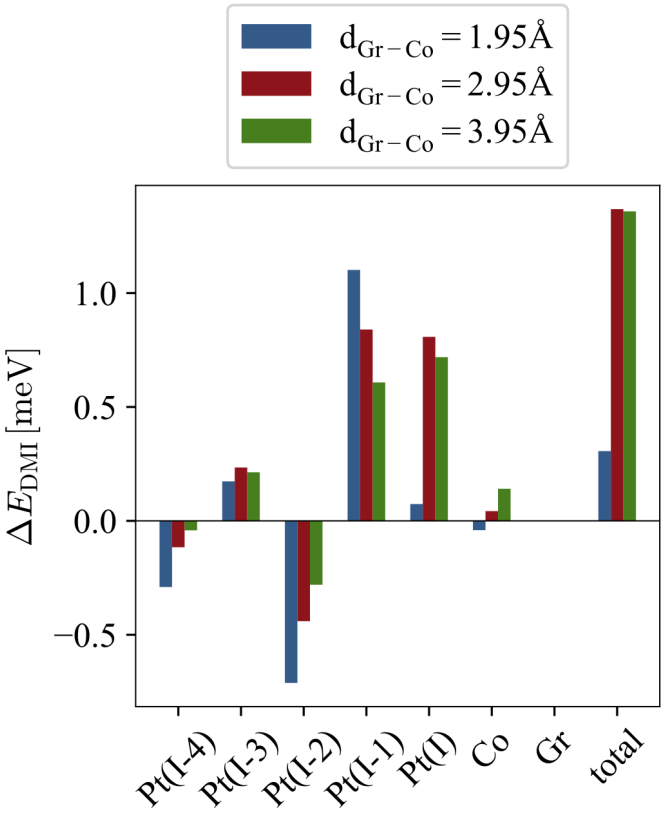



Figure 5.12.: Increasing the distance between Gr and Co results in an increase in DMI. Consequently, the contribution of Co is enhanced by the displacement of Gr. Only top-fcc stacking of Gr on Co/Pt(111) is considered.

| ML | $\Delta E_{MCA}$ |
|---|---|
| Gr(top-fcc)/Co/Pt | 2.38 |
| Gr(top-fcc)/Co/Ir | 0.30 |

Table 5.4.: The table provides magnetocrystalline anisotropy (MCA) for Gr(top-fcc)/Co/HM(111). The positive energy corresponds to the perpendicular MCA, and the energy values are expressed in meV.

which is almost double that of Co/Pt. The precise moirë pattern of Gr significantly influences the MAE values by a few tenths of meV [135]. Additionally, at these small thicknesses, the contribution of shape anisotropy remains weak. Our observation indicates that the MCA is eight times stronger for Pt. Other factors, including intermixing at the Co/HM interface, the specific moiré pattern formed between the Gr and Co unit cells, and shape anisotropy, could also contribute to the overall behavior of the system. However, these factors have been neglected in our study.
Given the Force Theorem approach [136], we evaluate the layer-resolved contribution of the MCA. In this method, SOC is included non-self-consistently after achieving the self-consistent solution of the Kohn-Sham equation.

$$\Delta E_{\mathrm{MCA}} \approx \sum_{\nu}^{\mathrm{occ.}} \epsilon_{\mathrm{ft},\nu} - \sum_{\nu}^{\mathrm{occ.}} \epsilon_{0,\nu}. \tag{5.22}$$

Here, the eigenvalues $\mathcal{E}_{\mathrm{ft},\nu}$ are derived from $\mathcal{H}_0 + \mathcal{H}_{\mathrm{SOC}}$. Due to the perturbative formalism, the Force Theorem qualitatively reproduces the self-consistent results effectively. The Figure (5.13) illustrates the layer-resolved contribution of the $\Delta E_{\mathrm{MCA}}$. It is apparent that the MCA for Gr/Co/Pt is much larger than for Gr/Co/Ir. However, in both structures, the largest contributions come from HM(I) and HM(I-1). This method can effectively determine the behavior of different contributions to MCA, though it may not yield precise magnitudes.
Examining Table (5.5), it is evident that the induced magnetic moments (MMs) in Pt and Ir vary significantly. Notably, the MMs at the Ir layers display oscillations in sign, indicating their smaller magnitude compared to the Pt layers. This observation suggests a marked difference in the magnetic behavior at the Co/Ir interface compared to the Co/Pt interface. Additionally, it is demonstrated that the higher

| MM | Pt | Ir |
|---|---|---|
| Co(I) | 1.67 | 1.31 |
| HM(I) | 0.35 | 0.13 |
| HM(I-1) | 0.14 | −0.05 |
| HM(I-2) | 0.10 | −0.01 |
| HM(I-3) | 0.08 | 0.03 |
| HM(I-4) | 0.06 | 0.04 |

Table 5.5.: The magnetic moment (MM) of Co and Pt(Ir) layers are represented in $\mu_{\mathrm{B}}$. The MMs exhibit better convergence within the five layers of Pt compared to Ir.

magnetization density at the Co/Pt interface is expected to be more influenced by the SOC compared to the case with Ir. This is attributed to the stronger magnetic

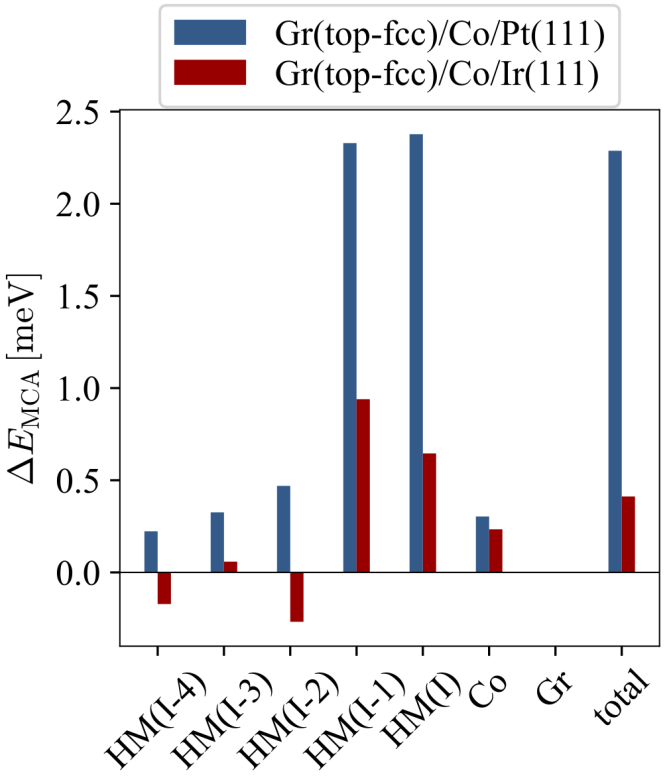



Figure 5.13.: Analysis of the MCA using the Force Theorem, showcasing diverse atomic contributions. The "total" denotes the combined contributions of SOC from all layers.

coupling between Co/Pt compared to Co/Ir across the interface, rather than solely the strength of SOC [135]. To evaluate the impact of Gr on Co/Pt(111), we extend the distances between Gr and Co. Concentrating on the top-fcc layer, Figure (5.14) depicts the layer-resolved contribution to the MCA for three different distances of the Gr/Co interface, utilizing the Force theorem. These results are visually presented in Figure (5.14). Expanding the interlayer distance between Gr and Co results

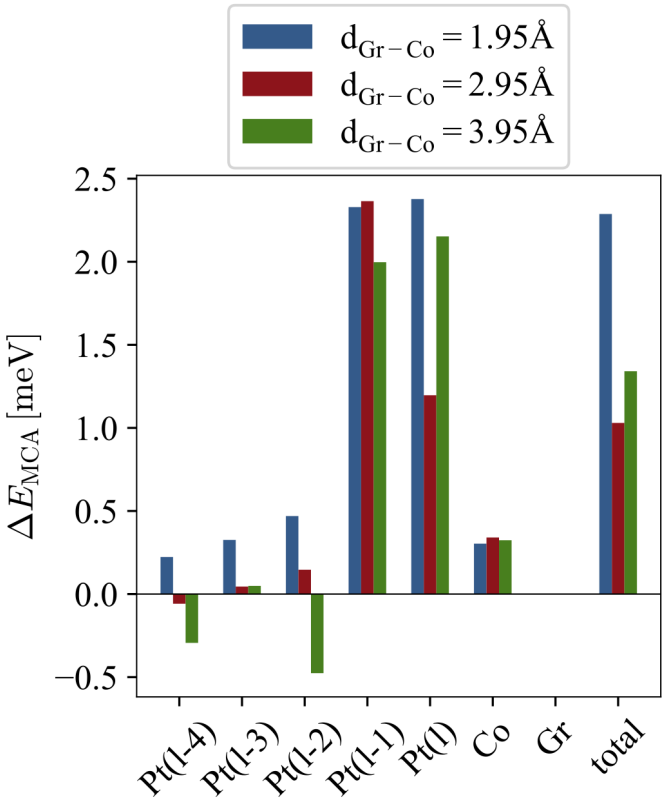



Figure 5.14.: We examine the MCA using the Force theorem. The MCA displays a decreasing tendency, highlighting a significant connection between the spatial arrangement of Gr and Co and the strength of the MCA.

in nearly halving the MCA, with the primary impact observed on the contributions from the HM layer. In contrast, the contribution from Co remains unchanged. This effect is also evident in the bandstructure of Gr shown in Figure (5.4).

# 6 The role of Co thickness in DMI enhancement

**Contents**


6.1. Enhancing structural optimization . . . . . 68
6.2. Evolution of spin texture of Gr adjacent to 3ML Co/5ML Pt(Ir) . . . . 69
6.3. DMI variations across different Co thicknesses . . . . . 71
6.3.1. Enhancing the thickness in HM layers . . . . . 76


Experimental findings reveal that Gr undergoes significant modification upon Co intercalation due to its robust interaction with the underlying Co layer. This phenomenon was previously explored in detail in the preceding chapter. We observed that the Dzyaloshinskii-Moriya interaction (DMI) energy contribution is concentrated at Pt(Ir), where the atomic SOC strength is notably large. Our findings indicate that Gr inverts the chirality of the vacuum/Co interface, which is in agreement with experimental results. Experimentally, it was shown that augmenting the thickness of the Co layer promotes the formation of twin boundaries or stacking faults. Additionally, the influence of the Gr/Co interface was compared with the contribution observed in the Co/Pt(Ir) interface [135]. Upon intercalation with Co, the electronic bandstructure of Gr is significantly modified due to the strong interaction with the Co layer. This interaction reduces the intensity and sharpness of the Gr bands compared to the Gr/Ir system. Further Co intercalation can be interpreted as a combination of the original Gr/Ir $\pi$-band, which remains near the Fermi level, and a more electronically doped $\pi'$ Gr/Co band at a deeper binding energy. This effect can be associated with the Moiré pattern of Gr on Co/Ir. Moreover, the growth of 2ML of Co exhibits the development of mini Dirac cones within a narrow energy range, approximately 0.2 eV below the $E_F$, particularly evident at Gr K-point [137].
Within this chapter, our focus shifts to an in-depth examination of Co-thickness

and its influence on both electronic and magnetic properties. This investigation involves distinct analyses for both Pt and Ir as heavy metals (HMs) through DFT calculations.

## 6.1 Enhancing structural optimization

To unravel the impact of the thickness of Co on spin texture as well as DMI, we expanded the number of Co layers to 3. Three MLs of Co are arranged in an fcc structure along the (111)-plane on a substrate of 5 MLs of Pt(Ir). Figure (6.1) displays the structural characterization of the Gr/3ML Co/5ML Pt(111) heterostructure. For Gr/3ML Co/5ML Ir, the structure is analogous, except for the substitution of Pt atoms with Ir atoms. Due to the expansion of Gr to match the Pt(Ir) lattice, in our

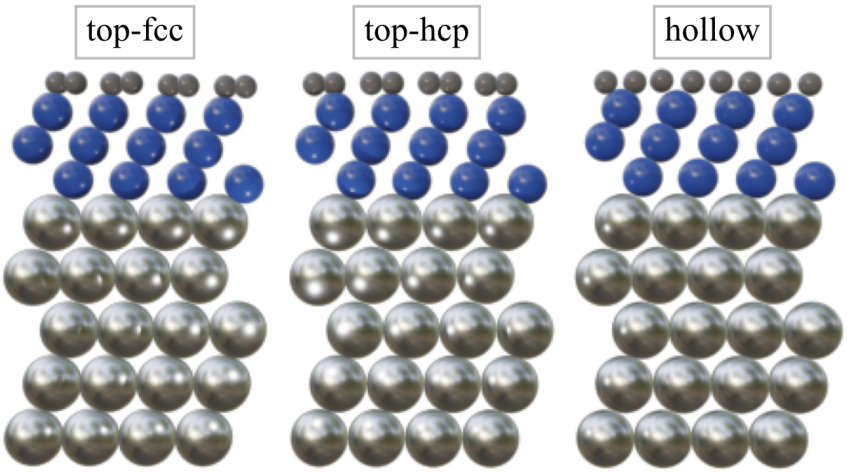



Figure 6.1.: A side view presents three potential stacking configurations of Gr atop 3ML Co/5ML Pt(111). For Ir, Pt is substituted by Ir.

calculations, contributions from the Gr Moiré superlattice to the electronic structure are disregarded. As in the case of Gr/Co/Pt(Ir), we conducted relaxation simulations for the three various stacking configurations of Gr on 3ML Co/5ML Pt(Ir)(111), maintaining consistent computational parameters. Hence, the planewave cutoff for the basis functions was set to $K_{max} = 4.0\,a_B^{-1}$. The charge density was expanded to a cutoff $G_{max} = 11.8\,a_B^{-1}$, along with 21 *k*-points, distributed within the primitive part of the hexagonal (2D) BZ in accordance with the p3m1 symmetry class. Given the chemical adsorption of Gr, there's no requirement for a van der Waals (vdW) correction. Table (6.1) displays the interlayer distances for Gr/3ML Co/5ML Pt as well as Gr/3 Co/5ML Ir, including top-fcc as well as top-hcp arrangements of Gr on 3ML Co/5ML Pt(Ir)(111). In Chapter 5, it was observed that these two stacking configurations exhibit very similar energy levels and are the most stable ones. Therefore, we focused our optimization efforts specifically on these two

configurations. The forces have been optimized for all structures until reaching a convergence threshold of 0.05 eV/Å. Based on the structural relaxation results, it is

| ML | Gr/3ML Co/5ML Pt | | Gr/3ML Co/5ML Ir | |
|---|---|---|---|---|
| Gr/Co stacking | top-fcc | top-hcp | top-fcc | top-hcp |
| $a$ | 2.75 | 2.75 | 2.73 | 2.73 |
| $d_{\mathrm{C(I-1)-C(I)}}$ | 0.02 | 0.02 | 0.02 | 0.02 |
| $d_{\mathrm{C(I)-Co(I)}}$ | 1.99 | 1.99 | 1.97 | 1.99 |
| $d_{\mathrm{Co(I)/Co(I-1)}}$ | 1.87 | 1.87 | 1.87 | 1.87 |
| $d_{\mathrm{Co(I-1)/Co(I-2)}}$ | 1.91 | 1.91 | 1.92 | 1.93 |
| $d_{\mathrm{Co(I-2)/HM(I)}}$ | 2.10 | 2.10 | 2.09 | 2.08 |
| $d_{\mathrm{HM(I)/HM(I-1)}}$ | 2.41 | 2.41 | 2.25 | 2.25 |
| $d_{\mathrm{HM(I-1)/HM(I-2)}}$ | 2.38 | 2.38 | 2.24 | 2.24 |
| $d_{\mathrm{HM(I-2)/HM(I-3)}}$ | 2.38 | 2.38 | 2.24 | 2.23 |
| $d_{\mathrm{HM(I-3)/HM(I-4)}}$ | 2.40 | 2.40 | 2.19 | 2.20 |
| Total energy | 0 | 0.01 | 0 | 0.01 |

Table 6.1.: $a$ and $d$ stand for in-plane lattice parameter and interlayer distances for different stacking positions of Gr on 3ML Co/5ML Pt(Ir) along the fcc(111) stacking, respectively. Distances are given in Å and total energies in eV, both relative to the top-fcc stacking position, for each structure.

evident that the top-fcc configuration exhibits a marginal energy advantage of just 0.01 eV, indicating its slightly higher stability compared to the top-hcp configuration. The optimized interlayer distances are nearly identical, particularly for the Gr/3ML Co/Pt configuration.

## 6.2 Evolution of spin texture of Gr adjacent to 3ML Co/5ML Pt(Ir)

The previously mentioned dual $\pi$ band component, linked to a corrugated Gr layer, aligns with the combined presence of the strongly interacting Gr/Co $\pi'$ band and the less interacting Gr/Pt(Ir) $\pi$ band. Similar observations have been reported in analogous systems [138]. To confirm the observed spin splitting in experiments, we performed DFT calculations aimed at assessing spin polarization within the plane. The notion of density matrix is extended to encompass spin-polarized systems [139].

The scalar density is replaced with a hermitian $2 \times 2$ matrix, denoted as

$$n_{\sigma\sigma'}(\boldsymbol{r}) = \left\langle \psi | \phi^{\dagger\sigma'}(\boldsymbol{r}) \phi^{\sigma}(\boldsymbol{r}) | \psi \right\rangle. \tag{6.1}$$

Consequently, the Schrödinger equation can be written as:

$$\left[ \left( -\frac{\hbar^2}{2m} \nabla^2 + \sum_{\sigma,\sigma'} \int \frac{n_{\sigma\sigma'}(\boldsymbol{r}')}{|\boldsymbol{r} - \boldsymbol{r}'|} d\boldsymbol{r}' \right) \underline{I} + \underline{V}(\boldsymbol{r}) + \frac{\delta \mathrm{E_{xc}}}{\delta \underline{n}(\boldsymbol{r})} + \underline{\mathcal{H}}_{\mathrm{so}} \right] \begin{pmatrix} \phi_i^{\uparrow}(\boldsymbol{r}) \\ \phi_i^{\downarrow}(\boldsymbol{r}) \end{pmatrix} = \epsilon_i \begin{pmatrix} \phi_i^{\uparrow}(\boldsymbol{r}) \\ \phi_i^{\downarrow}(\boldsymbol{r}) \end{pmatrix}, \tag{6.2}$$

The term $\underline{V}(\boldsymbol{r})$ is defined as the $2 \times 2$ potential matrix. In terms of the Kohn-Sham wavefunctions, the density matrix can be written as

$$n_{\sigma\sigma'}(\boldsymbol{r}) = \sum_{i=1}^{N} \phi_i^{*\sigma'}(\boldsymbol{r}) \phi_i^{\sigma}(\boldsymbol{r}). \tag{6.3}$$

Utilizing the Pauli matrices, $\underline{\sigma}$, the density matrix can be decomposed in

$$\underline{n}(\boldsymbol{r}) = \frac{1}{2} \left( n(\boldsymbol{r}) \underline{I} + \underline{\boldsymbol{\sigma}} \cdot \boldsymbol{m}(\boldsymbol{r}) \right) = \frac{1}{2} \begin{pmatrix} n(\boldsymbol{r}) + m_z(\boldsymbol{r}) & m_x(\boldsymbol{r}) - i m_y(\boldsymbol{r}) \\ m_x(\boldsymbol{r}) + i m_y(\boldsymbol{r}) & n(\boldsymbol{r}) - m_z(\boldsymbol{r}) \end{pmatrix}, \tag{6.4}$$

corresponding to the charge and magnetization density. Therefore, the in-plane configuration of the magnetization density can be defined as:

$$m_x = n^{\uparrow\downarrow} + n^{\downarrow\uparrow} = 2\,\mathrm{Re}\left(n^{\uparrow\downarrow}\right), \tag{6.5}$$

$$m_y = i\left(n^{\uparrow\downarrow} - n^{\downarrow\uparrow}\right) = 2\,\mathrm{Im}\left(n^{\uparrow\downarrow}\right). \tag{6.6}$$

Within this formalism, a general non-collinear structure can be determined in the framework of DFT [63].
To demonstrate the band-splitting at Gr, we traced the $k$-points along the high-symmetry lines, $\overline{\mathrm{M\Gamma KM}}$. As depicted schematically in Figure (6.2), along $\overline{\Gamma\mathrm{KM}}$, the sole in-plane spin contribution to the bandstructure perpendicular to the wavevector is $S_y$, whereas along $\overline{\mathrm{M\Gamma}}$ only $S_x$ becomes prominent. In Figure (6.3), separate plots, presenting the in-plane spin contribution to the bandstructure of Gr/3ML Co/5ML Pt(111) at Gr along $\overline{\mathrm{M\Gamma}}$ and $\overline{\Gamma\mathrm{KM}}$, are displayed. To discuss the hybridization between Gr and Pt at the interface, it is necessary for the wavefunction, $\psi_{k\nu}$ to be present simultaneously at both Gr and Pt(I), which can be defined as:

$$\langle \psi_{k\nu}(\boldsymbol{r}) | \psi_{k\nu}(\boldsymbol{r}) \rangle_{\mathrm{Gr}} \times \langle \psi_{k\nu}(\boldsymbol{r}) | \psi_{k\nu}(\boldsymbol{r}) \rangle_{\mathrm{Pt(I)}}. \tag{6.7}$$

Here, the first and second terms highlight the weight of Gr and Pt at the interface on the band structure, respectively. Consequently, the projected bandstructure of Gr/3ML Co/5ML Pt(111) is also presented, emphasizing the density of states (DOS) of Gr and Pt(I). The red and blue points correspond to the states with positive and negative spins. Similarly, Figure (6.4) showcases the interplay between Gr and

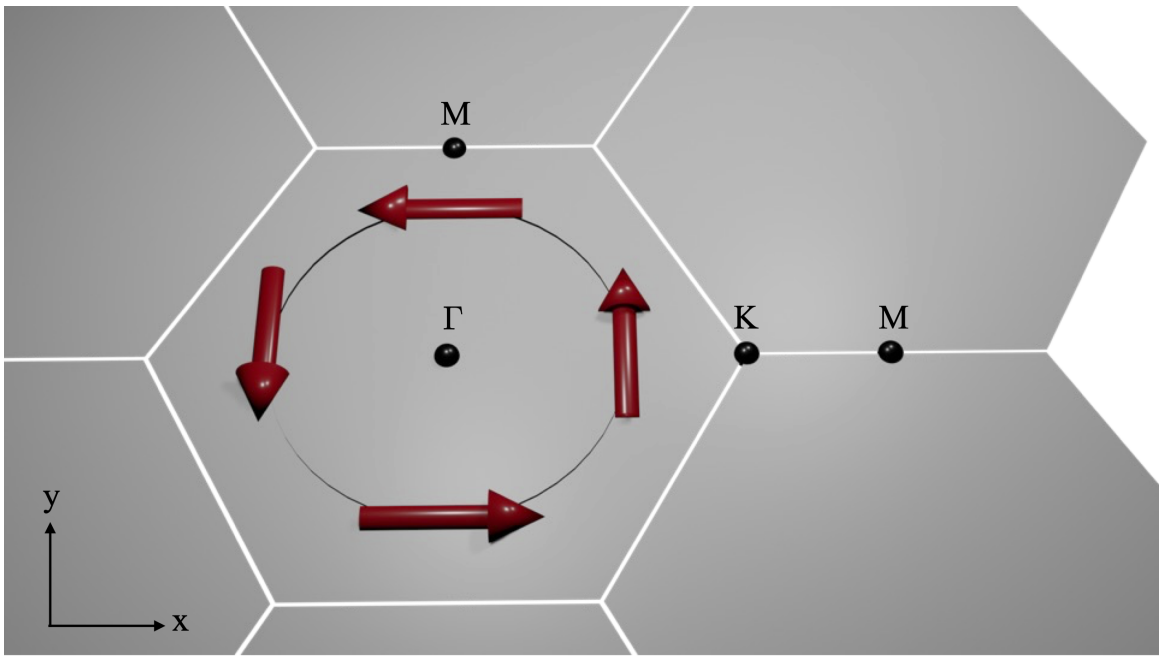



Figure 6.2.: The in-plane spin contributions to the bandstructure orthogonal to the wavevector within the BZ are illustrated: $S_x$ along $\overline{\mathrm{M\Gamma}}$ and $S_y$ along $\overline{\Gamma\mathrm{K}}$.

Ir at the interface, visualized through the Equation (6.7) as well as in-plane spin polarization along $\overline{\mathrm{M\Gamma KM}}$. In both structures, a subtle spin splitting around -4 to -7 meV is noticeable, as marked within a defined region in both figures, consistent with observations reported for Gr/2ML Co/5ML Ir [137]. However, this splitting appears less pronounced compared to the effect observed in the case of 2ML Co. A comparison of overlap and plots reveals that the in-plane spin polarization is a result of the interface's hybridization with the HM, contributing significantly to this effect.

## 6.3 DMI variations across different Co thicknesses

Drawing from the analysis of the partial slab decomposition, it has been demonstrated that at two layers Co, the Co/Pt and Gr/Co interfaces are effectively decoupled; however, their contributions still exhibit a dependency on the Co thickness. Notably, the Co/Pt interface contributes significantly to the DMI, and at the Gr/Co interface, the chirality is observed to be the opposite. Furthermore, employing atomic spin-orbit decomposition, it is found that the contribution of the interfacial Pt atomic plane dominates the whole DMI effect, demonstrating similar energy values with and without Gr. The Co atoms at this same interface contribute minimally compared to the Co atomic layer at the Co/Gr interface [131]. This observation aligned with a similar case reported in the literature for 3d/5d interfaces [140, 141]. Investigating DMI for Gr/3ML Co/Pt(Ir), we aim to compare the DMI effects be-

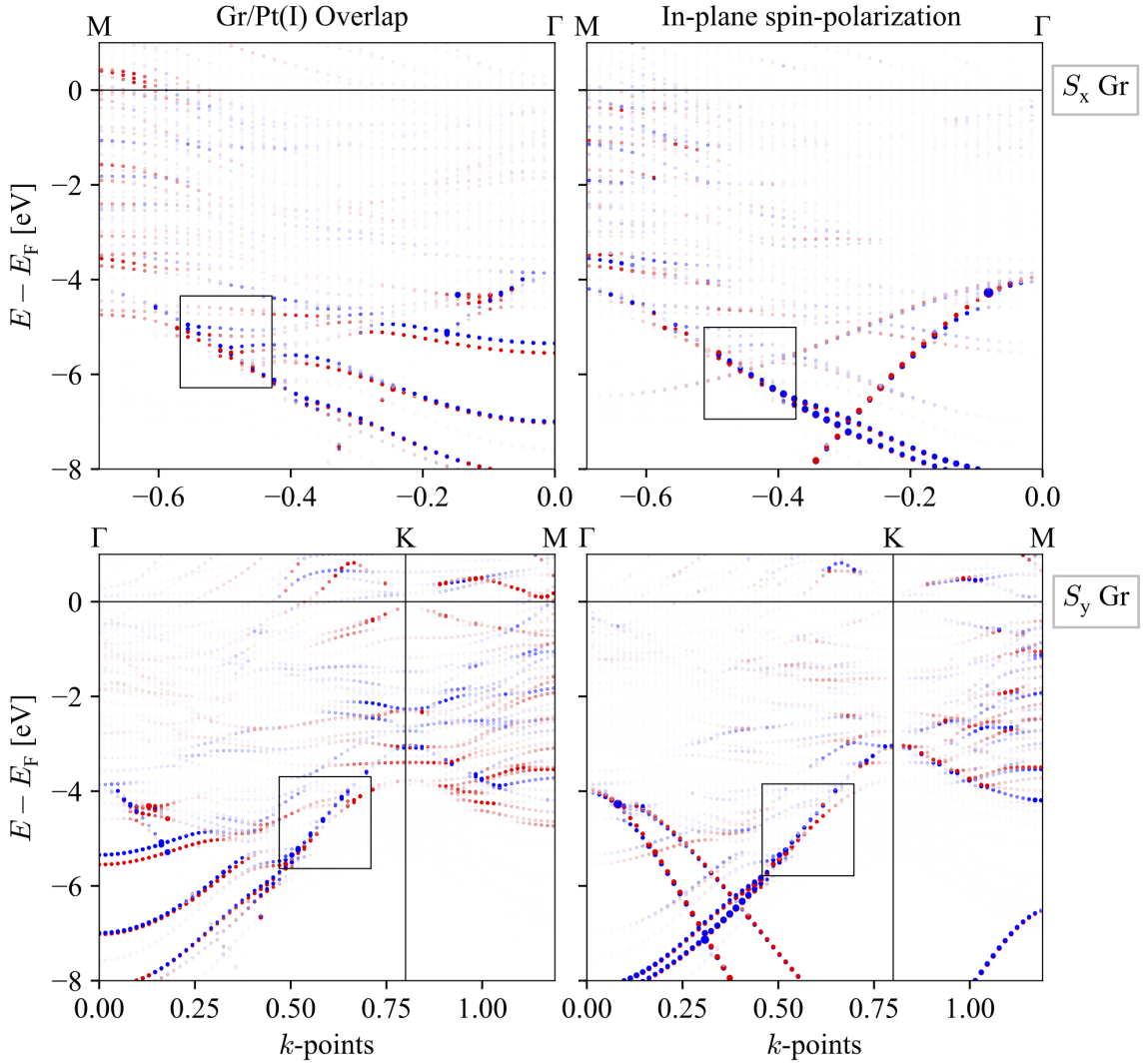



Figure 6.3.: The bandstructure for Gr/3ML Co/5ML Pt(111) along $\overline{\mathrm{M\Gamma}}$ (upper panels) $\overline{\Gamma\mathrm{KM}}$ (lower panels) are presented. In the plots on the left-hand side, circle sizes are proportional to the overlap between Gr and Pt at the interface, with blue and red indicating the spin character as given in the right panels. However, on the right-hand side, the in-plane contributions of spin-polarization ($S_x$ (upper), $S_y$ (lower)) are given.

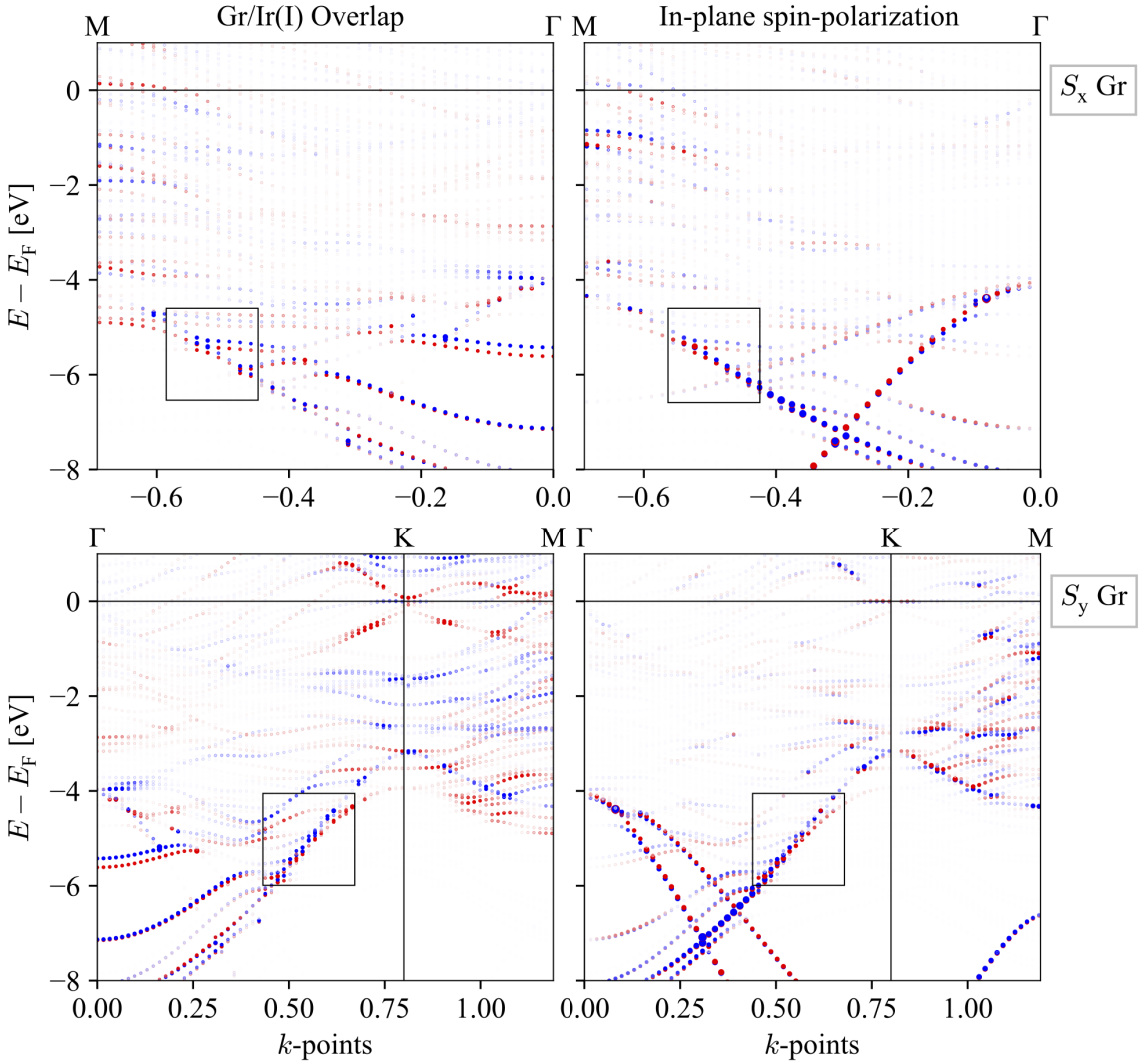



Figure 6.4.: The bandstructure for Gr/3ML Co/5ML Ir(111) along $\overline{\mathrm{M\Gamma}}$ (upper panels) $\overline{\Gamma\mathrm{KM}}$ (lower panels) are presented. In the plots on the left-hand side, circle sizes are proportional to the overlap between Gr and Ir at the interface, with blue and red indicating the spin character as given in the right panels. However, on the right-hand side, the in-plane contributions of spin-polarization ($S_x$ (upper), $S_y$ (lower)) are given.

tween single-layer Co and multiple layers for comparative analysis.
To account for all six nearest neighbors in a hexagonal lattice, depicted in Figure (5.6), the DMI for a linear chain along $\boldsymbol{q}$ can be achieved as

$$E_{\mathrm{DMI}} = 2D_y S^2 \sin(\phi_{ij})(1 + 2\cos(\phi_{ij})). \tag{6.8}$$

The parameter $D_y$ is derived from fitting a 2D model to interactions among nearest neighbors on a hexagonal lattice, a discussion thoroughly explored in Section (5.4). For a flat spin spiral, described by $\boldsymbol{q} = \frac{2\pi}{a}(\frac{1}{N}, \frac{1}{N}, 0)$, we can write $\phi_{ij} = \frac{2\pi}{N}$ [131].
To compute the DMI, the generalized Bloch theorem detailed in Section (3.6) is applied, which facilitates the calculation of DMI through a two-step computational approach. Initially, we performed a self-consistent spin-spiral calculation utilizing $45 \times 45$ grid in the complete 2D BZ, with $K_{\mathrm{max}} = 4.3\,\mathrm{a_B^{-1}}$ and $G_{\mathrm{max}} = 13\,\mathrm{a_B^{-1}}$ without accounting for SOC,

$$\mathcal{H}_0 \psi_{0,\nu} = \epsilon_{0,\nu} \psi_{0,\nu}. \tag{6.9}$$

Afterward, SOC is included in first-order perturbation theory,

$$\left\langle \psi_{\boldsymbol{k},\nu} | \hat{\mathcal{H}}_{\mathrm{soc}} | \psi_{\boldsymbol{k},\nu} \right\rangle, \tag{6.10}$$

where $|\psi_{\boldsymbol{k},\nu}\rangle$ is an eigenstate to the unperturbed $\mathcal{H}_0$ [99]. To evaluate the DMI, the sum of the eigenvalues of the occupied state is the concluding step. In Figure (6.5), the behavior of DMI in the vicinity of the $\Gamma$ point is shown. The linear characteristic of DMI within this low $q$ regime leads us to compute $D$ up to $q \leq (\frac{3}{64}, \frac{3}{64}, 0)$ along $\overline{\Gamma K}$. Extraction of the effective $D$ is performed through Equation (6.8) for left-handed spirals, assuming $\phi_{ij} = \frac{2\pi}{64}$. In Table (6.2), the effective component of $D$, for Gr/$\mathrm{n_{Co}}$ML Co/5ML Pt(Ir) is presented for two different Co thicknesses (n=1,3). In an alternative observation, there is a notable alignment between the effective

| $\mathrm{n_{Co}}$ | $D_y^{\mathrm{Gr/Co/Pt}}$ | $D_y^{\mathrm{Gr/Co/Ir}}$ |
|---|---|---|
| 1ML | 0.18 | 0.06 |
| 3ML | 0.32 | −0.06 |

Table 6.2.: The effective component of $\boldsymbol{D}$ is derived up to $q \leq 0.03\,\overline{\mathrm{\Gamma K}}$, expressed in $\mathrm{meV}\mu_{\mathrm{B}}^{-2}$, where $\mathrm{m_{Co}} = 1.84\,\mu_{\mathrm{B}}$.

in-plane $D$ vector within the framework of Gr/nML Co/5ML Pt for the $q = 0.25\,|\overline{\mathrm{\Gamma K}}|$ configuration and our findings [131]. Furthermore, the corresponding outcome for Co/5ML Pt without Gr stands at a value of $0.53\,\mathrm{meV}\mu_{\mathrm{B}}^{-2}$ [119]. Thus, by augmenting the thickness of Co within the Gr/Co/Pt(111), the effective $D$ vector demonstrates a rise, evidently converging closer to the Co/Pt(111) configuration. Conversely, considering an Ir substrate, the chirality undergoes alteration, yet the magnitude remains relatively steady.

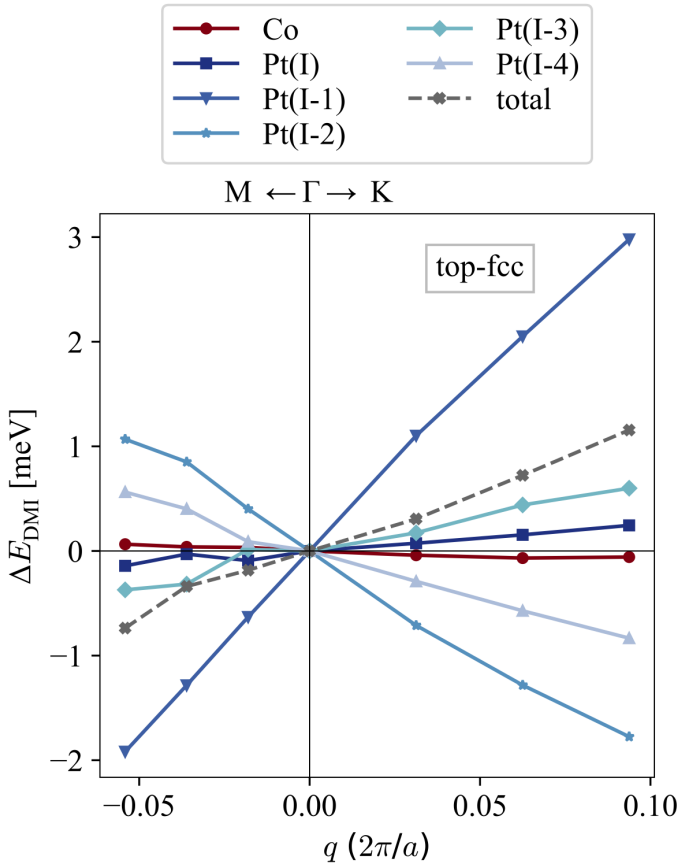



Figure 6.5.: The DMI energy near the Γ point is computed for left-handed spirals rotating in $xz$-plane. The dashed line represents the total DMI for Gr(top-fcc)/1ML Co/5ML Pt(111) heterostructure, exhibiting notably linear behavior, especially within the $q \leq (\frac{3}{64}, \frac{3}{64}, 0)$ range along $\overline{\Gamma K}$. The colored lines illustrate the diverse contributions from individual layers in the DMI.

A layer-resolved approach to DMI could shed more light on the role of the interfaces and help comprehend their impact on the DMI. Using the methodology explained, we can conduct an atomic analysis to compare the influence of each layer. In Figure (6.6), a comparative analysis of atomic contributions to DMI for both single-layer and three-layer Co configurations is presented. In the case of Gr/3ML Co/Pt,

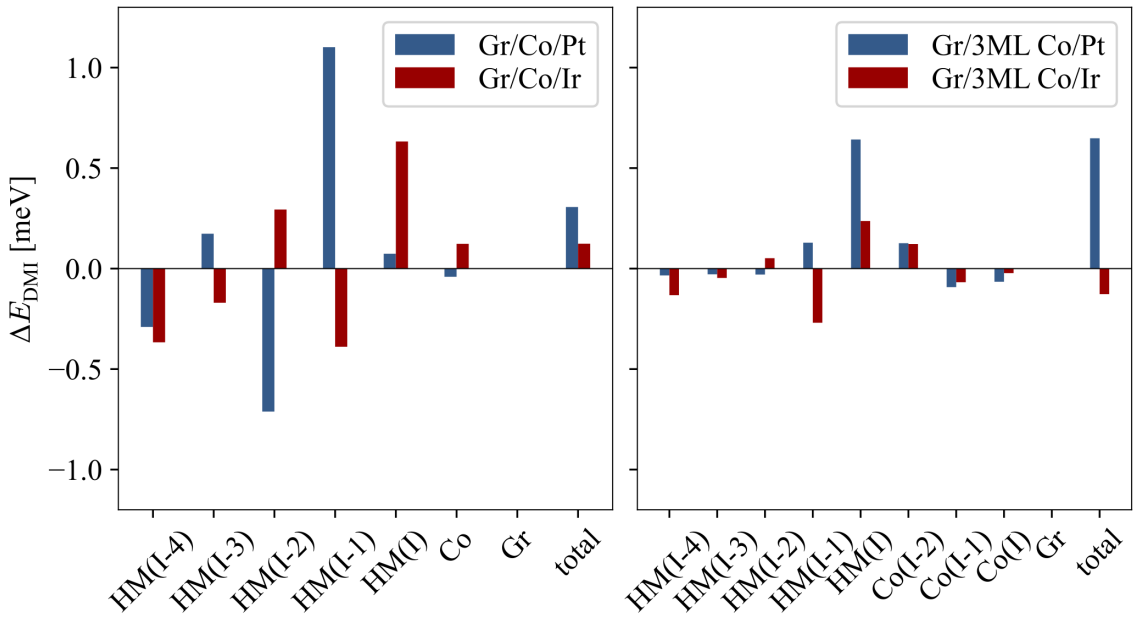



Figure 6.6.: The figures illustrate the atomic contributions for two configurations: Gr(top-fcc)/1ML Co/5ML Pt(Ir) on the left and Gr(top-fcc)/3ML Co/5ML Pt(Ir) on the right. The increase in Co thickness predominantly influences the Pt(I) layer, dictating the overall DMI. In contrast, in the case of Gr/3ML Co/Ir, the competition among the Ir layers is the determining factor for DMI.

it is evident that any reduction at Co(I) is effectively compensated for by Co(I-2) layers. The primary influence, however, originates from the Pt near the interface. Increasing the Co thickness led to a rise in the total DMI. Conversely, when the Co thickness is increased, the direction of the DMI vector for Gr/3ML Co/Ir undergoes an inversion compared to the single-layer Co configuration. Furthermore, the collective behavior of the Ir layers determines the overall DMI effect. Also, the bottom layers of the slab appear to influence the interface.

### 6.3.1 Enhancing the thickness in HM layers

To ascertain that DMI solely arises from the interfaces, an examination of the induced magnetic moments (MM) in the neighboring 3ML Co within the 5ML Pt(Ir) is conducted. The induced MM in both Ir and Pt, assessing the convergence of these

effects, are presented in Table (6.3). The incomplete convergence of MMs among the

| MM | 5ML Pt | 7ML Pt | 5ML Ir | 7ML Ir | 10ML Ir |
|---|---|---|---|---|---|
| Co(I-2) | 1.58 | 1.57 | 1.57 | 1.57 | 1.57 |
| Co(I-1) | 1.84 | 1.84 | 1.84 | 1.85 | 1.85 |
| Co(I) | 1.91 | 1.90 | 1.77 | 1.74 | 1.73 |
| HM(I) | 0.26 | 0.26 | 0.15 | 0.26 | 0.13 |
| HM(I-1) | 0.10 | 0.08 | −0.03 | −0.05 | −0.05 |
| HM(I-2) | 0.05 | 0.03 | 0.00 | −0.01 | −0.01 |
| HM(I-3) | 0.03 | 0.01 | 0.01 | 0.00 | 0.00 |
| HM(I-4) | 0.02 | 0.01 | 0.03 | 0.00 | 0.00 |

Table 6.3.: The magnetic moment (MM) of Co and the Pt(Ir) are represented in $\mu_B$. The relatively small induced MM from the bottom layers suggests that employing five layers of HM, particularly Ir, is insufficient to achieve convergence with the three layers of Co. Increasing the thickness of HMs improved the convergence for the bottom of the slab. Only the first five layers of HM were taken into consideration. For Gr/3ML Co/Ir, both 7 and 10 layers boost convergence.

initial 5ML of the HM suggests a potential influence from the underlying layers on the DMI. To illuminate the role of interfaces in DMI and minimize the impact of the bottom HM layers, we opted to increase the thickness of the HM. Figure (6.7) depicts the newly configured setups. Given the stronger influence of bottom layers in Ir, we decided to increase its thickness for a more pronounced effect. In Table (6.3), a comparison of the MMs for Gr/3ML Co/5ML Pt(Ir), Gr/3ML Co/7ML Pt(Ir), and Gr/3ML Co/10ML Ir is carried out. As the HM slab grows thicker, the MM convergence improves, albeit with only a subtle change. Examining the MM in thicker HM, it becomes evident that 7 layers of HM are sufficient to achieve a precise value of DMI. Nonetheless, employing a thicker substrate will eliminate the influence of the bottom surface on the interfaces. Figure (6.8) presents the layer-resolved DMI for both Gr/3ML Co/Pt and Gr/3ML Co/Ir systems across various thicknesses of the heavy metal (HM) substrate. In the case of Gr/3ML Co/5ML Pt, the DMI is primarily dominated by the Pt(I) layer near the interface, indicating a strong influence of this specific Pt layer on the total DMI. On the other hand, for Gr/3ML Co/5ML Ir, the DMI is determined by a competitive interaction between the Ir(I) layer and the adjacent Ir(I-1) layer, demonstrating that both layers contribute significantly to the overall DMI effect in this configuration. The contribution from the bottom layers, particularly in the 5-layer Ir substrate, is notably strong.

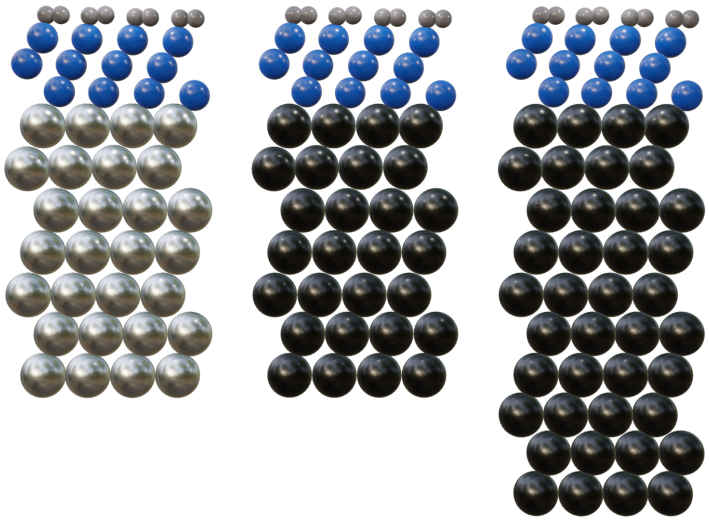


Figure 6.7.: A Lateral representation highlights the presence of thicker layers of heavy metals. Gr/3ML Co/7ML Pt (left), Gr/3ML Co/7ML Ir (center), and Gr/3ML Co/10ML Ir (right). Gr is positioned in a top-fcc configuration on the 3ML Co/HM(111) substrate.

To conclude, utilizing a total of 7 layers of HM can potentially yield a more accurate $D$ value. The $D_y$ is reevaluated for the enhanced configurations, and the updated outcome is presented in Table (6.4). The computation of $D$ for Gr/3ML Co/10ML Ir resulted in a similar value to that of 7 Ir. In the Gr/3ML Co/Pt system, a 5 ML

| $n_{HM}$ | $D_y^{Gr/3MLCo/Pt}$ | $D_y^{Gr/3MLCo/Ir}$ |
|---|---|---|
| 5ML | 0.32 | −0.06 |
| 7ML | 0.36 | −0.14 |
| 10ML | — | −0.15 |

Table 6.4.: The effective component of $\boldsymbol{D}$ is calculated within $q \leq (\frac{1}{64}, \frac{1}{64}, 0)$ along $\overline{\Gamma K}$, expressed in meV$\mu_B^{-2}$. The $D$ magnitude displays enhancement in the configuration featuring 7 layers of HMs.

Pt substrate is sufficient to ensure that the DMI arises predominantly from the interfaces, minimizing contributions from the deeper layers. However, for Gr/3ML Co/Ir, a 7 ML Ir substrate is necessary to achieve a similar effect, effectively isolating the DMI to the interface and eliminating the influence of the bottom layers. This outcome aligns with prior findings, suggesting that augmenting the thickness of Co diminishes the influence of the Gr/Co interface in DMI, which is consistent with other observations [131].

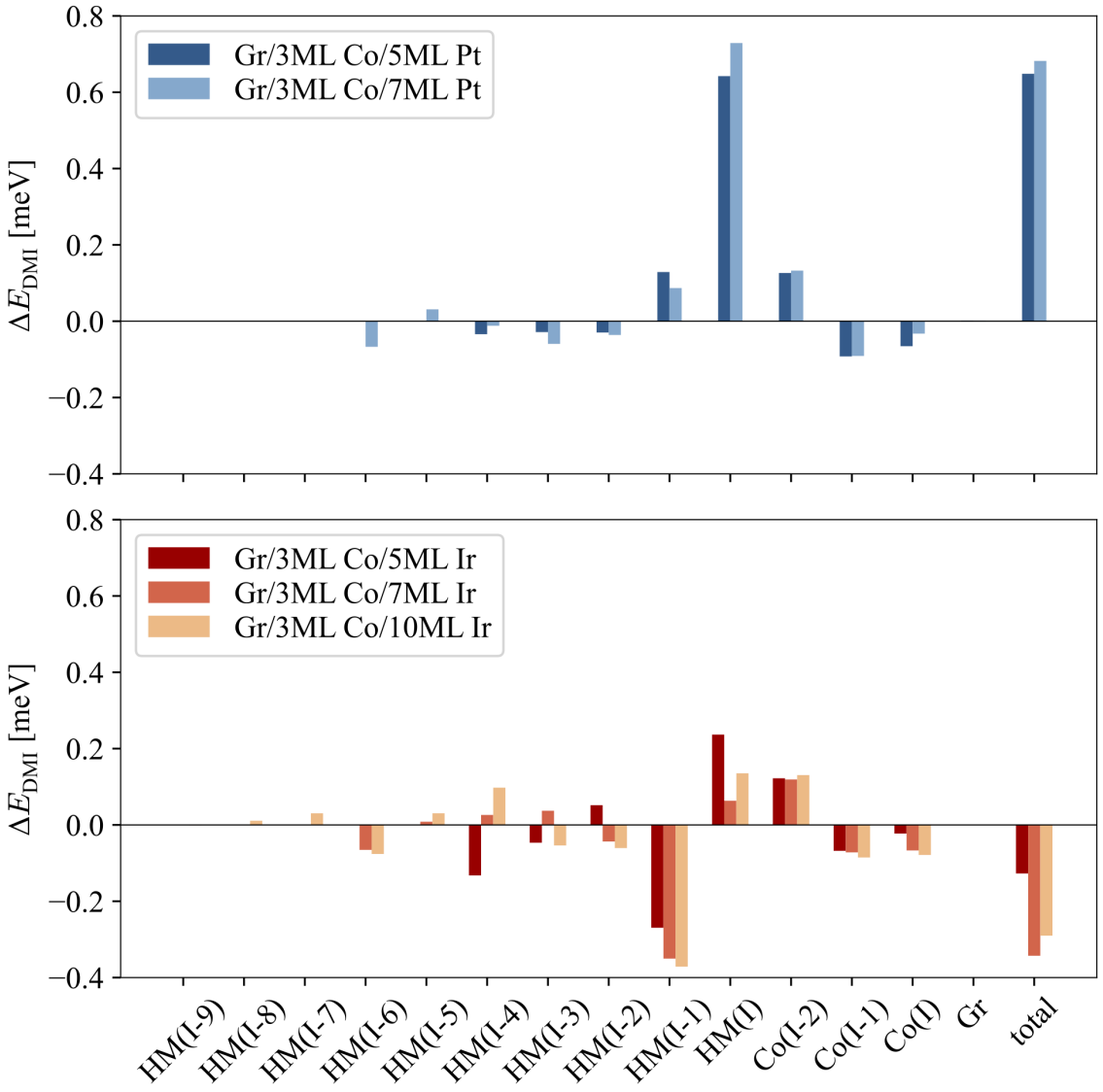



Figure 6.8.: The layer-resolved DMI for both Gr/3ML Co/Pt and Gr/3Co/Ir for various thicknesses of HM is shown. For Gr/3ML Co/5ML Pt, it is evident that Pt(I) dominates the total DMI. Conversely, for Gr/3ML Co/5ML Ir, the competition of Ir(I) as well as Ir(I-1) decides for DMI.

# 7

# DMI manipulation through electric field and oxide capping

**Contents**


7.1. Applying an external electric field . . . . . 82
7.1.1. Structural optimization . . . . . 82
7.1.2. DMI . . . . . 86
7.1.3. MCA . . . . . 91
7.2. Implementing an oxide capping layer . . . . . 93
7.2.1. Structural optimization . . . . . 93
7.2.2. DMI . . . . . 96
7.3. Electrical control of BeO/GrCoPt(111) . . . . . 101
7.3.1. Structural optimization . . . . . 101
7.3.2. DMI . . . . . 102


Enabling control over magnetic properties through external mechanisms without altering the temperature represents a significant goal from both fundamental and technological perspectives. The concept of employing electric fields to manipulate magnetism traces its origins back to the 1960s [142, 143]. The achievement of electric field modulation in the magnetic properties of both magnetic semiconductors and metals has opened approaches for the development of the field of spintronics devices controllable through electric fields. However, as a result of the screening induced by charge carriers within the ferromagnetic metals, the application of a significant electric field becomes impracticable [8].
The Dzyaloshinskii-Moriya interaction (DMI), originating from the spin-orbit coupling (SOC) in a broken inversion symmetry, plays a pivotal role in the formation of chiral magnetic textures. The impact of interfacial DMI on magnetic dynamics in multilayered materials has been explored in discussions on spin waves, domain wall motion, and skyrmions [41]. Therefore, discovering a more effective method

to regulate the strength and orientation of DMI holds immense value in crafting and maneuvering magnetic patterns crucial for spintronic applications. This can be enhanced through alterations in material compositions [144] and structure, augmentation of an oxide layer [145], the application of an electric field [140], or inducing lattice strain [146].
In this chapter, our focus will be on exploring the tuning of magnetic properties, particularly interfacial DMI in Gr/Co/Pt(111), by employing an external electric field and applying a capping oxide layer.

## 7.1 Applying an external electric field

Electric field manipulation of interfacial magnetism has attracted significant attention, given its capacity to offer an extra degree of freedom for controlling magnetization through the application of a gate electric field [47, 30, 147]. Applying an electric field induces changes in the electrostatic potential, thereby influencing magnetic anisotropy or DMI.
We employed a first-principles approach to investigate the manipulation of both DMI and magneto-crystalline anisotropy (MCA) through electric field modulation. To simulate the impact of the electric field, we adjusted the vacuum potential to introduce two electrodes of opposite polarity positioned approximately 5 Å above and below the surfaces of the film. The electric field is subsequently determined by the charges on the electrodes and is further influenced by the dielectric responses within septuple layers. In the illustrated configuration, a positive voltage change was applied perpendicular to the Gr layer, directed towards a monolayer of Co positioned atop five monolayers of Pt on the fcc(111) plane. Conversely, a negative field denotes the reverse direction of this voltage propagation. Our calculations, conducted in FLEUR-code [56, 55], establish that a positive field signifies a rise in potential from Pt to Co to Gr, while a negative field indicates the opposite, outlining the flow of potential in the opposite direction. Figure (7.1) visually illustrates the propagation of the electric field.

### 7.1.1 Structural optimization

In our analysis in section (5.1), three configurations of Gr on 1ML Co/5ML Pt(111) were observed, highlighting the top-fcc configuration as the most stable. To investigate the impact of an external electric field, perpendicular to the interface planes, we performed the structural relaxation for these three possible stacking of Gr on Co/Pt(111), as depicted in Figure (7.2). This enabled us to mitigate the potential impact of interlayer forces on the magnetic properties. Like the optimization performed for Gr/1ML Co/5ML Pt, we employed the FLAPW method within the PBE, implemented in FLEUR-code [55, 56]. Additionally, we utilized a cutoff parameter of $K_{max} = 4.0\, a_B$ and employed 21 $k$-points within the p3m1 symmetry class, distributed across 2D BZ. The forces have been optimized for all structures till reaching a convergence threshold of 0.05 eV/Å. Table (7.1) presents

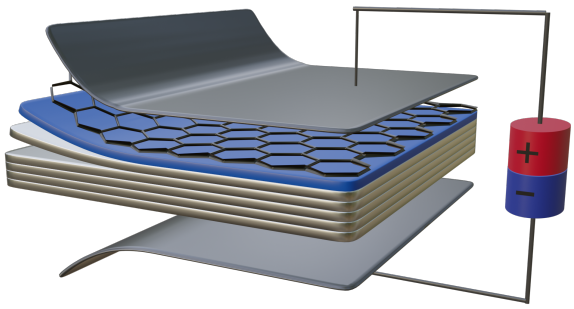



Figure 7.1.: Illustration of the simulated electric field setup, where the positive field denotes a potential increase from Pt to Co to Gr, while the negative field signifies the reverse flow of potential. The change in potential influences the dielectric responses within the separate layers.

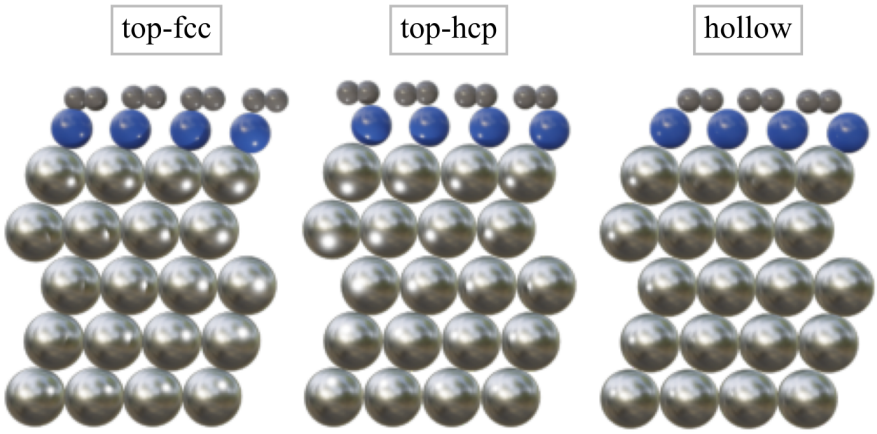



Figure 7.2.: A lateral depiction showcases three possible stacking configurations of Gr atop Co/Pt(111).

the interlayer distances within Gr/1ML Pt, including top-fcc, top-hcp, and hollow configurations. We investigated the impact of electric fields with magnitudes of 2.75 and 5.50 V/nm by enhancing the potential at the Pt (positive field), and conversely increasing it at the Gr (negative field). Comparing the data from the table for each

| Gr/Co stacking | top-fcc | top-hcp | hollow |
|---|---|---|---|
| $d_{\mathrm{C(I-1)/C(I)}}$ | 0.026 | 0.026 | 0.005 |
| $d_{\mathrm{C(I)/Co(I)}}$ | 1.959 | 1.985 | 1.970 |
| $d_{\mathrm{Co(I)/Pt(I)}}$ | 2.048 | 2.041 | 2.047 |
| $d_{\mathrm{Pt(I)/Pt(I-1)}}$ | 2.372 | 2.359 | 2.375 |
| $d_{\mathrm{Pt(I-1)/Pt(I-2)}}$ | 2.335 | 2.334 | 2.334 |
| $d_{\mathrm{Pt(I-2)/Pt(I-3)}}$ | 2.323 | 2.323 | 2.323 |
| $d_{\mathrm{Pt(I-3)/Pt(I-4)}}$ | 2.349 | 2.344 | 2.344 |

Table 7.1.: *d* stands for interlayer distances for different stacking positions of Gr on 1ML Co/5ML Pt along the fcc(111) stacking. Distances are given in Å and optimized for ±2.75, ±5.50 V/nm fields are measured in V/nm electric fields. A positive field denotes an increase in potential from Pt to 1ML Co/Gr, while a negative field implies the opposite.

configuration, the interlayer distances vary across different stacking configurations of Gr on Co/Pt(111). The variations among stackings are particularly evident at both interfaces of Co, primarily attributable to the doping of Gr. Nevertheless, the influence of the electric field on the forces was considerably minimal. Hence, the interlayer distances remained unchanged across different electric fields for each stacking of Gr on Co/Pt(111). Figure (7.3) illustrates the impact of the electric field on the total energies. Consistent with prior structural analyses of Gr/Co/Pt, the top-fcc stacking of Gr emerges as the most stable configuration. Therefore, the energy variations from the top-fcc arrangement are depicted for the top-hcp and hollow configurations. It's clear that the top-hcp configuration, differing by less than 0.1 eV from the top-fcc, is the closest. Furthermore, the electric field shows negligible influence on this proximity.
To further explore the role of the external electric field, we examined its influence on the bandstructure of Gr/Co/Pt(111), with a particular focus on the Dirac cone at the K point. As shown in Figure( 7.4), the orbital-resolved band structure analysis of Gr in the top-fcc configuration demonstrates a pronounced influence of the external electric field on the electronic structure near the K point. Under a negative electric field, the gap between the Dirac-like bands at the K point increases. In contrast, in the absence of an external field, this gap is significantly smaller. When the field direction is reversed (positive field), the electronic bands shift further, and the gap

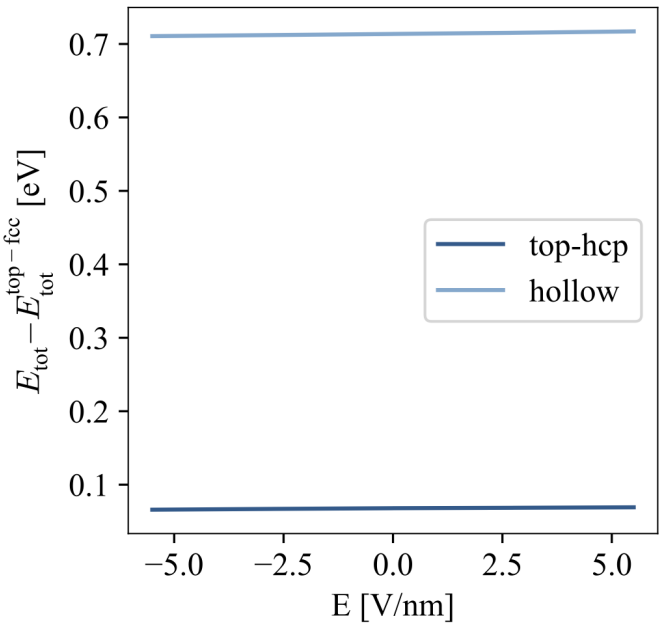



Figure 7.3.: The influence of the electric field on total energies is illustrated, highlighting the top-fcc stacking of Gr as the most stable configuration. Consequently, energy variations from the top-fcc arrangement are showcased in the presence of the electric field for the top-hcp and hollow configurations.

at the K point decreases even more, suggesting a tunable modulation of the Dirac cone through the electric field.

### 7.1.2 DMI

Applying an external electric field to the FM/HM structure presents a method to adjust structural inversion asymmetry, thereby enabling effective control of domain wall dynamics through modulation of interfacial DMI. Various FM thin films have been utilized to demonstrate the resulting alterations in interface magnetism [148, 149, 150]. Besides, in the absence of an external magnetic field, an analytical expression for the skyrmion radius has been derived, characterizing the profile of skyrmions in the small skyrmion limit [45]. Modifying the DMI and the magnetic crystalline anisotropy (MCA) will impact the skyrmion radius, as indicated by this analytical model. It has been experimentally shown that electric control of magnetism influences the interfacial DMI, which plays a critical role in the stability of magnetic skyrmions [151].
Following the first-principles calculations, we explored the changes of DMI under the impact of various electric fields on both Gr/Co as well as Co/Pt interfaces. Assuming a flat spin spiral ($\theta = \pi/2$), restricting $\boldsymbol{S}_i$ and $\boldsymbol{S}_j$ to rotate exclusively within the $xz$-plane, the DMI is characterized by

$$E_{\mathrm{DMI}}(\boldsymbol{q}) = 2S^2 D_y \sin(\phi_{ij}), \tag{7.1}$$

with $\phi_{ij} = 2\pi \boldsymbol{q}.(\boldsymbol{R}_j - \boldsymbol{R}_i)$. Taking into account all six nearest neighbors in a hexagonal lattice, as illustrated in Figure (5.6), the revised equation is provided as

$$E_{\mathrm{DMI}} = 2D_y S^2 \sin(\phi_{ij})(1 + 2\cos(\phi_{ij})), \tag{7.2}$$

where $\phi_{ij} = \frac{2\pi}{N}$ [131]. The $E_{\mathrm{DMI}}$ is computed using DFT. The response of various layers to the electric field resembles. In contrast, a notable decrease was observed in Co and Pt(I). Observing the linear nature of DMI around the $\Gamma$ point, illustrated in Figure (7.5), prompted us to calculate $D_y$ specially up to $q = (2\pi/a)(\frac{1}{64}, \frac{1}{64}, 0)$ along $\overline{\Gamma \mathrm{K}}$, shown in the Table (7.2) displaying $D_y$ corresponding to the different stacking of Gr on Co/Pt(111). The effective model, derived from fits in the low-$q$ region, accurately replicates the energies of spin-spirals [119]. For the DMI computation, we utilized the generalized Bloch theorem, which forms the basis for a computational approach to calculate DMI, explained in Section (5.4). The spin-spiral calculation was performed using a $45 \times 45$ grid spanning the entire 2D BZ. This computation was carried out $K_{\mathrm{max}} = 4.3\,\mathrm{a_B^{-1}}$ and $G_{\mathrm{max}} = 13\,\mathrm{a_B^{-1}}$ excluding SOC effects. Subsequently, the introduction of SOC was approached as a first-order perturbation theory. A response of DMI to the electric field is recognizable. Hence, we investigated the potential impacts of such an increase on the DMI. Interestingly, the adjustment in interlayer distances exhibits a subtle impact on the behavior of DMI. Therefore, it can be concluded that structural optimization under the electric field is essential to attain a precise understanding of the modifications to the DMI.

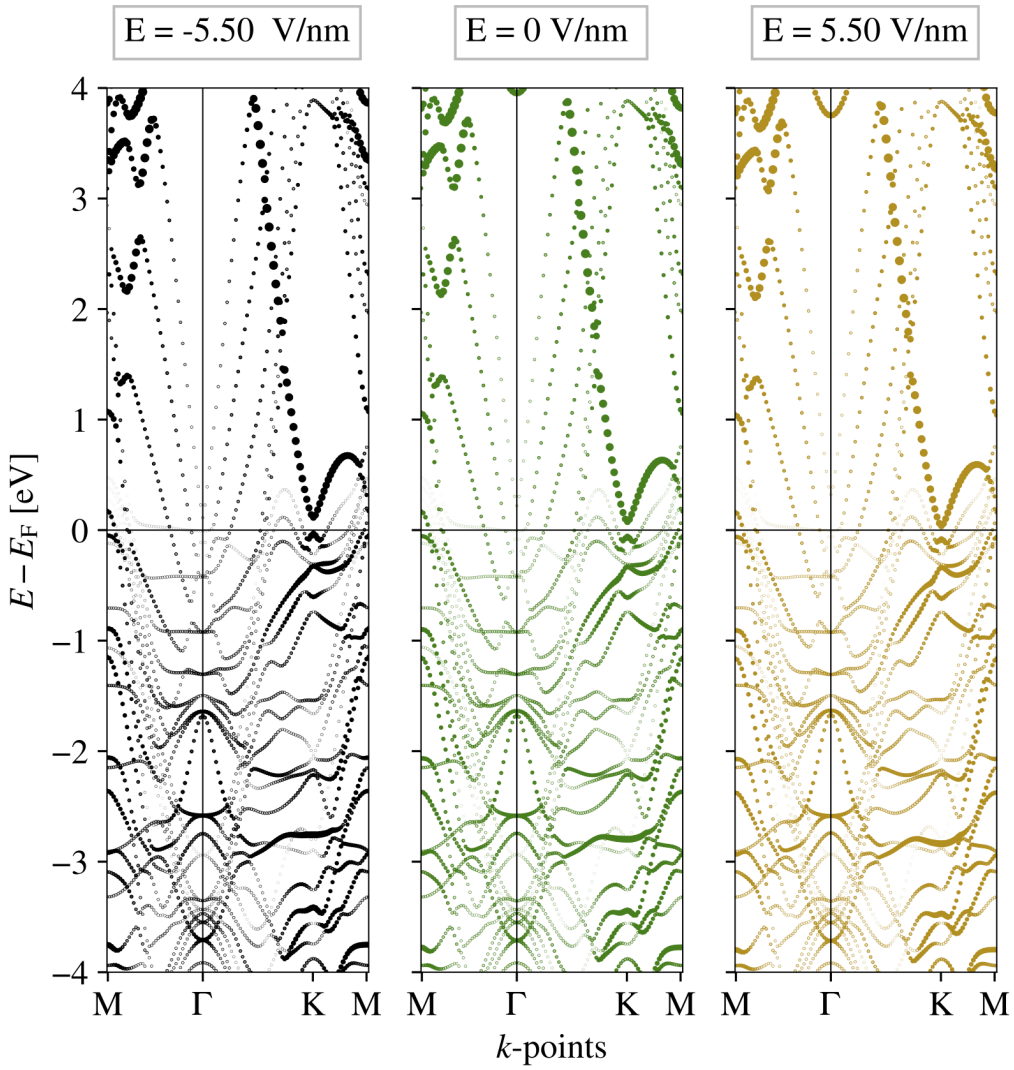



Figure 7.4.: Band structure of Gr on Co/Pt(111) around the K point under different external electric fields (E = ±5.50 V/nm and E = 0 V/nm). The application of the field modifies the Dirac cone, inducing a bandgap opening at the K point. The gap increases under a negative field and reduces under a positive field, reflecting a tunable field-driven modification of the electronic structure.

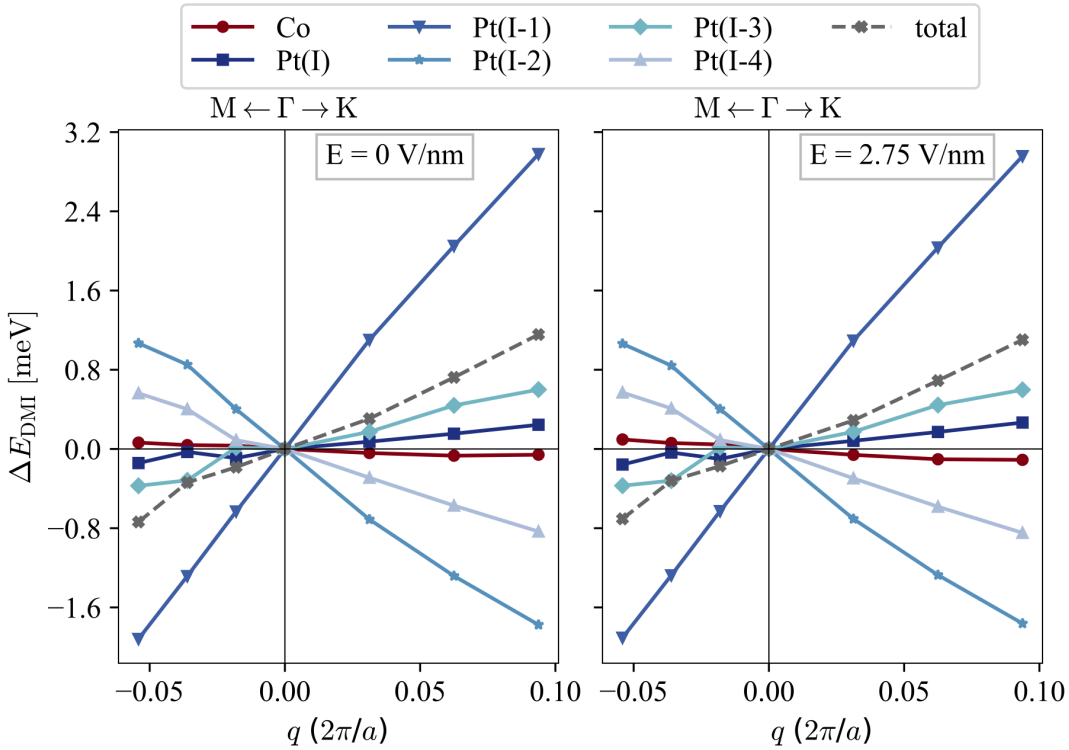



Figure 7.5.: The computation of DMI energy around the Γ point focuses on the left-handed spirals rotating specially within the $xz$-plane. The dashed line showcases the total DMI for the Gr(top-fcc)/1ML Co/5ML Pt(111) heterostructure, both with and without an applied electric field. Notably, it displays a prominently linear trend, particularly within the range of $q = \frac{6}{64}(2\pi/a)$ along $\overline{\Gamma K}$ or $q = \frac{1}{64}(2\pi/a)$ along $\overline{\Gamma M}$. The colored lines delineate the distinct contributions from individual layers to the DMI.

| Gr/Co/Pt(111) | $D_y$ | | | | |
|---|---|---|---|---|---|
| E-field (V/nm) | −5.50 | −2.75 | 0 | 2.75 | 5.50 |
| top-fcc | 0.17 | 0.16 | 0.15 | 0.14 | 0.13 |
| top-hcp | −0.15 | −0.16 | −0.12 | −0.18 | −0.19 |
| hollow | −0.21 | −0.21 | −0.22 | −0.22 | −0.23 |

Table 7.2.: The effective component of the DMI vector ($\boldsymbol{D}_y$) is determined up to $q \leq \frac{2}{64}$ of the BZ edge $\overline{\Gamma K}$, expressed in meV$\mu_B^{-2}$, where $m_{Co} = 1.84\,\mu_B$.

Taking the optimization into account, the application of electric fields leads to a decrease in the total DMI of Gr/Co/Pt(111). This shift is more explicitly illustrated in the Figure (7.6).

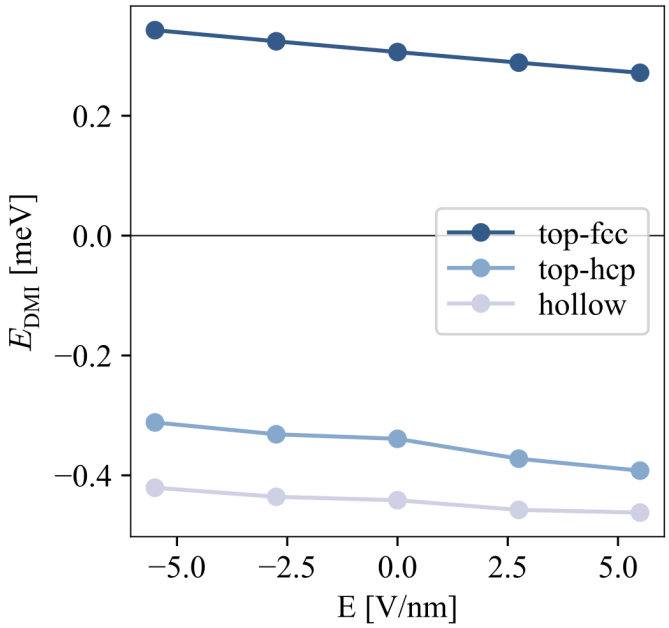



Figure 7.6.: The dependency of DMI is illustrated concerning the applied electric field for various stacking configurations of Gr on Co. A positive field signifies a positive voltage propagated perpendicular from Gr to 1ML Co atop 5MLs of Pt on the (111) plane. Conversely, a negative field indicates the opposite direction of this voltage. A diminishing trend is evident in the presence of the field. The behavior induced by the field appears similar for all configurations.

We characterized the observed shift by quantifying the slope of the nearly linear curve, defined as the ratio of DMI change to the applied electric field (E),

$$\beta = \frac{\Delta E_{\mathrm{DMI}}[\mathrm{meV}]}{\mathrm{E}[\mathrm{V/nm}]}, \tag{7.3}$$

displayed in Table (7.3). Remarkably, the consistent nature of the slope depicting the electric field control of DMI, denoted as $\beta$, across all Gr configurations on Co/Pt(111) allows us to compare the DMI shift with other similar studies.
Applying the generalized Bloch theorem, a detailed examination of the layer-resolved DMI during the modulation of the electric field is illustrated in Figure (7.7). Examining the layer-resolved DMI, there is a decrease in DMI in the presence of a perpendicular electric field. The contribution from Co displays a similarity to the total DMI for both the top-fcc and top-hcp configurations, while the contribution

| Gr/Co stacking | $\beta$ [fJ·m/V] |
|---|---|
| top-fcc | −15.4 |
| top-hcp | −15.4 |
| hollow | −15.4 |

Table 7.3.: $\beta$ is determined up to $q \leq (2\pi/a)(\frac{1}{64}, \frac{1}{64}, 0)$, encompassing the initial point in Figure (7.5) along $\overline{\Gamma K}$. This ratio signifies the variation of DMI with the application of an electric field.

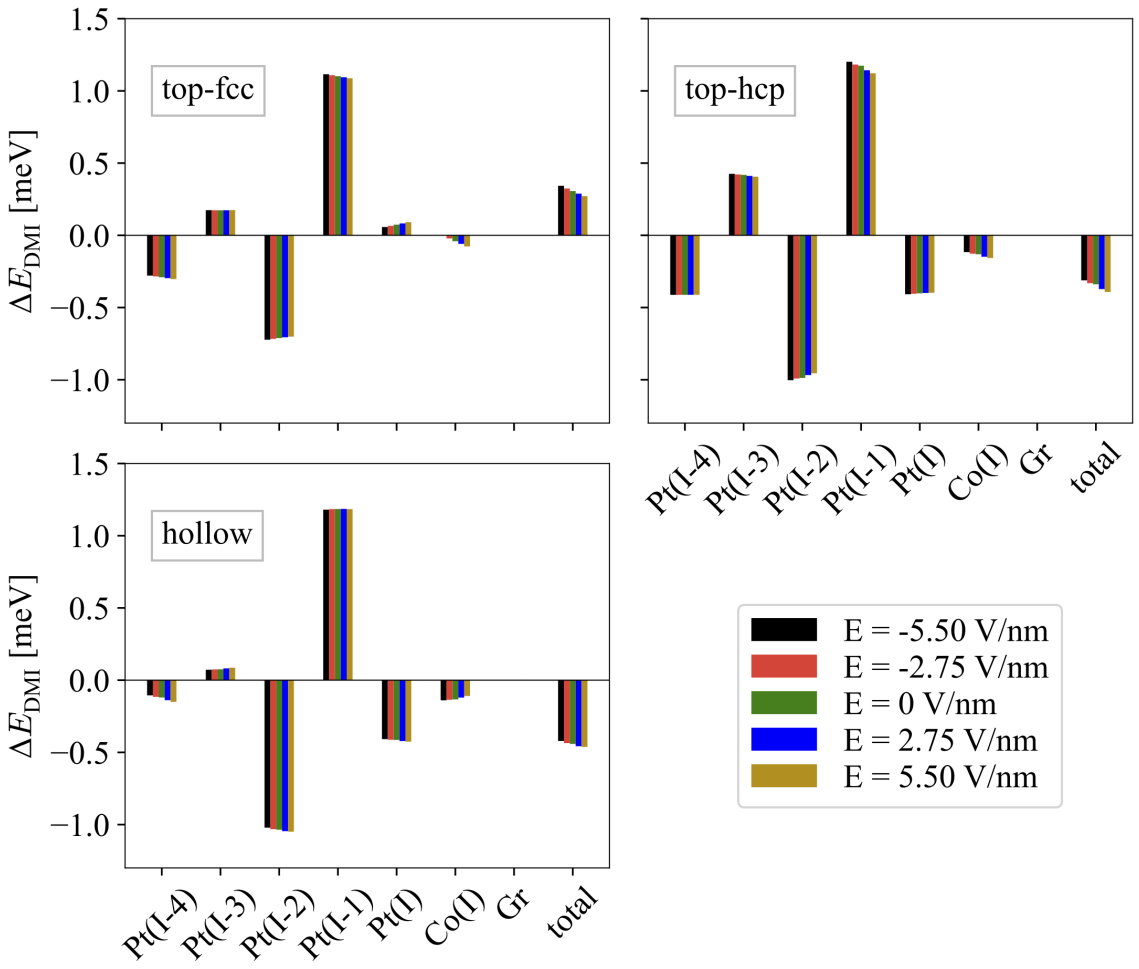



Figure 7.7.: Layer-resolved DMI for Gr/Co 1ML/5ML Pt(111) are presented. The modulation of the electric field influences the contributions of both Co and Pt layers, resulting in a consequent change in the DMI.

from Co for the hollow configuration remains constant under the influence of the field.
Furthermore, the sign of the DMI originating from Co in the top-fcc configuration is opposite to that of the total DMI. Therefore, the absolute value of DMI decreases for top-hcp stacking, while it increases for the other two stackings. Adjacent to Co, Pt(I) exhibits an increasing response for the top-fcc and top-hcp configurations and a decreasing response for hollow configurations. Moreover, there are variations in other layers of Pt; however, these changes compensate for each other. Ultimately, the competition between Co and Pt(I) determines the total DMI.

### 7.1.3 MCA

Investigating the magnetocrystalline anisotropy (MCA) within the Gr/Co/Pt(111) system, a significant out-of-plane MCA of 2.38 meV was observed. Experiments also confirm a robust perpendicular magnetic anisotropy (PMA) [12]. Adjusting both PMA and DMI enables us to manipulate magnetic skyrmions, given that their size and stability rely on both DMI and PMA [46]. Moreover, within an electric field, modifications to the equilibrium properties of skyrmions have been observed, and the mechanism behind the electric-field control of skyrmion motion has been identified. This control has been determined in terms of alterations to the static properties of skyrmions [152].
In the computation of MCA attributed to SOC, we incorporate SOC within a self-consistent collinear calculation. The MCA is defined by the expression:

$$\Delta E_{\mathrm{MCA}} = E_{\mathrm{tot}}^{\parallel} - E_{\mathrm{tot}}^{\perp}. \tag{7.4}$$

Here, $E_{\mathrm{tot}}$ denotes the total energies, including SOC terms, computed fully self-consistently for spins aligned along the in-plane ($E_{\mathrm{tot}}^{\parallel}$) and out-of-plane ($E_{\mathrm{tot}}^{\perp}$) axes within the application of electric fields. To ensure accurate MCA values, we achieved convergence for this quantity with $\mathrm{K_{max}} = 4.0\,\mathrm{a_B^{-1}}$ within 2025 $k$-points in the entire 2D BZ. In Table (7.4), these values are presented for various electric fields. Here, we exclusively focused on the Gr(top-fcc)/Co/Pt(111) configuration, which has been calculated to be the most stable configuration of Gr on Co/Pt(111) in the presence of an electric field. Despite the electric field's negligible influence on the electronic

| E [V/nm] | −5.50 | −2.75 | 0 | 2.75 | 5.50 |
|---|---|---|---|---|---|
| $\Delta E_{\mathrm{MCA}}$[meV] | 2.30 | 2.38 | 2.38 | 2.38 | 2.48 |

Table 7.4.: The $\Delta E_{\mathrm{MCA}}$ is determined for Gr(top-fcc)/Co/Pt(111) in the presence of electric field. The positive energy corresponds to the perpendicular MCA.

structure, we observed a contrast in the modification of the MCA compared to the

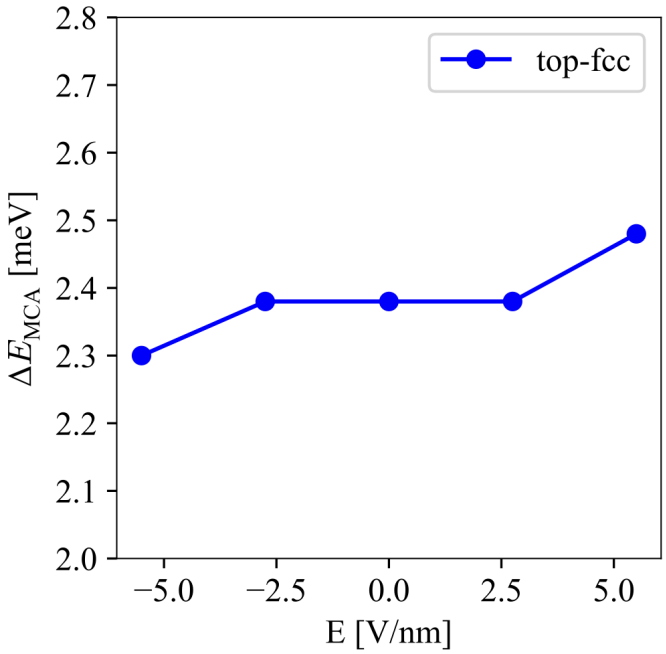



Figure 7.8.: The correlation between MCA and the applied electric field is depicted for Gr(top-fcc)/Co/Pt(111). Contrary to the observed decrease in DMI, a noticeable increase is apparent. The MCA is calculated self-consistently.

DMI, as depicted in Figure (7.8). The calculated ratio as a function of the applied field is denoted as $\gamma$ and defined in

$$\gamma = \frac{\Delta E_{\mathrm{MCA}}[\mathrm{meV}]}{\mathrm{E}[\mathrm{V/nm}]}, \tag{7.5}$$

is determined to be $\gamma = 24.9$ fJ·m/V. Experimental findings indicate voltage-induced alterations in magnetic anisotropy energy, with values ranging from 13 fJ·m/V in a few MLs of FeCo [153, 154], 26±6 fJ·m/V in Au/Fe/MgO [155], to 48 fJ·m/V for single-crystalline 5 nm Fe on MgO [156].
Besides, we employed the force theorem approach to obtain both MCA values and distinct atomic contributions in MCA. The change in total energy is primarily determined by the variation in the sum over the occupied single-particle energies in the first order. This connection is commonly referred to as the force theorem [136]. Using the force theorem, the SOC is incorporated non-self-consistently after establishing the self-consistent solution of the Kohn-Sham equation. Then, the total energy in the presence of the SOC can be approximated by

$$E - E_0 \approx \sum_{\nu}^{\mathrm{occ.}} \epsilon_{\mathrm{ft},\nu} - \sum_{\nu}^{\mathrm{occ.}} \epsilon_{0,\nu}. \tag{7.6}$$

The eigenvalues $\epsilon_{\mathrm{ft},\nu}$ are derived from $\mathcal{H}_0 + \mathcal{H}_{\mathrm{soc}}$. Figure (7.9) represents the MCA calculated using the Force theorem, showcasing distinct atomic contributions. Evaluating various contributions to MCA, it can be seen that the positive electric field reduces MCA. The contribution of Co and Pt(I) within the field exhibits minimal variation. However, Pt(I-1) as well as Pt(I-2) undergoes a reduction, resembling the total contributions. Additionally, there are modifications in the contributions of Pt(I-3) and Pt(I-4), which offset each other.
Both DMI and MCA undergo modifications in the presence of an electric field.

## 7.2 Implementing an oxide capping layer

Several studies have investigated the enhancement of DMI through the use of oxide/ferromagnetic materials. A comprehensive analysis has been conducted on the O/Fe/Ir(001) system examining charge transfer and induced dipole moment [145]. Significant changes emerge across varying O. This reveals a clear correlation between the strength and the sign of DMI with both charge transfer and induced electrostatic moment. Another investigation involving MgO/Co/Pt indicates an augmentation in the DMI of the Co/Pt system. This enhancement is attributed to the enhanced Rashba effect at the interface of MgO(111)/Co [147].
Building on these investigations, we explored the DMI by introducing an oxide layer onto the Gr/Co/Pt(111).

### 7.2.1 Structural optimization

In order to enhance magnetic properties, we deliberately introduced a dipole layer, choosing BeO for its lattice structure compatibility and close proximity to the lattice

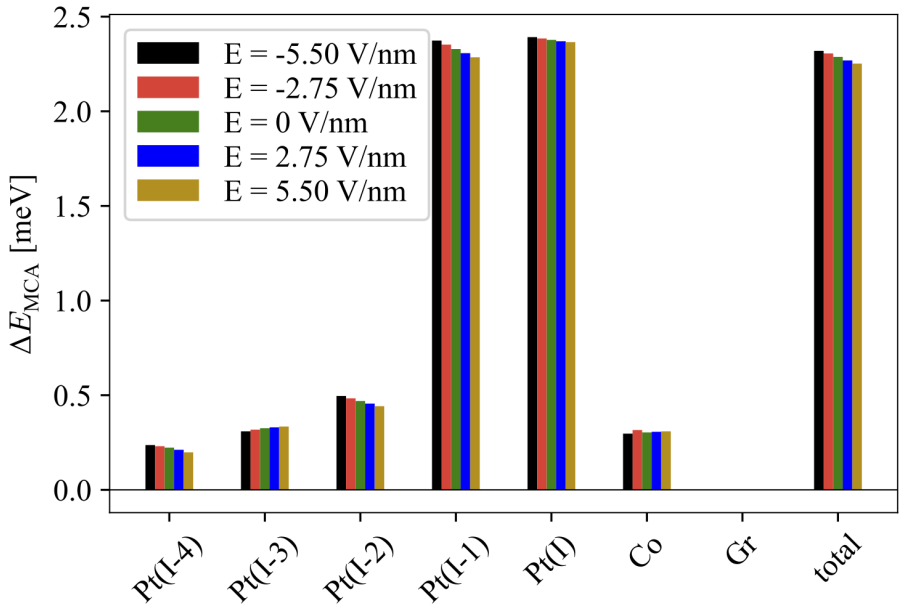



Figure 7.9.: MCA analysis using the Force Theorem, presenting various atomic contributions. The "total" corresponds to the contributions of SOC from all layers. The positive field denotes a rise in potential from the bottom layer of the film (Pt(I-4)) to the Gr. In the presence of an electric field, the MCA decreases.

constant for Gr/Co/Pt(111).
Moreover, it was shown that combining the wurtzite-BeO barrier and the fcc-Co electrode can form a new type of interfacial spin-filter-based magnetic tunnel junction with highly spin-polarized transport properties and a strong spin-transfer torque effect. The underlying mechanism, which was modeled within a tight binding model, is the significant spin-polarized charge transfer solely at the O/Co interface [157].
In our calculation, the oxide capping layer has been placed on top of the Gr. The studied composition showcases 2 MLs of BeO on Gr/1 ML Co/5 ML Pt, visually represented in Figure (7.11). There exist 12 potential stacking configurations for placing either Be or O on top of Gr. We performed relaxation simulations for each of these configurations. However, to enhance structural optimization, we chose a symmetrical structure, as depicted in Figure (7.10). The symmetrical structure undergoes relaxation until the forces converge to 0.05 eV/Å.
For the relaxation process, the basis functions were subjected to a plane-wave cutoff

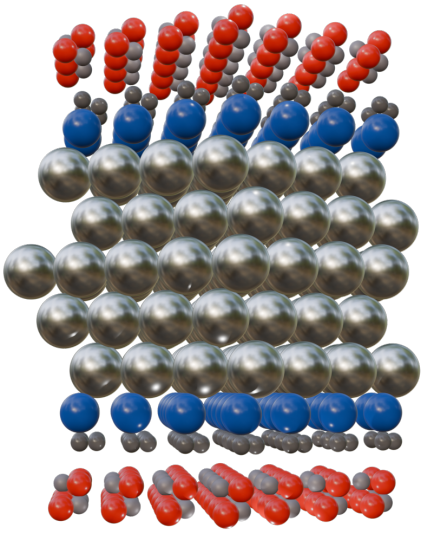


Figure 7.10.: The symmetrical structure of BeO/Gr(top-fcc)/Co/Pt(111) was chosen for structural relaxation, shown on the left side, while the optimized BeO film is depicted on the right side.

set at $K_{max}$ = 4.0 $a_B^{-1}$. 21 k-points were distributed within the primitive hexagonal BZ, following the p3m1 symmetry class. Achieving convergence in both charge density and total energy necessitated treating the semicore-states of Co using local orbitals [83], as implemented in the FLEUR-code [158]. Besides, to stabilize the bonding of Gr and BeO, the inclusion of van der Waals (vdW) correction is essential. In our approach, we incorporated the vdW-D3 correction [159], implemented within the framework of the FLEUR-code [56, 55].
Following the structural optimization, 6 stackings where Be initially occupied the

top position on Gr, optimization resulted in O taking its place. Consequently, the initial 12 configurations have been condensed into 6 distinct stackings, with O always positioned atop graphene throughout the relaxation process. The Figure (7.11) depicts six distinctive stacking configurations of 2 MLs of BeO on Gr(top-fcc)/Co/Pt. The vdW gap between the oxide and Gr leads to a negligible influence on the stacking of Gr on Co. Hence, we settled on the top-fcc arrangement of Gr on Co. Notably, a preference is observed in settling O above a C atom of Gr beyond this

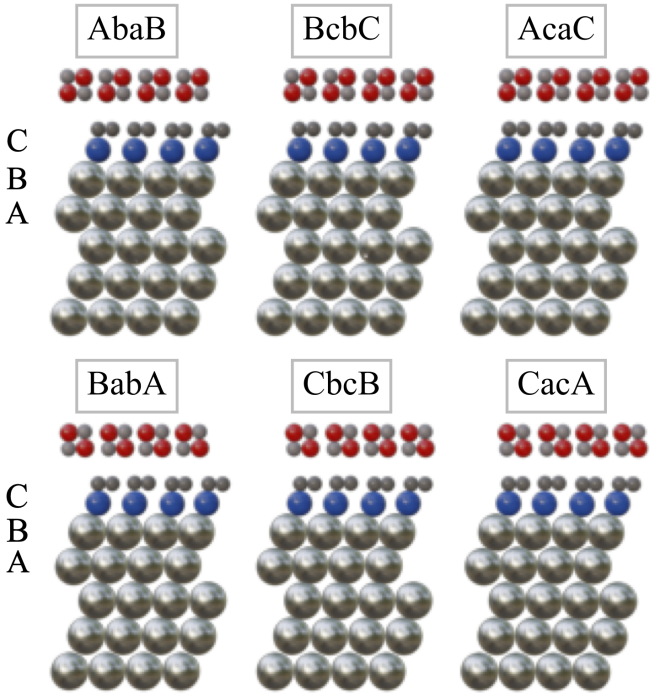



Figure 7.11.: A side view presents three potential stacking configurations of 2MLs of BeO atop Gr/3ML Co/5ML Pt(111). The 12 initial configurations have been optimized into six unique stackings.

refined set. The relaxed interlayer distances are shown in Table (7.5).
Comparing interlayer distances of BeO/Gr(top-fcc)/Co/Pt(111) with those of the Gr(top-fcc)/Co/Pt(111) structure, it is evident that the interfacial dipole has a modest impact on $d$. The bottom layers remain almost unaffected.

### 7.2.2 DMI

It has been reported that the robust PMA observed in (Co)Fe/MgO($AlO_x$) primarily originates from strong hybridization between the interfacial (Co)Fe-3$d$ and O-2$p$ orbitals, influenced by SOC [29]. The strong correlation between the interfacial dipole and PMA persists even in the absence of an applied electric field [52], prompting us to investigate the enhancement of DMI with a capping layer of oxide, particularly,

| BeO/Gr stacking | AbaB | BabA | BcbC | CbcB | AcaC | CacA |
|---|---|---|---|---|---|---|
| $d_{\mathrm{Be(I-1)/O(I-1)}}$ | 0.04 | 0.04 | 0.04 | 0.04 | 0.04 | 0.04 |
| $d_{\mathrm{O(I-1)/Be(I)}}$ | 2.56 | 2.56 | 2.56 | 2.56 | 2.56 | 2.56 |
| $d_{\mathrm{Be(I)/O(I)}}$ | 0.03 | 0.03 | 0.03 | 0.03 | 0.03 | 0.03 |
| $d_{\mathrm{O(I)/C(I-1)}}$ | 3.71 | 3.71 | 3.71 | 3.71 | 3.71 | 3.71 |
| $d_{\mathrm{C(I-1)/C(I)}}$ | 0.03 | 0.03 | 0.03 | 0.03 | 0.03 | 0.03 |
| $d_{\mathrm{C(I)/Co}}$ | 1.94 | 1.94 | 1.94 | 1.94 | 1.94 | 1.94 |
| $d_{\mathrm{Co/Pt(I)}}$ | 2.03 | 2.03 | 2.03 | 2.03 | 2.03 | 2.03 |
| $d_{\mathrm{Pt(I)/Pt(I-1)}}$ | 2.36 | 2.36 | 2.36 | 2.36 | 2.36 | 2.36 |
| $d_{\mathrm{Pt(I-1)/Pt(I-2)}}$ | 2.34 | 2.34 | 2.34 | 2.34 | 2.34 | 2.34 |
| Total energy | 10.19 | 0 | 2.17 | 6.3 | 9.26 | 5.33 |

Table 7.5.: The relaxation of BeO on Gr(top-fcc)/Co/Pt(111) is shown. All forces are optimized, reaching 0.05 eV/Å. $d$ stands for interlayer distances, given in Å and total energies in meV. The lattice constant of Gr(top-fcc)/Co/Pt(111), which is consistently set at 2.75 Å, is considered for all structures. Capital letters correspond to the stacking of O, while lowercase letters represent the stacking of Be.

BeO in our case.
To provide a comparison between the effective DMI vector, $D_y$, of BeO/Gr(top-fcc)/Co/Pt(111) and Gr(top-fcc)/Co/Pt(111), we extended our calculations up to $q = \left(\frac{2\pi}{a}\right)\left(\frac{1}{64}, \frac{1}{64}, 0\right)$ along $\overline{\Gamma K}$ in accordance with Equation (7.1). The total DMI is computed via DFT employing the generalized Bloch theorem. These results are presented in Table (7.6). The presence of an oxide layer dipole induces a magnification

| ML | $D_y$ |
|---|---|
| Gr(top-fcc)/Co/Pt | 0.15 |
| BeO/Gr(top-fcc)/Co/Pt | 0.18 |
| BeO(modified)/Gr(top-fcc)/Co/Pt | 0.17 |

Table 7.6.: The effective component of $\boldsymbol{D}$ is determined within the range of $q \leq \frac{2}{64}\overline{\Gamma K}$, and the values are expressed in meV$\mu_B^{-2}$, considering a magnetic moment of 1.84 $\mu_B$ for Co. This adjustment leads to an increase in DMI. In the modified configuration of BeO/Gr/Co/Pt, BeO(I-1) undergoes modulation to $d_{\mathrm{Be(I-1)/O(I-1)}}$=0.26 Å.

in the DMI strength, surpassing the impact of an externally applied electric field. By altering the dipole amplitude of BeO, we can effectively manipulate its properties. Consequently, we constrained the Be(I-1) layer to shift away from the O(I-1) plane by a magnitude of 0.26 Å. This modification was made to investigate the correlation between dipole size and the resulting enhancement in DMI. The modification in BeO leads to a lesser enhancement in DMI.
We utilized the generalized Bloch Theorem to assess the layer-resolved contributions to the total DMI, aiming to examine the impact of the oxide capping layer on various layers. Initially, a spin spiral calculation was conducted using a $45 \times 45$ grid covering the entire 2D BZ. This computation was performed with a cutoff of $K_{max} = 4.3\, a_B^{-1}$, excluding SOC effects. Subsequently, the inclusion of SOC was approached using first-order perturbation theory. The layer-resolved analysis of the DMI is depicted in Figure (7.12). The impact of the oxide capping layer extends to both Co and Pt(I), causing an inversion in their respective contributions to DMI. Specifically, there is a small decrease in Pt(I) and an increase in Co contributions. Additionally, Pt(I-3) and Pt(I-4) exhibit expansions, while Pt(I-2) and Pt(I-1) effectively cancel each other. Consequently, the total DMI increases. In the structurally modified BeO, the contributions exhibit slight variations, resulting in a comparatively modest augmentation in the total DMI.
Having observed a positive influence of the oxide capping layer on the DMI contribution in Co, we investigated the impact of the oxide layer on thicker Co. Therefore, we proceed to examine the configuration consisting of 2ML BeO on Gr(top-fcc)/3ML Co/5ML Pt, as illustrated in Figure (7.13). After computing $D_y$ using Equation (7.2), the resulting value is compared under the presence of an oxide layer and with

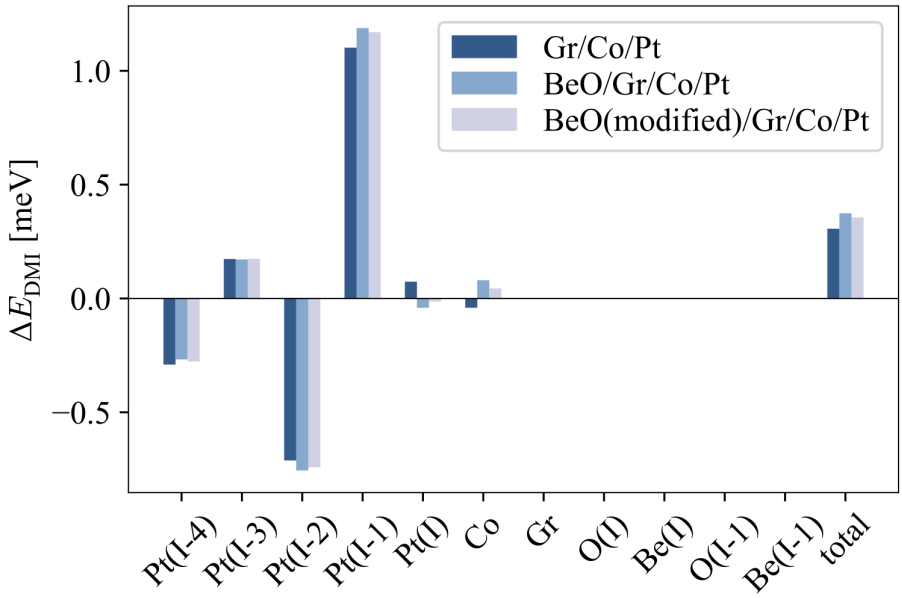



Figure 7.12.: Layer-resolved contributions to the DMI are shown. In the modified configuration with BeO, we induced a displacement of the Be(I-1) layer away from the O(I-1) plane by 0.26 Å.

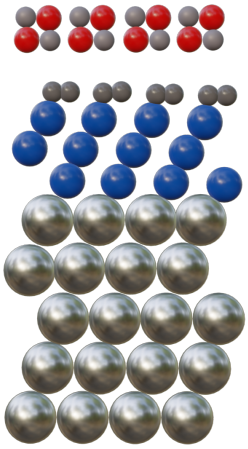


Figure 7.13.: A side view of AbaB stacking of Gr(top-fcc)/3ML Co/5ML Pt(111) is presented.

increased thickness of Co. This value is presented in Table (7.7). The DMI is com-

| ML | $D_y$ |
|---|---|
| Gr(top-fcc)/3ML Co/Pt | 0.32 |
| BeO(modified)/Gr(top-fcc)/3ML Co/Pt | 0.82 |

Table 7.7.: The determination of the effective component of $\boldsymbol{D}$ is conducted within the specified range of $q \leq (\frac{2\pi}{a})(\frac{1}{64}, \frac{1}{64}, 0)$ along $\overline{\Gamma K}$. The resultant values are expressed in meV$\mu_B^{-2}$, considering a magnetic moment of 1.84 $\mu_B$ for Co.

puted utilizing the generalized Bloch theorem, employing a grid of 45×45 $k$-points spanning the 2D BZ. The layer-resolved contributions to the DMI are illustrated within the specified range of $q \leq (\frac{1}{64}, \frac{1}{64}, 0)$ along $\overline{\Gamma K}$ in Figure (7.14). Remarkably,

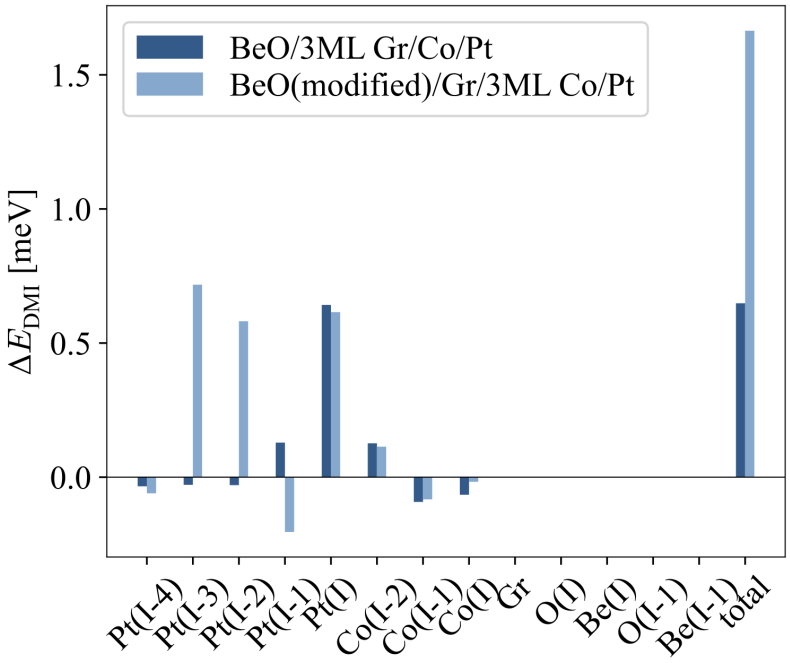



Figure 7.14.: Layer-resolved contributions to the DMI are shown. Augmenting the thickness of Co results in a substantial increase in the DMI.

the DMI exhibits a substantial increase. This augmentation can be attributed to the competitive influence originating from the bottom layers of Pt, particularly Pt(I-1), Pt(I-2), and Pt(I-3).

## 7.3 Electrical control of BeO/GrCoPt(111)

Building on our previous studies into the modulation of magnetic properties through the utilization of electric fields and capping oxide layers, we delved deeper into the combined effects of both the oxide layer and electric fields. Theoretical investigations conducted on Fe/MgO junctions have revealed that the hybridization of Fe $3d$ and O $2p$ orbitals leads to modifications in the electronic structure at the interface. This leads to changes in both the direction and intensity of magnetic anisotropy. When an electric field is applied, it induces a shift in the Fermi energy positions at the interface, consequently altering the orbital occupancy and thereby influencing the magnetic anisotropy at the interface [28, 160]. Furthermore, experimental findings on FeCo/MgO systems suggest that the application of an electric field can dynamically alter the degree of oxidation of Fe at the interface. This reversible change in oxidation state may have implications for the overall magnetism of the system [161].
In this section, we incorporate electric fields into the BeO/Gr(top-fcc)/Co/Pt(111) system, as illustrated in Figure (7.15), with a primary focus on examining structural modifications prior to investigating the DMI.

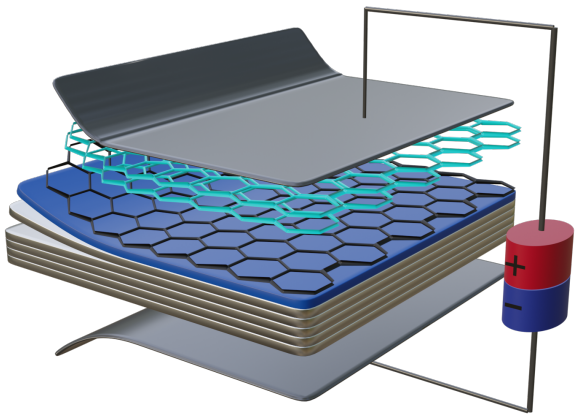



Figure 7.15.: Visual representation of the simulated electric field configuration, wherein a positive field is applied from the BeO bilayer to the Gr/Co/Pt film.

### 7.3.1 Structural optimization

In the studied asymmetric configuration, the introduction of additional dipoles within the vacuum region along the electric field complicates the structural optimization. A similar investigation aiming to control the MAE via electric fields in Fe/MgO was also performed for a symmetric structure [52]. Consequently, we analyzed the forces within the Gr/1ML Co/5ML Pt/1ML Co/Gr structure sandwiched

between two layers of 2 MLs of BeO.
The optimization is conducted for BabA stacking, recognized as the energetically most stable arrangement of BeO on Gr(top-fcc)/Co/Pt(111). Following a methodology akin to the oxide optimization, we utilized 21 $k$-points within the p3m1 symmetry class of the primitive hexagonal BZ and $K_{max} = 4.0\, a_B^{-1}$ along with the vdW-D3 correction. Also, obtaining convergence required using local orbitals to handle the semi-core states of Co. Maintaining the interlayer distances, outlined in the Table (7.5), the forces under fields of 2.75 and 5.50 V/nm in both directions have been elevated to 0.5 eV/Å. Since quantifying further optimization within the influence of the electric field is challenging, the calculation of DMI proceeds with the AbaB stacking of Gr(top-fcc)/Co/Pt under the influence of an electric field.

### 7.3.2 DMI

Following the methodology employed in DMI studies concerning oxide layers on Gr(top-fcc)/Co/Pt, we initiated our investigation from an atomistic model. The computation utilized a cutoff $K_{max} = 4.3\, a_B^{-1}$ on a $45 \times 45$ grid in the 2D BZ. The difference between $\epsilon^{soc}$ and $\epsilon^0$ yields the DMI energy.
Based on Equation (7.1), the $D_y$ values are tabulated in Table (7.8) for various field strengths, in accordance Comparing the $D_y$ component, the electric field induces a

| E-field (V/nm) | −2.75 | 0 | 2.75 | 5.50 |
|---|---|---|---|---|
| $D_y$ (meV$\mu_B^{-2}$) | 0.179 | 0.175 | 0.171 | 0.164 |

Table 7.8.: Within the range of $q \leq (\frac{2\pi}{a})(\frac{1}{64}, \frac{1}{64}, 0)$ along $\overline{\Gamma K}$, the effective component of $\boldsymbol{D}$ is given for BeO/Gr/Co/Pt(111), while considering a magnetic moment of 1.84 $\mu_B$ for Co. This application of electric field leads to a decrease in DMI.

reduction in DMI. The modification of the dipole of the oxide layer by increasing the interlayer distance of Be(I-1)/O(I-1), $d_{Be(I-1)/O(I-1)} = 0.26$, enhances the convergence of both charge density and total energy. However, it The combined effect of applying an electric field and utilizing an oxide capping layer is illustrated in Figure (7.16), depicting a layer-resolved contribution to the DMI. The impact of the electric field is negligible for Co, especially with smaller fields. However, there is an increasing contribution from Pt(I) and Pt(I-2), while Pt(I-1) exhibits a decreasing contribution. These changes result in the overall reduction of DMI. We compare the layer-resolved contribution to the DMI both in the presence and absence of the modification of the BeO dipole, under the influence of an electric field, as shown in Figure (7.17). The dipole modification impacts the contributions from all layers; nevertheless, these alterations tend to compensate for each other.

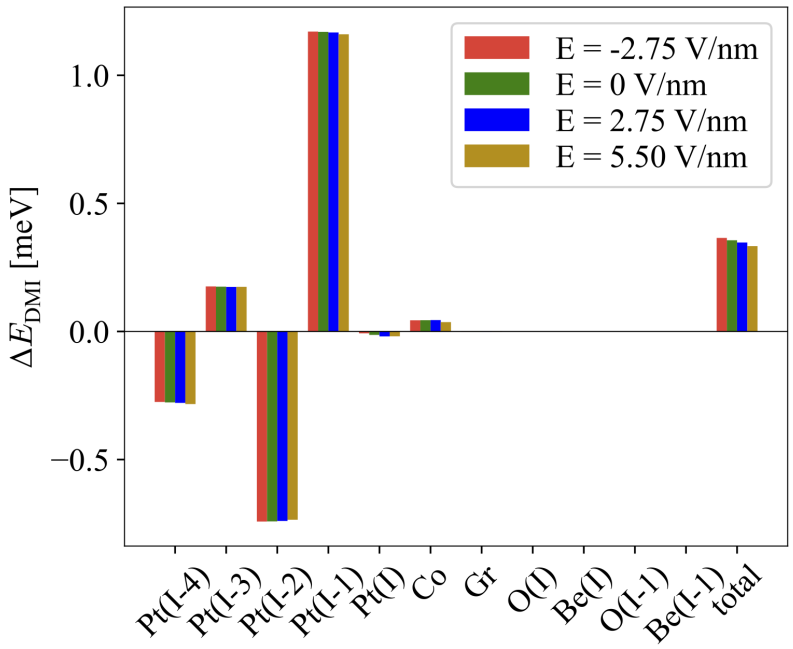



Figure 7.16.: Layer-resolved contributions to the DMI are shown. It is apparent that the application of an electric field on BeO/Gr(top-fcc)/Co/Pt causes diminishing DMI.

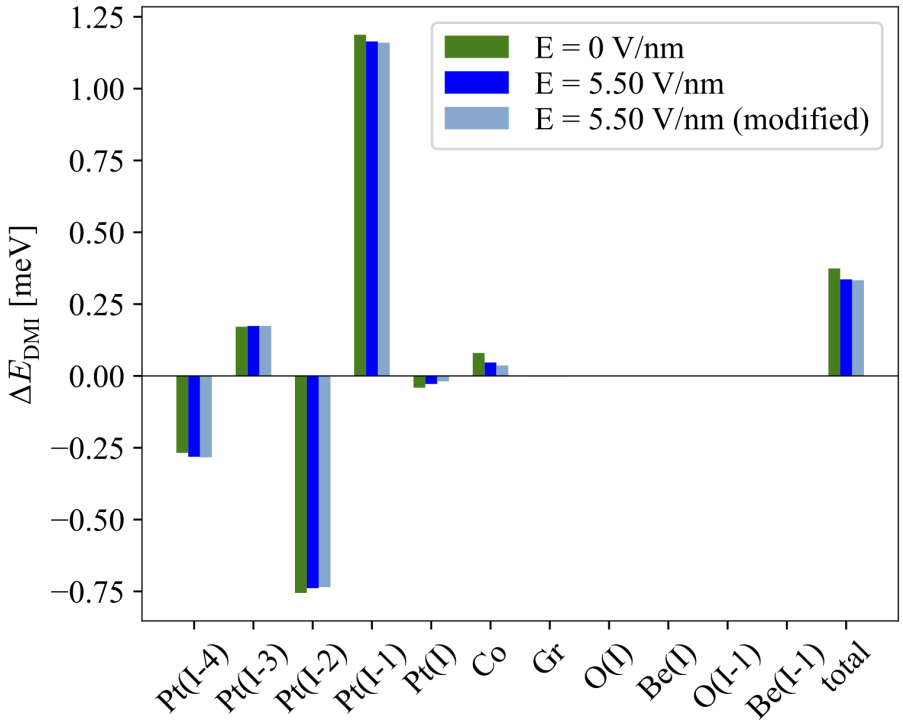



Figure 7.17.: Layer-resolved contributions to the DMI are shown. The alteration in the total DMI remains consistent. The modified heterostructure undergoes an expansion of the $d_{\mathrm{Be(I-1)/O(I-1)}}$ distance.

The ratio of DMI change to the applied electric field (E) is defined as:

$$\beta' = \frac{\Delta E_{\mathrm{DMI}}[\mathrm{meV}]}{\mathrm{E}[\mathrm{V/nm}]}. \tag{7.7}$$

The table presents the ratios (7.9). The correlation between DMI and the electric field

| ML | $\beta'$(fJ·m/V) |
|---|---|
| Gr(top-fcc)/Co/Pt | −15.4 |
| BeO/Gr(top-fcc)/Co/Pt | −8.8 |

Table 7.9.: $\beta'$ is derived from fit up to $q \leq (\frac{2\pi}{a})(\frac{1}{64}, \frac{1}{64}, 0)$ along $\overline{\Gamma\mathrm{K}}$. This ratio represents the change of DMI as a function of applied electric fields.

is also depicted in Figure (7.18). When an electric field is applied in conjunction with

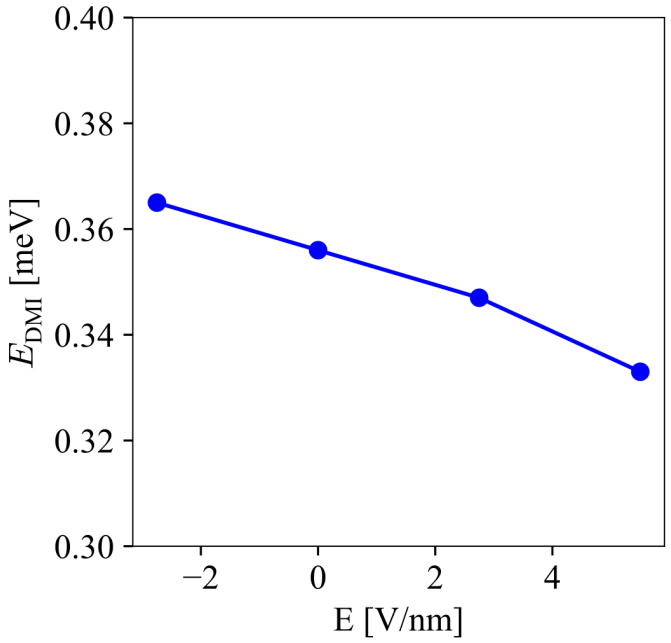



Figure 7.18.: The relationship between the DMI and the applied electric field is illustrated for the BeO/Gr(top-fcc)/Co/Pt(111) system. Similarly to Gr(top-fcc)/Co/Pt(111), shown in Figure (7.6), a reduction in DMI is observed.

an oxide capping layer, a reduction in DMI is observed. However, the magnitude of this reduction is weaker than the reduction observed in the absence of an oxide layer.

# 8 Evolution of material composition

**Contents**


8.1. Heavy metal capping layer . . . . . 108
8.1.1. Structural optimization . . . . . 108
8.1.2. DMI . . . . . 111
8.1.3. MCA . . . . . 115
8.2. Co/Pt multilayered films . . . . . 118
8.2.1. Structural optimization . . . . . 118
8.2.2. DMI . . . . . 121
8.2.3. MCA . . . . . 123


Research has shown that the Dzyaloshinskii-Moriya interaction (DMI) exhibits extreme sensitivity to interface quality [162]. Similarly, the strength of the magnetic anisotropy (MA) is sensitive to the flatness and intermixing of interfaces [163, 26]. Also, the strong perpendicular magnetic anisotropy (PMA) observed in $[NM/Co]_n$ structures is attributed to interface effects [164, 165, 166].
Different studies indicate that sandwiching the FM layer between NM layers can lead to enhanced DMI through additive induction [167, 129, 38]. In such systems, where various interfaces collectively contribute to the overall DMI, isolating the effects of each interface experimentally exhibits significant challenges. Hence, ab initio techniques like DFT play a pivotal role in unraveling the impact of interfaces in the DMI within multilayered systems [168]. A key aspect in handling large PMA systems involving 3*d* transition metals lies in understanding and controlling the spin-orbit coupling (SOC) at the interfaces and surfaces [169].
In this chapter, we are going to explore the impact of heavy metal (HM) capping layers on both DMI and magnetocrystalline anisotropy (MCA). Additionally, we will investigate Co-based multilayered films, where one Co layer is sandwiched between two HMs and the other is coated with graphene (Gr), to assess the potential for additive interfacial DMIs.

## 8.1 Heavy metal capping layer

This study aims to investigate the structural and magnetic properties by incorporating HMs on Gr/Co/Pt(111). For this purpose, we have selected Ir and Pt. Moreover, it has been noted that there is charge displacement upon the formation of the Gr/Pt(111) interface [19], resulting in an enhancement of the DMI. Well-optimized structures are hence prerequisites for the determination of both $\Delta E_{\mathrm{DMI}}$ and $\Delta E_{\mathrm{MCA}}$ within DFT calculations.

### 8.1.1 Structural optimization

To investigate the impact of HM monolayers, 1 ML of Ir(Pt) is placed onto the Gr/Co/Pt(111) substrate. Considering HM on top of Gr(top-fcc)/Co/Pt, we examine three unique stacking configurations for the HM layer on Gr. These configurations are illustrated in Figure (8.1). The described configurations illustrate the

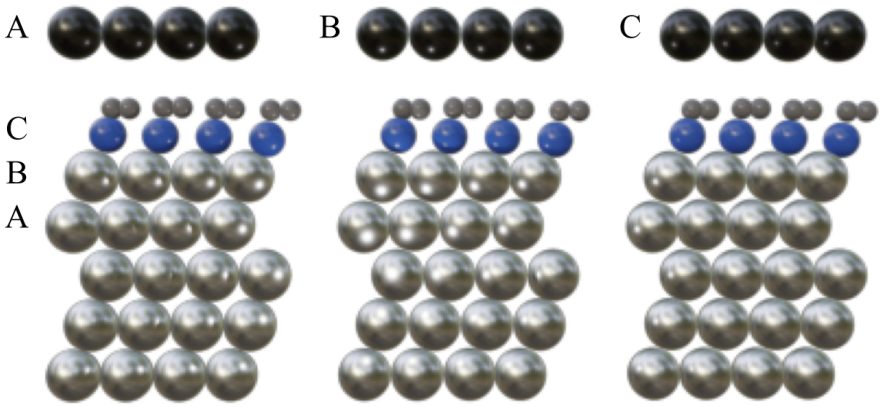



Figure 8.1.: A lateral depiction illustrates three distinct stacking arrangements of Ir on Gr(top-fcc)/Co/Pt(111). Notably, Ir displays variability in its sequence orders when deposited onto Gr(top-fcc)/Co/Pt(111). These sequences are denoted as A, B, and C, corresponding to the fcc stacking of Co/Pt(111). In the case involving a Pt overlayer, we replace the Ir layer with Pt.

arrangements of Ir(Pt) on Gr atop 1ML Co/5ML Pt substrate, along the (111)-plane in a fcc stacking.
We utilized the FLAPW method within PBE approximation to optimize the structures, implemented in the FLEUR-code [55, 56]. Our calculations employed a cutoff parameter of $K_{max} = 4.0\, a_B$ and included 21 $k$-points (within the p3m1 symmetry class) in the 2D IBZ. Structural optimizations were performed until the forces converged to a 0.05 eV/Å threshold for all studied configurations. In our analysis of

these systems, we maintained a consistent in-plane lattice constant of Pt at 2.76 Å throughout all configurations. This standardization facilitates comparison among the systems under study. It has been shown that the adsorption of Gr on Pt(111) is characterized by weak bonding interactions. Hence, we included the vdW-D3 correction [159], implemented in the FLEUR code. The interlayer distances in the relaxed structures are summarized in Table (8.1). In all these structures, Gr is posi-

| HM | Pt | | | Ir | | | - |
|---|---|---|---|---|---|---|---|
| HM/Gr stacking | A | B | C | A | B | C | - |
| $d_{\mathrm{HM/C(I-1)}}$ | 3.36 | 3.36 | 3.34 | 3.20 | 3.42 | 3.18 | - |
| $d_{\mathrm{C(I-1)/C(I)}}$ | 0.01 | 0.01 | 0.03 | −0.02 | 0.02 | 0.05 | 0.02 |
| $d_{\mathrm{C(I)/Co}}$ | 1.95 | 1.94 | 1.93 | 1.98 | 1.93 | 1.92 | 1.96 |
| $d_{\mathrm{Co/Pt(I)}}$ | 2.02 | 2.02 | 2.02 | 2.03 | 2.02 | 2.03 | 2.04 |
| $d_{\mathrm{Pt(I)/Pt(I-1)}}$ | 2.33 | 2.34 | 2.34 | 2.36 | 2.34 | 2.36 | 2.37 |
| $d_{\mathrm{Pt(I-1)/Pt(I-2)}}$ | 2.33 | 2.32 | 2.33 | 2.33 | 2.32 | 2.34 | 2.33 |
| $d_{\mathrm{Pt(I-2)/Pt(I-3)}}$ | 2.32 | 2.32 | 2.32 | 2.33 | 2.33 | 2.33 | 2.32 |
| $d_{\mathrm{Pt(I-3)/Pt(I-4)}}$ | 2.37 | 2.36 | 2.36 | 2.36 | 2.35 | 2.36 | 2.35 |

Table 8.1.: This table presents the interlayer distances ($d$) for various stacking configurations of a heavy metal (HM) overlayer on Gr(top-fcc)/Co/Pt(111), considering both Pt and Ir as HMs. The last column shows the interlayer distances for Gr(top-fcc)/Co/Pt(111) without an additional HM layer. All distances are measured in Å.

tioned in a top-fcc configuration on Co/Pt(111). The main difference among these configurations arises from variations within the interface of the Gr layer and HMs, particularly the B stacking of Ir on Gr. Additionally, the HM capping layer impacts the arrangement of C(I-1)/C(I) and the interlayer distances of Co/Pt(I) as well as Pt(I)/Pt(I-1). These fluctuations in interlayer distances are negligible towards the bottom of the film.
The Table (8.2) illustrates the total energy differences among the various stacking configurations of HM/Gr for both Pt and Ir, presented separately. According to the total energy results, the C stacking of Pt and the A stacking of Ir are the most stable configurations. The energy difference between the other stackings of Ir on Gr(top-fcc)/Co/Pt(111) compared to the most stable one is five times greater than that of the Pt capping layer. Based on study [19], it has been observed that doping Gr on Pt leads to $p$-type doping. The bandstructure analysis depicted in Figure (8.2) illustrates the adsorption of Pt(Ir). An upward shift indicates that electrons are donated by the capping HM to Gr, resulting in $n$-type doping, while a downward shift

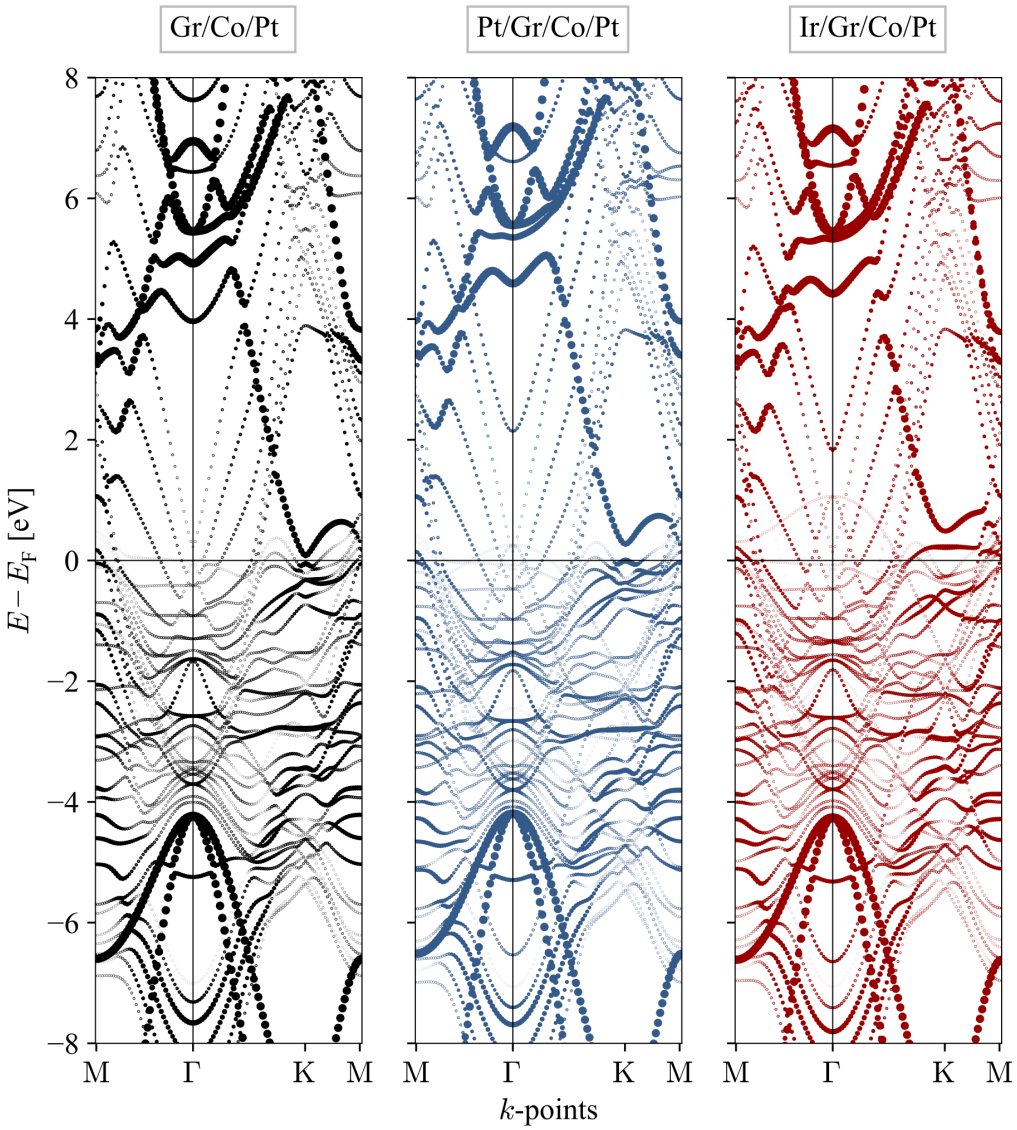



Figure 8.2.: The figure illustrates the orbital weight of Gr within the bandstructure for an HM overlayer on Gr(top-fcc)/Co/Pt(111). We consider the most stable configurations, denoted as C for Pt and A for Ir. The Dirac point aligns with the crossing of the $p_z$ bands of Gr at K.

| HM | Pt | | | Ir | | |
|---|---|---|---|---|---|---|
| HM/Gr stacking | A | B | C | A | B | C |
| Total energy (meV) | 7.30 | 8.84 | 0.00 | 0.00 | 41.18 | 41.89 |

Table 8.2.: The total energies for the three distinct stackings of HM are presented. Notably, the C stacking of Pt and the A stacking of Ir emerge as the most stable configurations.

suggests that holes are donated, leading to $p$-type doping of Gr. In the Gr/Co/Pt structure, Gr chemisorbs with Co, leading to the emergence of a gap at the K point in all these films. Remarkably, the presence of a Pt overlayer induces an upward shift in the upper band, while the inclusion of an Ir overlayer causes an upward shift of the gap at the K point. This observation suggests a stronger electron transfer within the Gr/Ir interface.
In the following analysis, we explore the DMI for the optimized configurations of Pt and Ir on Gr(top-fcc)/Co/Pt(111). We then discuss their respective impacts on enhancing DMI.

### 8.1.2 DMI

In Pt/Co/Ir(111) configurations, DMI at the Co/Ir and Co/Pt interfaces collectively contributes to an amplified total DMI. This enhancement occurs when Co is intercalated between two heavy metals, Pt and Ir, within a multilayer configuration [170]. This phenomenon is commonly referred to as additive DMI. The use of two DMI-active layers opens the way for enhancing the DMI in multilayer structures designed for domain walls and skyrmion racetrack memories [38]. Experimental measurements have determined that the insertion of a thin Ir layer at the top Co/Pt interface leads to a reversal of the effective DMI. This reversal continuously changes the domain wall structure from a right-handed to a left-handed Nëel wall. Comparing this configuration with an epitaxial Pt/Co/Pt multilayer has provided further insights into the origin of DMI in polycrystalline Pt/Co/Pt films, highlighting the exquisite sensitivity to atomic structure details at the film interfaces. Consequently, this approach offers an efficient method for tuning and enhancing DMI in thin magnetic films [129].
First-principles calculations are employed to investigate the impact of a heavy metal layer capping layer on Gr/Co/Pt(111) on the DMI. Similar to previous studies on DMI in Chapter (5), starting from the discrete atomistic limit and considering a flat spin-spiral while restricting the rotation of both $\boldsymbol{S}_i$ and $\boldsymbol{S}_j$ exclusively to the $xz$-plane, the DMI can be expressed as:

$$E_{\mathrm{DMI}}(\boldsymbol{q}) = 2S^2 D_y \sin(\phi_{ij})(1 + 2\cos(\phi_{ij})), \tag{8.1}$$

where $\phi_{ij} = \boldsymbol{q}.(\boldsymbol{R}_j - \boldsymbol{R}_i) = \frac{2\pi}{N}$. $D_y$ is interpreted as an effective parameter derived from fitting to a 2D model that incorporates nearest-neighbor interactions within a hexagonal lattice, as detailed in Section (5.4). Employing the generalized Bloch theorem, the DMI energy for spin-spirals with q-vectors close to the Γ-point is calculated and depicted in Figure (8.3). Examining the impact of HMs on Co, we observed an increase in the contribution of Co. However, the sign of the Co-contribution is opposite for Ir and Pt. This change in chirality is also evident in Pt(I) when Pt serves as the capping layer. Subsequently, concentrating on the first calculated $q$-point along $\overline{\Gamma K}$ ($q \leq \frac{2}{64}(2\pi/a)$), we examined the layer-resolved DMI for these films, in Figure (8.4). As compared to Gr/Co/Pt(111), the DMI is enhanced by both Pt and Ir. In the case of Ir, this increase is primarily due to the contribution of Ir, while for Pt, it arises from the combination of contributions of the Pt-capping layer and Co. The contribution of Co increases in both structures, exhibiting opposite chirality for Pt capping. The magnitude of the Pt(I) contribution remains nearly constant despite the change in chirality, compared to the Gr(top-fcc)/Co/Pt(111) film.
Using Equation (8.1), in Table (8.3), we conduct a comparison of the effective $\boldsymbol{D}$ for all these structures, considering the threshold $q \leq (\frac{1}{64}, \frac{1}{64}, 0)(2\pi/a)$ along $\overline{\Gamma K}$. The

| ML | $D_y$ |
|---|---|
| Gr/Co/Pt | 0.15 |
| Pt/Gr/Co/Pt | 0.25 |
| Ir/Gr/Co/Pt | 0.36 |

Table 8.3.: The effective component of $\boldsymbol{D}$ is determined within the specified range of $(q \leq (\frac{1}{64}, \frac{1}{64}, 0)(2\pi/a))$, $\overline{\Gamma K}$. The resulting values are expressed in meV$\mu_B^{-2}$, considering a magnetic moment of 1.84 $\mu_B$ for Co.

incorporation of an Ir overlayer results in a 140% modification of the DMI, while the incorporation of Pt leads to a 67% increase in DMI. In our analysis, DMI is influenced not only by a single interface. Particularly in the Pt capping layer system, Gr/Co, Pt(I-1)/Pt(I), and Pt(capping layer)/Gr all play roles in the modification of total DMI.
It has been demonstrated that the total DMI nearly doubles from Co/Ir(111) to Pt/Co/Ir(111); however, in the latter case, the DMI is predominantly due to Pt with only a minor contribution from Ir. Also, a simple additive effect, where both interfaces contribute significantly to the total DMI, is not observed when one atomic Co layer is sandwiched between Ir and Pt.
Given the significant contribution of the bottom layers to DMI, we decided to examine the magnetic moment (MM) to ensure convergence. Due to the smaller $d_{Gr/Ir}$, the significant increase in the induced MM of Ir in the C stacking, compared to the A stacking of the Pt capping layer, as illustrated in Table (8.1), emphasizes its

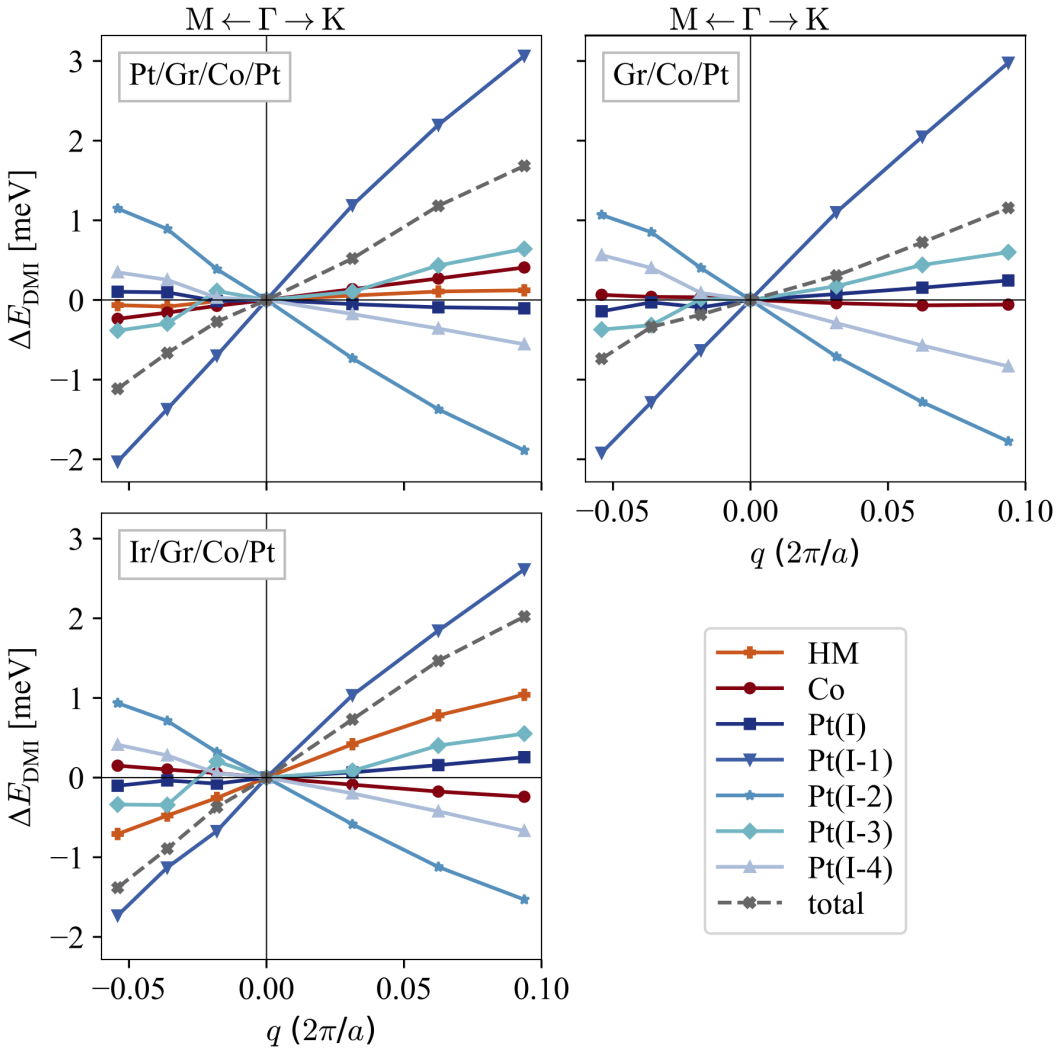



Figure 8.3.: The computation of DMI energy around the Γ-point emphasizes left-handed spirals rotating within the $xz$-plane. Each plot represents the DMI for the optimized stacking of HMs on Gr(top-fcc)/Co/Pt(111), denoted as C for Pt and A for Ir. Upon comparing the dashed lines, which represent the total DMI, it is evident that covering the film with an HM layer increases the total DMI.

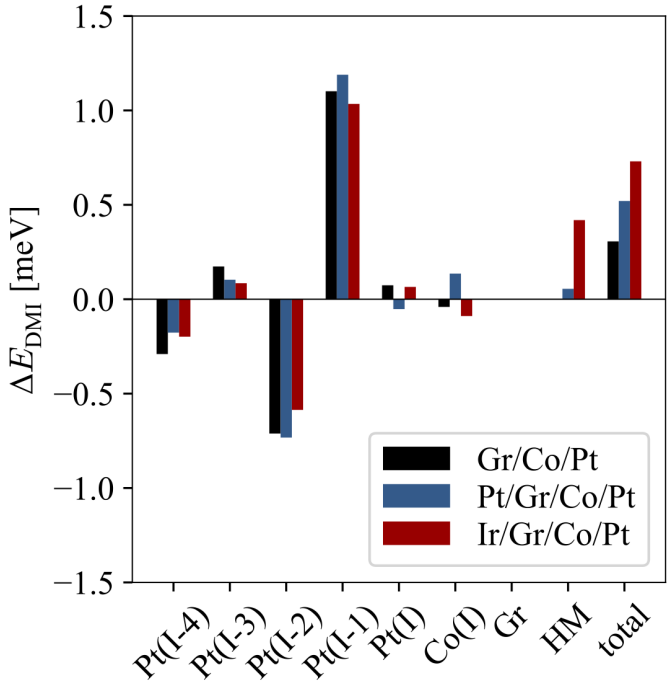



Figure 8.4.: The element-resolved DMI contribution at $q = (\frac{1}{64}, \frac{1}{64}, 0)(2\pi/a)$ is depicted. Both Pt and Ir result in an enhancement of DMI.

| MM | Gr/Co/Pt | Pt/Gr/Co/Pt | Ir/Gr/Co/Pt |
|---|---|---|---|
| HM | - | 0.05 | −0.90 |
| C(I-1) | −0.03 | −0.02 | −0.03 |
| C(I) | 0.01 | 0.01 | 0.01 |
| Co | 1.67 | 1.69 | 1.55 |
| Pt(I) | 0.35 | 0.35 | 0.33 |
| Pt(I-1) | 0.14 | 0.13 | 0.13 |
| Pt(I-2) | 0.10 | 0.08 | 0.08 |
| Pt(I-3) | 0.08 | 0.06 | 0.06 |
| Pt(I-4) | 0.06 | 0.05 | 0.04 |

Table 8.4.: The magnetic moment (MM) of Pt(Ir), Co, and the Pt are represented in $\mu_{\mathrm{B}}$. The magnetic moment converges throughout all films.

notable contribution to DMI. However, with increasing distance from Co, the MM approaches convergence. Therefore, we can conclude that the contributions from the lower layers diminish and compensate for each other. This conclusion can be affirmed by examining the element-resolved contributions in Table (8.5).

| $\Delta E_{\mathrm{DMI}}$ | Gr/Co/Pt | Pt/Gr/Co/Pt | Ir/Gr/Co/Pt |
|---|---|---|---|
| total | 0.30 | 0.52 | 0.73 |
| HM | - | 0.05 | 0.41 |
| Co | −0.04 | 0.13 | −0.08 |
| Pt(I) | 0.07 | −0.05 | 0.06 |
| Pt(I-1) | 1.10 | 1.18 | 1.03 |
| Pt(I-2) | −0.71 | −0.73 | −0.58 |
| Pt(I-3) | 0.17 | 0.10 | 0.08 |
| Pt(I-4) | −0.29 | −0.17 | −0.19 |

Table 8.5.: The element-resolved contributions to DMI, illustrated in Figure (8.4), are displayed. The contributions of graphene are negligible. All energies are in meV.

### 8.1.3 MCA

Experimental results confirm the emergence of a giant PMA in Ir/Co/Pt multilayers [32]. Including a metal capping layer can potentially influence MCA. Hence, we analyzed this effect using self-consistent calculations. The SOC is integrated within a self-consistent collinear calculation.
To ensure accurate values for the MCA, we attained convergence for this quantity with a cutoff parameter of $\mathrm{K_{max}} = 4.0\, a_{\mathrm{B}}^{-1}$ within 2025 $k$-points across the entire hexagonal BZ. MCA is defined by

$$\Delta E_{\mathrm{MCA}} = E_{\mathrm{tot}}^{\parallel} - E_{\mathrm{tot}}^{\perp}. \tag{8.2}$$

The computations were conducted fully self-consistently for spins aligned along the in-plane ($E_{\mathrm{tot}}^{\parallel}$) and out-of-plane ($E_{\mathrm{tot}}^{\perp}$) axes. Similar to the DMI calculations, we exclusively focused on the optimized structure, which consists of C stacking for Pt and A stacking for Ir on Gr(top-fcc)/Co/Pt. The results are presented in Table (8.6). It is evident that the Ir overlayer caused nearly a 6-fold modification in $\Delta E_{\mathrm{MCA}}$, resulting in an in-plane orientation. While $\Delta E_{\mathrm{MCA}}$ is reduced by 10% by integrating the Pt capping layer, remaining in an out-of-plane orientation. In another study, it

| ML | Gr/Co/Pt | Pt/Gr/Co/Pt | Ir/Gr/Co/Pt |
|---|---|---|---|
| $\Delta E_{\mathrm{MCA}}$ | 2.38 | 2.15 | −14.28 |

Table 8.6.: $\Delta E_{\mathrm{MCA}}$ is shown for Gr(Top-fcc)/Co/Pt and Pt(Ir)/Gr(Top-fcc)/Co/Pt. For both capping layers, we considered their respective optimized stacking sequences, with A for Ir and C for Pt. Positive energy values correspond to the out-of-plane MCA. All energies are in meV.

is demonstrated that MCA has increased by 30% in the Co/Ir(111) system with the inclusion of a Pt overlayer. However, despite this increase, the orientation of the MCA remained out-of-plane [171].
To investigate the contribution of each layer to MCA, a detailed analysis of the element-resolved MCA can provide further insights. We utilized the force theorem approach to compute both MCA values and individual atomic contributions to MCA [136]. The change in total energy is predominantly determined by variations in the sum of occupied single-particle energies in the first variation. In this scheme, a collinear calculation neglecting SOC is done. Subsequently, SOC is treated in a non-self-consistent manner for both in-plane and out-of-plane orientations, following the self-consistent solution of the Kohn-Sham equation. MCA energy can be written as

$$E - E_0 \approx \sum_{\nu}^{\mathrm{occ.}} \mathcal{E}_{\mathrm{ft},\nu} - \sum_{\nu}^{\mathrm{occ.}} \mathcal{E}_{0,\nu}. \tag{8.3}$$

The eigenvalues are derived from $\mathcal{H}_0 + \mathcal{H}_{\mathrm{SOC}}$. Using Equation (8.3), the element-resolved MCA is depicted in Figure (8.5). Analyzing MCA using the force theorem reveals that Ir plays a decisive role in the large MCA and causes the in-plane orientation. Meanwhile, Pt(I) and Pt(I-1) contribute to the MCA in Pt/Gr/Co/Pt. It can be concluded that the elemental behavior in MCA for Pt/Gr/Co/Pt is very similar to Gr/Co/Pt. However, this approach fails to explain the interfacial additive effect in MCA. To provide further insight into the induced magnetic field and its effects on the capping layer, we compute the induced MM as well as orbital MM separately for the out-of-plane and in-plane orientations. The results are presented in Table (8.7). Upon comparing the results for Pt and Ir capping layers, it becomes

| HM | $\mathrm{MM}^{\parallel}$ | $\mathrm{MM}^{\perp}$ | orbital $\mathrm{MM}^{\parallel}$ | orbital $\mathrm{MM}^{\perp}$ |
|---|---|---|---|---|
| Pt | 0.00 | 0.05 | 0.00 | 0.03 |
| Ir | −0.41 | −0.55 | −0.02 | −0.36 |

Table 8.7.: Spin magnetic moment (MM) and orbital MM are displayed for both out-of-plane and in-plane orientation. All values are in $\mu_{\mathrm{B}}$. $\mathrm{MM}^{\parallel}$ and $\mathrm{MM}^{\perp}$ indicate out-of-plane and on-plane directions, respectively.

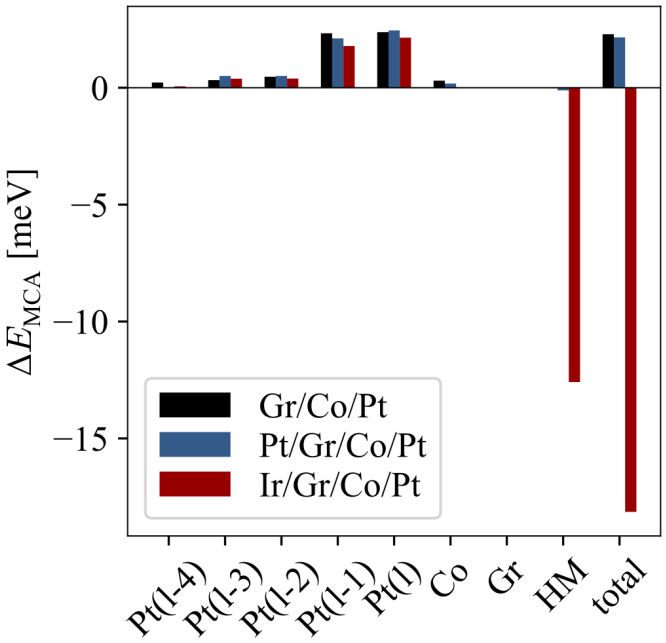



Figure 8.5.: MCA analysis using the Force Theorem, presenting various atomic contributions. The "total" corresponds to the contributions of SOC from all layers. The Ir capping layer significantly leads to the large in-plane MCA.

evident that Ir exhibits a significant induced orbital magnetic moment.
In the following, our focus will shift to the Co/Pt multilayer system and the impact of Gr on both DMI and MCA.

## 8.2 Co/Pt multilayered films

The [Pt/Co] multilayer system is one of the most popular multilayer systems exhibiting a strong PMA [172, 173]. An investigation using a model system comprising a trilayer structure of [Pt/Co/Pt] has shown a comprehensive understanding of the roles played by the Pt/Co and Co/Pt interfaces in influencing the PMA strength [174]. Besides, Experimental findings have concluded that Co induces magnetic polarization in Pt, leading to out-of-plane ferromagnetic behavior in the Pt/Co bilayer [171].
Investigating the influence of Gr on the electronic and magnetic characteristics of Co/Pt multilayers, here particularly Gr/Co/Pt/Co/Pt, we conducted comparisons of the DMI and MCA in the absence and presence of Gr.

### 8.2.1 Structural optimization

Considering the influence of Gr on [Co/Pt] multilayers, we apply Gr coating to the structure consisting of 1ML Co/1ML Pt/1ML Co/4ML Pt. Assuming a constant in-plane lattice parameter for Pt in this configuration, $a_{\mathrm{Pt}}$ = 2.75 Å, we proceed with the analysis similar to that outlined in Chapter 5. In this study, we consider that Gr may have three possible stacking configurations, all of which could be realized in a Moiré lattice, given that Gr possesses a smaller lattice constant compared to Pt. Figure (8.6) depicts these three different stacking configurations of Gr on 1ML Co/1ML Pt/1ML Co/4ML Pt along [111]-direction in an fcc stacking. To refine the stacking arrangements, we employed again DFT calculation using FLEUR-code [56, 55]. Our approach utilized a $\mathrm{K_{max}}$ cutoff of $4.0 a_B^{-1}$ and incorporated 21 $k$-points within the irreducible BZ, exploiting the P3m1 symmetry class. Structural optimizations were conducted until the forces reached convergence with a threshold set at 0.05 eV/Å. The interlayer distances in the relaxed structures are summarized in Table (8.8). The distances between Gr and Co(I) in both top-fcc and top-hcp stackings are highly similar. Generally, the introduction of Gr doping tends to result in small or negligible distance changes between all layers. We present the energy differences between these stacking configurations in the Table (8.9). It's evident that the top-fcc configuration stands out as the most stable arrangement of Gr on Co/Pt/Co/Pt(111). Similar to Gr/Co/Pt(111), the top-hcp configuration is notably close to the top-fcc arrangement.
To delve deeper into the alterations in the interlayer distances of the underlying layers, we investigate the convergence of the magnetic MM in the top-fcc configuration of Gr on Co/Pt/Co/Pt. Consequently, we present the induced MM in Table (8.10). The induced MM experiences a complete decay, as presented in Table (8.10). Prior to Gr doping, the Co(I) layer exhibits a larger MM relative to the Co(I-1) layer

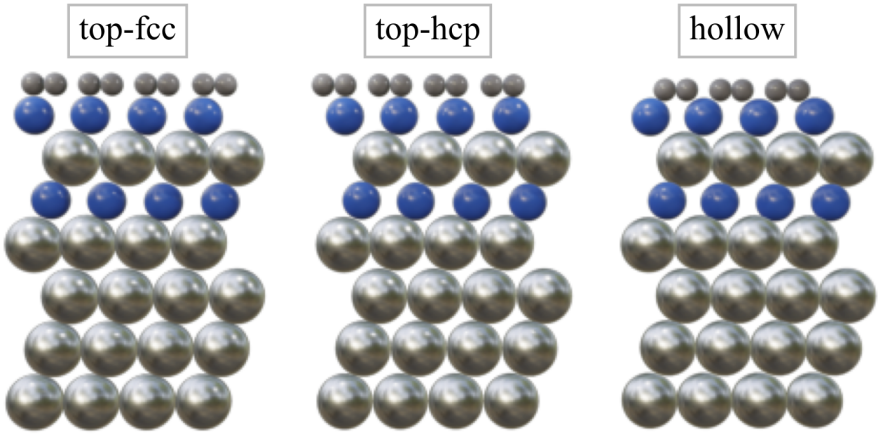



Figure 8.6.: Lateral view illustrating various stacking arrangements of Gr Co/Pt/Co/Pt(111).

| ML | Gr/Co/Pt/Co/Pt | | | Co/Pt/Co/Pt |
|---|---|---|---|---|
| Gr/Co(I) stacking | top-fcc | top-hcp | hollow | - |
| $d_{C(I-1)/C(I)}$ | 0.02 | 0.02 | 0 | - |
| $d_{C(I)/Co(I)}$ | 1.92 | 1.93 | 1.78 | - |
| $d_{Co(I)/Pt(I)}$ | 2.07 | 2.08 | 2.10 | 2.08 |
| $d_{Pt(I)/Co(I-1)}$ | 2.11 | 2.10 | 2.11 | 2.14 |
| $d_{Co(I-1)/Pt(I-1)}$ | 2.03 | 2.03 | 2.05 | 2.05 |
| $d_{Pt(I-1)/Pt(I-2)}$ | 2.36 | 2.36 | 2.38 | 2.40 |
| $d_{Pt(I-2)/Pt(I-3)}$ | 2.34 | 2.34 | 2.34 | 2.38 |
| $d_{Pt(I-3)/Pt(I-4)}$ | 2.36 | 2.36 | 2.36 | 2.39 |

Table 8.8.: Interlayer distances ($d$) exhibit variation across different stacking configurations of Gr on 1ML Co/1ML Pt/1ML Co/4ML Pt(111), which include top-fcc, top-hcp, and hollow arrangements. The last column displays the interlayer distances of 1ML Co/1ML Pt/1ML Co/4ML Pt along fcc(111). All distances are measured in Å.

| ML | Gr/Co/Pt/Co/Pt | | |
|---|---|---|---|
| Gr/Co(I) stacking | top-fcc | top-hcp | hollow |
| Total energy (eV) | 0 | 0.08 | 0.66 |

Table 8.9.: The total energies for the three distinct stackings of Gr on Co/Pt/Co/Pt are presented. The top-fcc stacking emerges as the most stable configuration.

| MM | Co/Pt/Co/Pt(111) | Gr(top-fcc)/Co/Pt/Co/Pt(111) |
|---|---|---|
| Co(I) | 2.01 | 1.57 |
| Pt(I) | 0.36 | 0.33 |
| Co(I-1) | 1.98 | 1.98 |
| Pt(I-1) | 0.33 | 0.34 |
| Pt(I-2) | 0.13 | 0.12 |
| Pt(I-3) | 0.03 | 0.03 |
| Pt(I-4) | 0.01 | 0.01 |

Table 8.10.: The magnetic moment (MM) of Co and Pt layers are represented in $\mu_B$. The MM converges throughout all films. The diminishing effect of MM at the Gr/Co interface results from Gr doping electrons into Co.

within the Co/Pt/Co/Pt(111) configuration. However, upon depositing Gr, there is a notable reduction in the magnetic moment of the Co(I) layer, while the MM of the Co(I-1) layer remains unchanged.

### 8.2.2 DMI

In thin magnetic films, DMI originates at the interfaces [37]. Therefore, to generate a net DMI effect in Pt/Co/Pt multilayers, the contributions from the top and bottom interfaces should vary. This variation is crucial for inducing and manipulating DMI in such multilayer systems. Experimental investigation has revealed that a similar stack composed of Pt(3 nm)/Co(0.7 nm)/Pt(1 nm) epitaxially exhibits strong DMI. An important insight drawn from the conducted experiment is the noticeable sensitivity of DMI to the atomic-scale details, such as the roughness, degree of intermixing, and density of stacking faults, of the interfacial structure within the multilayers [129].
In our analysis, initially, we examine the interfacial DMI in a 1ML Co/1ML Pt/1ML Co/4ML Pt(111) system using first-principle calculations. Subsequently, we explore the influence of an ML of Gr stacked on top-fcc configuration on this DMI. Similar to the previous analysis, a spin spiral calculation was conducted using a $45 \times 45$ grid within the entire 2D BZ, with a cutoff of $K_{max} = 4.3\, a_B^{-1}$ excluding SOC effects. Utilizing first-order perturbation theory, the inclusion of SOC was addressed based on the generalized Bloch theorem [99]. The distribution of DMI energy around $\Gamma$-point for different $q$-points is depicted in Figure (8.7). It becomes apparent that the contributions from both Co layers decrease in the presence of Gr. The magnitude of Pt(I) is significantly increased. However, the change in chirality of Pt(I) results in a reduction of the total DMI. The reduction in net DMI caused by Gr has also been observed in Gr/Co/Pt(111) [12], as discussed in detail in the Chapter 5. According to Equation (8.1), the effective $\boldsymbol{D}$ for both monolayers can be determined, and is presented in Table (8.11). Gr leads to an almost 50% reduction in total DMI compared

| ML | $D_y$ |
|---|---|
| Co/Pt/Co/Pt | 0.48 |
| Gr(top-fcc)/Co/Pt | 0.15 |
| Gr(top-fcc)/Co/Pt/Co/Pt | 0.25 |

Table 8.11.: Within the defined range of $q \leq (\frac{1}{64}, \frac{1}{64}, 0)(2\pi/a))$, along the $\overline{\Gamma K}$ direction in Figure (8.7), we calculate the effective component of $\boldsymbol{D}$. These values are presented in units of meV$\mu_B^{-2}$, considering a Co magnetic moment of 1.84 $\mu_B$.

to the Co/Pt multilayer. Given that the effective $\boldsymbol{D}$ for Co/Pt(111) was reported roughly as 0.43 meV$/\mu_B^{-2}$ [119], the impact of Gr on Co/Pt(111) is more significant

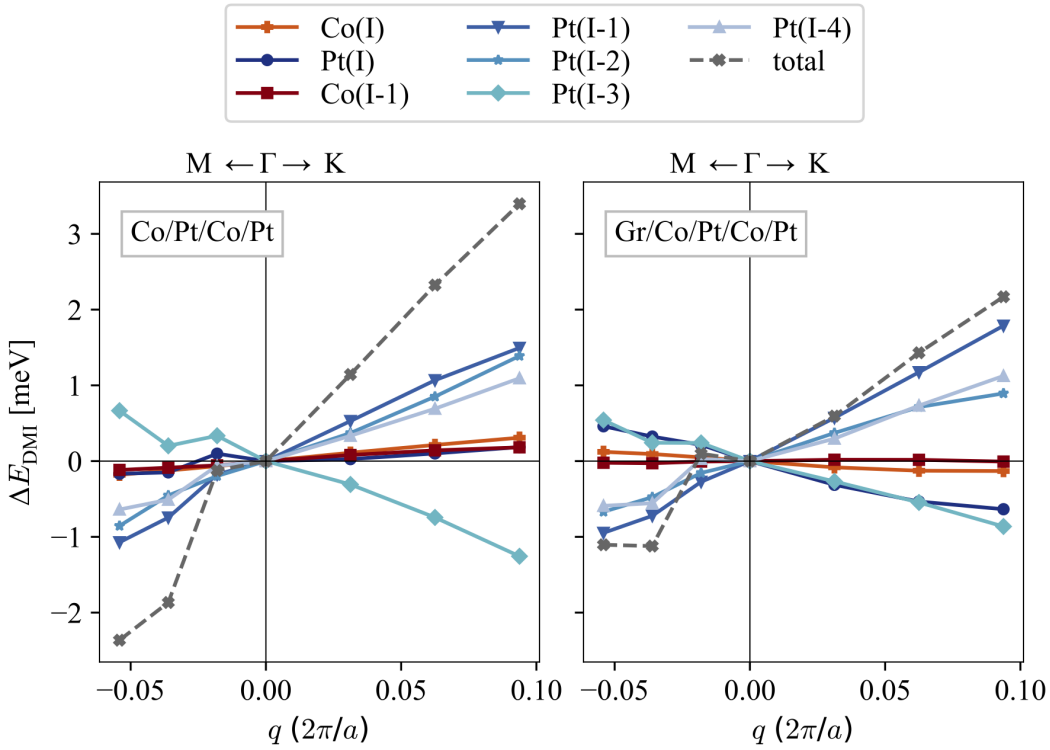



Figure 8.7.: Both plots illustrate the DMI energy near the Γ point, extending along the $\overline{\Gamma K}$ and $\overline{\Gamma M}$ directions, for left-handed spirals rotating in the $xz$-plane. In the left plot, the presence of Pt(I) is overshadowed by Co(I-1), whereas in the right plot, it is outweighed by the contribution of Pt(I-3). The inclusion of Gr results in a decrease in the net DMI.

than on Co/Pt/Co/Pt(111). The maximum value for $D_y$ in Gr/2ML Co/5ML Pt is reported as 0.5 meV/$\mu_B^{-2}$ [131], which is nearly double the value observed in Gr/1ML Co/1ML Pt/1ML Co/4ML Pt and similar to Co/Pt/Co/Pt(111). For the same $\boldsymbol{q}$ (= $(\frac{1}{64}, \frac{1}{64}, 0)(2\pi/a)$), the layer-resolved DMI is depicted in Figure (8.8). After introducing Gr, contributions from Co(I) and Co(I-1) decrease. However, the

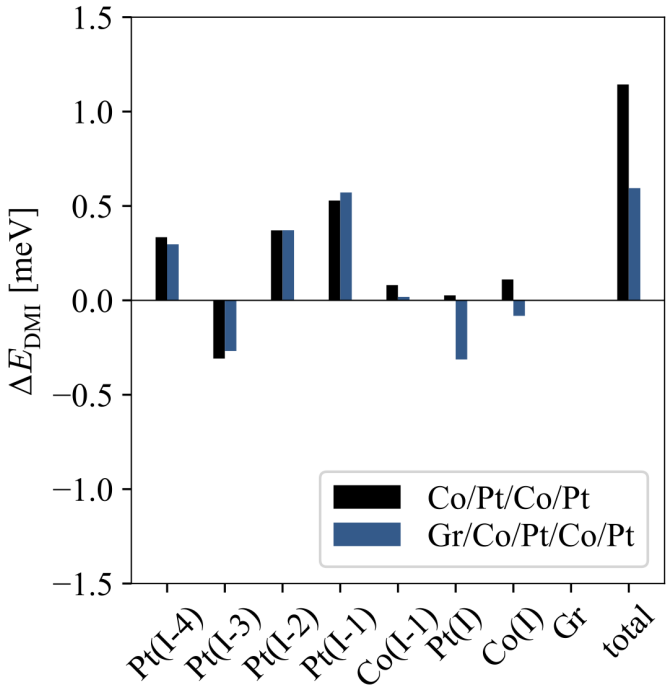



Figure 8.8.: The layer-resolved DMI contribution at $q \leq \frac{2}{64}(2\pi/a)$ is depicted. The alteration in chirality and magnitude of Pt (Ir) plays the most significant role in the decrease of DMI after doping the film with Gr.

sign of Co contribution at the interface with Gr occurs in the opposite direction to the Co(I-1). Meanwhile, the negative contribution from Pt(I) increases, and that leads to a 50% reduction of the DMI. Additionally, there is a slight change in Pt(I-1). Moreover, partial slab decomposition analysis revealed that for the Gr/2ML Co/Pt heterostructure, the contribution of Co/Pt primarily accounts for the DMI. Importantly, the chirality at the Gr/Co interface is opposite and of comparable magnitude to that of Co/Pt(111) [131].

### 8.2.3 MCA

As previously noted, interfaces can significantly influence magnetic anisotropy. The correlation between interface quality and perpendicular PMA strength in [Co/Pt] multilayer systems has been extensively investigated [173, 32, 175].
To further illuminate the MCA, induced by SOC, in the asymmetrical Co/Pt/Co/Pt(111)

multilayer and the influence of Gr on it, we perform a fully self-consistent calculation using a cutoff parameter of $K_{max} = 4.0\, a_B^{-1}$ within 2025 $k$-points sampling the entire hexagonal BZ. Referring to Equation (8.2), we calculated and summarized the values of $\Delta E_{MCA}$ in Table (8.12). The introduction of Gr to Co/Pt/Co/Pt(111) is

| ML | Co/Pt/Co/Pt | Gr/Co/Pt/Co/Pt | Co/Pt[119] | Gr/Co/Pt |
|---|---|---|---|---|
| $\Delta E_{MCA}$(meV) | 1.67 | 1.21 | 1.38 | 2.15 |

Table 8.12.: $\Delta E_{MCA}$ is shown for 1ML Co/1ML Pt/1ML Co/4ML Pt, Gr(top-fcc)/1ML Co/5ML Pt and Gr(top-fcc)/1ML Co/1ML Pt/1ML Co/4ML Pt. Positive energy values correspond to the out-of-plane MCA.

associated with a decrease in the MCA. Interestingly, this contrasts with the effect observed when depositing Gr onto Co/Pt(111), where the MCA exhibits an increase. The force theorem approach is employed to analyze the contribution of each layer in MCA. Referring to Equation (8.3), the change in total energy is determined by the first variation. In this approach, SOC is considered non-self-consistently, but all order perturbations are included. The layer-resolved MCA is depicted in Figure (8.9). Using the force theorem, individual element contributions do not fully explain the total MCA. However, examining the trend reveals that depositing Gr causes a shift in the contribution of Co(I) from in-plane to out-of-plane. Additionally, the contribution of Pt(I) becomes stronger.

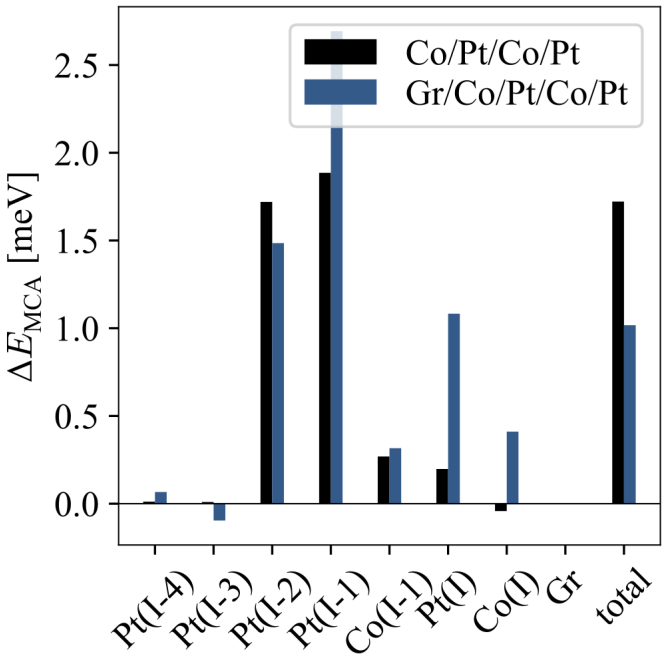



Figure 8.9.: MCA analysis using the Force Theorem, presenting various atomic contributions. The "total" corresponds to the contributions of SOC from all layers.

# 9 Summary and Conclusions

Density Functional Theory (DFT) is needed to have a good basis for the parameter-free ab-initio method in order to study the magnetism of surfaces, thin films, and systems with reduced symmetry in general, discussed in Chapter 2. Therefore, Chapters 2 and 3 presented a comprehensive review of the DFT and full-potential linearized augmented planewave (FLAPW) method, highlighting its accuracy and uniqueness as a computational tool. This method enabled the determination of ground-state properties in the following, which aligned well with experimental observations. Where available, the FLAPW method serves as a robust tool for exploring non-collinearity in various systems, including bulk materials, magnetic surfaces, thin films, and low-dimensional magnets. To deepen our understanding and connect these calculations to spin interactions, we map them to spin models, as discussed in Chapter 4. This chapter also provides a thorough discussion of spin models to enhance our understanding of the magnetic properties inherent in 2D systems.

In Chapter 5, we conducted an investigation into the impact of graphene (Gr) on an ML of Co supported on a heavy metal (HM) substrate, specifically focusing on Pt(111) and Ir(111). The significant difference in lattice constants between Gr and the Co/HM structure leads to the formation of a Moiré lattice. This lattice mismatch results in different stacking configurations of Gr on the Co/HM substrate represented by: top-fcc, top-hcp, and hollow sites.

Our investigation indicates profound alterations in the electronic properties of the Gr/Co interface with adsorption, notably manifesting in the emergence of a gapped Dirac cone at the K point due to hybridization and charge transfer effects. Moreover, the chemisorption of Gr onto Co results in a decrease in the Heisenberg parameters and spin stiffness compared to Co/Pt(111). Furthermore, doping Gr transfers electrons from Co to Gr, amplifying the magnetic crystalline anisotropy (MCA) of the magnetic layer twofold. We ascertained that the DMI orientation at the Gr/Co interface is opposite to that observed at the Co/HM interface, consistent with experimental findings [12]. Various stacking configurations of Gr on Co/HM

influence distinct magnitudes and orientations of the total DMI vector. By analyzing the $\boldsymbol{k}$-resolved DMI across the BZ for different stackings of Gr/Co/Pt, near the Fermi level, a concentration of DMI changes around the vicinity of the $\Gamma$ point can be observed.
In Chapter 6, we explored the impact of increasing the thickness of Co. This led to an augmentation in the DMI, approaching that of the Co/HM interface. However, with an increased number of Co layers, the induced magnetic moment of the HM did not reach convergence even through 5 ML. Consequently, the bottom layers exerted an influence on the DMI, necessitating 7 ML for Pt(111). This was also used for the Ir(111) substrate. By augmenting the thickness of the HM layer, we mitigated the influence of the bottom layers, leading to a larger DMI. In a single-layer Co system, the interface Pt layer, Pt(I), played a decisive role in determining the DMI, a characteristic observed similarly in the case of 3 ML Co for both 5 and 7 layers of Pt(111). Conversely, for Ir, both interface Ir layer, Ir(I), and sub-interface Ir layer, Ir(I-1), contributed significantly to the DMI.
Subsequently, our focus shifted toward finding methods to manipulate DMI and MCA within these heterostructures. Such efforts promise additional flexibility for modern electronics, particularly in the dynamics of magnetic domain walls and the radius of skyrmions. In Chapter 7, we investigated the application of electric fields, which induced similar changes across all stacking configurations of Gr on Co/Pt. The effective $D$ vector experienced a 30% reduction when subjected to an electric field of 5.50 V/nm. We quantified a ratio, denoted as $\beta$ = -15.4 fJ/V·m for DMI and $\gamma$ = 24.9 fJ/V·m for MCA. Experimental results demonstrate varying voltage-induced changes in magnetic anisotropy energy: 13 fJ/V·m for a few monolayers of FeCo [153, 154], 26±6 fJ/V·m for Au/Fe/MgO [155], and 48 fJ/V·m for single-crystalline 5 nm Fe on MgO [156].
Our second strategy involved the implementation of an oxide capping layer, a two-layered BeO, which exerted a modest influence on DMI. Attempting to enhance the effect by modifying the dipole effect, we expanded the distance between $d_{\mathrm{Be(I–1)/O(I–1)}}$, yet this alteration yielded minimal impact, with the primary contribution still originating from the strongly screened Co/Pt interface. Following that, we applied electric fields to Gr/Co/Pt(111) covered by oxide capping layers. The resulting ratio, denoted as $\beta'$, exhibited a substantial reduction, reaching -8.8 fJ/V·m, nearly halving its value of $\beta$ without the capping layer.
In Chapter 8, in another approach, we implemented a capping layer of HMs, specifically choosing again Pt and Ir. Emphasizing the physisorption characteristics of Gr and Pt (Ir), we incorporated van der Waals corrections for the relaxation of the capping layer. This method yielded a remarkable 140% increase in the effective $D$ vector for Ir and a substantial 67% increase for Pt on Gr/Co/Pt(111). Moreover, the MCA increases 6-fold for Ir/Gr/Co/Pt(111). The pronounced effect of Ir on DMI can be attributed to its strong induced spin and orbital moments compared to Pt. This results in an observable upward shift in the gapped Dirac cone at the K point for Ir.
Drawing upon previous reports, indicating that Co/Pt multilayers exhibit perpen-

dicular magnetic anisotropy, we opted to utilize this composition to capitalize on its potential for further enhancements in the Gr/Co/Pt structure. We conducted a comparative analysis between the stacking structure of 1ML Co/1ML Pt/1ML Co/4ML Pt(111) and the Gr top-fcc stacking within this framework. Our findings reveal a notable shift in both the DMI and MCA parameters, with each experiencing a significant reduction by 50% compared to Co/Pt/Co/Pt(111).
In conclusion, this thesis has extensively examined the electronic and magnetic implications of the Gr capping layer on Co/HM(111) systems. Additionally, our research has delved into the modulation of DMI and MCA through various methods. These include the application of electric fields, introducing capping oxide layers, employing HM capping layers, and exploring the influence of [Co/Pt] multilayers.

# List of Figures


3.1. Muffin-Tin spheres and interstitial regions . . . . . 21
3.2. Side view of a slab model used in film calculations, showing a finite-thickness slab (center) separated by two vacuum regions. The blue spheres represent atoms in the slab, and the dashed box indicates the unit cell. . . . . 25
3.3. Slab geometry with vacuum regions and corresponding external potential profile . . . . . 26
3.4. Visualizing non-collinear magnetization density . . . . . 29
3.5. Spin-spiral . . . . . 32

4.1. $J_1$ is counted as the first-neighbour exchange parameter and $J_2$ and $J_3$ are the second- and third-exchange terms. . . . . 37
4.2. Dzyalonshinskii-Moriya interaction (DMI) is an asymmetric interaction that is observed in thin films with strong spin-orbit coupling (SOC) and symmetry breaking. . . . . 38

5.1. Within the formation of moiré configurations, three distinct arrangements of Gr($10 \times 10$) on Co/Pt(111)($9 \times 9$) can be observed: top-hcp (green), top-fcc (red), and hollow (blue) sites. . . . . 43
5.2. A lateral depiction showcases three potential stacking configurations of Gr atop Co/Pt(111). Gr on Co/Ir(111) is essentially identical to the Gr on Co/Pt(111) where Pt is substituted with adjacent metal, Ir. . . 44
5.3. The self-consistently calculated total energies as a function of the spin-spiral $q$-vectors along the high symmetry path are depicted by blue dots. Subsequently, these energies are mapped within the framework of the Heisenberg model to extract the exchange interactions, $(J(\boldsymbol{q}))$. . . . . 48

5.4. The figure illustrates the orbital weight of Gr in the bandstructure of Gr/Co/Pt(111). Here, $d_{\mathrm{Gr-Co}}$ denotes the interlayer distance of Gr on Co. Only the top-fcc stacking of Gr on Co is considered in all three cases. By decreasing $d_{\mathrm{Gr/Co}}$, we show the effect of the chemisorption of Gr on Co. As Gr is positioned further away, the bonding weakens. The Dirac point aligns with the crossing of the $p_z$ bands of Gr at K. . 50
5.5. The impact of Gr coverage on the DMI of various configurations in Co/Pt(111) is illustrated. When we observe the dashed lines depicting the total DMI, a noticeable distinction arises: the top-fcc stacking of Gr demonstrates a different chirality in contrast to the other stacking configurations. . . . . 53
5.6. The diagram illustrates the short-range DMI vectors between the first in-plane Co–Co nearest neighbors. Red arrows indicate the magnetization directions, while black arrows represent the corresponding $D$ vectors. . . . . 54
5.7. Layer-resolved DMI is illustrated. The rotation sense follows Pt(I) contributions. In the case of Ir, Co plays a decisive role in top-fcc stacking, whereas other contributions of Ir influence strongly both top-hcp and hollow stackings. . . . . 55
5.8. The bandstructure is displayed for top-fcc, top-hcp, and hollow configurations, with colors corresponding to the DMI values. The color of the points represents their direction, while the size of the points corresponds to DMI magnitudes. . . . . 57
5.9. The bandstructure plots illustrate top-fcc, top-hcp, and hollow configurations, showcasing Pt(I) contributions to DMI values. Point colors indicate direction, while sizes denote DMI magnitudes. . . . . 58
5.10. The DMI values are plotted as a function of energy, relative to the Fermi levels of each slab calculated without SOC, for the representative point $q = (\frac{2\pi}{a})(\frac{1}{64}, \frac{1}{64}, 0)$ along $\overline{\Gamma\mathrm{K}}$. . . . . 59
5.11. The DMI, computed across the entire BZ, is illustrated, including the total DMI contributions, particularly from the interface Pt. . . . . 61
5.12. Increasing the distance between Gr and Co results in an increase in DMI. Consequently, the contribution of Co is enhanced by the displacement of Gr. Only top-fcc stacking of Gr on Co/Pt(111) is considered. . . . . 62
5.13. Analysis of the MCA using the Force Theorem, showcasing diverse atomic contributions. The "total" denotes the combined contributions of SOC from all layers. . . . . 64
5.14. We examine the MCA using the Force theorem. The MCA displays a decreasing tendency, highlighting a significant connection between the spatial arrangement of Gr and Co and the strength of the MCA. . 65

6.1. A side view presents three potential stacking configurations of Gr atop 3ML Co/5ML Pt(111). For Ir, Pt is substituted by Ir. . . . . 68

6.2. The in-plane spin contributions to the bandstructure orthogonal to the wavevector within the BZ are illustrated: $S_x$ along $\overline{\mathrm{M\Gamma}}$ and $S_y$ along $\overline{\mathrm{\Gamma K}}$. . . . . 71

6.3. The bandstructure for Gr/3ML Co/5ML Pt(111) along $\overline{\mathrm{M\Gamma}}$ (upper panels) $\overline{\mathrm{\Gamma KM}}$ (lower panels) are presented. In the plots on the left-hand side, circle sizes are proportional to the overlap between Gr and Pt at the interface, with blue and red indicating the spin character as given in the right panels. However, on the right-hand side, the in-plane contributions of spin-polarization ($S_x$ (upper), $S_y$ (lower)) are given. . . . . 72

6.4. The bandstructure for Gr/3ML Co/5ML Ir(111) along $\overline{\mathrm{M\Gamma}}$ (upper panels) $\overline{\mathrm{\Gamma KM}}$ (lower panels) are presented. In the plots on the left-hand side, circle sizes are proportional to the overlap between Gr and Ir at the interface, with blue and red indicating the spin character as given in the right panels. However, on the right-hand side, the in-plane contributions of spin-polarization ($S_x$ (upper), $S_y$ (lower)) are given. . . . . 73

6.5. The DMI energy near the Γ point is computed for left-handed spirals rotating in $xz$-plane. The dashed line represents the total DMI for Gr(top-fcc)/1ML Co/5ML Pt(111) heterostructure, exhibiting notably linear behavior, especially within the $q \leq (\frac{3}{64}, \frac{3}{64}, 0)$ range along $\overline{\Gamma K}$. The colored lines illustrate the diverse contributions from individual layers in the DMI. . . . . 75

6.6. The figures illustrate the atomic contributions for two configurations: Gr(top-fcc)/1ML Co/5ML Pt(Ir) on the left and Gr(top-fcc)/3ML Co/5ML Pt(Ir) on the right. The increase in Co thickness predominantly influences the Pt(I) layer, dictating the overall DMI. In contrast, in the case of Gr/3ML Co/Ir, the competition among the Ir layers is the determining factor for DMI. . . . . 76

6.7. A Lateral representation highlights the presence of thicker layers of heavy metals. Gr/3ML Co/7ML Pt (left), Gr/3ML Co/7ML Ir (center), and Gr/3ML Co/10ML Ir (right). Gr is positioned in a top-fcc configuration on the 3ML Co/HM(111) substrate. . . . . 78

6.8. The layer-resolved DMI for both Gr/3ML Co/Pt and Gr/3Co/Ir for various thicknesses of HM is shown. For Gr/3ML Co/5ML Pt, it is evident that Pt(I) dominates the total DMI. Conversely, for Gr/3ML Co/5ML Ir, the competition of Ir(I) as well as Ir(I-1) decides for DMI. 79

7.1. Simulated electric field setup: analyzing potential gradients and dielectric responses across Pt, Co, and Gr layers . . . . . 83

7.2. A lateral depiction showcases three possible stacking configurations of Gr atop Co/Pt(111). . . . . 83

7.3. The influence of the electric field on total energies is illustrated, highlighting the top-fcc stacking of Gr as the most stable configuration. Consequently, energy variations from the top-fcc arrangement are showcased in the presence of the electric field for the top-hcp and hollow configurations. . . . . 85
7.4. Band structure of Gr on Co/Pt(111) around the K point under different external electric fields (E = ±5.50 V/nm and E = 0 V/nm). The application of the field modifies the Dirac cone, inducing a bandgap opening at the K point. The gap increases under a negative field and reduces under a positive field, reflecting a tunable field-driven modification of the electronic structure. . . . . 87
7.5. The computation of DMI energy around the Γ point focuses on the left-handed spirals rotating specially within the $xz$-plane. The dashed line showcases the total DMI for the Gr(top-fcc)/1ML Co/5ML Pt(111) heterostructure, both with and without an applied electric field. Notably, it displays a prominently linear trend, particularly within the range of $q = \frac{6}{64}\,(2\pi/a)$ along $\overline{\Gamma K}$ or $q = \frac{1}{64}\,(2\pi/a)$ along $\overline{\Gamma M}$. The colored lines delineate the distinct contributions from individual layers to the DMI. . . . . 88
7.6. The dependency of DMI is illustrated concerning the applied electric field for various stacking configurations of Gr on Co. A positive field signifies a positive voltage propagated perpendicular from Gr to 1ML Co atop 5MLs of Pt on the (111) plane. Conversely, a negative field indicates the opposite direction of this voltage. A diminishing trend is evident in the presence of the field. The behavior induced by the field appears similar for all configurations. . . . . 89
7.7. Layer-resolved DMI for Gr/Co 1ML/5ML Pt(111) are presented. The modulation of the electric field influences the contributions of both Co and Pt layers, resulting in a consequent change in the DMI. . . . . 90
7.8. The correlation between MCA and the applied electric field is depicted for Gr(top-fcc)/Co/Pt(111). Contrary to the observed decrease in DMI, a noticeable increase is apparent. The MCA is calculated self-consistently. . . . . 92
7.9. MCA analysis using the Force Theorem, presenting various atomic contributions. The "total" corresponds to the contributions of SOC from all layers. The positive field denotes a rise in potential from the bottom layer of the film (Pt(I-4)) to the Gr. In the presence of an electric field, the MCA decreases. . . . . 94
7.10. The symmetrical structure of BeO/Gr(top-fcc)/Co/Pt(111) was chosen for structural relaxation, shown on the left side, while the optimized BeO film is depicted on the right side. . . . . 95
7.11. A side view presents three potential stacking configurations of 2MLs of BeO atop Gr/3ML Co/5ML Pt(111). The 12 initial configurations have been optimized into six unique stackings. . . . . 96

7.12. Layer-resolved contributions to the DMI are shown. In the modified configuration with BeO, we induced a displacement of the Be(I-1) layer away from the O(I-1) plane by 0.26 Å. . . . . 99
7.13. A side view of AbaB stacking of Gr(top-fcc)/3ML Co/5ML Pt(111) is presented. . . . . 99
7.14. Layer-resolved contributions to the DMI are shown. Augmenting the thickness of Co results in a substantial increase in the DMI. . . . . 100
7.15. Visual representation of the simulated electric field configuration, wherein a positive field is applied from the BeO bilayer to the Gr/Co/Pt film. . . . . 101
7.16. Layer-resolved contributions to the DMI are shown. It is apparent that the application of an electric field on BeO/Gr(top-fcc)/Co/Pt causes diminishing DMI. . . . . 103
7.17. Layer-resolved contributions to the DMI are shown. The alteration in the total DMI remains consistent. The modified heterostructure undergoes an expansion of the $d_{\mathrm{Be(I-1)/O(I-1)}}$ distance. . . . . 104
7.18. The relationship between the DMI and the applied electric field is illustrated for the BeO/Gr(top-fcc)/Co/Pt(111) system. Similarly to Gr(top-fcc)/Co/Pt(111), shown in Figure (7.6), a reduction in DMI is observed. . . . . 105

8.1. A lateral depiction illustrates three distinct stacking arrangements of Ir on Gr(top-fcc)/Co/Pt(111). Notably, Ir displays variability in its sequence orders when deposited onto Gr(top-fcc)/Co/Pt(111). These sequences are denoted as A, B, and C, corresponding to the fcc stacking of Co/Pt(111). In the case involving a Pt overlayer, we replace the Ir layer with Pt. . . . . 108
8.2. The figure illustrates the orbital weight of Gr within the bandstructure for an HM overlayer on Gr(top-fcc)/Co/Pt(111). We consider the most stable configurations, denoted as C for Pt and A for Ir. The Dirac point aligns with the crossing of the $p_z$ bands of Gr at K. . . . . 110
8.3. The computation of DMI energy around the Γ-point emphasizes left-handed spirals rotating within the $xz$-plane. Each plot represents the DMI for the optimized stacking of HMs on Gr(top-fcc)/Co/Pt(111), denoted as C for Pt and A for Ir. Upon comparing the dashed lines, which represent the total DMI, it is evident that covering the film with an HM layer increases the total DMI. . . . . 113
8.4. The element-resolved DMI contribution at $q = (\frac{1}{64}, \frac{1}{64}, 0)(2\pi/a)$ is depicted. Both Pt and Ir result in an enhancement of DMI. . . . . 114
8.5. MCA analysis using the Force Theorem, presenting various atomic contributions. The "total" corresponds to the contributions of SOC from all layers. The Ir capping layer significantly leads to the large in-plane MCA. . . . . 117
8.6. Lateral view illustrating various stacking arrangements of Gr Co/Pt/Co/Pt(111).119

8.7. Both plots illustrate the DMI energy near the Γ point, extending along the $\overline{\Gamma K}$ and $\overline{\Gamma M}$ directions, for left-handed spirals rotating in the $xz$-plane. In the left plot, the presence of Pt(I) is overshadowed by Co(I-1), whereas in the right plot, it is outweighed by the contribution of Pt(I-3). The inclusion of Gr results in a decrease in the net DMI. . . 122
8.8. Element-resolved DMI contribution for Gr/Co/Pt/Co/Pt(111) . . . . 123
8.9. MCA analysis using the Force Theorem, presenting various atomic contributions. The "total" corresponds to the contributions of SOC from all layers. . . . . 125

# List of Tables


5.1. $a$ and $d$ indicate in-plane lattice parameters and interlayer distances for different stacking positions of Gr on Co/Pt(111), respectively. Distances are given in Å and total energies in eV relative to the top-fcc stacking of Gr on Co/Pt(111). HM(I) denotes the interface Pt(Ir). 45

5.2. It indicates that the $J_{ij}$ coefficients are derived by fitting the energy dispersion of spin-spirals, expressed in meV. Here, we regard the top-fcc stacking of Gr on Co/Pt as the energetically most stable configuration. . . . . 49

5.3. The effective component of $\boldsymbol{D}$ is determined within a range extending up to $\boldsymbol{q} = \frac{2\pi}{a}(\frac{1}{64}, \frac{1}{64}, 0)$ of the BZ edge $\overline{\Gamma\mathrm{K}}$, calculated in meV$\mu_{\mathrm{B}}^{-2}$. Given that the magnetic moment of Co is denoted as $\mathrm{m_{Co}} = 1.84\,\mu_{\mathrm{B}}$. . . . . 55

5.4. The table provides magnetocrystalline anisotropy (MCA) for Gr(top-fcc)/Co/HM(111). The positive energy corresponds to the perpendicular MCA, and the energy values are expressed in meV. . . . . 62

5.5. The magnetic moment (MM) of Co and Pt(Ir) layers are represented in $\mu_{\mathrm{B}}$. The MMs exhibit better convergence within the five layers of Pt compared to Ir. . . . . 63

6.1. $a$ and $d$ stand for in-plane lattice parameter and interlayer distances for different stacking positions of Gr on 3ML Co/5ML Pt(Ir) along the fcc(111) stacking, respectively. Distances are given in Å and total energies in eV, both relative to the top-fcc stacking position, for each structure. . . . . 69

6.2. The effective component of $\boldsymbol{D}$ is derived up to $q \leq 0.03\,\overline{\Gamma\mathrm{K}}$, expressed in meV$\mu_{\mathrm{B}}^{-2}$, where $\mathrm{m_{Co}} = 1.84\,\mu_{\mathrm{B}}$. . . . . 74

6.3. The magnetic moment (MM) of Co and the Pt(Ir) are represented in $\mu_B$. The relatively small induced MM from the bottom layers suggests that employing five layers of HM, particularly Ir, is insufficient to achieve convergence with the three layers of Co. Increasing the thickness of HMs improved the convergence for the bottom of the slab. Only the first five layers of HM were taken into consideration. For Gr/3ML Co/Ir, both 7 and 10 layers boost convergence. . . . . 77
6.4. The effective component of $\boldsymbol{D}$ is calculated within $q \leq (\frac{1}{64}, \frac{1}{64}, 0)$ along $\overline{\Gamma K}$, expressed in meV$\mu_B^{-2}$. The $D$ magnitude displays enhancement in the configuration featuring 7 layers of HMs. . . . . 78

7.1. $d$ stands for interlayer distances for different stacking positions of Gr on 1ML Co/5ML Pt along the fcc(111) stacking. Distances are given in Å and optimized for ±2.75, ±5.50 V/nm fields are measured in V/nm electric fields. A positive field denotes an increase in potential from Pt to 1ML Co/Gr, while a negative field implies the opposite. . 84
7.2. The effective component of the DMI vector ($\boldsymbol{D}_y$) is determined up to $q \leq \frac{2}{64}$ of the BZ edge $\overline{\Gamma K}$, expressed in meV$\mu_B^{-2}$, where $m_{Co} = 1.84\,\mu_B$. 88
7.3. $\beta$ is determined up to $q \leq (2\pi/a)(\frac{1}{64}, \frac{1}{64}, 0)$, encompassing the initial point in Figure (7.5) along $\overline{\Gamma K}$. This ratio signifies the variation of DMI with the application of an electric field. . . . . 90
7.4. The $\Delta E_{MCA}$ is determined for Gr(top-fcc)/Co/Pt(111) in the presence of electric field. The positive energy corresponds to the perpendicular MCA. . . . . 91
7.5. The relaxation of BeO on Gr(top-fcc)/Co/Pt(111) is shown. All forces are optimized, reaching 0.05 eV/Å. $d$ stands for interlayer distances, given in Å and total energies in meV. The lattice constant of Gr(top-fcc)/Co/Pt(111), which is consistently set at 2.75 Å, is considered for all structures. Capital letters correspond to the stacking of O, while lowercase letters represent the stacking of Be. . . . . 97
7.6. The effective component of $\boldsymbol{D}$ is determined within the range of $q \leq \frac{2}{64}\,\overline{\Gamma K}$, and the values are expressed in meV$\mu_B^{-2}$, considering a magnetic moment of 1.84 $\mu_B$ for Co. This adjustment leads to an increase in DMI. In the modified configuration of BeO/Gr/Co/Pt, BeO(I-1) undergoes modulation to $d_{Be(I-1)/O(I-1)}$=0.26 Å. . . . . 98
7.7. The determination of the effective component of $\boldsymbol{D}$ is conducted within the specified range of $q \leq (\frac{2\pi}{a})(\frac{1}{64}, \frac{1}{64}, 0)$ along $\overline{\Gamma K}$. The resultant values are expressed in meV$\mu_B^{-2}$, considering a magnetic moment of 1.84 $\mu_B$ for Co. . . . . 100
7.8. Within the range of $q \leq (\frac{2\pi}{a})(\frac{1}{64}, \frac{1}{64}, 0)$ along $\overline{\Gamma K}$, the effective component of $\boldsymbol{D}$ is given for BeO/Gr/Co/Pt(111), while considering a magnetic moment of 1.84 $\mu_B$ for Co. This application of electric field leads to a decrease in DMI. . . . . 102

7.9. $\beta'$ is derived from fit up to $q \leq (\frac{2\pi}{a})(\frac{1}{64}, \frac{1}{64}, 0)$ along $\overline{\Gamma K}$. This ratio represents the change of DMI as a function of applied electric fields. 105

8.1. This table presents the interlayer distances ($d$) for various stacking configurations of a heavy metal (HM) overlayer on Gr(top-fcc)/Co/Pt(111), considering both Pt and Ir as HMs. The last column shows the interlayer distances for Gr(top-fcc)/Co/Pt(111) without an additional HM layer. All distances are measured in Å. . . . . 109

8.2. The total energies for the three distinct stackings of HM are presented. Notably, the C stacking of Pt and the A stacking of Ir emerge as the most stable configurations. . . . . 111

8.3. The effective component of $\boldsymbol{D}$ is determined within the specified range of $(q \leq (\frac{1}{64}, \frac{1}{64}, 0)(2\pi/a))$, $\overline{\Gamma K}$. The resulting values are expressed in meV$\mu_B^{-2}$, considering a magnetic moment of 1.84 $\mu_B$ for Co. . . . . 112

8.4. The magnetic moment (MM) of Pt(Ir), Co, and the Pt are represented in $\mu_B$. The magnetic moment converges throughout all films. . . . . 114

8.5. The element-resolved contributions to DMI, illustrated in Figure (8.4), are displayed. The contributions of graphene are negligible. All energies are in meV. . . . . 115

8.6. $\Delta E_{MCA}$ is shown for Gr(Top-fcc)/Co/Pt and Pt(Ir)/Gr(Top-fcc)/Co/Pt. For both capping layers, we considered their respective optimized stacking sequences, with A for Ir and C for Pt. Positive energy values correspond to the out-of-plane MCA. All energies are in meV. . . . . 116

8.7. Spin magnetic moment (MM) and orbital MM are displayed for both out-of-plane and in-plane orientation. All values are in $\mu_B$. MM$^{\parallel}$ and MM$^{\perp}$ indicate out-of-plane and on-plane directions, respectively. . . 116

8.8. Interlayer distances ($d$) exhibit variation across different stacking configurations of Gr on 1ML Co/1ML Pt/1ML Co/4ML Pt(111), which include top-fcc, top-hcp, and hollow arrangements. The last column displays the interlayer distances of 1ML Co/1ML Pt/1ML Co/4ML Pt along fcc(111). All distances are measured in Å. . . . . 119

8.9. The total energies for the three distinct stackings of Gr on Co/Pt/Co/Pt are presented. The top-fcc stacking emerges as the most stable configuration. . . . . 120

8.10. The magnetic moment (MM) of Co and Pt layers are represented in $\mu_B$. The MM converges throughout all films. The diminishing effect of MM at the Gr/Co interface results from Gr doping electrons into Co. 120

8.11. Within the defined range of $q \leq (\frac{1}{64}, \frac{1}{64}, 0)(2\pi/a))$, along the $\overline{\Gamma K}$ direction in Figure (8.7), we calculate the effective component of $\boldsymbol{D}$. These values are presented in units of meV$\mu_B^{-2}$, considering a Co magnetic moment of 1.84 $\mu_B$. . . . . 121

8.12. $\Delta E_{\mathrm{MCA}}$ is shown for 1ML Co/1ML Pt/1ML Co/4ML Pt, Gr(top-fcc)/1ML Co/5ML Pt and Gr(top-fcc)/1ML Co/1ML Pt/1ML Co/4ML Pt. Positive energy values correspond to the out-of-plane MCA. . . . 124

# List of Abbreviations

| | |
|---|---|
| APW | augmented planewave |
| BZ | Brillouin zone |
| DFT | density functional theory |
| DMI | Dzyaloshinskii-Moriya interaction |
| DW | domain wall |
| FLAPW | full-potential linearized augmented planewave |
| GGA | generalized gradient approximation |
| HM | heavy metal |
| LAPW | linearized augmented planewave |
| LDA | local density approximation |
| LO | local orbital |
| LSDA | local spin density approximation |
| MAE | magnetic anisotropy energy |
| MCA | magnetocrystalline anisotropy |
| MRAM | magnetoresistive random-access memory |
| MSA | magnetic shape anisotropy |
| PBE | Perdew, Burke, and Ernzerhof |
| PMA | perpendicular magnetic anisotropy |
| SOC | spin-orbit coupling |
| SOT | spin-orbit torque |

| | |
|---|---|
| STT | spin-transfer torque |

# Appendix

# A

# Computational details

In our study, we conducted self-consistent density functional calculations using the FLAPW method implemented in the FLEUR-code [56, 55]. Initially, we ensured the convergence of the electronic charge density by selecting computational parameters that ensure predictive accuracy. Subsequently, we gathered data on wave functions and band energies using a grid that adequately samples the Brillouin zone (BZ). For our computations, we employed the generalized gradient approximation (GGA) with the Perdew, Burke, and Ernzerhof (PBE) functional [176]. In the following, the input file for the top-fcc, top-hcp, and hollow stackings of Gr on Co/Pt(111) are shown.
For the structural optimization, we employed 21 *k*-points distributed within the primitive section of the hexagonal (2D) Brillouin Zone (BZ), adhering to the P3m1 symmetry class. For the self-consistent, we used a grid of 45×45 *k*-points.
Furthermore, for the structural optimization involving the oxide overlayer, both with and without an electric field, we used the following local orbital configuration for Co:

```
<lo type="SCLO" l="1" n="1" eDeriv="0"/>
```

```
Pt(5)(111)/Co(1)/C(2)/fcc

&input film=T /

&lattice latsys='hP'  a=5.21133 /

8
6   -1.0   1.0  13.336063
6    1.0  -1.0  13.278908
27   2.0   1.0   9.575839
78   0.0   0.0   5.717778
78   1.0   2.0   1.233066
78   2.0   1.0  -3.180012
78   0.0   0.0  -7.570539
78   1.0   2.0 -12.010064
&factor   3.0   3.0   1.0

&atom  element="C"   id=6    rmt=1.42  jri=473  lmax=6  /
&atom  element="Co"  id=27   rmt=2.17  jri=819  lmax=10 /
&atom  element="Pt"  id=78   rmt=2.47  jri=787  lmax=8  /
&comp  kmax=4.0   gmaxxc=10.4   gmax=12 /
&kpt     div1=45 div2=45 div3=1 /
```

```
Pt(5)(111)/Co(1)/C(2)/hcp

&input film=T /

&lattice latsys='hP'  a=5.21133 /

8
6   -1.0   1.0  12.850845
6    0.0   0.0  12.805688
27   2.0   1.0   9.053923
78   0.0   0.0   5.181338
78   1.0   2.0   0.722884
78   2.0   1.0  -3.689716
78   0.0   0.0  -8.079484
78   1.0   2.0 -12.510064
&factor   3.0   3.0   1.0

&atom  element="C"   id=6    rmt=1.42  jri=473  lmax=6  /
&atom  element="Co"  id=27   rmt=2.17  jri=819  lmax=10 /
&atom  element="Pt"  id=78   rmt=2.47  jri=787  lmax=8  /
&comp  kmax=4.0   gmaxxc=10.4   gmax=12 /
&kpt     div1=45 div2=45 div3=1 /
```

```
Pt(5)(111)/Co(1)/C(2)/hollow

&input film=T /

&lattice latsys='hP'  a=5.21133 /

8
6     0.0    0.0   12.708832
6     0.0    0.0   12.660626
27    2.0    1.0    8.939792
78    0.0    0.0    5.080376
78    1.0    2.0    0.612698
78    2.0    1.0   -3.828971
78    0.0    0.0   -8.269617
78    1.0    2.0  -12.762814
&factor   3.0    3.0    1.0

&atom   element="C"    id=6     rmt=1.42  jri=473  lmax=6   /
&atom   element="Co"   id=27    rmt=2.17  jri=819  lmax=10 /
&atom   element="Pt"   id=78    rmt=2.47  jri=787  lmax=8   /
&comp  kmax=4.0   gmaxxc=10.4   gmax=12 /
&kpt     div1=45 div2=45 div3=1 /
```

# Bibliography


[1] W. Han et al. "Graphene spintronics." In: *Nature Nanotechnology* 9.10 (2014), pp. 794–807. DOI: 10.1038/nnano.2014.214.

[2] R. Jansen. "Silicon spintronics." In: *Nature Materials* 11.5 (2012), pp. 400–408. DOI: 10.1038/nmat3293.

[3] A. Hirohata et al. "Review on spintronics: Principles and device applications." In: *Journal of Magnetism and Magnetic Materials* 509 (2020), p. 166711. DOI: 10.1016/j.jmmm.2020.166711.

[4] A. Manchon et al. "Current-induced spin-orbit torques in ferromagnetic and antiferromagnetic systems." In: *Reviews of Modern Physics* 91.3 (2019), p. 035004. DOI: 10.1103/RevModPhys.91.035004.

[5] L. Thomas et al. "Perpendicular spin transfer torque magnetic random access memories with high spin torque efficiency and thermal stability for embedded applications." In: *Journal of Applied Physics* 115.17 (2014). DOI: 10.1063/1.4870917.

[6] M. Cubukcu et al. "Spin-orbit torque magnetization switching of a three-terminal perpendicular magnetic tunnel junction." In: *Applied Physics Letters* 104.4 (2014). DOI: 10.1063/1.4863407.

[7] S. Fukami et al. "A spin-orbit torque switching scheme with collinear magnetic easy axis and current configuration." In: *Nature Nanotechnology* 11.7 (2016), pp. 621–625. DOI: 10.1038/nnano.2016.29.

[8] F. Matsukura, Y. Tokura, and H. Ohno. "Control of magnetism by electric fields." In: *Nature Nanotechnology* 10.3 (2015), pp. 209–220. DOI: 10.1038/nnano.2015.22.

[9] A. Fert, V. Cros, and J. Sampaio. "Skyrmions on the track." In: *Nature Nanotechnology* 8.3 (2013), pp. 152–156. DOI: 10.1038/nnano.2013.29.

[10] S. S. Parkin, M. Hayashi, and L. Thomas. "Magnetic domain-wall racetrack memory." In: *Science* 320.5873 (2008), pp. 190–194. DOI: 10.1038/nnano.2013.29.

[11] R. H. Baughman, A. A. Zakhidov, and W. A. De Heer. "Carbon nanotubes–the route toward applications." In: *Science* 297.5582 (2002), pp. 787–792. DOI: 10.1126/science.1060928.

[12] F. Ajejas et al. "Unraveling Dzyaloshinskii–Moriya interaction and chiral nature of graphene/cobalt interface." In: *Nano Letters* 18.9 (2018), pp. 5364–5372. DOI: 10.1021/acs.nanolett.8b00878.

[13] K. S. Novoselov et al. "Two-dimensional gas of massless Dirac fermions in graphene." In: *nature* 438.7065 (2005), pp. 197–200. DOI: 10.1038/nature04233.

[14] K. S. Novoselov et al. "Electric field effect in atomically thin carbon films." In: *Science* 306.5696 (2004), pp. 666–669. DOI: 10.1126/science.1102896.

[15] Y. Zhang et al. "Origin of spatial charge inhomogeneity in graphene." In: *Nature Physics* 5.10 (2009), pp. 722–726. DOI: 10.1038/nphys1365.

[16] H.-X. Yang et al. "Proximity effects induced in graphene by magnetic insulators: first-principles calculations on spin filtering and exchange-splitting gaps." In: (2013). DOI: 10.1103/PhysRevLett.110.046603.

[17] M. Garnica et al. "Long-range magnetic order in a purely organic 2D layer adsorbed on epitaxial graphene." In: *Nature Physics* 9.6 (2013), pp. 368–374. DOI: 10.1038/nphys2610.

[18] F. Calleja et al. "Spatial variation of a giant spin-orbit effect induces electron confinement in graphene on Pb islands." In: *Nature Physics* 11.1 (2015), pp. 43–47. DOI: 10.1038/nphys3173.

[19] G. Giovannetti et al. "Doping graphene with metal contacts." In: *Physical Review Letters* 101.2 (2008), p. 026803. DOI: 10.1103/PhysRevLett.101.026803.

[20] A.-D. Vu et al. "Unconventional magnetization texture in graphene/cobalt hybrids." In: *Scientific Reports* 6.1 (2016), p. 24783. DOI: 10.1038/srep24783.

[21] P. Gargiani et al. "Graphene-based synthetic antiferromagnets and ferrimagnets." In: *Nature Communications* 8.1 (2017), p. 699. DOI: 10.1038/s41467-017-00825-9.

[22] R. Decker et al. "Atomic-scale magnetism of cobalt-intercalated graphene." In: *Physical Review B* 87.4 (2013), p. 041403. DOI: 10.1103/PhysRevB.87.041403.

[23] M.-B. Martin et al. "Sub-nanometer atomic layer deposition for spintronics in magnetic tunnel junctions based on graphene spin-filtering membranes." In: *ACS Nano* 8.8 (2014), pp. 7890–7895. DOI: 10.1021/nn5017549.

[24] M. Piquemal-Banci et al. "2D-MTJs: introducing 2D materials in magnetic tunnel junctions." In: *Journal of Physics D: Applied Physics* 50.20 (2017), p. 203002. DOI: 10.1088/1361-6463/aa650f.

[25] G. Daalderop, P. Kelly, and F. Den Broeder. "Prediction and confirmation of perpendicular magnetic anisotropy in Co/Ni multilayers." In: *Physical Review Letters* 68.5 (1992), p. 682. DOI: 10.1103/PhysRevLett.68.682.

[26] M. Johnson et al. "Magnetic anisotropy in metallic multilayers." In: *Reports on Progress in Physics* 59.11 (1996), p. 1409. DOI: 10.1088/0034-4885/59/11/002.

[27] P. Bruno. "Tight-binding approach to the orbital magnetic moment and magnetocrystalline anisotropy of transition-metal monolayers." In: *Physical Review B* 39.1 (1989), p. 865. DOI: 10.1103/PhysRevB.39.865.

[28] K. Nakamura et al. "Giant modification of the magnetocrystalline anisotropy in transition-metal monolayers by an external electric field." In: *Physical Review Letters* 102.18 (2009), p. 187201. DOI: 10.1103/PhysRevLett.102.187201.

[29] H. Yang et al. "First-principles investigation of the very large perpendicular magnetic anisotropy at Fe/MgO and Co/MgO interfaces." In: *Physical Review B* 84.5 (2011), p. 054401. DOI: 10.1103/PhysRevB.84.054401.

[30] B. Dieny and M. Chshiev. "Perpendicular magnetic anisotropy at transition metal/oxide interfaces and applications." In: *Reviews of Modern Physics* 89.2 (2017), p. 025008. DOI: 10.1103/RevModPhys.89.025008.

[31] H. Sato et al. "Properties of magnetic tunnel junctions with a MgO/CoFeB/Ta /CoFeB/MgO recording structure down to junction diameter of 11 nm." In: *Applied Physics Letters* 105.6 (2014). DOI: 10.1063/1.4892924.

[32] Y.-C. Lau et al. "Giant perpendicular magnetic anisotropy in Ir/Co/Pt multilayers." In: *Physical Review Materials* 3.10 (2019), p. 104419. DOI: 10.1103/PhysRevMaterials.3.104419.

[33] S. Heinze et al. "Spontaneous atomic-scale magnetic skyrmion lattice in two dimensions." In: *Nature Physics* 7.9 (2011), pp. 713–718. DOI: 10.1038/nphys2045.

[34] N. Romming et al. "Writing and deleting single magnetic skyrmions." In: *Science* 341.6146 (2013), pp. 636–639. DOI: 10.1126/science.1240573.

[35] A. Thiaville et al. "Dynamics of Dzyaloshinskii domain walls in ultrathin magnetic films." In: *Europhysics Letters* 100.5 (2012), p. 57002. DOI: 10.1209/0295-5075/100/57002.

[36] M. Heide, G. Bihlmayer, and S. Blügel. "Dzyaloshinskii-Moriya interaction accounting for the orientation of magnetic domains in ultrathin films: Fe/W (110)." In: *Physical Review B* 78.14 (2008), p. 140403. DOI: 10.1103/PhysRevB.78.140403.

[37] A. Fert. "Magnetic and transport properties of metallic multilayers." In: *Materials Science Forum*. Vol. 59. Trans Tech Publ. 1990, pp. 439–480. DOI: 10.4028/www.scientific.net/MSF.59-60.439.

[38] C. Moreau-Luchaire et al. "Additive interfacial chiral interaction in multilayers for stabilization of small individual skyrmions at room temperature." In: *Nature Nanotechnology* 11.5 (2016), pp. 444–448. DOI: 10.1038/nnano.2015.313.

[39] O. Boulle et al. "Room-temperature chiral magnetic skyrmions in ultrathin magnetic nanostructures." In: *Nature Nanotechnology* 11.5 (2016), pp. 449–454. DOI: 10.1038/nnano.2015.315.

[40] A. Soumyanarayanan et al. "Tunable room-temperature magnetic skyrmions in Ir/Fe/Co/Pt multilayers." In: *Nature Materials* 16.9 (2017), pp. 898–904. DOI: 10.1038/nmat4934.

[41] M. Shen et al. "Effects of the interfacial Dzyaloshinskii–Moriya interaction on magnetic dynamics." In: *Journal of Physics D: Applied Physics* 55.21 (2022), p. 213002. DOI: 10.1088/1361-6463/ac4366.

[42] A. Thiaville and J. Miltat. "Topology and magnetic domain walls." In: *Topology in Magnetism* (2018), pp. 41–73. DOI: 10.1007/978-3-319-97334-0_2.

[43] C. Deger, I. Yavuz, and F. Yildiz. "Current-driven coherent skyrmion generation." In: *Scientific Reports* 9.1 (2019), p. 3513. DOI: 10.1038/s41598-019-40220-6.

[44] W. Jiang et al. "Blowing magnetic skyrmion bubbles." In: *Science* 349.6245 (2015), pp. 283–286. DOI: 10.1126/science.aaa1442.

[45] S. Komineas, C. Melcher, and S. Venakides. "The profile of chiral skyrmions of small radius." In: *Nonlinearity* 33.7 (2020), p. 3395. DOI: 10.1088/1361-6544/ab81eb.

[46] H. Jia et al. "Material systems for FM-/AFM-coupled skyrmions in Co/Pt-based multilayers." In: *Physical Review Materials* 4.9 (2020), p. 094407. DOI: 10.1103/PhysRevMaterials.4.094407.

[47] M. Weisheit et al. "Electric field-induced modification of magnetism in thin-film ferromagnets." In: *Science* 315.5810 (2007), pp. 349–351. DOI: 10.1126/science.1136629.

[48] D. D. Awschalom and M. E. Flatté. "Challenges for semiconductor spintronics." In: *Nature Physics* 3.3 (2007), pp. 153–159. DOI: 10.1038/nphys551.

[49] C.-G. Duan et al. "Surface magnetoelectric effect in ferromagnetic metal films." In: *Physical Review Letters* 101.13 (2008), p. 137201. DOI: 10.1103/PhysRevLett.101.137201.

[50] T. Maruyama et al. "Large voltage-induced magnetic anisotropy change in a few atomic layers of iron." In: *Nature Nanotechnology* 4.3 (2009), pp. 158–161. DOI: 10.1038/nnano.2008.406.

[51] M. Endo et al. "Electric-field effects on thickness dependent magnetic anisotropy of sputtered MgO/Co40Fe40B20/Ta structures." In: *Applied Physics Letters* 96.21 (2010). DOI: 10.1063/1.3429592.

[52] F. Ibrahim et al. "Anatomy of electric field control of perpendicular magnetic anisotropy at Fe/MgO interfaces." In: *Physical Review B* 93.1 (2016), p. 014429. DOI: 10.1103/PhysRevB.93.014429.

[53] P. Hohenberg and W. Kohn. "Inhomogeneous electron gas." In: *Physical Review* 136 (1964), B864. DOI: 10.1103/PhysRev.136.B864.

[54] W. Kohn and L. J. Sham. "Self-consistent equations including exchange and correlation effects." In: *Physical Review* 140.4A (1965), A1133. DOI: 10.1103/PhysRev.140.A1133.

[55] *The FLEUR project*. https://www.flapw.de/.

[56] D. Wortmann et al. *FLEUR*. Zenodo. May 2023. DOI: 10.5281/zenodo.7576163.

[57] R. O. Jones. "Density functional theory: Its origins, rise to prominence, and future." In: *Reviews of Modern Physics* 87.3 (2015), p. 897. DOI: 10.1103/RevModPhys.87.897.

[58] M. Born and W. Heisenberg. "Zur quantentheorie der molekeln." In: *Original Scientific Papers Wissenschaftliche Originalarbeiten* (1985), pp. 216–246. DOI: 10.1007/978-3-642-61659-4_16.

[59] L. H. Thomas. "The calculation of atomic fields." In: *Mathematical Proceedings of the Cambridge Philosophical Society*. Vol. 23. 5. Cambridge University Press. 1927, pp. 542–548. DOI: 10.1017/S0305004100011683.

[60] E. Fermi. "Eine statistische Methode zur Bestimmung einiger Eigenschaften des Atoms und ihre Anwendung auf die Theorie des periodischen Systems der Elemente." In: *Zeitschrift für Physik* 48.1 (1928), pp. 73–79. DOI: 10.1007/BF01351576.

[61] E. Fermi. "Application of statistical gas methods to electronic systems." In: *Atti accad. naz. Lincei* 6 (1927), pp. 602–607.

[62] O. Gunnarsson and H. Hjelmberg. "Hydrogen chemisorption by the spin-density functional formalism. I." In: *Physica Scripta* 11.2 (1975), p. 97. DOI: 10.1088/0031-8949/11/2/004.

[63] S. Blügel. *Computing Solids: Models, Ab-initio Methods and Supercomputing; Lecture Notes of the 45th IFF Spring School 2014*. Forschungszentrum Jülich, 2014.

[64] G. Bihlmayer. "Density functional theory for magnetism and magnetic anisotropy." In: *Handbook of Materials Modeling, Vol.1*. Ed. by S. Yip. Springer Science & Business Media, 2018. DOI: 10.1007/978-3-319-42913-7_73-1.

[65] D. M. Ceperley and B. Alder. "Ground state of the electron gas by a stochastic method." In: *Physical Review Letters* 45.2 (1980), p. 566. DOI: 10.1103/PhysRevLett.45.566.

[66] W. Kohn and L. J. Sham. "Self-consistent equations including exchange and correlation effects." In: *Physical Review* 140.4A (1965), A1133. DOI: 10.1103/PhysRev.140.A1133.

[67] P. A. Dirac. "Note on exchange phenomena in the Thomas atom." In: *Mathematical Proceedings of the Cambridge Philosophical Society*. Vol. 26. 3. Cambridge University Press. 1930, pp. 376–385. DOI: 10.1017/S0305004100016108.

[68] G. Ortiz and P. Ballone. "Correlation energy, structure factor, radial distribution function, and momentum distribution of the spin-polarized uniform electron gas." In: *Physical Review B* 50.3 (1994), p. 1391. DOI: 10.1103/PhysRevB.50.1391.

[69] J. P. Perdew, K. Burke, and M. Ernzerhof. "Generalized gradient approximation made simple." In: *Physical Review Letters* 77.18 (1996), p. 3865. DOI: 10.1103/PhysRevLett.77.3865.

[70] A. D. Becke. "A new mixing of Hartree–Fock and local density-functional theories." In: *The Journal of Chemical Physics* 98.2 (1993), pp. 1372–1377. DOI: 10.1063/1.464304.

[71] U. von Barth and L. Hedin. "A local exchange-correlation potential for the spin-polarized case. I." In: *Journal of Physics C: Solid State Physics* 5.13 (1972), p. 1629. DOI: 10.1088/0022-3719/5/13/012.

[72] E. R. Cohen et al. "Quantum Mechanics of One-and Two-Electron Systems." In: *Atoms I/Atome I* (1957), pp. 88–436. DOI: 10.1007/978-3-642-45869-9_2.

[73] E. Wimmer et al. "Full-potential self-consistent linearized-augmented-plane-wave method for calculating the electronic structure of molecules and surfaces: O 2 molecule." In: *Physical Review B* 24.2 (1981), p. 864. DOI: 10.1103/PhysRevB.24.864.

[74] E. Bosoni et al. "How to verify the precision of density-functional-theory implementations via reproducible and universal workflows." In: *Nature Reviews Physics* 6.1 (2024), pp. 45–58. DOI: https://doi.org/10.1038/s42254-023-00655-3.

[75] D. J. Singh and L. Nordstrom. *Planewaves, Pseudopotentials, and the LAPW method*. Springer Science & Business Media, 2006. DOI: 10.1007/978-0-387-29684-5.

[76] T. Loucks and J. C. Slater. "Augmented plane wave method: a guide to performing electronic structure calculations." In: *Physics Today* 20.11 (1967), pp. 92–93. DOI: 10.1063/1.3034041.

[77] O. K. Andersen. "Linear methods in band theory." In: *Physical Review B* 12.8 (1975), p. 3060. DOI: 10.1103/PhysRevB.12.3060.

[78] D. Koelling and G. Arbman. "Use of energy derivative of the radial solution in an augmented plane wave method: application to copper." In: *Journal of Physics F: Metal Physics* 5.11 (1975), p. 2041. DOI: 10.1088/0305-4608/5/11/016.

[79] P. M. Marcus. "Variational methods in the computation of energy bands." In: *International Journal of Quantum Chemistry* 1.S1 (1967), pp. 567–588. DOI: 10.1002/qua.560010659.

[80] S. Blügel and G. Bihlmayer. "Full-potential linearized augmented planewave method." In: *Computational Nanoscience: do it yourself* 31 (2006), pp. 85–129.

[81] D. Hamann. "Semiconductor charge densities with hard-core and soft-core pseudopotentials." In: *Physical Review Letters* 42.10 (1979), p. 662. DOI: 10.1103/PhysRevLett.42.662.

[82] G. Michalicek. "Extending the precision and efficiency of the all-electron full-potential linearized augmented plane-wave density-functional theory method." Prüfungsjahr: 2014. - Publikationsjahr: 2015; Zugl.: Aachen, Techn. Hochsch., Diss., 2014. Dr. Jülich: Aachen, Techn. Hochsch., 2015, 195 S. : Ill., graph. Darst. ISBN: 978-3-95806-031-9. URL: http://publications.rwth-aachen.de/record/464499.

[83] D. Singh. "Ground-state properties of lanthanum: Treatment of extended-core states." In: *Physical Review B* 43.8 (1991), p. 6388. DOI: 10.1103/PhysRevB.43.6388.

[84] M. Betzinger et al. "Local exact exchange potentials within the all-electron FLAPW method and a comparison with pseudopotential results." In: *Phys. Rev. B* 83 (4 2011), p. 045105. DOI: 10.1103/PhysRevB.83.045105. URL: http://link.aps.org/doi/10.1103/PhysRevB.83.045105.

[85] C. Friedrich et al. "Elimination of the linearization error in *GW* calculations based on the linearized augmented-plane-wave method." In: *Phys. Rev. B* 74.4 (2006), p. 045104. DOI: 10.1103/PhysRevB.74.045104.

[86] G. Michalicek et al. "Elimination of the linearization error and improved basis-set convergence within the {FLAPW} method." In: *Computer Physics Communications* 184.12 (2013), pp. 2670–2679. ISSN: 0010-4655. DOI: http://dx.doi.org/10.1016/j.cpc.2013.07.002. URL: http://www.sciencedirect.com/science/article/pii/S0010465513002300.

[87] H. Krakauer, M. Posternak, and A. J. Freeman. "Linearized augmented plane-wave method for the electronic band structure of thin films." In: *Physical Review B* 19.4 (1979), p. 1706. DOI: 10.1103/PhysRevB.19.1706.

[88] M. Weinert et al. "FLAPW: applications and implementations." In: *Journal of Physics: Condensed Matter* 21.8 (2009), p. 084201. DOI: 10.1088/0953-8984/21/8/084201.

[89] N. Lang. "Self-consistent properties of the electron distribution at a metal surface." In: *Solid State Communications* 7.15 (1969), pp. 1047–1050. DOI: 10.1016/0038-1098(69)90467-0.

[90] G. Aers and J. Inglesfield. "Electric field and Ag (001) surface electronic structure." In: *Surface Science* 217.1-2 (1989), pp. 367–383. DOI: 10.1016/0039-6028(89)90554-2.

[91] J. Inglesfield. "The screening of an electric field at an Al (001) surface." In: *Surface Science* 188.3 (1987), pp. L701–L707. DOI: 10.1016/S0039-6028(87)80183-8.

[92] N. Lang and W. Kohn. "Theory of metal surfaces: work function." In: *Physical Review B* 3.4 (1971), p. 1215. DOI: 10.1103/PhysRevB.3.1215.

[93] P. Kurz et al. "Ab initio treatment of noncollinear magnets with the full-potential linearized augmented plane wave method." In: *Physical Review B* 69.2 (2004), p. 024415. DOI: 10.1103/PhysRevB.69.024415.

[94] L. Nordström and D. J. Singh. "Noncollinear intra-atomic magnetism." In: *Physical Review Letters* 76.23 (1996), p. 4420. DOI: 10.1103/PhysRevLett.76.4420.

[95] E. Sjöstedt and L. Nordström. "Noncollinear full-potential studies of $\gamma$- Fe." In: *Physical Review B* 66.1 (2002), p. 014447. DOI: 10.1103/PhysRevB.66.014447.

[96] J. C. Slater. "Wave functions in a periodic potential." In: *Physical Review* 51.10 (1937), p. 846. DOI: 10.1063/1.372622.

[97] P. Kurz, G. Bihlmayer, and S. Blügel. "Noncollinear magnetism of Cr and Mn monolayers on Cu(111)." In: *Journal of Applied Physics* 87 (May 2000), pp. 6101–6103. DOI: 10.1063/1.372622.

[98] L. Sandratskii. "Noncollinear magnetism in itinerant-electron systems: theory and applications." In: *Advances in Physics* 47.1 (1998), pp. 91–160. DOI: 10.1080/000187398243573.

[99] M. Heide, G. Bihlmayer, and S. Blügel. "Describing Dzyaloshinskii–Moriya spirals from first principles." In: *Physica B: Condensed Matter* 404.18 (2009), pp. 2678–2683. DOI: 10.1103/PhysRevB.82.245412.

[100] G. T. Rado and H. Suhl. *Magnetism: Exchange interactions among itinerant electrons, by C. Herring*. Vol. 4. Academic Press, 1963.

[101] L. Sandratskii. "Symmetry analysis of electronic states for crystals with spiral magnetic order. I. General properties." In: *Journal of Physics: Condensed Matter* 3.44 (1991), p. 8565. DOI: 10.1088/0953-8984/3/44/004.

[102] D. Koelling and B. Harmon. "A technique for relativistic spin-polarised calculations." In: *Journal of Physics C: Solid State Physics* 10.16 (1977), p. 3107. DOI: 10.1088/0022-3719/10/16/019.

[103] A. MacDonald, W. Picket, and D. Koelling. "A linearised relativistic augmented-plane-wave method utilising approximate pure spin basis functions." In: *Journal of Physics C: Solid State Physics* 13.14 (1980), p. 2675. DOI: 10.1088/0022-3719/13/14/009.

[104] S. Youn, W. Mannstadt, and A. Freeman. "Analytic spin-orbit coupling matrix element formulae in FLAPW calculations." In: *Journal of Computational Physics* 172.1 (2001), pp. 387–391. DOI: 10.1006/jcph.2001.6830.

[105] T. Yildirim et al. "Anisotropic spin Hamiltonians due to spin-orbit and Coulomb exchange interactions." In: *Physical Review B* 52.14 (1995), p. 10239. DOI: 10.1103/PhysRevB.52.10239.

[106] W. Heisenberg. "Zur Theorie des Ferromagnetismus." In: *Z. Phys* 49 (1928), p. 619. DOI: 10.1007/978-3-642-61659-4_35.

[107] J. Hubbard. "Electron correlations in narrow energy bands." In: *Proceedings of the Royal Society of London. Series A. Mathematical and Physical Sciences* 276.1365 (1963), pp. 238–257. DOI: 10.1098/rspa.1963.0204.

[108] M. C. Gutzwiller. "Effect of correlation on the ferromagnetism of transition metals." In: *Physical Review Letters* 10.5 (1963), p. 159. DOI: 10.1103/PhysRevLett.10.159.

[109] M. Hoffmann and S. Blügel. "Systematic derivation of realistic spin models for beyond-Heisenberg solids." In: *Physical Review B* 101.2 (2020), p. 024418. DOI: 10.1103/PhysRevB.101.024418.

[110] I. Dzyaloshinsky. "A thermodynamic theory of "weak" ferromagnetism of antiferromagnetics." In: *Journal of Physics and Chemistry of Solids* (1958), pp. 241–255. DOI: 10.1016/0022-3697(58)90076-3.

[111] T. Moriya. "Anisotropic superexchange interaction and weak ferromagnetism." In: *Physical Review* 120.1 (1960), p. 91. DOI: 10.1103/PhysRev.120.91.

[112] H. Yang, J. Liang, and Q. Cui. "First-principles calculations for Dzyaloshinskii–Moriya interaction." In: *Nature Reviews Physics* 5.1 (2023), pp. 43–61. DOI: 10.1038/s42254-022-00529-0.

[113] S. Mühlbauer et al. "Skyrmion lattice in a chiral magnet." In: *Science* 323.5916 (2009), pp. 915–919. DOI: 10.1126/science.1166767.

[114] U. K. Roessler, A. Bogdanov, and C. Pfleiderer. "Spontaneous skyrmion ground states in magnetic metals." In: *Nature* 442.7104 (2006), pp. 797–801. DOI: 10.1038/nature05056.

[115] S. Konschuh, M. Gmitra, and J. Fabian. "Tight-binding theory of the spin-orbit coupling in graphene." In: *Physical Review B* 82.24 (2010), p. 245412. DOI: 10.1103/PhysRevB.82.245412.

[116] D. Marchenko et al. "Giant Rashba splitting in graphene due to hybridization with gold." In: *Nature Communications* 3.1 (2012), p. 1232. DOI: 10.1038/ncomms2227.

[117] S. Woo et al. "Observation of room-temperature magnetic skyrmions and their current-driven dynamics in ultrathin metallic ferromagnets." In: *Nature Materials* 15.5 (2016), pp. 501–506. DOI: 10.1038/nmat4593.

[118] D. Maccariello et al. "Electrical detection of single magnetic skyrmions in metallic multilayers at room temperature." In: *Nature Nanotechnology* 13.3 (2018), pp. 233–237. DOI: 10.1038/s41565-017-0044-4.

[119] B. Zimmermann et al. "Comparison of first-principles methods to extract magnetic parameters in ultrathin films: Co/Pt (111)." In: *Physical Review B* 99.21 (2019), p. 214426. DOI: 10.1103/PhysRevB.99.214426.

[120] C. Busse et al. "Graphene on Ir (111): physisorption with chemical modulation." In: *Physical review letters* 107.3 (2011), p. 036101. DOI: 10.1103/PhysRevLett.107.036101.

[121] A. Preobrajenski et al. "Controlling graphene corrugation on lattice-mismatched substrates." In: *Physical Review B—Condensed Matter and Materials Physics* 78.7 (2008), p. 073401. DOI: 10.1103/PhysRevB.78.073401.

[122] C. Xia et al. "Si intercalation/deintercalation of graphene on 6 H-SiC (0001)." In: *Physical Review B* 85.4 (2012), p. 045418. DOI: 10.1103/PhysRevB.85.045418.

[123] G. T. Rado and H. Suhl. "Exchange interactions among itinerant electrons." In: *Magnetism* 4 (1966).

[124] T. Ando, Y. Zheng, and H. Suzuura. "Dynamical conductivity and zero-mode anomaly in honeycomb lattices." In: *Journal of the Physical Society of Japan* 71.5 (2002), pp. 1318–1324. DOI: 10.1143/JPSJ.71.1318.

[125] M. I. Katsnelson, K. S. Novoselov, and A. K. Geim. "Chiral tunneling and the Klein paradox in graphene." In: *Nature Physics* 2.9 (2006), pp. 620–625. DOI: 10.1038/nphys384.

[126] J. Sławińska and J. I. Cerdá. "Spin–orbit proximity effect in graphene on metallic substrates: Decoration versus intercalation with metal adatoms." In: *New Journal of Physics* 21.7 (2019), p. 073018. DOI: 10.1088/1367-2630/ab2bc7.

[127] D. Koelling and B. Harmon. "A technique for relativistic spin-polarised calculations." In: *Journal of Physics C: Solid State Physics* 10.16 (1977), p. 3107. DOI: 10.1088/0022-3719/10/16/019.

[128] A. MacDonald, W. Picket, and D. Koelling. "A linearised relativistic augmented-plane-wave method utilising approximate pure spin basis functions." In: *Journal of Physics C: Solid State Physics* 13.14 (1980), p. 2675. DOI: 10.1088/0022-3719/13/14/009.

[129] A. Hrabec et al. "Measuring and tailoring the Dzyaloshinskii-Moriya interaction in perpendicularly magnetized thin films." In: *Physical Review B* 90.2 (2014), p. 020402. DOI: 10.1088/1367-2630/ab2bc7.

[130] A. Crépieux and C. Lacroix. "Dzyaloshinsky–Moriya interactions induced by symmetry breaking at a surface." In: *Journal of Magnetism and Magnetic Materials* 182.3 (1998), pp. 341–349. DOI: 10.1016/S0304-8853(97)01044-5.

[131] M. Blanco-Rey et al. "Nature of interfacial Dzyaloshinskii-Moriya interactions in graphene/Co/Pt (111) multilayer heterostructures." In: *Physical Review B* 106.6 (2022), p. 064426. DOI: 10.1103/PhysRevB.106.064426.

[132] M. Blanco-Rey, J. I. Cerdá, and A. Arnau. "Validity of perturbative methods to treat the spin-orbit interaction: Application to magnetocrystalline anisotropy." In: *New Journal of Physics* 21.7 (2019), p. 073054. DOI: 10.1088/1367-2630/ab3060.

[133] G. Daalderop, P. Kelly, and M. Schuurmans. "Magnetic anisotropy of a free-standing Co monolayer and of multilayers which contain Co monolayers." In: *Physical Review B* 50.14 (1994), p. 9989. DOI: 10.1103/PhysRevB.50.9989.

[134] T. Ueno et al. "Enhanced orbital magnetic moments in magnetic heterostructures with interface perpendicular magnetic anisotropy." In: *Scientific Reports* 5.1 (2015), pp. 1–7. DOI: 10.1038/srep14858.

[135] M. Blanco-Rey et al. "Large Perpendicular Magnetic Anisotropy in Nanometer-Thick Epitaxial Graphene/Co/Heavy Metal Heterostructures for Spin–Orbitronics Devices." In: *ACS Applied Nano Materials* 4.5 (2021), pp. 4398–4408. DOI: 10.1021/acsanm.0c03364.

[136] G. Daalderop, P. Kelly, and M. Schuurmans. "First-principles calculation of the magnetocrystalline anisotropy energy of iron, cobalt, and nickel." In: *Physical Review B* 41.17 (1990), p. 11919. DOI: 10.1103/PhysRevB.41.11919.

[137] A. Gudín et al. "Rashba-like Spin Textures in Graphene Promoted by Ferromagnet-Mediated Electronic Hybridization with a Heavy Metal." In: *ACS Nano* (2024). DOI: 10.1021/acsnano.4c02154.

[138] D. Pacile et al. "Electronic structure of graphene/Co interfaces." In: *Physical Review B* 90.19 (2014), p. 195446. DOI: 10.1103/PhysRevB.90.195446.

[139] U. Von Barth and L. Hedin. "A local exchange-correlation potential for the spin-polarized case. i." In: *Journal of Physics C: Solid State Physics* 5.13 (1972), p. 1629. DOI: 10.1088/0022-3719/5/13/012.

[140] H. Yang et al. "Anatomy of Dzyaloshinskii-Moriya interaction at Co/Pt interfaces." In: *Physical review letters* 115.26 (2015), p. 267210. DOI: 10.1103/PhysRevLett.115.267210.

[141] A. Belabbes et al. "Hund's rule-driven dzyaloshinskii-moriya interaction at 3 d- 5 d interfaces." In: *Physical Review Letters* 117.24 (2016), p. 247202. DOI: 10.1103/PhysRevLett.117.247202.

[142] S. Methfessel. "Potential applications of magnetic rare earth compunds." In: *IEEE Transactions on Magnetics* 1.3 (1965), pp. 144–155. DOI: 10.1109/TMAG.1965.1062951.

[143] E. Ascher et al. "Some properties of ferromagnetoelectric nickel-iodine boracite, Ni3B7O13I." In: *Journal of Applied Physics* 37.3 (1966), pp. 1404–1405. DOI: 10.1063/1.1708493.

[144] H. Jia et al. "Electric dipole moment as descriptor for interfacial Dzyaloshinskii-Moriya interaction." In: *Physical Review Materials* 4.2 (2020), p. 024405. DOI: 10.1103/PhysRevMaterials.4.024405.

[145] A. Belabbes et al. "Oxygen-enabled control of Dzyaloshinskii-Moriya Interaction in ultra-thin magnetic films." In: *Scientific Reports* 6.1 (2016), p. 24634. DOI: 10.1038/srep24634.

[146] C. Deger. "Strain-enhanced Dzyaloshinskii-Moriya interaction at Co/Pt interfaces." In: *Scientific Reports* 10.1 (2020), p. 12314. DOI: 10.1038/s41598-020-69360-w.

[147] H. Yang et al. "Controlling Dzyaloshinskii-Moriya interaction via chirality dependent atomic-layer stacking, insulator capping and electric field." In: *Scientific Reports* 8.1 (2018), p. 12356. DOI: 10.1038/s41598-018-30063-y.

[148] A. Schellekens et al. "Electric-field control of domain wall motion in perpendicularly magnetized materials." In: *Nature Communications* 3.1 (2012), p. 847. DOI: 10.1038/ncomms1848.

[149] D. Chiba et al. "Electric-field control of magnetic domain-wall velocity in ultrathin cobalt with perpendicular magnetization." In: *Nature Communications* 3.1 (2012), p. 888. DOI: 10.1038/ncomms1888.

[150] T. Koyama et al. "Electric field control of magnetic domain wall motion via modulation of the Dzyaloshinskii-Moriya interaction." In: *Science Advances* 4.12 (2018), eaav0265. DOI: 10.1126/sciadv.aav0265.

[151] T. Srivastava et al. "Large-voltage tuning of Dzyaloshinskii–Moriya interactions: A route toward dynamic control of skyrmion chirality." In: *Nano Letters* 18.8 (2018), pp. 4871–4877. DOI: 10.1021/acs.nanolett.8b01502.

[152] P. Upadhyaya et al. "Electric-field guiding of magnetic skyrmions." In: *Physical Review B* 92.13 (2015), p. 134411. DOI: 10.1103/PhysRevB.92.134411.

[153] Y. Shiota et al. "Induction of coherent magnetization switching in a few atomic layers of FeCo using voltage pulses." In: *Nature Materials* 11.1 (2012), pp. 39–43. DOI: 10.1038/nmat3172.

[154] T. Nozaki et al. "Electric-field-induced ferromagnetic resonance excitation in an ultrathin ferromagnetic metal layer." In: *Nature Physics* 8.6 (2012), pp. 491–496. DOI: 10.1038/nphys2298.

[155] K. Nawaoka et al. "Voltage induction of interfacial Dzyaloshinskii–Moriya interaction in Au/Fe/MgO artificial multilayer." In: *Applied Physics Express* 8.6 (2015), p. 063004. DOI: 10.7567/APEX.8.063004.

[156] K. Nawaoka et al. "Voltage modulation of propagating spin waves in Fe." In: *Journal of Applied Physics* 117.17 (2015). DOI: 10.1063/1.4914060.

[157] Y.-H. Tang and F.-C. Chu. "Interfacial spin-filter assisted spin transfer torque effect in Co/BeO/Co magnetic tunnel junction." In: *Journal of Applied Physics* 117.9 (2015). DOI: 10.1063/1.4913780.

[158] G. Michalicek et al. "Elimination of the linearization error and improved basis-set convergence within the FLAPW method." In: *Computer Physics Communications* 184.12 (2013), pp. 2670–2679. DOI: 10.1016/j.cpc.2013.07.002.

[159] S. Grimme et al. "A consistent and accurate ab initio parametrization of density functional dispersion correction (DFT-D) for the 94 elements H-Pu." In: *The Journal of Chemical Physics* 132.15 (2010). DOI: 10.1063/1.3382344.

[160] K. Nakamura et al. "Role of an interfacial FeO layer in the electric-field-driven switching of magnetocrystalline anisotropy at the Fe/MgO interface." In: *Physical Review B* 81.22 (2010), p. 220409. DOI: 10.1103/PhysRevB.81.220409.

[161] F. Bonell et al. "Reversible change in the oxidation state and magnetic circular dichroism of Fe driven by an electric field at the FeCo/MgO interface." In: *Applied Physics Letters* 102.15 (2013). DOI: 10.1063/1.4802030.

[162] A. W. Wells et al. "Effect of interfacial intermixing on the Dzyaloshinskii-Moriya interaction in Pt/Co/Pt." In: *Physical review B* 95.5 (2017), p. 054428. DOI: 10.1103/PhysRevB.95.054428.

[163] F. Den Broeder, W. Hoving, and P. Bloemen. "Magnetic anisotropy of multilayers." In: *Journal of Magnetism and Magnetic Materials* 93 (1991), pp. 562–570. DOI: 10.1016/0304-8853(91)90404-X.

[164] K. Yakushiji et al. "Ultrathin Co/Pt and Co/Pd superlattice films for MgO-based perpendicular magnetic tunnel junctions." In: *Applied Physics Letters* 97.23 (2010). DOI: 10.1063/1.3524230.

[165] T. Young Lee et al. "High post-annealing stability in [Pt/Co] multilayers." In: *Journal of Applied Physics* 113.21 (2013). DOI: 10.1063/1.4809130.

[166] T. Y. Lee et al. "Effects of Co layer thickness and annealing temperature on the magnetic properties of inverted [Pt/Co] multilayers." In: *Journal of Applied Physics* 114.17 (2013). DOI: 10.1063/1.4829024.

[167] K. Hotta et al. "Atomic-layer alignment tuning for giant perpendicular magnetocrystalline anisotropy of 3 d transition-metal thin films." In: *Physical Review Letters* 110.26 (2013), p. 267206. DOI: 10.1103/PhysRevLett.110.267206.

[168] B. Dupé et al. "Engineering skyrmions in transition-metal multilayers for spintronics." In: *Nature Communications* 7.1 (2016), p. 11779. DOI: 10.1038/ncomms11779.

[169] R. Wu and A. J. Freeman. "Spin–orbit induced magnetic phenomena in bulk metals and their surfaces and interfaces." In: *Journal of Magnetism and Magnetic Materials* 200.1-3 (1999), pp. 498–514. DOI: 10.1016/S0304-8853(99)00351-0.

[170] G. J. Vida et al. "Domain-wall profiles in Co/Ir n/Pt (111) ultrathin films: Influence of the Dzyaloshinskii-Moriya interaction." In: *Physical Review B* 94.21 (2016), p. 214422. DOI: 10.1103/PhysRevB.94.214422.

[171] M. Perini et al. "Domain walls and Dzyaloshinskii-Moriya interaction in epitaxial Co/Ir (111) and Pt/Co/Ir (111)." In: *Physical Review B* 97.18 (2018), p. 184425. DOI: 10.1103/PhysRevB.97.184425.

[172] A. Zarefy et al. "Influence of Co layer thickness on the structural and magnetic properties of multilayers." In: *Journal of Physics D: Applied Physics* 43.21 (2010), p. 215004. DOI: 10.1088/0022-3727/43/21/215004.

[173] Y. C. Won and S. H. Lim. "Interfacial properties of [Pt/Co/Pt] trilayers probed through magnetometry." In: *Scientific Reports* 11.1 (2021), p. 10779. DOI: 10.1038/s41598-021-90239-x.

[174] S. Bandiera et al. "Asymmetric interfacial perpendicular magnetic anisotropy in Pt/Co/Pt trilayers." In: *IEEE Magnetics Letters* 2 (2011), pp. 3000504–3000504. DOI: 10.1109/LMAG.2011.2174032.

[175] T. Lee et al. "Strength of perpendicular magnetic anisotropy at the bottom and top interfaces in [Pt/Co/Pt] trilayers." In: *IEEE Magnetics Letters* 5 (2014), pp. 1–4. DOI: 10.1109/LMAG.2014.2321350.

[176] J. P. Perdew, K. Burke, and M. Ernzerhof. "Generalized gradient approximation made simple." In: *Physical review letters* 77.18 (1996), p. 3865. DOI: 10.1103/PhysRevLett.77.3865.

# Publication

**Rashba-like Spin Textures in Graphene Promoted by Ferromagnet-Mediated Electronic Hybridization with a Heavy Metal**

Beatriz Muñiz Cano, Adrián Gudín, Jaime Sánchez-Barriga, Oliver Clark, Alberto Anadón, Jose Manuel Díez, Pablo Olleros-Rodríguez, Fernando Ajejas, Iciar Arnay, Matteo Jugovac, Julien Rault, Patrick Le Fèvre, François Bertran, **Donya Mazhjoo**, Gustav Bihlmayer, Oliver Rader, Stefan Blügel, Rodolfo Miranda, Julio Camarero, Miguel Angel Valbuena, and Paolo Perna

*ACS Nano* **2024**, *18* (24), 15716–15728.
**DOI:** 10.1021/acsnano.4c02488

# Acknowledgement

Undertaking a doctoral degree in physics has been a profound journey, made possible through the immense support and patience of numerous individuals to whom I owe my gratitude.
First and foremost, I wish to express my deepest appreciation to Prof. Dr. Stefan Blügel for granting me the opportunity to pursue my Ph.D. at his esteemed international and multicultural institute within the Forschungszentrum Jülich. His guidance as the primary referee of this thesis and his persistent assistance throughout my Ph.D. journey have been essential. I am also grateful to Prof. Dr. Carsten Honerkamp for providing a valuable second opinion on the present work.
I would like to express my profound gratitude to Dr. Gustav Bihlmayer, an exceptional supervisor whose commitment and patience have been truly remarkable. His unwavering support and readiness to address my numerous questions have been invaluable. Dr. Bihlmayer's extensive knowledge has significantly enhanced my understanding of scientific concepts, and his thoughtful guidance and insightful feedback have played a crucial role in the development and refinement of this thesis.
My sincere thanks go to Markus Hoffmann for generously sharing his expertise on the FLEUR code and for his invaluable advice. I also extend my gratitude to Dr. Gregor Michalicek for his deep knowledge of the FLEUR code. I have thoroughly enjoyed engaging in discussions with my colleagues at the Peter Grünberg Institute, especially Dr. Imara Lima Fernandes and Uriel Aceves. Their insights have greatly enhanced my programming skills. I also cherished our lunchtime conversations with the Funsilab group, where we explored a wide range of topics. Special thanks go to Ute Winkler and Yasmin Ergüven for their impeccable assistance with all administrative matters.
Last but not least, I would like to express my heartfelt gratitude for the unconditional love and support I receive every day from my friends and family, especially my husband, mother, and sister.

Donya Mazhjoo

Band / Volume 286
***Ab initio* investigation of intrinsic antiferromagnetic solitons**
Amal Jawdat Nayef Aldarawsheh (2024), xv, 164 pp
ISBN: 978-3-95806-785-1

Band / Volume 287
**Understanding the dynamics of Plant-Bacteria-Bacteriophage interactions as a means to improve plant performance**
S. H. Erdrich (2024), ix, 176 pp
ISBN: 978-3-95806-791-2

Band / Volume 288
**Prediction of Magnetic Materials for Energy and Information Combining Data-Analytics and First-Principles Theory**
R. Hilgers (2024), xv, 215 pp
ISBN: 978-3-95806-795-0

Band / Volume 289
**Biodegradation and microbial upcycling of plastics**
J. de Witt (2025), XVI, 259 pp
ISBN: 978-3-95806-804-9

Band / Volume 290
**Practical Methods for Efficient Analytical Control in Superconducting Qubits**
B. Li (2025), 202 pp
ISBN: 978-3-95806-807-0

Band / Volume 291
**Ab initio investigation of topological magnetism in two-dimensional van der Waals heterostructures**
N. Abuawwad (2025), xviii, 135 pp
ISBN: 978-3-95806-808-7

Band / Volume 292
**Tolerance engineering of Pseudomonas for the efficient conversion and production of aldehydes**
T. Lechtenberg (2025), XVI, 185 pp
ISBN: 978-3-95806-817-9

Band / Volume 293
**Exploring the process window for production of itaconic, 2-hydroxyparaconic, and itatartaric acid with engineered *Ustilago* strains**
P. Ernst (2025), x, 145 pp
ISBN: 978-3-95806-825-4

Schriften des Forschungszentrums Jülich
Reihe Schlüsseltechnologien / Key Technologies

Band / Volume 294
**Surface Plasmon Resonance Microscopy for the Characterization of Cell-Substrate Distances**
J. Bednar (2025), xxiii, 187 pp
ISBN: 978-3-95806-830-8

Band / Volume 295
**Microfluidic-MEA hybrid systems for electrophysiological recordings of neuronal co-cultures**
J. Stevanović (2025), ix, 186 pp
ISBN: 978-3-95806-831-5

Band / Volume 296
**Structural and Magnetic Properties of Biocompatible Iron Oxide Nanoparticles for Medical Applications**
A. Nasser (2025), xii, 140 pp
ISBN: 978-3-95806-837-7

Band / Volume 297
**Metabolic engineering of *Pseudomonas taiwanensis* for the improved production of styrene**
J. Rönitz (2025), XII, 147 pp
ISBN: 978-3-95806-841-4

Band / Volume 298
**Elucidation of anti-viral strategies in *Streptomyces***
B. U. Rackow (2025), xii, 148 pp
ISBN: 978-3-95806-842-1

Band / Volume 299
**Ab initio investigations of spin-orbit functionalized graphene**
D. Mazhjoo (2025), 163 pp
ISBN: 978-3-95806-847-6

Weitere ***Schriften des Verlags im Forschungszentrum Jülich*** unter
http://wwwzb1.fz-juelich.de/verlagextern1/index.asp

Schlüsseltechnologien / Key Technologies
Band / Volume 299
ISBN 978-3-95806-847-6

Mitglied der Helmholtz-Gemeinschaft

